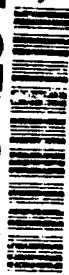


AD-A275 254



✓

ESL-TR-92-24

# CHEMICAL MECHANISMS OF TOXIC SOLUTE INTERACTIONS WITH SOIL CONSTITUENTS

C.T. JOHNSTON, M.T. VALA

DEPT. OF SOIL SCIENCE/CHEMISTRY  
DEPT.  
UNIVERSITY OF FLORIDA  
GAINESVILLE FL 32611

APRIL 1993

FINAL REPORT

DECEMBER 1988 - DECEMBER 1991

APPROVED FOR PUBLIC RELEASE:  
DISTRIBUTION UNLIMITED

DTIC  
ELECTE  
FEB 02 1994  
S B D



94-03367



ENVIRONICS DIVISION  
Air Force Civil Engineering Support Agency  
Civil Engineering Laboratory  
Tyndall Air Force Base, Florida 32403



94 2 01 193

REPORT DOCUMENTATION PAGE			Form Approved OMB No. 0704-0188	
<small>Public reporting burden for this collection of information is estimated to average 1 hour per response, including the time for reviewing instructions, searching existing data sources, gathering and maintaining the data needed, and completing and reviewing the collection of information. Send comments regarding this burden estimate or any other aspect of this collection of information, including suggestions for reducing this burden, to Washington Headquarters Services, Directorate for Information Operations and Reports, 1215 Jefferson Davis Highway, Suite 1204, Arlington, VA 22202-4302, and to the Office of Management and Budget, Paperwork Reduction Project (0704-0188), Washington, DC 20503.</small>				
1. AGENCY USE ONLY (Leave blank)	2. REPORT DATE April 1993	3. REPORT TYPE AND DATES COVERED Final, 12/88 to 12/91		
4. TITLE AND SUBTITLE  Chemical Mechanisms of Toxic Solute Interactions with Soil Constituents		5. FUNDING NUMBERS  PE 6.1 PR 1900 TA 2099		
6. AUTHOR(S)  Clifford T. Johnston Martin T. Vala				
7. PERFORMING ORGANIZATION NAME(S) AND ADDRESS(ES)  Dept. of Soil Science / Chemistry Dept. University of Florida Gainesville, FL 32611		8. PERFORMING ORGANIZATION REPORT NUMBER  CEL-TR-92-24		
9. SPONSORING/MONITORING AGENCY NAME(S) AND ADDRESS(ES)  Air Force Civil Engineering Support Agency RAVC, 139 Barnes Drive Tyndall AFB, FL 32403-5319		10. SPONSORING/MONITORING AGENCY REPORT NUMBER		
11. SUPPLEMENTARY NOTES				
12a. DISTRIBUTION / AVAILABILITY STATEMENT  Approved for Public Release Distribution Unlimited		12b. DISTRIBUTION CODE		
13. ABSTRACT (Maximum 200 words)  This report describes fundamental studies on the interaction of several organic solutes commonly found in fuels and solvents with soil and subsurface components. The principal objective was to determine the chemical mechanisms of interaction of these organic molecules and soil sorbents. Ultraviolet, infrared, gravimetric, and matrix-isolation methods were used to characterize the sorption of water and fuel compounds on a model soil consisting of montmorillonite clay. The results showed that water can compete for surface sites more effectively than the organic sorbents that were studied. Chemisorption reactions of unsaturated fuel compounds can occur on natural clays via transfer of an electron from the fuel molecule to an iron or copper cation on a clay surface, but only under very dry conditions.				
14. SUBJECT TERMS Montmorillonite clay, fuels, infrared spectroscopy, ultraviolet-visible spectroscopy, gravimetric analysis, matrix isolation, sorption			15. NUMBER OF PAGES	
			16. PRICE CODE	
17. SECURITY CLASSIFICATION OF REPORT Unclassified	18. SECURITY CLASSIFICATION OF THIS PAGE Unclassified	19. SECURITY CLASSIFICATION OF ABSTRACT Unclassified	20. LIMITATION OF ABSTRACT Unlimited	

## **Executive Summary**

### **A. OBJECTIVES**

The main goal of this research project was to study the interactions of selected organic pollutants with soil constituents on a mechanistic level. Experiments were designed to study the behavior of the organic pollutants on the surfaces of selected soil and subsurface materials. The central questions addressed by these research activities were the following:

- What was the overall sorption behavior of the organic pollutant on the selected solid phase?
- What was the chemical identity of the sorbed pollutant?
- Did the organic pollutants undergo chemical transformations (i.e., chemisorption reactions) on the surface?
- How was the sorption behavior influenced by water content and by the type of exchangeable metal cation present on the surface?
- What surface functional groups were involved in binding the organic pollutant to the surface?

The long-range goal of this research effort was to contribute information about the fate and transport of organic pollutants of concern to the Air Force in soil and subsurface environments. Specifically, this research effort focused on the ability of certain soil constituents to irreversibly bind or transform organic pollutants rendering them immobile and non-toxic. Emphasis was placed on understanding the surface interactions on a molecular-level as revealed by surface spectroscopy.

### **B. BACKGROUND**

Previous research on clay-organic reactions involving unsaturated organic compounds has shown that chemisorption reactions can occur under dry conditions if certain exchangeable cations are present. Chemisorption reactions involve the

irreversible transformation of the organic compound on the surface. Although macroscopic sorption data may suggest that a chemisorption reaction has occurred (e.g., hysteresis), surface spectroscopy is the only definitive way to observe the changes of the organic pollutant on the surface. IR and Raman spectroscopy, in particular, are identified in the literature as the most sensitive techniques to probe the surface reactions of interest. Thus, we focused on these methods to explore the interaction of selected organic pollutants on solid phases identified as being the most likely to facilitate chemisorption reactions. The solid phase of interest for these studies was montmorillonite because this clay has been identified in the literature as an active chemisorption-promoting surface. In addition, montmorillonite is ubiquitous in soils and sediments and has an extremely high surface area ( $> 700 \text{ m}^2/\text{g}$ ). Thus, montmorillonite is often the dominant solid phase present in soils and sediments on a surface area basis.

### C. SCOPE

We investigated the chemisorption reactions of several organic pollutants on high-charge and low-charge montmorillonite clays exchanged with one of the following metal cations:  $\text{Na}^+$ ,  $\text{Ca}^{2+}$ ,  $\text{K}^+$ ,  $\text{Co}^{2+}$ , and  $\text{Cu}^{2+}$ . A gravimetric / FTIR cell was designed to collect the FTIR spectrum and gravimetric data simultaneously. This allowed spectroscopic adsorption and desorption isotherms to be collected. Water content was one of the key factors in influencing the chemisorption reactions. Consequently, the sorption studies included sorbed water as a variable. Preliminary studies had shown that the chemisorption reaction involved the formation of radical organic cations. Thus, a cell was designed to produce, isolate, and observe the radical organic cations of interest.

### D. METHODOLOGY

Previous studies suggested that a single-electron-transfer (SET) reaction occurred between the sorbed organic species and the exchangeable metal cation. This mechanism was proposed on the basis of changes that took place in the IR, UV-visible, and electron spin resonance (ESR) spectra of the clay organic complex. No attempt had been made previously, however, to relate the changes in the IR spectra with either the UV-visible or ESR data. Furthermore, the amount of organic sorbed on the surface had not been determined in these spectroscopic studies. Thus, the

approach adopted here was to design a cell that would allow both FTIR and UV-visible spectra to be obtained on the sample and permit the mass of the clay-organic complex to be monitored. Our objective was to obtain macroscopic sorption data on the clay-organic complexes of interest and to relate the observed spectroscopic data to the adsorption or desorption isotherms.

Although the formation of radical organic cations on the surface of the clay had been proposed, no direct evidence had been obtained to confirm or deny their presence. Thus, spectroscopic studies of the radical organic cations themselves were undertaken to characterize their vibrational and electronic spectra. With this data in hand, the presence of the radical organic cations on the clay surface could be determined.

## **E. TEST DESCRIPTION**

Experiments were performed using a combined macroscopic / spectroscopic approach. Vapor phase desorption isotherms and FTIR spectra were obtained on selected sorbate-sorbent systems simultaneously. Diagnostic bands in the FTIR spectra were used as indicators of the chemisorption reaction. These diagnostic bands were determined from the literature and from the studies on the isolated radical organic cations.

## **F. RESULTS**

Under dry conditions, Fe-exchanged and Cu-exchanged montmorillonite clay samples promoted chemisorption reactions involving aromatic cations. The presence of radical organic cations was confirmed by spectroscopic studies of the isolated radical cations. Thus, the proposed single electron transfer (SET) reaction mechanism was supported by the spectroscopic studies. The ability of montmorillonite to promote chemisorption reactions depended strongly on the nature of the exchangeable metal cation on the water content. Chemisorption reactions only occurred for Cu- and Fe-exchanged clays. Furthermore, the presence of water reduced the rate of reaction. Water functioned as a ligand that could effectively compete for coordination sites around the metal cation. At lower water contents, coordination sites around the metal cation were made available allowing the organic sorbents to coordinate to the metal cation and receive an electron from the metal cation.

The active sorption site for the chemisorption reactions were the sites of isomorphic substitution within the clay occupied by  $\text{Fe}^{3+}$  or  $\text{Cu}^{2+}$ . The initial step of the SET reaction required removal of water from the metal cation. Upon coordination of the organic sorbent to the metal cation, a SET reaction could take place if the ionization potential of the metal cation was favorable. The electron transfer step was evidenced by the strong color change and strong perturbation to the IR spectra of the adsorbed species. The two diagnostic vibrational bands were the  $\nu_{19}$  (C-C ring stretch) and  $\nu_{11}$  (out-of-plane C-H bending) bands. The frequency of the  $\nu_{19}$  band decreased and that of the  $\nu_{11}$  band increased upon chemisorption. A theoretical model was used to predict the frequencies of the neutral and cationic organic species. In the case of 1,4-dimethoxybenzene, the predicted vibrational frequencies agreed well with experimental results.

In addition to the organic sorbents, the vibrational properties of water was examined during the sorption process. Upon dehydration of the clay-water system, the frequency of the  $\nu_2$  band decreased. This decrease in frequency was examined as a function of water content for Na-, K-, Co- and Cu-exchanged montmorillonite clays. For each cation a similar trend was observed. At high water contents, the vibrational properties of water were similar to those of bulk water. Upon lowering the water content, however, the position of the  $\nu_2$  band decreased and the molar absorptivity of this band increased. The data indicate that at low water content the coordinated water molecules are highly polarized by the metal cations. As a result of this polarization, the water molecules are more acidic at low water contents. Thus, the ability of the clays to promote the chemisorption reactions at low water contents is attributed, in part, to the increased polarization of the water molecules by the metal cations.

## G. CONCLUSIONS

These studies have shown that water influences the sorption of organic solutes on mineral surfaces. In fact, water can compete for surface sites more effectively than the organic sorbents studied here. This is due to hydration of the exchangeable metal cations on the surface, thus, rendering the surface with an increased hydrophylic character. Upon removal of water from the system, chemisorption reactions of unsaturated organic sorbents may occur provided that Fe- or Cu- cations are present. The role of the cation is to accept an electron from the coordinated organic solute species forming a radical organic cation on the surface.

Although  $\text{Cu}^{2+}$  cations are only present in trace amounts in soil and subsurface environments,  $\text{Fe}^{3+}$  is ubiquitous. Thus, the potential for chemisorption reactions in soil and subsurface environments will depend on the type of mineral surfaces present, amount of free  $\text{Fe}^{3+}$  available, and the water content.

## H. RECOMMENDATIONS

This research has provided molecular-level insight into a potentially significant means of attenuating the toxicity and concentration of several organic compounds. The extent of SET reactions that could occur on natural sorbents would depend on the mineralogy, nature of exchangeable cations, and on the water content. The results obtained in this study have identified the diagnostic bands of the organic solutes and have shown how water influences the SET reactions. The data obtained in this research effort could be extended to include a broader class of Air Force related organic compounds and natural sorbents. One hypothesis that would be especially useful to test would be the ability of free  $\text{Fe}^{3+}$  to promote SET reactions. It is not clear how naturally occurring humic substances would effect SET reactions. One possibility is that the hydrophobic organic solutes would partition into the humic substances and would not be able to participate with mineral surfaces of interest. Finally, all of the chemisorption reactions required removal of water. It is not clear if the low water contents required to facilitate these reactions could be obtained in field conditions.

DTIC QUALITY INSPECTED &

Accession For	
NTIS GRA&I	<input checked="" type="checkbox"/>
DTIC TAB	<input type="checkbox"/>
Unannounced	<input type="checkbox"/>
Justification	
By	
Distribution/	
Availability Codes	
Dist	Avail and/or Special
A-1	

## PREFACE

This report was prepared by members of the Departments of Chemistry and Soil Science of the University of Florida, Gainesville, FL 32611. The work was sponsored by the Civil Engineering Laboratory of the Air Force Civil Engineering Support Agency (AFCESA/RAVC), Tyndall Air Force Base, FL 32403-5319.

This report summarizes work accomplished between December 1988 and December 1991 under the direction of professors Clifford T. Johnston of the Department of Soil Science and Martin T. Vala of the Department of Chemistry.

Dr. Daniel A. Stone was the AFCESA/RAVC project officer for this contract from its inception through December 1991. Dr. Terence L. Tipton was the project officer after December 1991.

This report has been reviewed by the Public Affairs Office (PA) and is releasable to the National Technical Information Service (NTIS). At NTIS, it will be available to the general public including foreign nationals.

This technical report has been reviewed and is approved for publication.

*Terence L. Tipton*

TERENCE L. TIPTON, GS-12  
Research Chemist

*Neil J. Lamb*

NEIL J. LAMB, Colonel, USAF, BSC  
Chief, Environics Division

*Howard R. Meyer Jr.*

HOWARD R. MEYER Jr., Maj, USAF  
Chief, Environmental Interactions  
R&D Branch

## TABLE OF CONTENTS

<b>I</b>	<b>INTRODUCTION</b>	<b>1</b>
	<b>A. OBJECTIVES</b>	<b>1</b>
	<b>B. BACKGROUND</b>	<b>1</b>
	1. Need for Mechanistic Information	1
	2. Vibrational Spectroscopy of Adsorbed Species	2
	3. Spectroscopic Characterization of Environmental Particles	3
	4. Molecular Probes and Reporter Groups	5
	<b>C. APPROACH</b>	<b>6</b>
<b>II</b>	<b>VIBRATIONAL PROBE STUDIES OF WATER INTERACTIONS WITH MONTMORILLONITE</b>	<b>9</b>
	<b>A. INTRODUCTION</b>	<b>9</b>
	<b>B. EXPERIMENTAL</b>	<b>10</b>
	1. Preparation of Clay Minerals	10
	2. Preparation of Self-Supporting Films	11
	3. FTIR/Gravimetric Cell	12
	4. Desorption Isotherms	14
	<b>C. RESULTS AND DISCUSSION</b>	<b>14</b>
	1. Water Desorption Isotherms	14
	2. FTIR/Gravimetric Spectra	16
<b>III</b>	<b>PHYSISORPTION OF AROMATIC HYDROCARBONS ON MONTMORILLONITE</b>	<b>29</b>
	<b>A. INTRODUCTION</b>	<b>29</b>
	<b>B. RESULTS AND DISCUSSION</b>	<b>31</b>

1. Spectroscopic Adsorption Isotherm	31
2. Physisorbed p-Xylene on Co-montmorillonite	37
<b>IV CHEMISORPTION OF AROMATIC HYDROCARBONS ON MINERAL SURFACES</b>	<b>41</b>
A. INTRODUCTION	41
B. EXPERIMENTAL	45
C. RESULTS AND DISCUSSION	47
1. p-Xylene	47
a. Chemisorption of p-Xylene on Cu-montmorillonite	47
b. 750 to 950 $\text{cm}^{-1}$ Region	50
c. 1200 to 1800 $\text{cm}^{-1}$ Region	50
d. UV-Visible Spectra	52
2. PDMOB	56
a. FTIR Spectra of PDMOB Sorbed on Cu-montmorillonite	58
b. Electronic Spectra of PDMOB Sorbed on Cu-montmorillonite	62
c. Discussion	62
D. CONCLUSION	70
<b>V MATRIX ISOLATION STUDIES OF ORGANIC CATIONS</b>	<b>71</b>
A. INTRODUCTION	71
B. EXPERIMENTAL APPARATUS AND PROCEDURES	72
1. Matrix Isolation System	72
2. Spectroscopic Instruments	73
3. Ionization Sources	74
a. Photoionization	74

b. Conical Pulse Glow Discharge	74
c. Electron Bombardment	79
d. Hemispherical Pulse Glow Discharge	79
4. Mass Spectrometer	81
a. Interfacing	81
b. Programs	83
1. Masspec.C	83
2. Mastrack.C	86
3. Pulse.C	93
5. Ion Quadrupole Deflector	100
C. RESULTS AND DISCUSSION	105
1. Naphthalene	105
a. Experimental Results	105
b. Discussion	109
1. Are the New Bands Due to Naphthalene Radical Cation?	109
2. Comparison to Theoretical Frequencies	111
3. Mechanism of Enhanced Ionization and Stabilization	113
4. Cation Yield and Absolute Infrared Band Intensities	114

2. Para-dichlorobenzene	116
a. Experimental Results	116
b. Theoretical results	128
c. Discussion	137
3. Para-dimethoxybenzene	140
a. Experimental results	140
b. Theoretical Results	146
c. Discussion	151
VI CONCLUSION	154
VII RECOMMENDATION	155
VIII REFERENCES	156
IX APPENDIX	170

## LIST OF FIGURES

Figure	Title	Page
1.	Schematic of the In Situ FTIR/Gravimetric Cell	13
2.	Desorption Isotherms of Water from Self-Supporting Clay Films of Na-SAz1, Na-SWy1, and Cu-SAz1	15
3.	Comparison of the Desorption Isotherm of Water from a Self-Supporting Clay Film of Na-SAz1 to the FTIR Spectra (right side) of Water Sorbed on the Na-SAz1 Clay Film.	17
4.	FTIR Spectrum of Water Sorbed on a Self-Supporting Film of Na-SAz1 at a Relative Water Vapor Pressure of 0.008.	18
5.	Basal Spacing (Å) of a Na-SAz1 Self-Supporting Clay Film Plotted as a Function of Water Content	22
6.	Position of the $\nu_2$ Band of Water Sorbed on SAz-1 Montmorillonite Exchanged with $\text{Na}^+$ , $\text{K}^+$ , $\text{Co}^{+2}$ and $\text{Cu}^{+2}$ Plotted as a Function of Water Content Expressed as the Number of Water Molecules Sorbed Per Exchangeable Metal Cation.	23
7.	Position of the $\nu_2$ Band of Water as a Function of the d-Spacing	24
8.	Change in the Molar Absorptivity of the $\nu_2$ Band as a Function of Water Content	27
9.	FTIR Spectra of Co-montmorillonite Exposed to $\text{P}_2\text{O}_5$ and p-Xylene	32
10.	Surface Loading of Water and p-Xylene on Co-montmorillonite as a Function of Time	36
11.	FTIR Spectra in the 1200 to 1800 $\text{cm}^{-1}$ Region of a Self Supporting Film of Cu-exchanged and Co-exchanged SAz-1 Montmorillonite Exposed to p-Xylene Vapor	38
12.	FTIR Spectra of a CoX Exposed to p-Xylene Vapor	39
13.	FTIR Spectra of Cu-montmorillonite Exposed to p-Xylene Vapor	48
14.	Growth of Selected Bands Observed in the CuX - p-Xylene Complex	49
15.	FTIR Spectra of Cu-exchanged and Co-exchanged SAz-1 Montmorillonite Exposed to p-Xylene Vapor	51

16. Ultraviolet-Visible Spectra of Cu-montmorillonite Exposed to p-Xylene Vapor	53
17. Surface Loading of H <sub>2</sub> O and PDMOB on the Cu-montmorillonite Film	57
18. FTIR Spectra of Cu-montmorillonite and of PDMOB on Cu-montmorillonite	59
19. UV-Visible Spectra of Cu-montmorillonite and of PDMOB Sorbed onto Cu-montmorillonite	63
20. Integrated intensities of Selected IR and UV-Visible Bands of PDMOB on Cu-montmorillonite Plotted as a Function of Time.	68
21. Visible-Ultraviolet Spectrum of Pyrene in Boric Acid Matrix at Room Temperature	75
22. Visible-Ultraviolet Spectrum of Anthracene in Boric Acid Matrix at Room Temperature	76
23. Conical Pulsed Glow Discharge Apparatus	78
24. Electron Bombardment Source	80
25. Hemispherical Pulsed Glow Discharge Source	82
26. Schematic of Mass Spectrometer, Controller, Digital Data Acquisition (DDA) Board and Computer.	84
27. Single Mass Spectrometric Scan in Range 1 to 500 amu	85
28. Ten Accumulated Mass Spectrometric Scans	87
29. One Hundred Accumulated Mass Spectrometric Scans	89
30. One Thousand Accumulated Mass Spectrometric Scans	90
31. Ten Thousand Accumulated Mass Spectrometric Scans	90
32. Effect on Mass Spectrum (10 - 36 amu range) of Varying Signal Filters	91
33. Time Response of Mass Spectrometer Set on 40 amu (for Argon) with Needle Valve Closed and Pulsed Valve Operational. 5000 Data Points Per Accumulation; 10 Accumulations	94

34. Time Response of Mass Spectrometer Set on 40 amu (for Argon) with Needle Valve Closed and Pulsed Valve Operational. 500 Data Points Per Accumulation; 100 Accumulations	95
35. Time Response of Mass Spectrometer Set on 40 amu (for Argon) with Needle Valve Closed and Pulsed Valve Operational. 50 Data Points Per Accumulation; 1000 Accumulations	96
36. Time Response of Mass Spectrometer Set on 40 amu (for Argon) with Needle Valve Open and Pulsed Valve Operational. 5000 Data Points Per Accumulation; 10 Accumulations	97
37. Time Response of Mass Spectrometer Set on 40 amu (for Argon) with Needle Valve Open and Pulsed Valve Operational	98
38. Time Response of Mass Spectrometer Set on 40 amu (for Argon) with Needle Valve Open and Pulsed Valve Operational	99
39. Quadrupole Ion Deflector	101
40. Visible-Ultraviolet Spectra of Neutral and Cationic Naphthalene in Ar at 12 K between 290 and 700 nm	107
41. Infrared Spectra of Neutral (bottom) and Neutral and Cationic (top) Naphthalene in Ar at 12 K. New Peaks Due to the Cation are Marked with Solid Circles	108
42. Correlation of 675 nm Visible Band Absorbance of Naphthalene Cation with 1218 $\text{cm}^{-1}$ IR Band Absorbance.	110
43. UV Spectrum of Neutral para-Dichlorobenzene (PDCB) in Ar Matrix at 12 K, Showing Band System at 280 nm	117
44. Fourier Transform Infrared Spectrum of Neutral PDCB (bottom) and Neutral Plus Cation PDCB (top) in Ar Matrix at 12 K	121
45. Correlation of 520 nm Visible Absorption Band Absorbance of PDCB Cation with Four IR Band Absorbances	122
46. Fluorescence and Resonance Raman Bands of PDCB Cation (Ar Matrix, 12 K) Excited by 514.5 nm Ar Ion Laser Radiation	124
47. Fluorescence of PDCB Cation (Ar Matrix, 12 K) Excited by 488.0 nm Ar Ion Laser Radiation	125

48. Schematic of HOMO (Highest Occupied Molecular Orbital) of PDCB Cation (Adapted from Reference 36)	132
49. Visible/UV Spectra of PDMOB Neutral (< 300 nm) and Radical Cation (300 nm << 470 nm) in an Ar Matrix at 2 K	141
50. Infrared Spectra of Discharged PDMOB/CCl <sub>4</sub> /Ar Mixture (top) Showing Neutral and Radical Cation (black circles) Bands and Neutral PDMOB Molecules in an Ar Matrix at 12 K.	142
51. Correlation Diagram between 460 nm Visible Band and Four IR Peaks (Varying Absorbances Produced by Different Photolysis 7 Times)	144
52. Visible/UV Spectra of: A) Unphotolyzed PDMOB Radical Cation Formed From Discharged PDMOB/CCl <sub>4</sub> /Ar mMixture; B) Spectrum A After 25 min. Photolysis; C) Discharged CCl <sub>4</sub> /Ar Mixture Before Photolysis; D) Spectrum C After 25 min. Photolysis.	145

## LIST OF TABLES

Table	Description	Page
1.	Determination of d-Spacing from Interference Fringes	21
2.	Vibrational Band Assignments of p-Xylene	34
3.	Compounds Susceptible to Clay-Mediated SET Reactions	42
4.	Infrared and Raman Frequencies $\text{cm}^{-1}$ of PDMOB, PDMOB <sup>+</sup> , and PDMOB Sorbed on Cu-montmorillonite	61
5.	Mass Spectrometric Scanning Speeds	92
6.	Theoretical and Experimental Frequencies and Intensities for Neutral and Cationic Naphthalene	112
7.	Visible-Ultraviolet Absorption Bands of para-Dichlorobenzene (PDCB) Cation in Ar at 12 K	119
8.	Comparison of para-Dichlorobenzene Cation Optical Absorption Transitions with Photoelectron Bands	120
9.	Resonance Raman Bands of para-Dichlorobenzene Cation in Ar at 12 K	126
10.	Fluorescence Bands of PDCB Radical Cation in Ar/12 K	127
11.	Calculated and Observed Electronic Spectra of PDCB Cation	130
12.	Calculated and Observed Vibrational Frequencies for Neutral PDCB	133
13.	Calculated and Observed Vibrational Frequencies for Radical Cation of PDCB	135
14.	Calculated and Observed Vibrational Frequency Shifts Upon Ionization of PDCB	136
15.	Calculated Intrinsic Stretching Frequencies and Force Constants for Neutrals and Radical Cationic PDCB (in parentheses)	136
16.	Optimized Theoretical Bond Distances for Neutral and Cationic para-Dimethoxybenzene (PDMOB)	147

17. Theoretical and Experimental IR Frequencies and Intensities for Neutral PDMOB	147
18. Theoretical and Experimental IR Frequencies and Intensities for Radical Cation PDMOB	149
19. Calculated Intrinsic Stretching Frequencies and Force Constants for Neutral PDMOB and Radical Cation PDMOB (in parentheses)	150

## SECTION I

### INTRODUCTION

#### A. OBJECTIVES

The Air Force Installation Restoration Program has identified several sites of soil and subsurface pollution requiring remedial action. Current knowledge is insufficient to understand the environmental fate of numerous organic pollutants found at those locations, making it difficult to develop technologies that are more cost-effective than current cleanup methods. In addition, there is a need to focus on research to predict organic contaminant transport. The purpose of the project was to study the sorption of several organic chemicals on selected sorbents and to characterize the interaction of the reaction mechanisms on the sorption process.

#### B. BACKGROUND

##### 1. Need for Mechanistic Information

Measurements of the reactions between environmental particles and aqueous solutions are typically limited to providing chemical composition data (References 1,2). These kinds of data are essential to characterize the stoichiometry and, to some extent, the overall pathways of a surface reaction, but they are not sensitive to the details of molecular configuration needed to deduce the reaction mechanism. To do this, molecular spatial and temporal scales on particle surfaces must be resolved through spectroscopic methods adapted to heterogeneous systems containing water.

The molecular spectroscopy of adsorbed chemical species has two principal subdivisions: invasive methods, such as X-ray photoelectron or secondary ion mass

spectrometry, that require sample desiccation and high vacuum; and noninvasive methods that require little or no alteration of a sample from its natural state. Invasive methods have an important role to play in the characterization of solid particle surfaces, but to use them for resolving surface speciation on particles suspended in aqueous solution may not be applicable. Noninvasive surface spectroscopies can be applied in the presence of liquid water; most involve the input and detection of photons. The best known examples are nuclear magnetic resonance (NMR), electron spin resonance (ESR), Raman, Fourier-transform infrared (FTIR), UV-visible fluorescence, X-ray absorption, and Mössbauer spectroscopies, although Brown (Reference 3) has enumerated many others that are available to detect adsorbed molecules. These methods can be used noninvasively in conjunction with in situ probes. A homologous adsorptive probe can be introduced into a sample without affecting the type and distribution of the indigenous surface species; but this will permit or enhance the use of a noninvasive spectroscopic technique. This strategy was used to examine the interaction of selected aromatic hydrocarbons with soil and subsurface materials. The primary thrust was to evaluate the potential of mineral surfaces to facilitate chemisorption reactions. The organics solutes of interest and their cations were examined in detail in rare gas matrices.

## 2. Vibrational Spectroscopy of Adsorbed Species

During the past 15 years, Fourier transform infrared (FTIR) spectrometers have replaced dispersive spectrometers for most applications. In contrast to dispersive infrared instruments, which utilize gratings and slits to pass a nearly monochromatic component to the detector, FTIR spectrometry is based on optical interference between the two beams. The two main advantages of FTIR spectrometry are the optical throughput (referred to as the Jacquinot advantage)

and the multiplex or Fellgett's advantage. A thorough comparison of the performance and optical efficiency of FTIR to that of dispersive IR spectrometers is given by (References 4-7). For comparable resolution and sensitivity in the mid-infrared region, the overall efficiency advantage of FT over dispersive spectrometers has been estimated to be between a factor of 10 and 200 depending on the spectral region (References 5,6).

Application of IR methods to the study of adsorbed species has a long history and has been the subject of numerous reviews (References 4-6,8-12). Of consequence to infrared studies of adsorbed species, these sample presentation methods include diffuse reflectance (DR) (References 5,6,12-21) photoacoustic (PAS) (References 19,20,22-29), and attenuated-total-reflectance (ATR) (References 30-33). The most common sample presentation method for both IR and FTIR studies of mineral surfaces (transmission spectroscopy) was the method chosen for this study. Included in this category are methods using KBr pellets, self-supporting clay films, deposits on IR windows, and compressed wafers. Surface studies and descriptions of transmission cells using this technique have been reviewed extensively (References 4-7,9,10,12,19,34).

### 3. Spectroscopic Characterization of Environmental Particles

Surface studies of natural colloids using spectroscopic methods have been characterized by three common traits. The first is development and application of in situ techniques that provide noninvasive information about a sample to obtain molecular information without disturbing or altering the interface. Conventional surface methods often involve harsh measurement techniques. Electron microscopy and microprobe analysis, inelastic electron tunneling (IETS), electron energy loss (EELS) and X-ray photoelectron spectroscopy, for example, all require that a sample be subjected to high vacuum. These methods have

contributed significantly to understanding mineral surfaces; however, the invasive nature of the sample presentation technique can perturb significantly the interfacial species of interest. It is not clear if the mechanistic information obtained from desiccated systems can be applied to aqueous environments. Mineral surface reactions generally occur at hydrated interfaces; thus, there is a need for techniques that can detect surface species in the presence of water. Although vibrational spectroscopy has long been recognized as a sensitive chemical technique, severe interferences from water, impurities, and bulk adsorbent has restricted its application to environmental substrates. The presence of even trace amounts of water can mask a significant portion of an IR spectrum because of the large molar absorptivity for the O-H stretching and bending modes of H<sub>2</sub>O.

A second trait is the significant improvement in sensitivity and spectral discrimination of vibrational methods over the past few years. The introduction of continuous wave (cw) near-IR lasers, and the application of quantum mid-IR detectors to surface studies are providing researchers with powerful tools to detect adsorbates at submonolayer coverages on those substrates that are difficult to analyze. Two approaches are typically invoked to achieve this objective. The first attempts to enhance the spectroscopic signature of the adsorbate or surface functional group of interest, whereas the second involves minimizing the predominant interferences from the solvent, usually water, and from the bulk adsorbent.

The third trait that has emerged in recent years is the mutual relationship of vibrational and NMR data, as well as their relation to data obtained using experimental methods characterized by different time and energy scales (References 35-37). The molecular structural information obtained by a particular method is intimately related to the time and energy scales probed by the method. In addition, each technique is characterized by a particular set of strengths and limitations for a

given application. Thus, a multiple-technique approach can provide a more complete picture of the system of interest. (References 1,38) Correlation of the spectroscopic data to macroscopic observables, however, is a major objective for molecular studies of mineral surfaces. (References 35,39)

#### 4. Molecular Probes and Reporter Groups

Surface studies try to answer questions relating to the chemical identity of adsorbed species, their location on an adsorbent, including what functional groups are involved, and their molecular dynamics. One approach to characterize surfaces and adsorption phenomena is to use in situ molecular probes that can explore the surface or adsorption process of interest. In situ molecular probes are any solute or solvent species capable of interacting with a surface. For vibrational studies, the molecular probes of choice have diagnostic properties that are sensitive to changes in the local environment around the probe. An example of a diagnostic property is the vibrational modes of coordinated functional groups. As the probe interacts with the surface, its diagnostic properties are perturbed (e.g., change in the intensity or position of a vibrational mode). These changes serve as a powerful way to explore solid-solution and solid-vapor interfaces to gain insight into the chemical and physical properties of a surface. Reporter groups provide another way of obtaining information about the surface. Similar to molecular probes, reporter groups are part of the adsorbent itself, but have diagnostic properties that are perturbed by changes at the interface. Examples of reporter groups are structural hydroxyl groups of clay minerals and the surface function groups of humic substances. Their diagnostic properties include vibrational modes corresponding to the function group of interest.

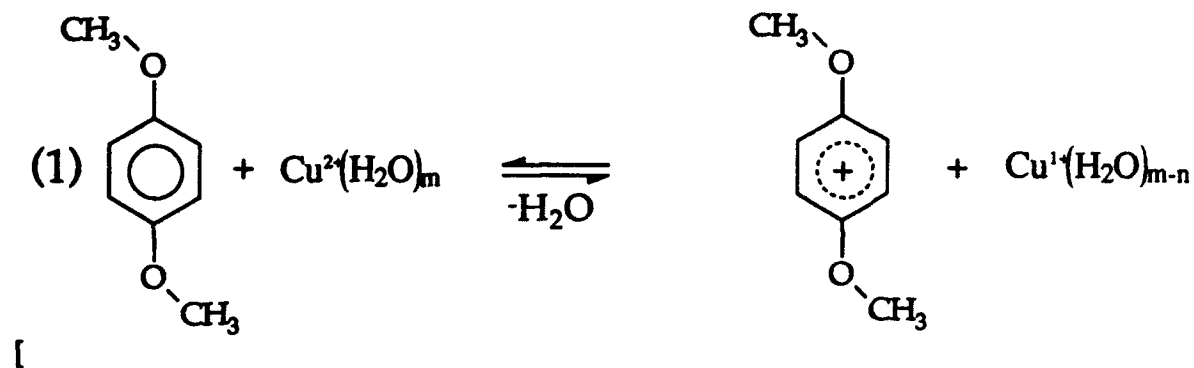
### C. APPROACH

The focus of the present study was to examine the interaction of several organic solutes with specimen sorbents. Because water affects sorption of organics on polar sorbents, the first goal was to use the  $\nu_2$  band of water as a molecular probe of sorbent-water interactions by establishing a direct relationship between the vibrational data and (i) the surface loading of water on the sorbent. In addition to influencing the hydrophobic nature of the sorbent, previous studies have suggested that at low water contents sorbed water molecules become highly polarized. Thus, we were interested in the developing an optical method to evaluate the surface acidity of selected sorbents. Although previous IR studies of water-smectite systems (References 40,42) have shown that water coordinated to exchangeable metal cations is distinct from physisorbed or bulk water, correlation of this data to the amount of water sorbed was either not measured or determined indirectly. Furthermore, the relationship between the vibrational modes and the basal spacing of the clay has not been reported. An in situ Fourier transform infrared (FTIR) gravimetric cell (Reference 34) was used in the present study to collect FTIR spectra and gravimetric data simultaneously for Na, K, Co, and Cu-exchanged SAz-1 montmorillonites.

The second thrust was to investigate the physisorption mechanism(s) of several aromatic solutes on specimen sorbents, and to study the influence of water content on the sorption reaction of interest. p-Xylene was selected as a model solute and Co- and Cu-exchanged montmorillonite was used for the sorbent. The two exchangeable cations, which complement each other, were selected for several reasons; first,  $\text{Cu}^{+2}$  and  $\text{Co}^{+2}$  have almost identical hydration energies, and second, chemisorption of p-xylene has been observed on Cu-montmorillonite (CuX) (References 43-45) but not for CoX due to the difference in the reduction potentials

of the two cations. Our approach utilized a FTIR/gravimetric cell which permitted FTIR spectra and gravimetric data to be collected simultaneously.

The third goal was to determine the chemisorption mechanism(s) for selected solute-sorbent combinations. Emphasis here was placed on developing the optical diagnostics to observe the surface species, examining the influence of the exchangeable metal cation, and evaluating the role of water in hindering the chemisorption reactions. Our primary interest was to examine the single electron transfer reaction of selected aromatic solutes on montmorillonite. In a previous note on the interaction of p-dimethoxybenzene (PDMOB) with Cu-montmorillonite, Soma et al. (References 46) suggested that the Reaction (1):



was reversible depending upon the water content, and that only the monomeric cation species was formed upon dehydration (i.e., dimerization and or polymerization did not occur). Soma et al. (Reference 46) utilized resonance Raman spectroscopy to characterize the adsorbed species by taking advantage of the fact that the chemisorbed species produced a significant electronic transition in the 425 to 475 nm region which was exploited using resonance enhancement (i.e., Raman excitation using the 457.9 nm line of an Ar<sup>+</sup> laser). Although resonance Raman spectroscopy is a useful method to examine the strongly colored, chemisorbed species, it is not a sensitive technique to investigate the presence of

other surface species which are not resonantly enhanced and may have been present. In addition, no definitive evidence has been reported in the literature to support the hypothesis that Reaction (1) is reversible other than the fact that the color change is reversible. We obtained in-situ FTIR, UV-visible and gravimetric data on the sorption of PDMOB and p-xylene by Co- and Cu-montmorillonite (CoX and CuX) to examine the reversibility of Reaction (1), and to observe the electronic and vibrational spectra of the surface species formed upon driving Reaction (1) to the right.

The fourth objective was to investigate the aromatic radical cations isolated in rare gas matrices. Although single-electron-transfer (SET) reaction mechanisms have been proposed to account for many chemisorption reactions, no definitive IR spectra of the radical cations themselves have been published. In previous, surface spectroscopic investigations of the aromatic-clay interactions, it is not clear if the spectra of the adsorbed species correspond to the radical cation of the original aromatic species or to some polymerized by-product.

## SECTION II

### VIBRATIONAL PROBE STUDIES OF WATER INTERACTIONS WITH MONTMORILLONITE

#### A. INTRODUCTION

The interaction of water with smectite surfaces relates to a broad range of applications including abiotic organic transformations (References 47-49), surface acidity (Reference 50), hydrolysis (Reference 51), and catalysis (References 52-54). Understanding the behavior of water on or near surfaces is critical to determining the reactivity of mineral surfaces. Since the early work of Mooney (References 55,56), the behavior of water on smectite surfaces was found to be influenced strongly by the size and charge of the exchangeable metal cations. When less than three molecular layers of water are present in the interlamellar region, the structure of interlamellar water has been shown to be influenced predominantly by exchangeable cations (References 35,41,50,51,53-55,57-64). Spectroscopic investigations of smectite-water interactions suggest that two distinct environments of sorbed water are present (Reference 61): (1) water molecules coordinated to exchangeable metal cations, and (2) physisorbed water molecules occupying interstitial pores, void spaces between exchangeable metal cations and accumulated on external surfaces.

On the basis of NMR (References 53,54,64), complex permittivity (Reference 35) and dielectric (References 63,65) measurements, water molecules coordinated to metal cations are considered to be in less mobile, restricted environments on the clay surface relative to those in bulk water. This molecular "picture" of coordinated water in the interlamellar region is consistent with vibrational studies of water

sorbed on smectites. Russell and Farmer (Reference 40) found that the OH stretching and bending bands of water sorbed on montmorillonite and saponite were perturbed on going from higher to lower hydration states. In the case of the H-O-H bending band ( $\nu_2$  mode) in the 1610 to 1640  $\text{cm}^{-1}$  region, the frequency decreased and its molar absorptivity increased upon dehydration. A similar result was reported by Poinsignon et al. (Reference 41), who observed that the molar absorptivities of the OH stretching and bending bands of sorbed water depended strongly on the hydration energy of the exchangeable metal cation, water content, and surface charge density of the clay surface.

The focus of the present study is to examine the use of the  $\nu_2$  band as a molecular probe of smectite water interactions by establishing a direct relationship between the vibrational data and (1) the surface loading of water on the clay, and (2) the observed basal spacing of the clay. Although previous IR studies of water-smectite systems (References 40,41) have shown that water coordinated to exchangeable metal cations is distinct from physisorbed or bulk water, correlation of this data to the amount of water sorbed was either not measured or determined indirectly. Furthermore, the relationship between the vibrational modes and the basal spacing of the clay has not been reported. An in situ Fourier transform infrared (FTIR) gravimetric cell (References 34) was used to collect FTIR spectra and gravimetric data simultaneously for Na, K, Co, and Cu-exchanged SAz-1 montmorillonites.

## B. EXPERIMENTAL

### 1. Preparation of Clay Minerals

The samples studied were the Cheto montmorillonite (SAz-1) collected from Apache County, Arizona, and the SWy-1 montmorillonite collected from

Crook County, Wyoming. These clays were obtained from the Source Clays Repository of The Clay Minerals Society. A complete description of their physical properties is given by Van Olphen and Fripiat (Reference 66). Prior to size fractionation, a homoionic Na-montmorillonite clay suspension was prepared by placing 10 grams of the raw clay in 1.0 liters of 0.5 M NaCl. The Na-montmorillonite suspension was then washed free of excess salts by repeated centrifugation with distilled-deionized water. The  $< 0.5 \mu\text{m}$  size fraction (estimated spherical diameter, e.s.d.) was collected by centrifugation. Homoionic clay suspensions of Cu-, Co-, and K-exchanged SAz-1 montmorillonite were prepared by adding approximately 0.7 L of 0.05 M solutions of the metal chloride to the salt-free clay suspension (volume = 0.3 L) such that the total volume was 1.0 L; the final pH values of these suspensions were 5. The washing and size fractionation steps were completed within a 24 hour period to minimize degradation of the clay.

## 2. Preparation of Self-Supporting Films

Self-supporting clay films were prepared by washing 20 ml of the stock montmorillonite clay suspensions free of excess salts. The solids concentration of the suspension was diluted to 0.0025 g of clay/(g of suspension). One ml aliquots of this suspension were deposited on a polyethylene sheet and allowed to dry. The dry clay films were then "peeled" off of the polyethylene sheet as self-supporting clay films. These clay films were approximately 2.5 cm in diameter and weighed between 3.1 - 3.4 mg corresponding to cross-sectional density of approximately 0.65 mg/cm<sup>2</sup>. The cation exchange capacity of the clay films was determined by placing a known amount of the dry clay film (3 to 5 mg) in 5 ml. of 0.25 M MgCl<sub>2</sub> and allowing the suspension to stand for 12 hours. A portion of the supernatant was removed for analysis of Na and Cu and the procedure was repeated twice. The cation exchange

capacities of the clay films were  $0.99 \text{ mmol C g}^{-1}$  for Na-SAz-1 and  $1.11 \pm 0.02 \text{ mmol C g}^{-1}$  for Cu-SAz-1.

### 3. FTIR/Gravimetric Cell

For the coupled FTIR/gravimetric measurements, FTIR spectra were obtained using a Bomem DA3.10 FTIR spectrometer equipped with a MCT detector ( $D^* = 3.13 \times 10^9 \text{ cm Hz}^{0.5}$  and a low-frequency cutoff of  $400 \text{ cm}^{-1}$ ) and a KBr beamsplitter. The Bomem DA3.10 spectrometer was controlled through a general-purpose-interface-bus (IEEE-488) interfaced to a DEC Vaxstation-II computer. The unapodized resolution for the FTIR spectra was  $2.0 \text{ cm}^{-1}$ .

A 15-cm pathlength gas cell, fitted with two ZnSe windows, Viton® O-rings, and two stopcocks was modified to interface with a Cahn® controlled-environment Model D200-01 electrobalance (Figure 1). The modified gas cell allowed FTIR spectra and gravimetric data to be collected simultaneously; a complete description of the cell is given in (Reference 34). The cell was connected to a gas/vacuum manifold which permitted the atmosphere in the cell to be controlled and the pressure to be monitored. A self-supporting homoionic montmorillonite clay film was placed on a 0.2 mm Pt hangdown wire in the Cahn electrobalance. The modified gas cell was mounted on an NRC optic table and was positioned using NRC x-y-z translational stages which permitted adjustment of the cell. Mounting the cell on the optic table mechanically decoupled the electrobalance assembly from vibrations originating from the FTIR spectrometer and other sources. The cell was positioned so that the clay film was centered on, and nearly perpendicular to, the incident modulated IR beam in the sample compartment.

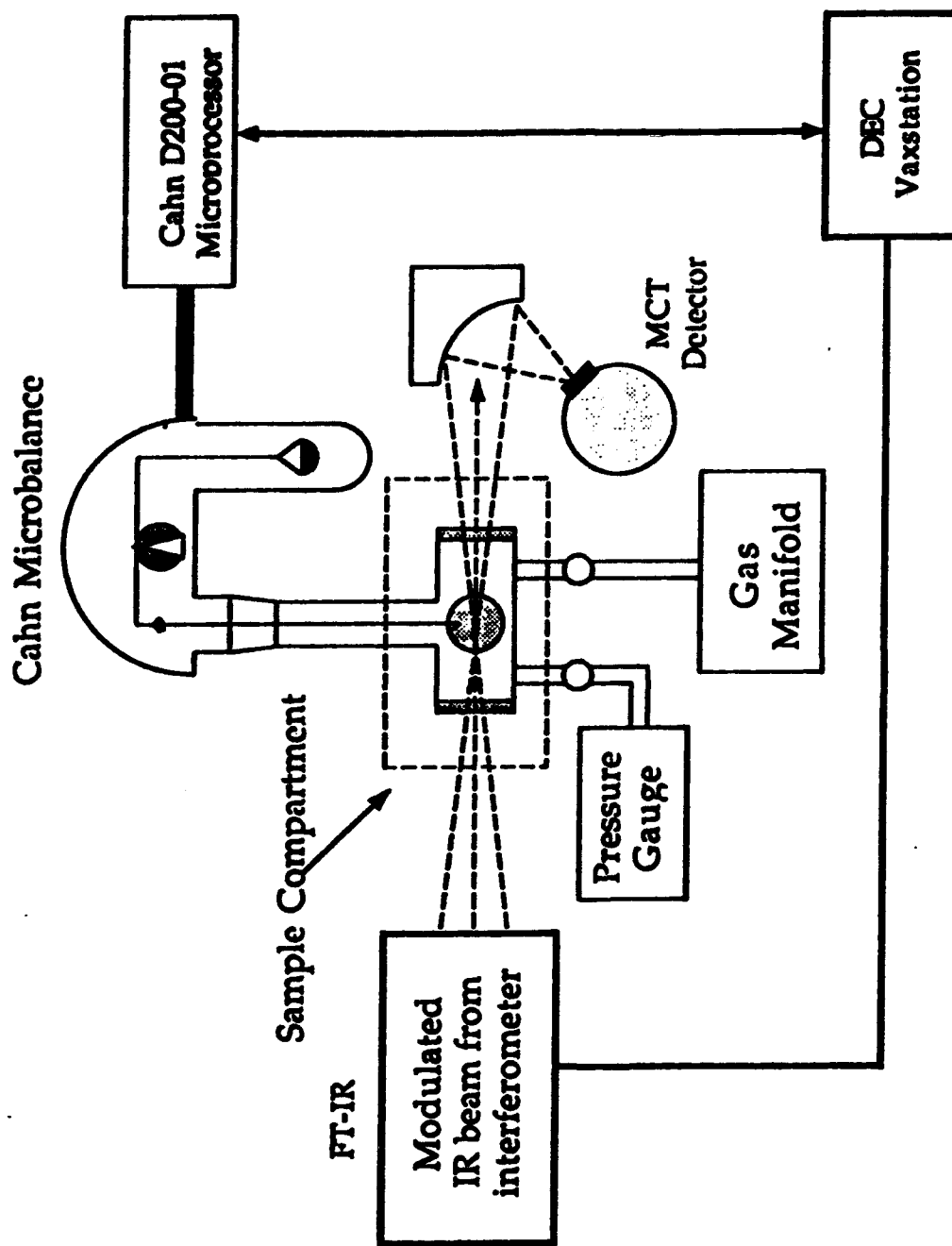


**Figure 1.** Schematic of the In Situ FTIR/Gravimetric Cell Showing a 16 cm Gas Cell Fitted with 50 x 3 mm ZnSe Windows, Viton O-rings, and Two Kontes Stopcocks in Relation to the Bomem DA3 Sample Compartment, Cahn D200 Electrobalance, and Gas/Vacuum Manifold.

#### **4. Desorption Isotherms**

Desorption isotherms were obtained by placing 1.5 ml of water in one of the hangdown tubes of the Cahn® balance after the clay film had been mounted and tared on the balance. The water was then frozen by placing a dewar of liquid nitrogen around the hangdown tube. The Cahn® balance and FTIR cell were then evacuated to 0.005 torr using a roughing pump. At this point, the isolation valve located between the Cahn balance/IR cell and the vacuum manifold was shut and the liquid nitrogen was removed. The water was allowed to slowly equilibrate and the pressure inside the Cahn balance/IR cell was determined using a Baratron gauge. The clay film was allowed to equilibrate for 24 hours in the presence of a small excess of liquid water to obtain the  $p/p_0$  value of 1.0. At this point the mass of the sample, pressure inside the cell, and the temperature were recorded along with the FTIR spectrum of the clay film. The mass of the clay film was recorded every 10 to 30 seconds using a Zenith 286 computer interfaced to the D200 balance. After the clay film had come to equilibrium, a small amount of vapor was removed from the cell by opening the isolation valve and the system was allowed to equilibrate.

### **C. RESULTS AND DISCUSSION**

#### **1. Water Desorption Isotherms**

Desorption isotherms of water from Na- and Cu-exchanged SAz-1, Na-exchanged SWy-1 montmorillonite are compared to the desorption isotherm of Mooney et al. (Reference 55) obtained for a Na-exchanged Wyoming Bentonite shown in Figure 2. As these data indicate, the water sorption characteristics are

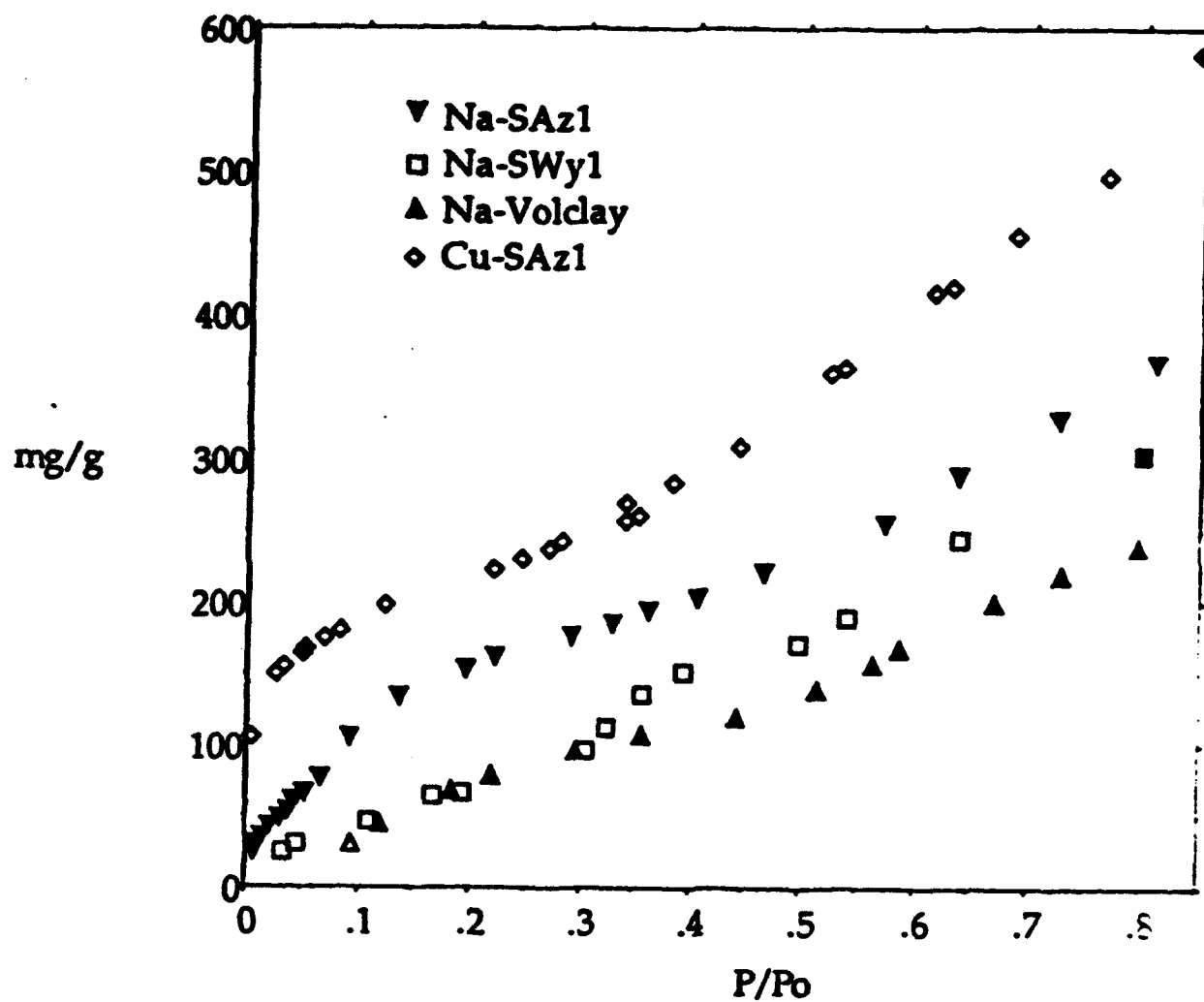


Figure 2. Desorption Isotherms of Water from Self-Supporting Clay Films of Na-SAaz1, Na-SWy1, and Cu-SAaz1

influenced by the type of exchangeable metal cation present on the clay and by the surface charge density. Replacement of  $\text{Na}^+$  cations by  $\text{Cu}^{+2}$  resulted in increased water sorption due to the greater hydration energy of  $\text{Cu}^{+2}$  relative to  $\text{Na}^+$ . Furthermore, increased sorption was observed for the SAz-1 clay ( $1.2 \text{ mmol C g}^{-1}$ ) compared to the Wyoming montmorillonite which reflects the higher surface charge density of the SAz-1 clay ( $1.2 \text{ mmol C g}^{-1}$ ) relative to that of the SWy-1 clay ( $0.9 \text{ mmol C g}^{-1}$ ). Reasonable agreement between the Na-SWy-1 and Mooney et al. (Reference 55) desorption data sets was obtained in the lower partial pressure range ( $0.0 < P/P_0 < 0.3$ ); however, increased uptake was observed for the Na-SWy-1 clay at higher water contents (Reference 55). This difference in water uptake may be caused by a difference in the surface charge density of the Na-SWy-1 montmorillonite to the SPV Volclay used by Mooney et al. (Reference 55).

## 2. FTIR / Gravimetric Spectra

For each data point shown in Figure 2, a corresponding FTIR spectrum was obtained using the FTIR/gravimetric cell shown in Figure 3. The three dimensional plot of the FTIR spectra in the  $1400$  to  $1800 \text{ cm}^{-1}$  region is plotted with the z-axis representing the relative pressure of water. The band shown at  $1640 \text{ cm}^{-1}$  corresponds to the  $\nu_2$  mode (H-O-H bend) of sorbed water on the Na-SAz-1 clay film. The intensity of the  $\nu_2$  band is directly proportional to the amount of water sorbed on the clay; upon lowering the water content, the intensity of the  $\nu_2$  band decreases. Simultaneous collection of the gravimetric and spectroscopic data provides a direct method to correlate the macroscopic sorption characteristics with the observed vibrational data.

The FTIR spectrum of the Na-SAz-1 montmorillonite film obtained at a relative pressure of  $0.008$  is shown in Figure 4 with an expanded portion of the

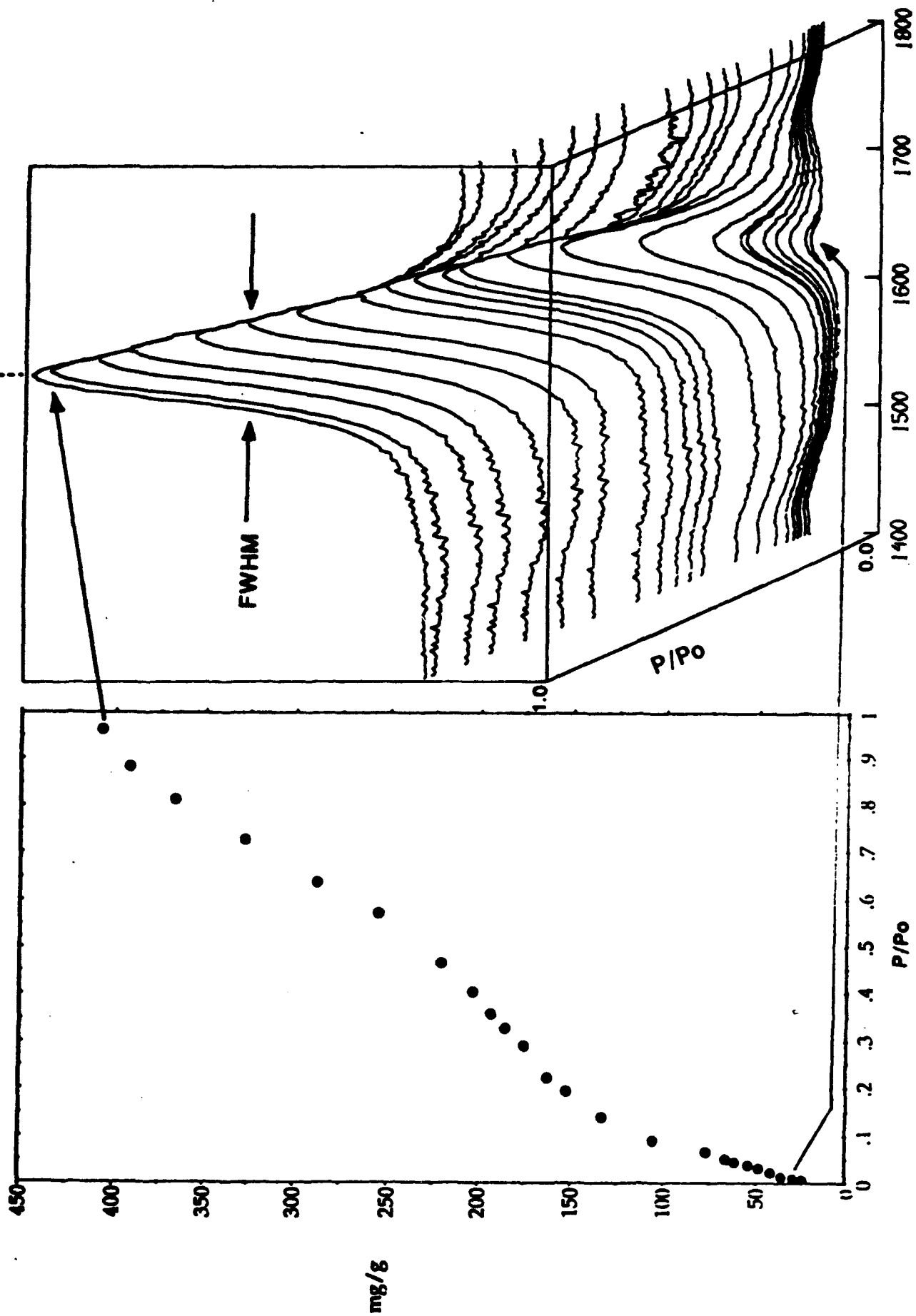
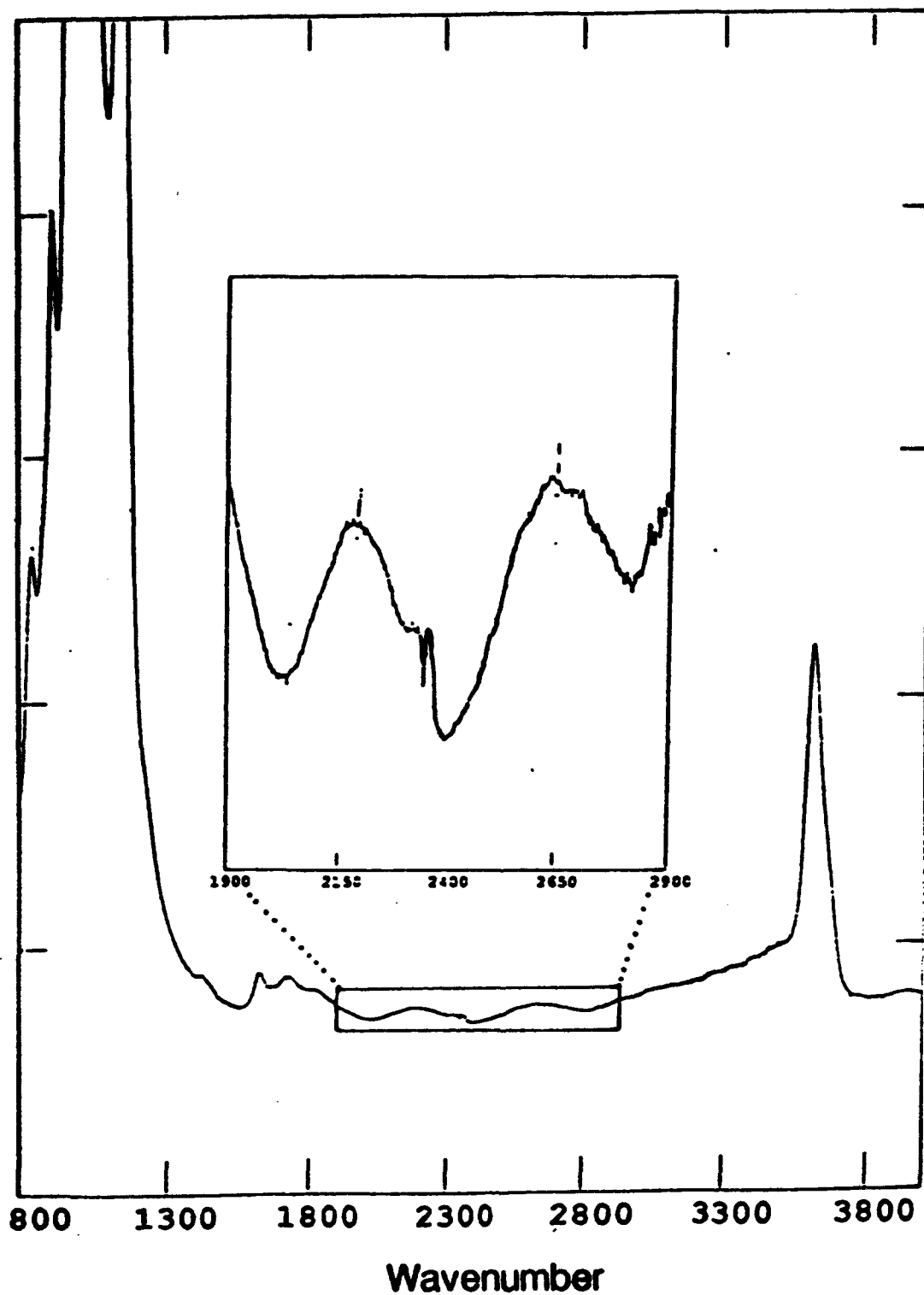


Figure 3. Comparison of the Desorption Isotherm of Water from a Self-Supporting Clay Film of Na-SAZ1 to the FTIR Spectra (right side) of Water Sorbed on the Na-SAZ1 Clay Film



**Figure 4.** FTIR Spectrum of Water Sorbed on a Self-Supporting Film of Na-SAz1 at a Relative Water Vapor Pressure of 0.008.

spectrum in the 1900 to 2900  $\text{cm}^{-1}$  region shown in the inset. The interference fringes shown in the inset of Figure 4 were used to calculate the thickness of the clay film assuming a value of 1.555 for the index of refraction. Similar sets of interference fringes were present in each of the spectra; however, the distance between the fringes varied depending upon the water content. Interference fringes develop from optical interference of internally reflected waves inside the clay film. Assuming that the surface of the clay film was normal to the incident IR beam, the thickness of the clay film was determined according to Equation (1):

$$b = \frac{1}{2n} \frac{N}{(\nu_1 - \nu_2)} \quad (1)$$

where  $b$  is thickness of the sample,  $N$  is the number of interference fringes over the the wavenumber range  $(\nu_1 - \nu_2)$ , and  $n$  is the refractive index of the clay film. The measured fringe spacings and film thickness values are included in Table 1. Since the area and dry mass were known for each clay film, the  $d$ -spacing was calculated from the optical interference fringes using Equation (2). The influence of water content on the  $d$ -spacing of a Na-SAz-1 clay film is shown in Figure 5 as determined by the fringe method (open circles). For comparison, a similar experiment was conducted using a controlled-environment X-ray diffraction cell and the data are shown in Figure 5 by the closed triangles. The fringe-method overestimates the  $d$ -spacing of the clay film which we attribute to the void volume of the clay film due to imperfect stacking of the clay platelets in the film.

$$d\text{-spacing} = \frac{b}{\frac{m_{\text{NaX}} N_A A_1}{MW_{\text{NaX}} A_2}} \quad (2)$$

where:

$m_{\text{NaX}}$ = dry mass of Na-clay film	(g clay film <sup>-1</sup> )
$N_A$ = Avogadro's number = $6.0225 \times 10^{23}$	(molecules mole <sup>-1</sup> )
$A_1$ = molecular area of unit cell ( $a \cdot b$ )	(Å <sup>2</sup> unit cell <sup>-1</sup> )
$MW_{\text{NaX}}$ = formula wt. of NaX = 738	(g mole <sup>-1</sup> )
$A_2$ = cross sectional area of clay film = 1.44	(Å <sup>2</sup> clay film <sup>-1</sup> )
$b$ = measured thickness of clay film	(Å clay film <sup>-1</sup> )

The dry mass of the clay film was determined by plotting the intensity of the OH bending or stretching band versus the mass of the sample and extrapolating to zero intensity. The observed fringe spacings, calculated film thicknesses, and calculated d-spacings are listed in Table 1 for water desorption from the Na-SAz-1 film.

The position of the  $\nu_2$  band, of water sorbed on SAz-1 montmorillonite exchanged with Na<sup>+</sup>, K<sup>+</sup>, Co<sup>+2</sup> and Cu<sup>+2</sup>, is plotted in Figure 6 as a function of water content expressed as the number of water molecules per metal cation. At high water contents, the position of the  $\nu_2$  band was relatively stable. In the case of Na-SAz-1, the high water content limit on the position of the  $\nu_2$  band was 1640 cm<sup>-1</sup> which compares to a value of 1635 for Cu-SAz-1. Upon reducing the water content, however, to less than 10 water molecules per Cu<sup>+2</sup> ion or 6 water molecules per Na<sup>+</sup> ion, the position of the  $\nu_2$  band was observed to shift to lower frequency in agreement with previous IR studies of water on smectite (References 40,41). The shift in frequency can also be related to the d-spacing as illustrated in Figure 7. Similar to the frequency response of the data shown in Figure 6, the position of the OH bending band remains virtually constant until the d-spacing of the clay is reduced to less than 11-12 Å.

**Table 1**      **Determination of d-spacing from interference fringes for Na-SAz1 montmorillonite**

<b>P/P<sub>0</sub></b> <b>(H<sub>2</sub>O)</b>	<b>mg/g</b>	<b>Fringe</b> <b>spacing</b> <b>(cm<sup>-1</sup>)</b>	<b>Film</b> <b>thickness</b> <b>(μm)</b>	<b>d-spacing</b> <b>(Å)</b>
0.962	406.6	282	11.40	16.69
0.884	391.7	289	11.13	16.28
0.811	367.2	289	11.13	16.28
0.726	327.5	298	10.79	15.79
0.637	287.7	313	10.27	15.03
0.571	255.4	331	9.71	14.22
0.465	221.2	345	9.32	13.64
0.327	185.8	358	8.98	13.14
0.290	175.9	360	8.93	13.07
0.221	162.4	365	8.81	12.89
0.196	152.8	365	8.81	12.89
0.137	133.2	380	8.46	12.38
0.090	105.4	392	8.20	12.00
0.064	76.7	410	7.84	11.48
0.050	66.4	412	7.80	11.42
0.042	61.1	415	7.75	11.34
0.036	54.0	415	7.75	11.34
0.031	48.5	429	7.50	10.97
0.022	42.1	428	7.51	10.99
0.007	25.6	430	7.48	10.94

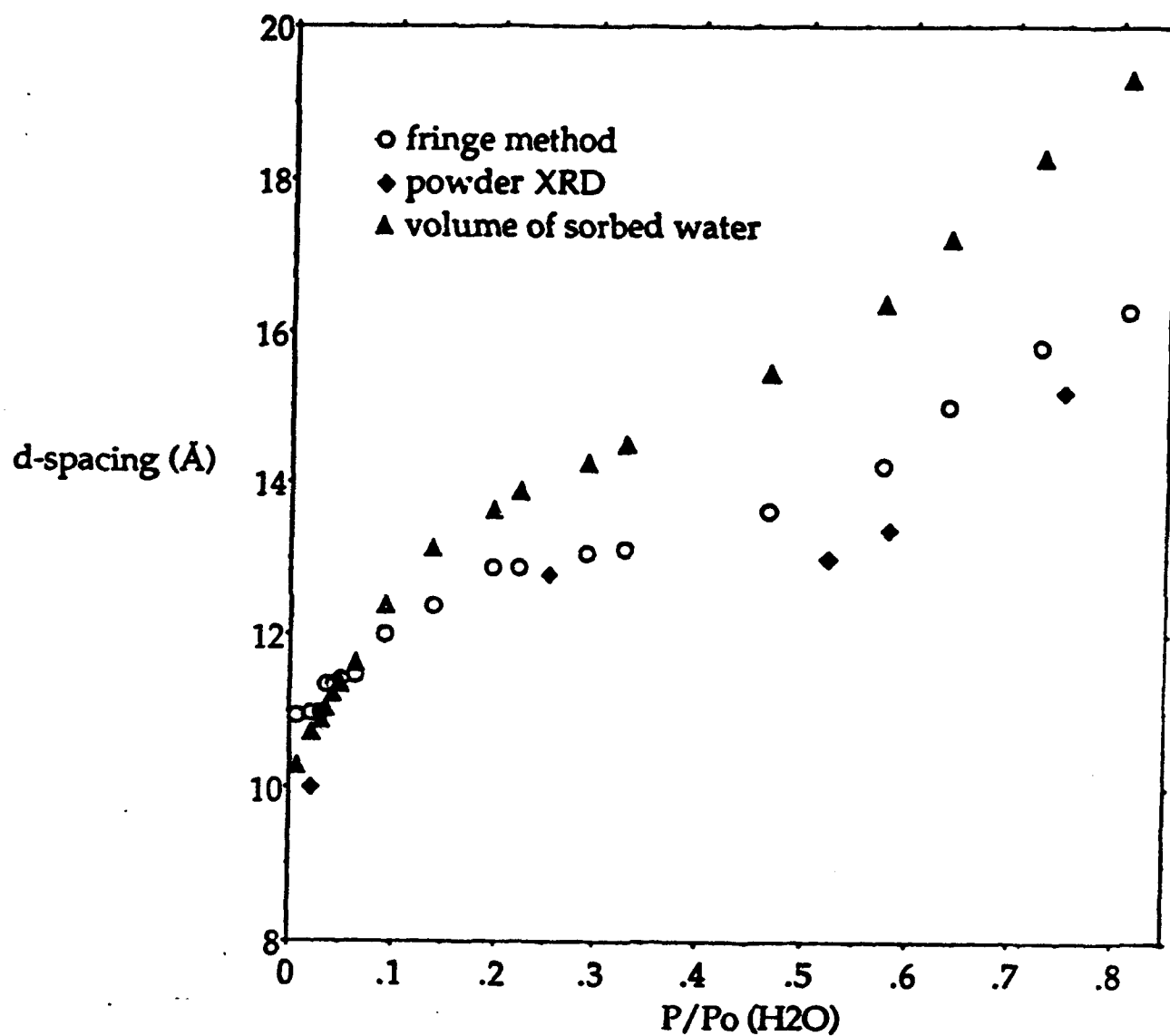


Figure 5. Basal Spacing (Å) of a Na-SAz1 Self-Supporting Clay Film Plotted as a Function of Water Content

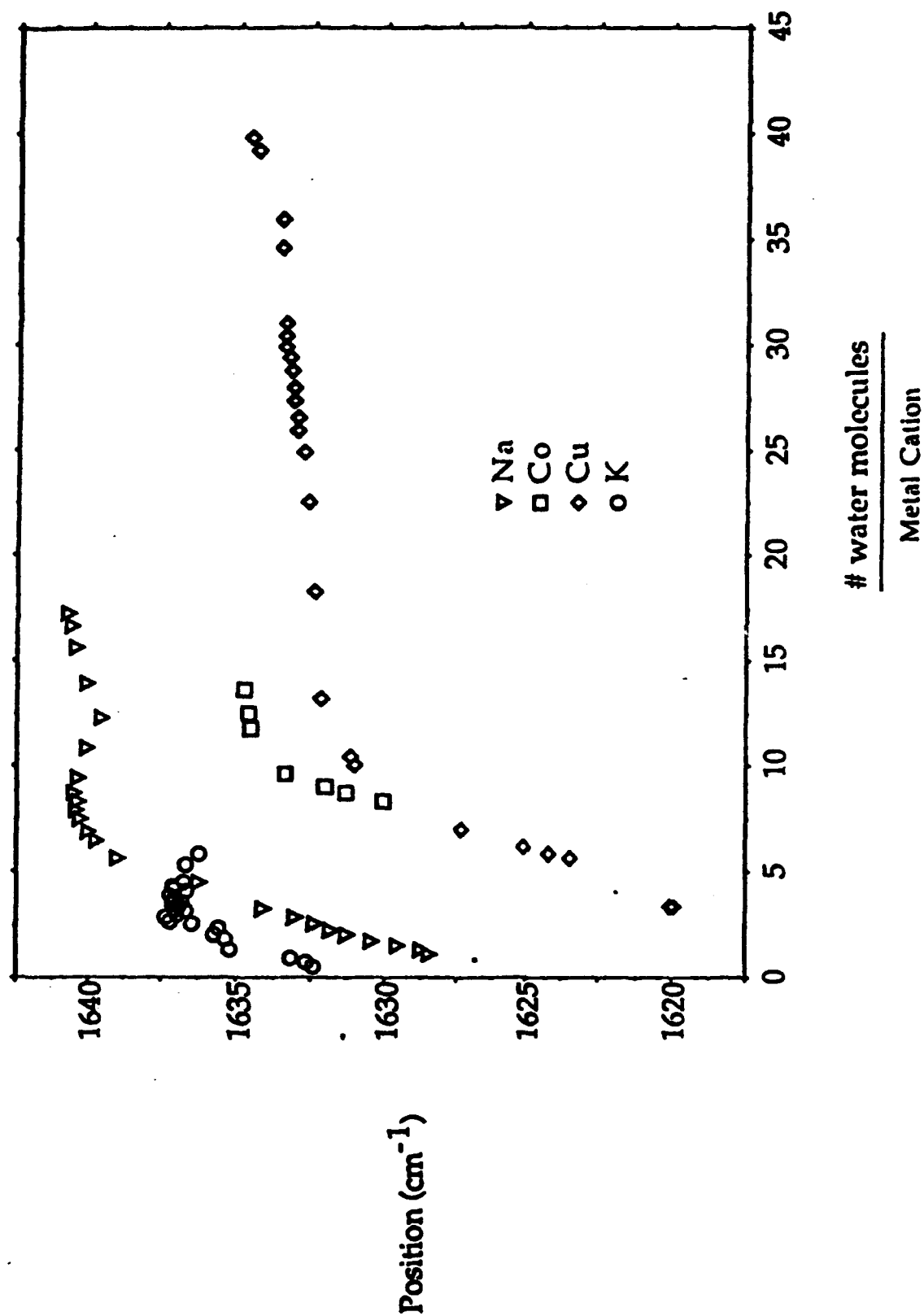


Figure 6. Position of the  $\nu_2$  Band of Water Sorbed on SAZ-1 Montmorillonite Exchanged with  $\text{Na}^+$ ,  $\text{K}^+$ ,  $\text{Co}^{+2}$  and  $\text{Cu}^{+2}$  Plotted as a Function of Water Content Expressed as the Number of Water Molecules Sorbed Per Exchangeable Metal Cation.

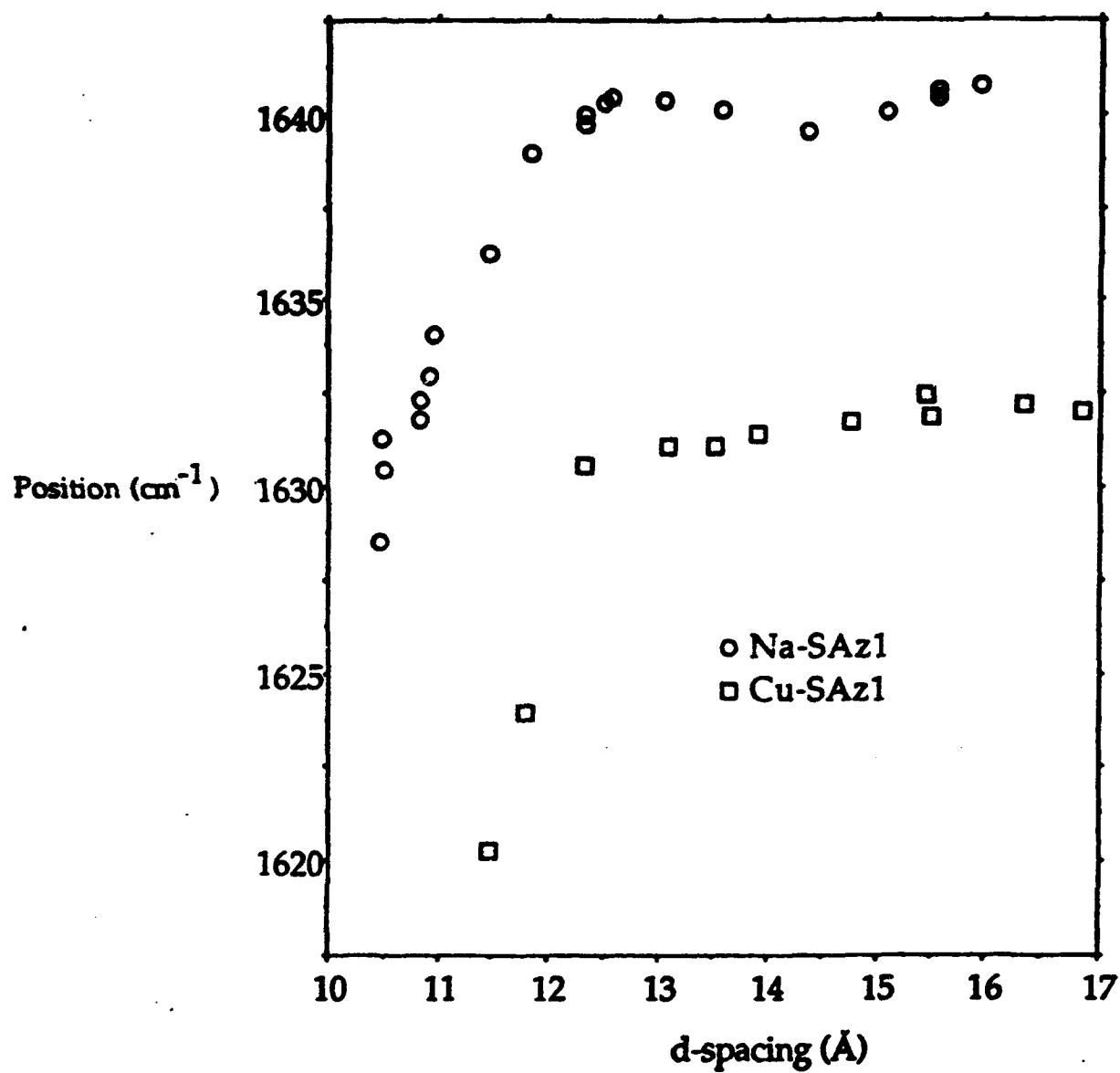


Figure 7. Position of the  $\nu_2$  Band of Water as a Function of the d-Spacing

The surface concentration of water sorbed on the clay films was determined using the familiar expression for the Bouguer-Beer-Lambert law (Beer's law) expressed as (3):

$$A(\nu) = \epsilon(\nu) c d = \ln \left( \frac{I_0(\nu)}{I(\nu)} \right) \quad (3)$$

where  $A(\nu)$  is the absorbance of the band of interest at frequency  $\nu$ ,  $\epsilon(\nu)$  is the molar absorptivity at  $\nu$  ( $\text{cm}^2/\text{mmole}$ ),  $c$  is the concentration of the solute expressed as ( $\text{mmoles}/\text{cm}^3$ ),  $d$  is the thickness of the clay film in  $\text{cm}$ ,  $I_0(\nu)$  is the intensity of the incident beam, and  $I(\nu)$  is the intensity of the transmitted beam. For solute sorption on thin films, it is more convenient to replace the quantity  $(c d)$  with  $\bar{c}$  which has units of ( $\text{mmoles}/\text{cm}^2$ ) and corresponds to the number of absorbers per unit area defined by

$$\bar{c} = c d \text{ (mmoles}/\text{cm}^2) \quad (4)$$

$$= \text{(mmoles of solute)} / (\text{cm}^2 \text{ of clay film})$$

$$\bar{c}_{(\text{single solute})} = \frac{(m_{cs} - m_c)}{(a_c M_{\text{solute}})} \quad (5)$$

where  $m_{cs}$  is the total mass of the clay film (combined mass of clay and sorbed solute) in  $\text{mg}$ ,  $m_c$  is the dry mass of the clay film in  $\text{mg}$ ,  $a_c$  is the area of the clay film in  $\text{cm}^2$ , and  $M_{\text{solute}}$  is the molecular weight of the solute (i.e., water in this case).

Using the measured peak height of a selected solute band, the molar absorptivity can be obtained using Equation (6):

$$\epsilon(v_{\max}) = \frac{A(v_{\max})_{\text{peak height}}}{\bar{C}} \quad (6)$$

The molar absorptivities of water sorbed on Na- and Cu-SAz-1 determined using Equation (6) are shown in Figure 8 as a function of water content. At high water contents, the observed molar absorptivity is the same as that of bulk water. Upon lowering the water content, however, the molar absorptivity value increases. In the case of Cu-SAz1, a steady increase in the molar absorptivity occurs until the lowest water content of approximately 3 water molecules/cation is reached. In contrast to water sorbed on Cu-SAz1, a smaller increase is observed for the Na-exchanged clay film. A maximum molar absorptivity of 35 cm mmol<sup>-1</sup> occurs at a (H<sub>2</sub>O/Na<sup>+</sup>) ratio of 6. Upon reducing the water content further, the molar absorptivity value decreases to a value slightly less than that of bulk water.

The desorption isotherms and basal spacing measurements obtained here are in reasonable agreement with published desorption data for montmorillonite (References 55,56,65). The monolayer sorption value of 122 mg g<sup>-1</sup> reported by Mooney et al. (Reference 55) for Na-Wyoming montmorillonite, for example, compares to a value of 138 mg g<sup>-1</sup> obtained in this study. The abrupt change in the plot of the BET function versus the relative vapor pressure of water is attributed to the collapse of the Na-SAz-1 clay at low vapor pressure to a basal spacing of approximately 10 Å. At low water contents ( $p/p_0 < 0.04$ ), the sorption sites in the interlamellar region are no longer accessible and sorption is restricted to the external surfaces of the clay particles (Reference 65). A similar break in the BET function for the Cu-SAz-1 clay is not observed because the hydration energy of the Cu<sup>+2</sup> cations is sufficient to prevent the collapse of the clay; the lowest d-spacing observed for the Cu-SAz-1 clay was approximately 11.5 Å.

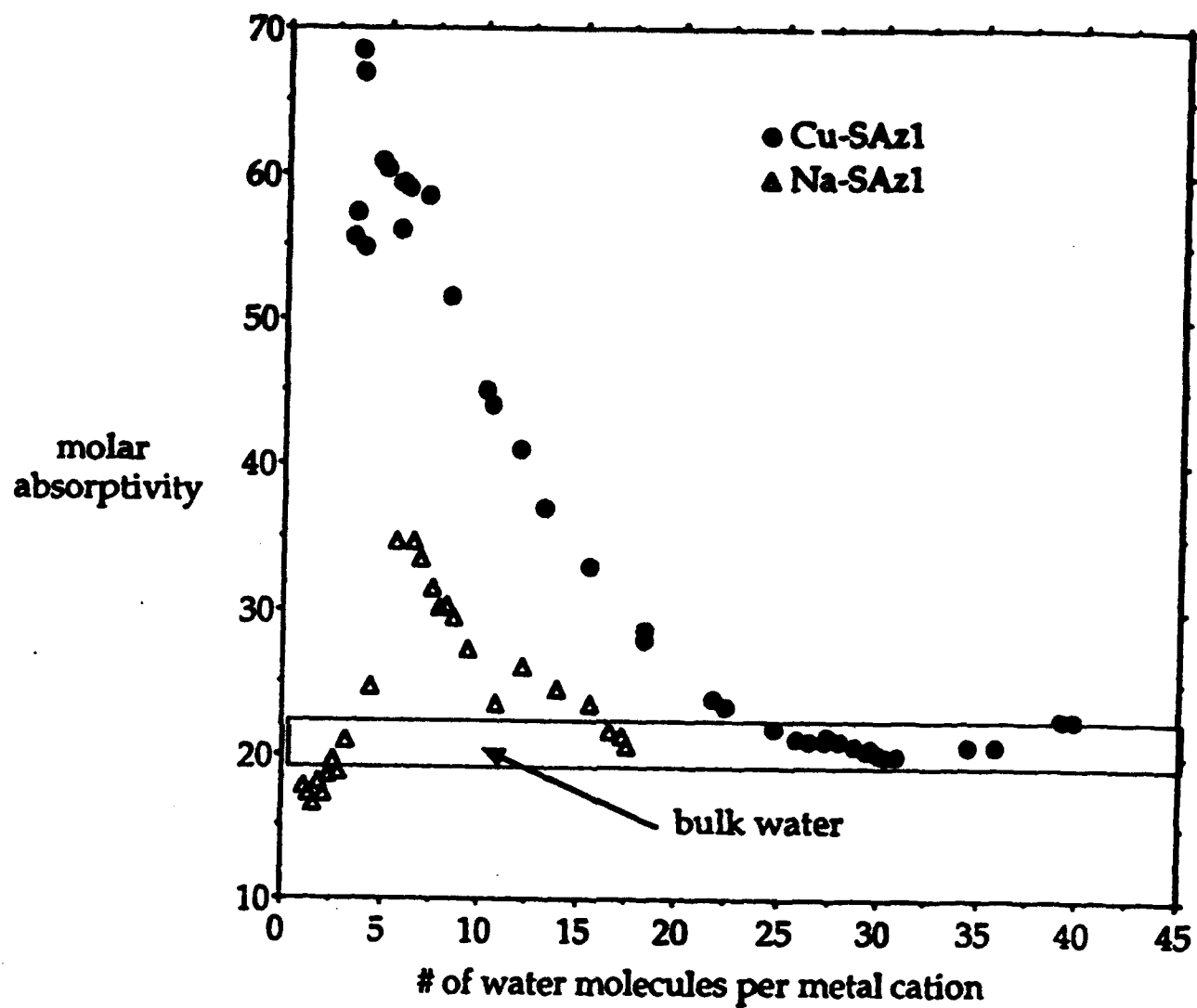


Figure 8. Change in the Molar Absorptivity of the  $\nu_2$  Band as a Function of Water Content

The decrease of the basal spacing of the Na-SAz-1 clay upon lowering the water content agrees well with published values (References 56,65). The notable feature of these data is, however, that the d-spacings were determined optically from the interference fringes of the self-supporting clay film. The d-spacings obtained from the interference fringes were consistently larger than those determined using powder XRD by approximately 0.5 Å. Comparison of the d-spacings obtained using the two methods at the lowest water content (approx. 2 percent relative humidity) indicates that the void volume of the self-supporting clay film was about 9 percent assuming that the "true" d-spacing of the clay film was 10Å as determined from the powder XRD measurements. The index of refraction used to calculate the thickness of the film from the fringe spacing was 1.56. The index of refraction of montmorillonite decreases as the water content increases; however, this was not taken into account in the present study. A decrease in the index of refraction would result in a slight increase in the d-spacing at higher water contents.

The shift in frequency of the  $\nu_2$  band of water to lower frequencies upon reducing the water content is attributed to a decrease in hydrogen bonding (Reference 40). Upon dehydration, the more labile water is removed from the interlamellar region leaving the water molecules which are coordinated to the exchangeable metal cations, thus, reducing the intermolecular interactions between water molecules. In addition, the remaining water molecules are polarized by the cation itself. A decrease in the  $\nu_2$  band generally accompanies an increase in the  $\nu_1$  and  $\nu_3$  (O-H stretching bands). The position of the OH stretching bands could not be determined unambiguously in this study due to significant overlap and broadening of the OH stretching bands with each other and with the structural  $\nu(\text{O-H})$  band at 3630  $\text{cm}^{-1}$ .

## SECTION III

### PHYSISORPTION OF AROMATIC HYDROCARBONS ON MONTMORILLONITE

#### A. INTRODUCTION

Vapor-phase sorption of volatile organic compounds (VOCs) on soil and subsurface materials is strongly influenced by water content (References 67-71). Recent studies have suggested that two distinct sorption processes are responsible for the uptake of VOCs by soils and sediments. At low water contents, VOC sorption is dominated by mineral surfaces with minimal contributions from soil organic matter. Upon increasing the amount of water present, the sorption capacity decreases sharply and a partitioning mechanism of VOC into soil organic matter has been suggested to be the dominant uptake mechanism. Chiou et al. (Reference 71) proposed that the two processes operate independent of each other. The VOC sorption capacity of mineral surfaces under dry conditions is significantly larger than that of wet surfaces. The suppression of VOC uptake by hydrated mineral surfaces has been attributed to competition from water for active sorption sites (References 68-71). This hypothesis assumes that VOCs and water molecules compete for similar sites. Although it is clear that exchangeable metal cations are the active sites for water molecules (References 35,55,61,72,73), it is not well understood where the active sorption sites for VOCs on dry mineral surfaces are.

In addition to increased sorption of VOCs at low water contents, the potential for chemisorption reactions to occur is much greater on dry mineral surfaces compared to hydrated systems (References 47,74). One class of abiotic reactions which can enhance the degradation of unsaturated toxic organic solutes in soils and sediments under dry conditions are single electron transfer (SET) reactions (References 43-45,75-83). These reactions proceed through a single electron transfer

(SET) from the unsaturated organic solute to a transition metal cation (e.g.,  $\text{Fe}^{+3}$ ). If the SET reaction is to occur, the organic solute must assume a direct ligand position with the metal cation. Under hydrated conditions, hydrophobic organic solutes such as benzene or xylenes have little, if any, affinity for hydrophilic mineral surfaces; thus, minimal sorption of the VOC occurs in the presence of water (References 67,71). Dehydration of the clay enhances sorption of the organic solute by removal of water molecules which strongly compete for coordination sites around the metal cation (Reference 34). Many clay mediated SET studies have required the use of strong desiccants (e.g.,  $\text{P}_2\text{O}_5$ ) or anhydrous solvents to achieve low water content and increase the surface Lewis acidity of the interlamellar cations (References 43,44,78-80). It is generally accepted that clay mediated SET reactions depend upon the reduction potential of the exchangeable metal cation and on the ionization potential of unsaturated organic solute; however, it is not known how much water is needed for the reaction.

The objectives of this study were to investigate sorption of p-xylene on Co-montmorillonite, and to study the influence of water content on the sorption reaction of p-xylene on Co- and Cu-exchanged montmorillonite. The two exchangeable cations, which complement each other, were selected for several reasons;  $\text{Cu}^{+2}$  and  $\text{Co}^{+2}$  have almost identical hydration energies, and chemisorption of p-xylene has been observed on Cu-montmorillonite (CuX) (References 43-45) but not for CoX due to the difference in the reduction potentials of the two cations. Our approach utilized a gravimetric / FTIR cell which permitted FTIR spectra and gravimetric data to be collected simultaneously (Reference 34). Surface spectroscopy can provide molecular information about the identity of the surface species, the type of chemical bonds formed between the adsorbent and the adsorbate, and the influence of the adsorbent on the ground vibrational states of the adsorbate. Chemisorption binding energies are similar in magnitude to those of

primary chemical bonds in free molecules. Thus, the presence of chemisorbed surface species is readily distinguished by the appearance of new bands and/or large frequency shifts of fundamental vibrational modes provided that the concentration of chemisorbed species is above the detection limit associated with the particular spectroscopic method. The corresponding binding energies of guest-host interactions for physisorption processes are intrinsically weak (e.g., van der Waals interactions). The strength of these interactions may or may not be sufficient to perturb the guest species and permit discrimination of the sorbed species from that present in the bulk solution or vapor phase (Reference 84). Collecting spectroscopic and gravimetric data simultaneously provided the additional benefit of correlating the changes in molecular structure of a particular surface species to the amount of solute sorbed.

## B. RESULTS AND DISCUSSION

### 1. Spectroscopic Adsorption Isotherm

FTIR spectra of a self-supporting Co-montmorillonite (CoX) clay film showing the  $P_2O_5$  induced desorption of water from the clay (Spectra A-G) followed immediately by exposure of the dry-clay film to p-xylene vapor (Spectra H-O) are shown in Figure 9. The offset of each spectrum along the z-axis corresponds to the time of collection. The mass of the sample was determined using the apparatus shown in Figure 1 for each of these spectra and the corresponding  $Q_{total}$  values are shown in Figure 10 by the solid triangles. The spectra in the 1350 to 1700  $cm^{-1}$  region are characterized by four bands at 1383, 1450, 1515, and 1628  $cm^{-1}$  (Figure 9a) corresponding to the methyl umbrella, methyl HCH bend, and  $\nu_{19}$  (C-C ring stretch) modes of p-xylene, and to the  $\nu_2$  band of water (OH bend), respectively. A complete listing of the observed and literature band positions and assignments are given in

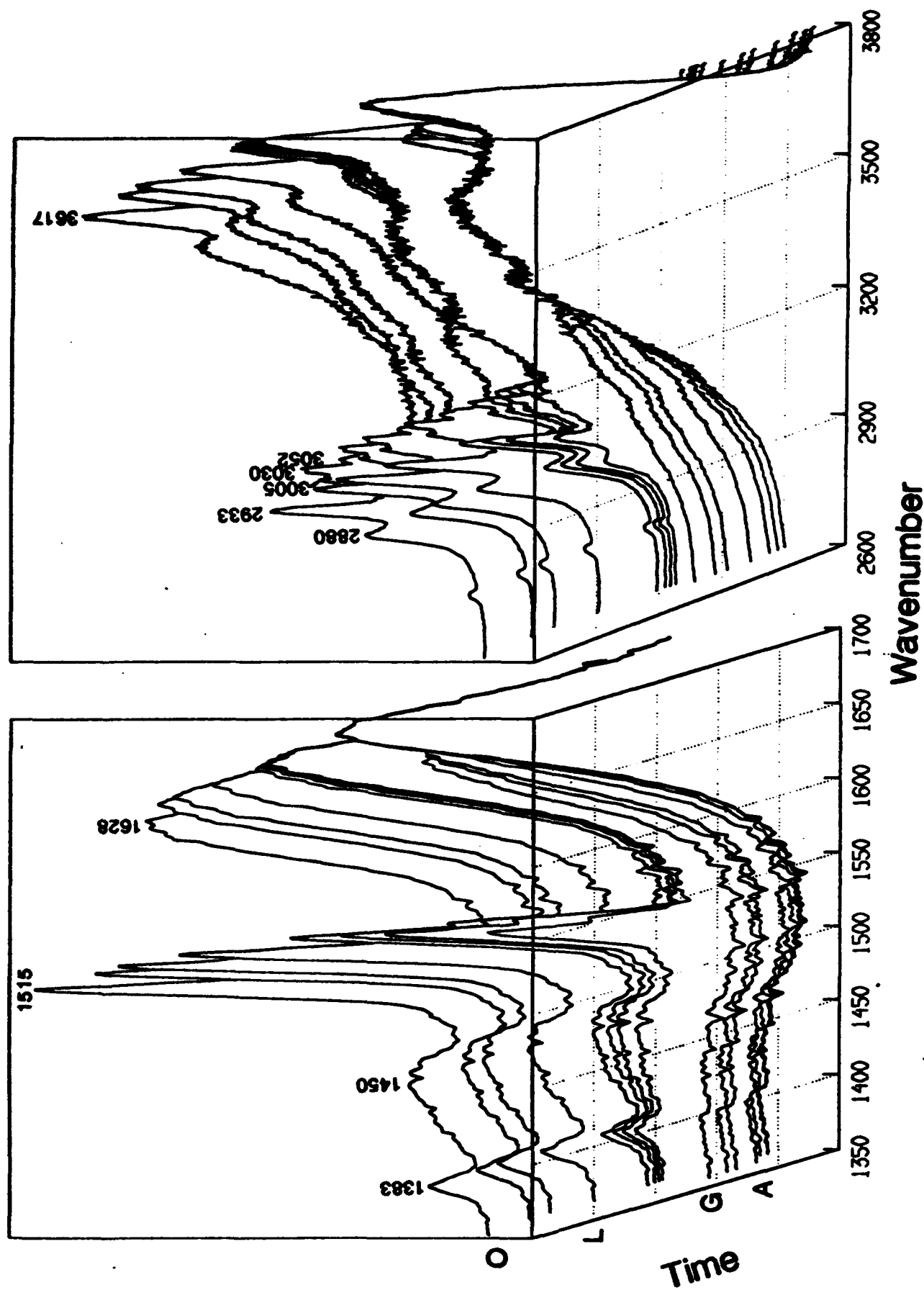


Figure 9. FTIR spectra of a Self-Supporting Film of Co-montmorillonite Exposed to  $P_2O_5$  (Spectra A-G) Followed by Exposure to p-Xylene Vapor (Spectra H-O) in the  $1350 - 1700 \text{ cm}^{-1}$  Region (right side). the Offset of Each Spectrum Along the z Axis Corresponds to the Time at Which Each Spectrum Was Collected.

**Table 2.** The  $\nu(\text{C-H})$  modes of p-xylene at 2880, 2933, 3005, 3030, and 3052  $\text{cm}^{-1}$ , the  $\nu(\text{OH})$  ( $\nu_1$  and  $\nu_3$ ) modes of water, and the structural  $\nu(\text{OH})$  band of the SAz-1 clay at 3617  $\text{cm}^{-1}$  are shown in Figure 9b. The integrated intensities of the 1515 and 1628  $\text{cm}^{-1}$  bands were used to determine the amounts of water and p-xylene on the surface of the clay using Beer's law, a similar approach to that of Bell (Reference 6). These bands were selected because they had minimal interferences from other clay, water, or p-xylene vibrational modes.

The surface concentrations of water and p-xylene on the clay films were determined using the familiar expression for the Bouguer-Beer-Lambert law (Beer's law) expressed in equations (3) and (4) in Section II. Using the integrated intensity of a selected solute band, Beer's law can be expressed as

$$\bar{A} = \bar{\epsilon} \bar{c}, \quad (7)$$

where  $\bar{A}$  has been defined as the integrated area of the band of interest

$$\bar{A} = \int_{\bar{\nu}_1}^{\bar{\nu}_2} A(\bar{\nu}) d\bar{\nu} \quad (8)$$

and  $e$  is the integrated molar absorptivity. Since the area of the clay film is a constant, Equation (7) can be expressed as

$$q_i = \frac{\bar{A}}{\bar{\epsilon}} \quad (9)$$

where  $\bar{\epsilon} \equiv \bar{\epsilon} a_c$  and  $q_i$  is the amount of solute species  $i$  sorbed in units of (mg/g).

Values of  $q_{\text{water}}$  and  $q_{\text{p-xylene}}$  were determined using Equation (6) using the

Table 1 Observed Vibrational Bands and Assignments of *p*-Xylene and Co- and Co-GAx1 Montmorillonite<sup>a</sup>

vapor, cm <sup>-1</sup>	MI, cm <sup>-1</sup>	rel int		St.	CaX	CaX-pz	CaX-pz	assignment	symm
		vapor	MI						
				153				ring torsion	
				286				methyl ring CCC bend	
				313				out-of-plane bend of methyl C	
				389				methyl ring CCC bend	
				480				ring CCC bend	
				484				out-of-plane bend of methyl C	
				646				ring CCC bend	
				689				ring CCC bend	
				730				C-C stretch, methyl to ring	
785	784	1.00	1.00	801		796	796	out-of-plane ring CH bend	
				830		823			
					842	844	844	C-C ring stretch	
					915	915	915		
970	970	0.01	0.06	936				out of plane of ring H	
1024	1023	0.05	0.08	971				ring CH bend	
				1022				ring C-COC bend	
				1038				methyl rock	
1048	1040	0.05	0.18	1044				methyl rock	
1115	1121	0.08	0.35	1125				in-plane ring CH bend	
1221	1221	0.03	0.07	1226		1223	1223	X-sensitive C-C str	
						1248			
				1286		1286		C-C ring stretch	
						1304			
						1324			
						1355			
1384	1380	0.05	0.41	1379				methyl umbrella	
				1383		1383	1383	methyl umbrella	
				1403				C-C ring stretch and ring HCC bend	
						1424			
	1451	0.07	0.14	1449				methyl HCH asymmetric bend	
	1451	0.09	0.39	1450		1450	1451	methyl HCH asymmetric bend	
				1456				methyl HCH asymmetric bend	
						1468			
						1502			
1520	1518								
	1523	0.52	1.02	1522		1522	1515	conformation/site splitting of 1523 cm <sup>-1</sup> band	
						1550	1525	in-plane ring CH bend	
						1586			
1627		0.03			1625	1625	1628	b <sub>1g</sub> × b <sub>2g</sub> = b <sub>2g</sub> combination band (846 + 794)	
							1729		
1788	1790	0.02	0.14					a <sub>g</sub> × b <sub>1g</sub> = b <sub>1g</sub> combination band (970 + 846)	
1829	1890	0.04	0.17					A <sub>g</sub> × b <sub>2g</sub> = b <sub>2g</sub> combination band (970 + 936)	
						2149			
2744	2738	0.03	0.12			2744			
						2871			
2861	2879	0.32	0.20				2879		
						2928			
2936	2934	0.63	0.55				2933		
2960	2960		0.27						
2983	2986		0.29						
3004	3009	0.43	0.41				3006		
3028	3033	0.49	0.41			3023	3030	ring CH stretch	
3051	3058	0.32	0.42					ring CH stretch	
3100	3105	0.05	0.05						
3145	3145	0.02	0.03						
				3369	3363				
							3544		
				3622	3652				
					3633		3615		

<sup>a</sup>MI, matrix isolation; CaX<sup>N</sup>pz, CaX<sup>N</sup>*p*-xylene.

integrated intensities of the  $\nu_2$  mode of water at  $1628\text{ cm}^{-1}$  and the  $\nu_{19}$  mode of p-xylene at  $1515\text{ cm}^{-1}$ , respectively, and are plotted along with the gravimetric data in Figure 10. It was necessary to determine the dry mass of clay film ( $m_c$ ) in order to determine the absolute amount of water and p-xylene sorbed by the clay. This was accomplished by plotting the mass of the sample versus the integrated intensities of either the OH bending or OH stretching bands as a function of the water content and extrapolating to zero absorbance. This eliminated the problem of having to assume that all of the water was removed by heating the sample to an arbitrary temperature or by placing the sample in a vacuum desiccator.

Before p-xylene was introduced into the cell, the clay film was exposed to the desiccant  $\text{P}_2\text{O}_5$ , to lower the water content and thereby increase the amount of p-xylene sorbed (Reference 67). As the data in Figure 10 indicate, the water content did not decrease below  $90\text{ mg/g}$ , even under the influence of the desiccant. The significant amount of water retained by the clay is attributed to the high hydration energy of Co. As the data in Figure 10 indicate, there is good agreement between the amount of water sorbed determined using Beer's law (open circles) to the gravimetric data (closed triangles). Upon addition of p-xylene vapor ( $P/P_0 = 1$ ) into the cell the total surface loading of the sample increased from  $90$  to  $200\text{ mg/g}$  over a 45 minute period. The amount of water sorbed on the clay immediately increased from  $90\text{ mg/g}$  to  $140\text{ mg/g}$  upon addition of the p-xylene vapor and slowly decreased to  $100\text{ mg/g}$  due to the influence of  $\text{P}_2\text{O}_5$ . The sorption of p-xylene took place over a 4 hour period and reached a maximum value of  $98\text{ mg/g}$ . It is interesting to note that even under the influence of  $\text{P}_2\text{O}_5$ , the amount of water sorbed was always greater than that of p-xylene. Analysis of the spectra shown in Figure 9 allowed the relative contributions of water and p-xylene to the total mass of solute sorbed by the clay film to be determined unambiguously.

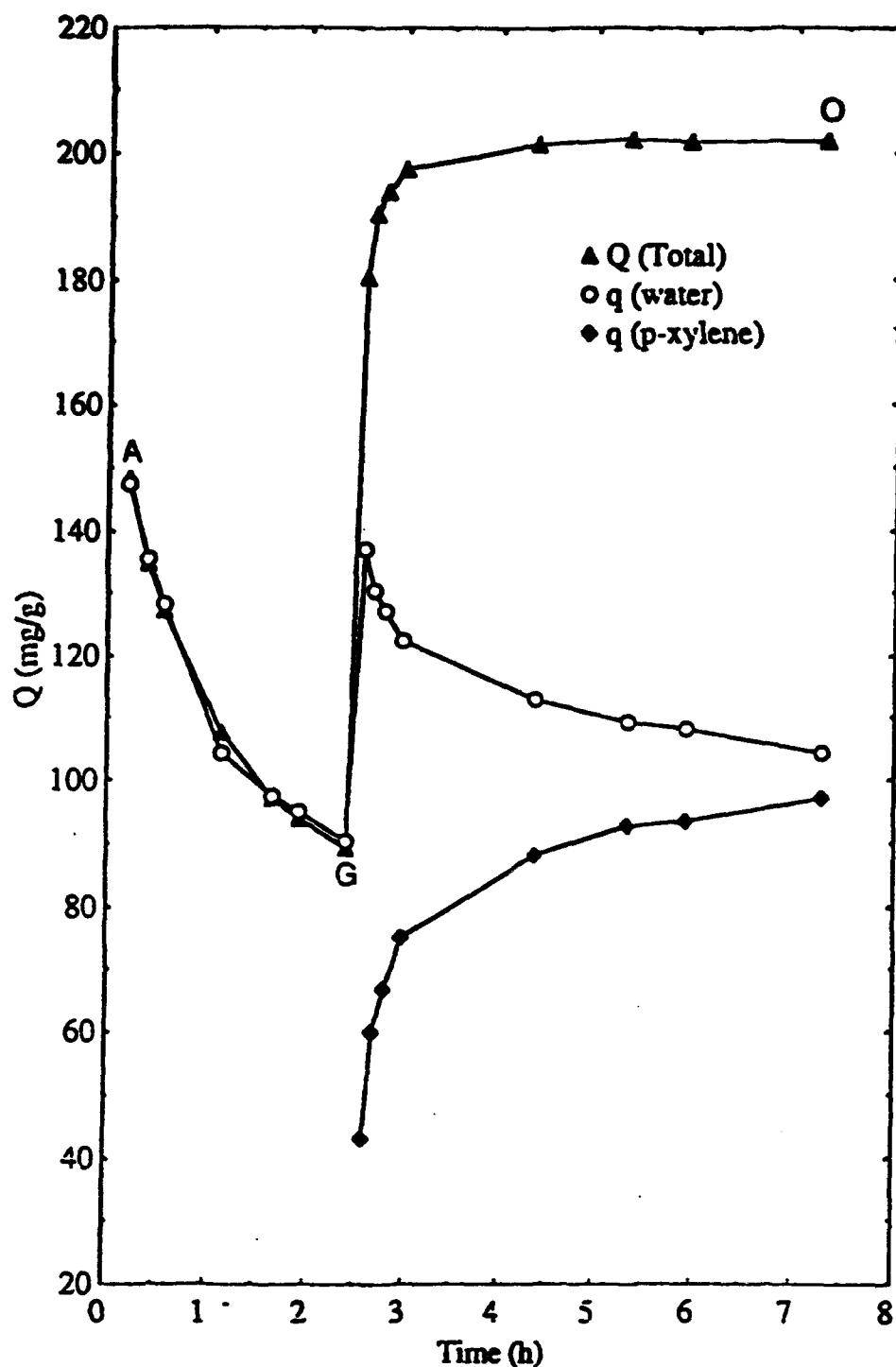


**Figure 10.** Total Surface Loading of Water and p-Xylene ( $Q_{\text{total}}$ ) on the Co-montmorillonite Clay Film Weight of the Self-Supporting Film Plotted as a Function of the Exposure Time to  $\text{P}_2\text{O}_5$  (A-G) and to p-Xylene Vapor and  $\text{P}_2\text{O}_5$  (H-O) as Measured from the Cahn Electrobalance. The  $q_{\text{water}}$  and  $q_{\text{p-xylene}}$  Values were Determined using the Integrated Intensities of the  $\nu_2$   $\text{H}_2\text{O}$  Band at  $1628\text{ cm}^{-1}$  and the  $\nu_{19}$  Mode of p-Xylene at  $1516\text{ cm}^{-1}$  Respectively.

## 2. Physisorbed p-Xylene on Co-montmorillonite

The FTIR spectrum of the Co-montmorillonite film exposed to p-xylene vapor for 4 hours is shown in Figure 11b in the 1200 to 1700  $\text{cm}^{-1}$  region. For comparison, a reference spectrum of vapor phase p-xylene (Fig. 11d), and the spectrum of a Co-montmorillonite clay film without p-xylene (Fig. 11a) is included. The vapor phase spectrum of p-xylene (Fig. 11d) is characterized by three distinct bands of similar intensity in the  $\nu(\text{C-C})$  region at 1515, 1520, and 1525  $\text{cm}^{-1}$  which have been assigned to the P-, Q-, and R-branches of the  $\nu_{19}$  mode (ring C-C stretch), respectively (Table 2). The lineshape of this band in the vapor phase spectrum (Figure 11d) is typical for an oblate shaped molecule ( $I_a \ll I_b, I_c$ ). The position of the Q-branch band at 1520  $\text{cm}^{-1}$  agrees with that reported by Lau and Snyder (Reference 85) (Table 2).

The spectrum of p-xylene sorbed on CoX (Fig. 11b) has spectral contributions from both p-xylene sorbed on the clay and a less intense contribution from p-xylene vapor in the cell. An expanded region showing the p-xylene - CoX complex, vapor phase p-xylene, and the difference spectrum obtained by subtraction of the vapor phase spectrum from the physisorbed spectrum are shown in Figure 12. The difference spectrum (Figure 12d) shows that the  $\nu_{19}$  mode of p-xylene is shifted from 1520  $\text{cm}^{-1}$  to 1516  $\text{cm}^{-1}$ . The loss of the P-Q-R lineshape for the physisorbed species is attributed to the loss of rotational and translation freedom resulting in the formation of a liquid-like layer of p-xylene upon sorption. A shift of 4  $\text{cm}^{-1}$  to lower frequency for the  $\nu_{19}$  mode is consistent with similar shifts observed in a Raman study of benzene physisorption on to silica (Reference 84). Although small in magnitude, this shift allows the physisorbed species to be distinguished from the vapor-phase component. No evidence for chemisorption of p-xylene on the CoX

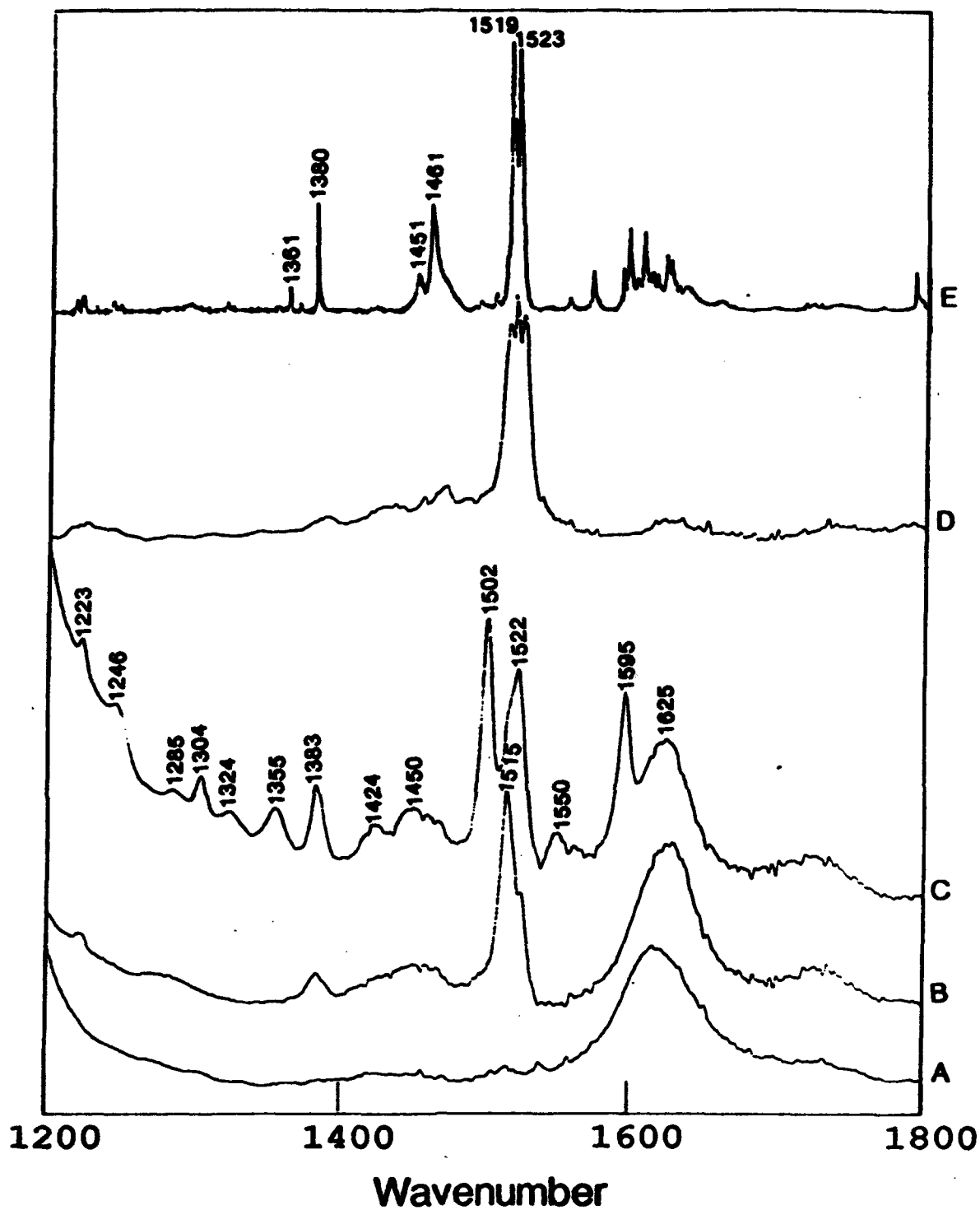


**Figure 11.** FTIR Spectra in the 1200 to 1800  $\text{cm}^{-1}$  Region of a Self Supporting Film of Co-Sxchanged SAz-1 Montmorillonite (CoX) (A), CoX Film Exposed to p-Xylene Vapor (B), and a CuX Film Exposed to p-Xylene Vapor (C) Obtained in the FTIR/Gravimetric Cell in the Presence of  $\text{P}_2\text{O}_5$ . The Vapor-Phase (D) and Matrix Isolation Spectra of p-Xylene (E) are Shown for Comparison.

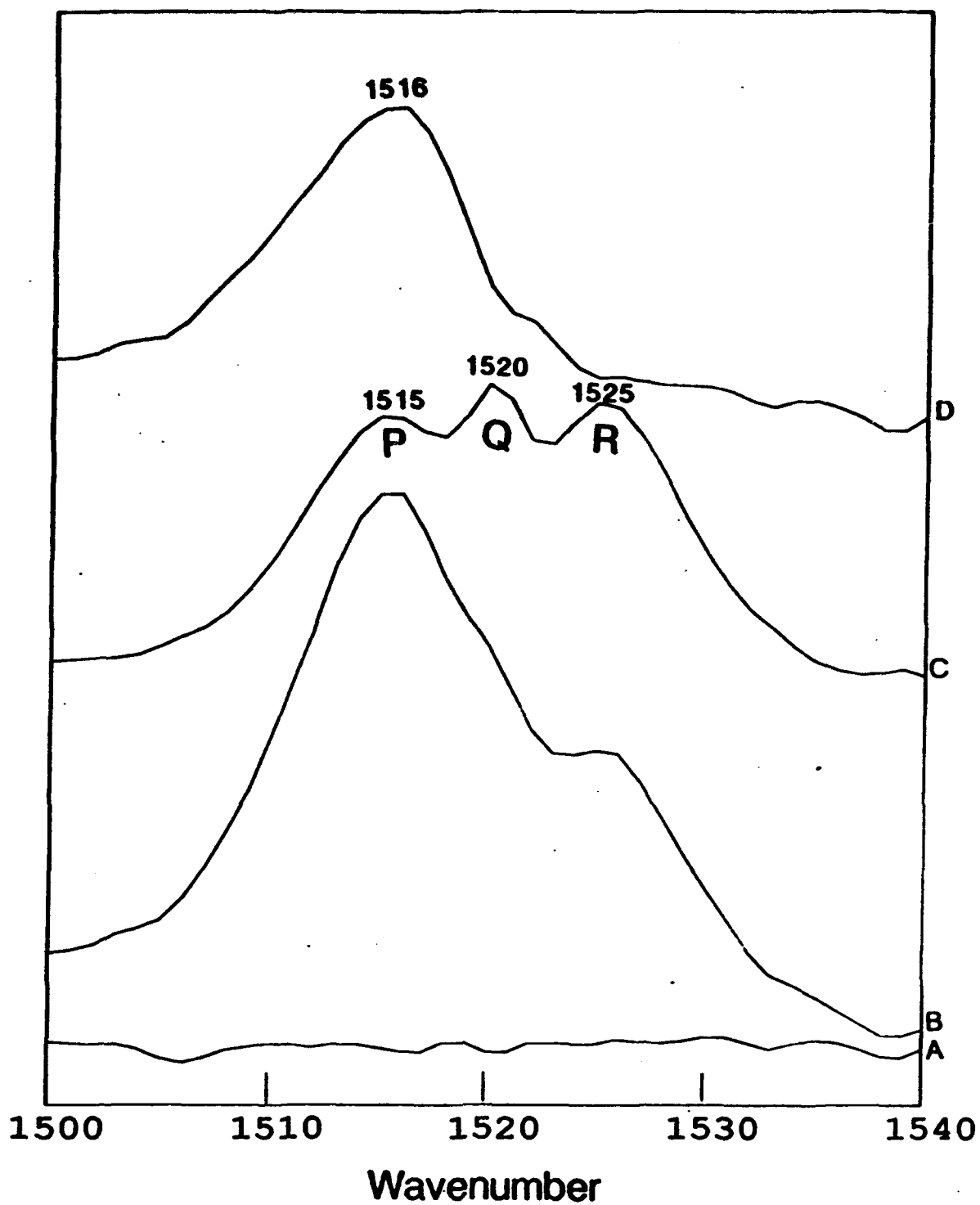


**Figure 12.** FTIR Spectra of a CoX Clay Film (A), CoX Film Exposed to p-Xylene Vapor (B), Vapor-Phase p-Xylene (C), and the Difference Spectrum (D) Obtained by Subtracting the Vapor-Phase Spectrum (C) from the Spectrum of p-Xylene Sorbed on the CoX Film (B)

film was found in that no new vibrational bands were observed nor was the color of the clay complex changed upon sorption of p-xylene.

## SECTION IV

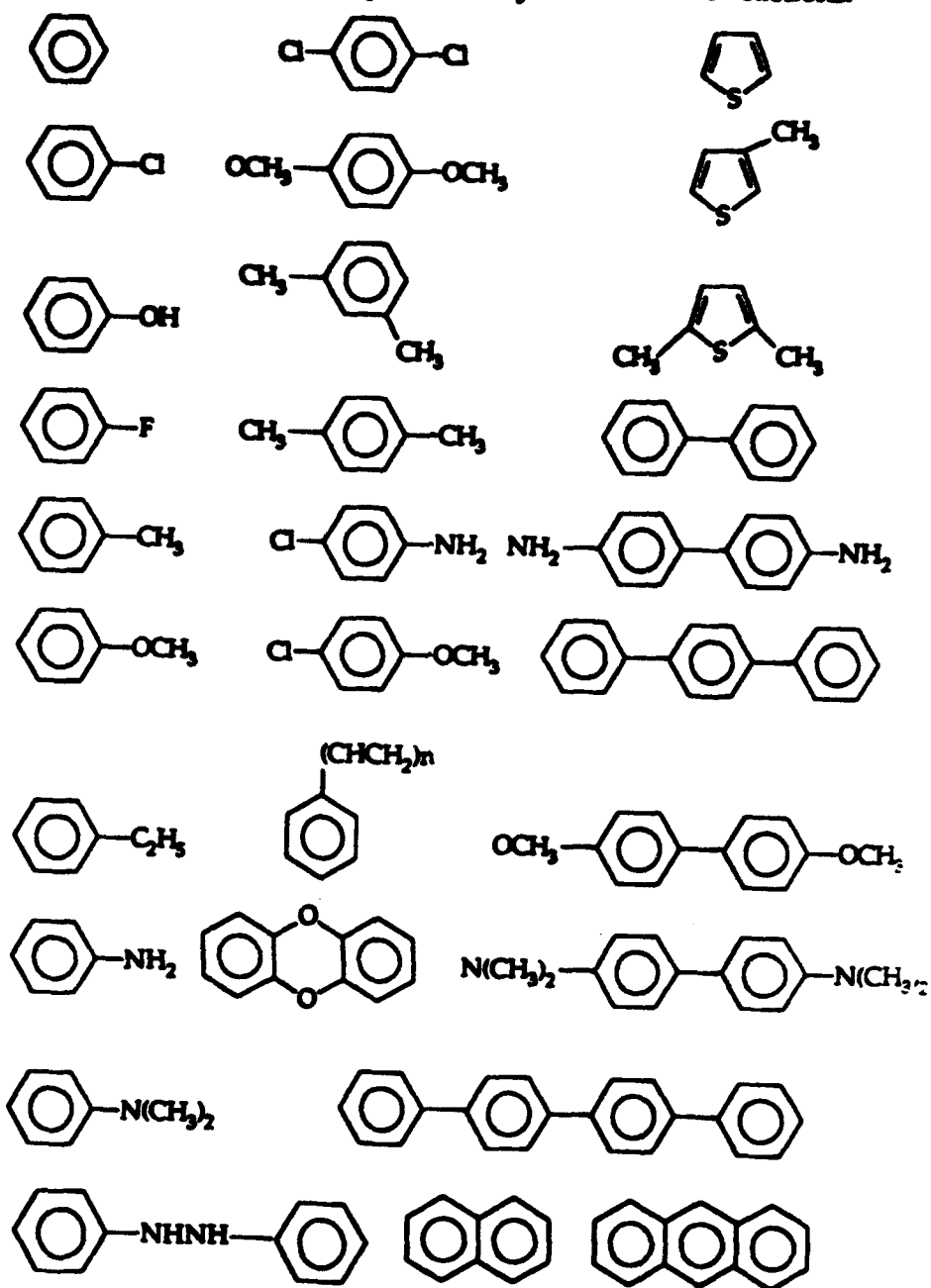
### CHEMISORPTION OF AROMATIC HYDROCARBONS ON MINERAL SURFACES

#### A. INTRODUCTION

Single-electron transfer (SET) reactions of unsaturated organic compounds on clay surfaces represent an important class of abiotic reactions which can enhance the degradation of toxic organic solutes in soils and sediments (References 47,71,74,86-88). Mortland and Pinnavaia (References 43,44,89,90) were among the first to show that simple arenes (e.g., benzene, toluene, and p-xylene) are chemisorbed onto transition metal (e.g.,  $\text{Cu}^{+2}$ ,  $\text{Fe}^{+3}$  and  $\text{Ru}^{+3}$ ) exchanged montmorillonites under dry conditions forming strongly colored complexes whose molecular properties are quite distinct from those of the unperturbed arene. Although the earlier work was restricted to simple arenes such as benzene, toluene, xylenes and mesitylene, these reactions have since been extended to a much broader class of unsaturated organic compounds including dioxins (Reference 81), chloroanisoles (Reference 82), and chloroethenes (Reference 83). Table 3 presents a partial listing of compounds which are known to participate in SET reactions on transition metal exchanged montmorillonites.

It has been established that these reactions proceed through a single electron transfer (SET) from the unsaturated organic solute to the transition metal cation (References 43-45,80,91). In order for the SET reaction to occur, the organic solute must coordinate with the transition metal cation by assuming a direct ligand position. Under hydrated conditions, hydrophobic organic solutes have little, if any, affinity for the hydrophylic, interlamellar environment of the clay. Thus, minimal sorption of the hydrophobic solute occurs (References 68,71). Dehydration of the

**Table 3** Compounds susceptible to clay mediated SET reactions.



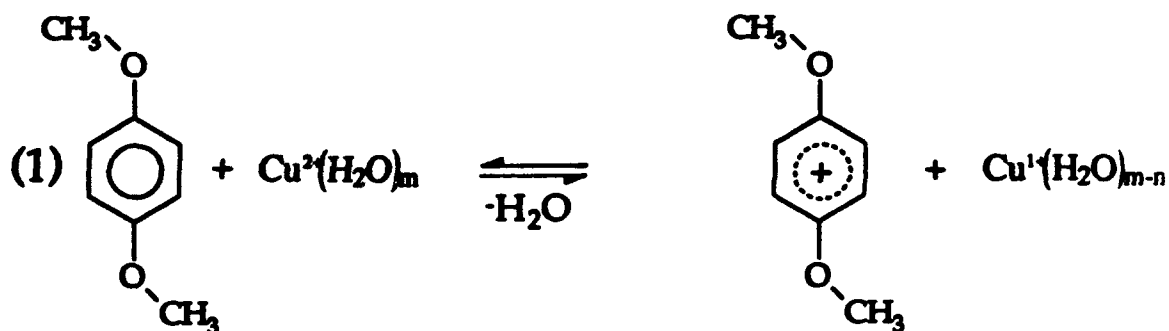
transition metal exchanged montmorillonite, however, enhances the sorption of the organic solute by removal of interlamellar water molecules which strongly compete for coordination sites around the metal cation. If the ionization potential of the organic solute is below 10 eV, and the reduction potential of the metal cation is favorable, an SET reaction can occur. Apparently, the negatively charged clay surface plays a critical role in: (1) increasing the surface Lewis acidity of the metal cation (Reference 50) which, in turn, promotes the SET reaction, and (2) stabilizing the radical organic cation.

Once an organic radical cation has been generated on the interlamellar surface of the clay, the radical cation can either remain as a cation (Reference 46), or undergo additional reactions involving other radical cations, neutral solute species in the clay, or interlamellar water molecules (Reference 92). For aromatic compounds, Soma et al. (Reference 79) proposed that if the para positions are occupied by a suitable blocking group, then the radical organic cation is stabilized on the surface of the clay (e.g., p-dimethoxybenzene (Reference 46)); if the para positions are not occupied, however, then subsequent dimerization and polymerization reactions can occur (e.g., benzene (References 91,93), anisole (Reference 77), aniline (References 94,95), and phenols (Reference 87)).

Clay-mediated SET reactions are characterized, in general, by (1) formation of a darkly colored complex (Reference 43), (2) loss of the ESR signal from the paramagnetic metal cation (Reference 45) (e.g., reduction of  $\text{Cu}^{+2}$  to  $\text{Cu}^{+1}$ ), (3) a concomitant appearance of a "new" ESR signal from the generation of an organic radical cation (Reference 80), and (4) strong perturbations in both the IR (Reference 77) and the Raman (References 79,91) spectra of the chemisorbed complex. Surprisingly little work has focused on the electron transfer reaction itself free from dimerization and/or polymerization reactions. With few exceptions, most SET clay studies have involved systems where subsequent redox, dimerization or

polymerization reactions have occurred. Chemisorption of benzene, for example, is known to proceed through an SET reaction followed by subsequent polymerization (Reference 92). For this complex, Eastman et al. (Reference 80) showed that a wide variety of radicals were formed, depending upon the availability of water and on the reaction time. The observed perturbations in the vibrational and electronic spectra of the chemisorbed benzene species, therefore, contain contributions from both (1) monomeric cations and (2) polymerization products.

The focus here was to examine the single-electron transfer reaction of several aromatic compounds on soil and subsurface material. In a previous note on the interaction of PDMOB with Cu-montmorillonite, Soma et al. (Reference 46) suggested that the Reaction (1):



was reversible depending upon the water content, and that only the monomeric cation species was formed upon dehydration (i.e., dimerization and or polymerization did not occur). Soma et al. (Reference 46) utilized resonance Raman spectroscopy to characterize the adsorbed species by taking advantage of the fact that the chemisorbed species produced a significant electronic transition in the 425 to 475 nm region which was exploited using resonance enhancement (i.e., Raman excitation using the 457.9 nm line of an Ar<sup>+</sup> laser). Although resonance Raman spectroscopy is useful to examine the strongly colored, chemisorbed species, it is not sensitive to the presence of other surface species and are not resonantly

enhanced which may have been present. In addition, no definitive evidence has been reported in the literature to support the hypothesis that Reaction (1) is reversible other than the fact that the color change is reversible.

In this study we have obtained in-situ FTIR, UV-visible and gravimetric data on the sorption of PDMOB, p-xylene, and benzene by Cu-montmorillonite (CuX) to examine the reversibility of reaction (1), and to observe the electronic and vibrational spectra of the surface species formed upon driving reaction (1) to the right. According to the hypothesis of Soma et al. (Reference 46), only the PDMOB<sup>+</sup> cation should be generated. The UV-visible spectra of the PDMOB<sup>+</sup> cation (Reference 96) are quite distinct with intense absorption maxima observed at  $\lambda = 443$  and 475 nm. Thus, an in situ FTIR and UV-visible cell was used to collect tandem FTIR and UV-visible spectra of the PDMOB - CuX complex in order to correlate the formation of the radical cation with the changes in its vibrational spectrum as a function of water content. In addition, an in situ FTIR/gravimetric cell was used to determine the surface loadings of water and PDMOB on the clay.

## B. EXPERIMENTAL

Infrared spectra were obtained on two Fourier transform infrared (FTIR) spectrometers. A Nicolet Model 740 FTIR spectrometer equipped with a mercury-cadmium-telluride (MCT) detector ( $720\text{ cm}^{-1}$  cutoff;  $D^* = 3.5 \times 10^{10}\text{ cm Hz}^{0.5}$ ) and a KBr beamsplitter was used for the tandem FTIR / UV-visible measurements. For the coupled FTIR/gravimetric measurements, FTIR spectra were obtained using a Bomem DA3.10 FTIR spectrometer equipped with a MCT detector ( $D^* = 3.13 \times 10^9\text{ cm Hz}^{0.5}$  and a low-frequency cutoff of  $400\text{ cm}^{-1}$ ) and a KBr beamsplitter. The Bomem DA3.10 spectrometer was controlled through a general-purpose-interface-bus (IEEE-488) interfaced to a DEC Vaxstation-II computer. The unapodized

resolution for the FTIR spectra was  $2.0\text{ cm}^{-1}$ . UV-visible spectra were recorded on a Perkin-Elmer 3840 photodiode array spectrophotometer at  $1.5\text{ nm}$  resolution.

The sample cell used for the tandem UV-visible / FTIR measurements a stainless steel, four-way KF cross with an extra vertical arm brazed onto it to enable a stainless steel sample holder to be suspended into the cross from above. Two pairs of cell windows were used: KCl for use with the infrared spectrometer; and sapphire for use with the uv-visible spectrometer. The clay films were stored in ambient air (approximately  $20^{\circ}\text{ C}$  and 50 percent relative humidity) prior to their use. Dehydration of the clay films was accomplished by inserting the film into the sample cell after loading the cell with granules of  $\text{P}_2\text{O}_5$  and PDMOB. The PDMOB granules were placed near the clay film and to the  $\text{P}_2\text{O}_5$ . Rehydration of the clay film was effected by removing the clay sample from the cell and then inserting it into another similar cell that was open to the ambient air. This cell was transported back and forth between the FTIR and UV-visible spectrometers during an experiment. The FTIR and UV-visible spectra were recorded 1 to 2 minutes apart. This delay was significant only in the first few minutes of the rehydration step where very rapid intensity losses occurred.

A 16-cm pathlength gas cell, fitted with two ZnSe windows, Viton<sup>®</sup> O-rings, and two stopcocks was modified to interface with a Cahn<sup>®</sup> controlled-environment Model D200-01 electrobalance. A schematic of the cell and the sample compartment of the FTIR spectrometer are shown in Figure 1. The modified gas cell provided for FTIR spectra and gravimetric data to be collected for the same sample simultaneously. The cell and electrobalance were connected to a gas manifold and vacuum pumping station. A self-supporting Cu-montmorillonite clay film was placed on a  $0.2\text{ mm}$  Pt hangdown wire in the Cahn electrobalance. The modified gas cell was mounted on an NRC optic table and was positioned using NRC translational stages which permitted adjustment of the cell. Mounting the cell on

the optic table mechanically decoupled the electrobalance assembly from vibrations originating from the FTIR spectrometer and other sources. The cell was positioned such that the clay film was centered on, and nearly perpendicular to, the incident modulated IR beam in the sample compartment.

The clay film was allowed to equilibrate in dry air under the influence of  $P_2O_5$  until a constant weight had been achieved. This typically required 2-3 hours. At this point, 500 mg of solid PDMOB was added to the gas cell and sorption of PDMOB on the dry-clay film was monitored using FTIR and gravimetric data. After a constant weight was obtained for the Cu-montmorillonite - PDMOB complex (approximately 12 hours), water was added to the cell and FTIR and gravimetric data were collected until a constant weight was obtained. The absorptivity of the OH bending band at  $1630\text{ cm}^{-1}$  and of selected PDMOB bands was determined by integrating the area of the band of interest and correlating this value with the known surface loading of water or PDMOB on the clay. These absorptivity values were then used to determine the surface loadings of water and PDMOB from the tandem FTIR / UV-visible spectra using Beer's law.

## C. RESULTS AND DISCUSSION

### 1 p-Xylene

#### a. Chemisorption of p-Xylene on Cu-montmorillonite

FTIR spectra of p-xylene sorbed onto a self-supporting Cu-montmorillonite (CuX) clay film are shown in Figure 13 as a function of the time of exposure to p-xylene vapor and  $P_2O_5$ . In contrast to the Co-montmorillonite system, a number of new vibrational bands appear at 820, 880, 1223, 1247, 1285, 1304, 1325, 1355, 1383, 1424, 1450-60, 1502, and  $1596\text{ cm}^{-1}$  upon dehydration. The normalized integrated intensities of these bands are plotted as a function of time in Figure 14.

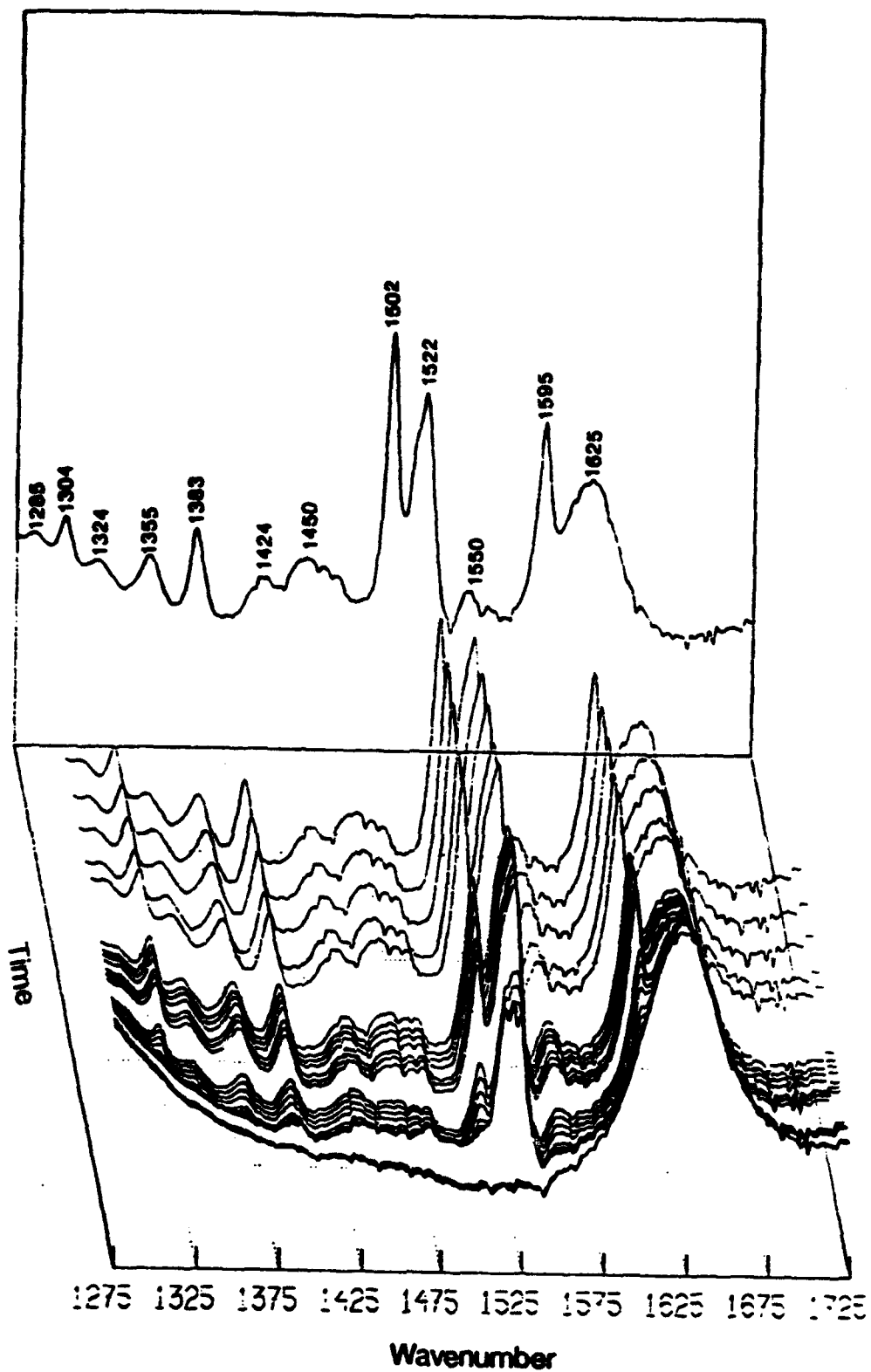


**Figure 13.** FTIR Spectra of Cu-montmorillonite Exposed to p-Xylene Vapor in the Presence of  $\text{P}_2\text{O}_5$  in the 1275 - 1725  $\text{cm}^{-1}$  Region. The Offset of Each Spectrum Along the z Axis Corresponds to the Time at which each Spectrum was Collected.

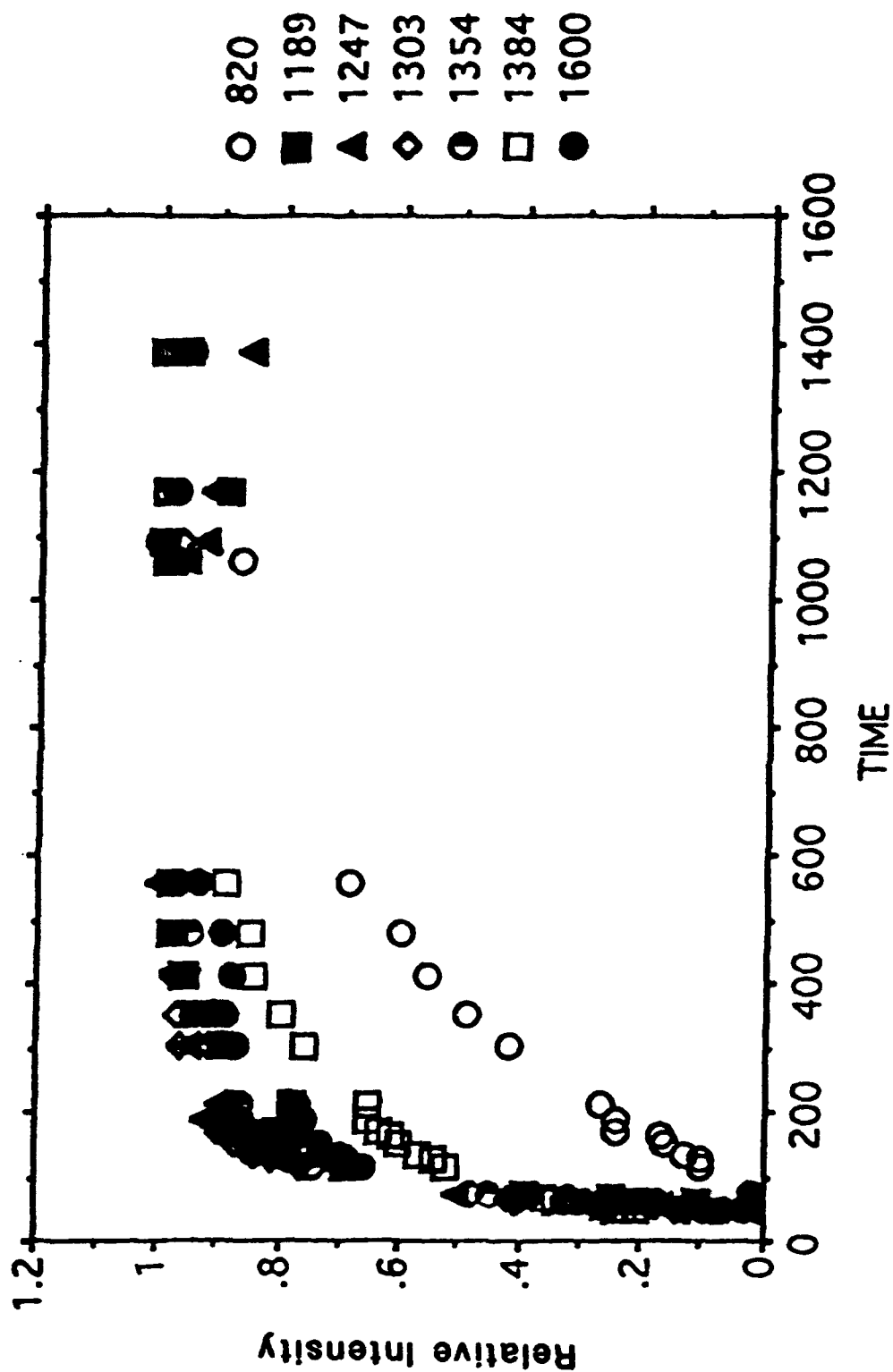


Figure 14. Growth of Selected Bands Observed in the CuX - p-Xylene Complex

The growth of the 1189, 1247, 1303, 354, 1384, 1502, and 1596  $\text{cm}^{-1}$  bands follow a similar growth pattern, whereas the time evolution of the 820  $\text{cm}^{-1}$  is slower. These data suggest that the 820  $\text{cm}^{-1}$  band may originate from a different chemisorbed species. With the exception of the 820 and 1502  $\text{cm}^{-1}$  bands (Reference 43), these bands have not been reported previously in the literature and do not correspond to modes which can be assigned to p-xylene or to the clay matrix.

b. 750 to 950  $\text{cm}^{-1}$  Region.

The spectrum of p-xylene sorbed onto CuX after exposure to p-xylene vapor for 4 hours is compared to vapor phase and matrix isolation spectra of p-xylene, and to the spectra of CoX and to that of p-xylene physisorbed on CoX in Figure 15 in the 725 to 950  $\text{cm}^{-1}$  region. The strong band at 795  $\text{cm}^{-1}$  in the vapor phase (Figure 15d) and matrix isolation (Figure 15e) FTIR spectra of p-xylene corresponds to the out-of-plane  $\text{C}_{\text{ring}}\text{-H}$  deformation mode (Reference 85). The C-type lineshape of the vapor phase band is representative of oblate shaped molecules ( $I_a < I_b = I_c$ ) (Reference 97). The bands at 844 and 917  $\text{cm}^{-1}$  correspond to the O-H deformation frequencies of  $\text{Al-(O-H)-Al}$  and  $\text{Al-(O-H)-Mg}$  structural moieties (Reference 98). The band at 820  $\text{cm}^{-1}$  and the weaker shoulder at 880  $\text{cm}^{-1}$  are unique to the CuX / p-xylene complex. No evidence of the 820 or 880  $\text{cm}^{-1}$  bands are found in the vapor phase (Figure 15d), or matrix isolation (Figure 15e) spectra of p-xylene, nor in the spectrum of p-xylene sorbed onto CoX.

c. 1200 to 1800  $\text{cm}^{-1}$  region

In addition to the perturbed bands in the out-of-plane C-H deformation region, "new" bands were observed at 1223, 1246, 1285, 1304, 1324, 1355, 1424, 1502, 1550, and 1595  $\text{cm}^{-1}$  which are not observed in the reference spectra of p-xylene (Fig. 11e-f) or in that of CuX clay (Fig. 11a). In a previous study of the CuX-p-

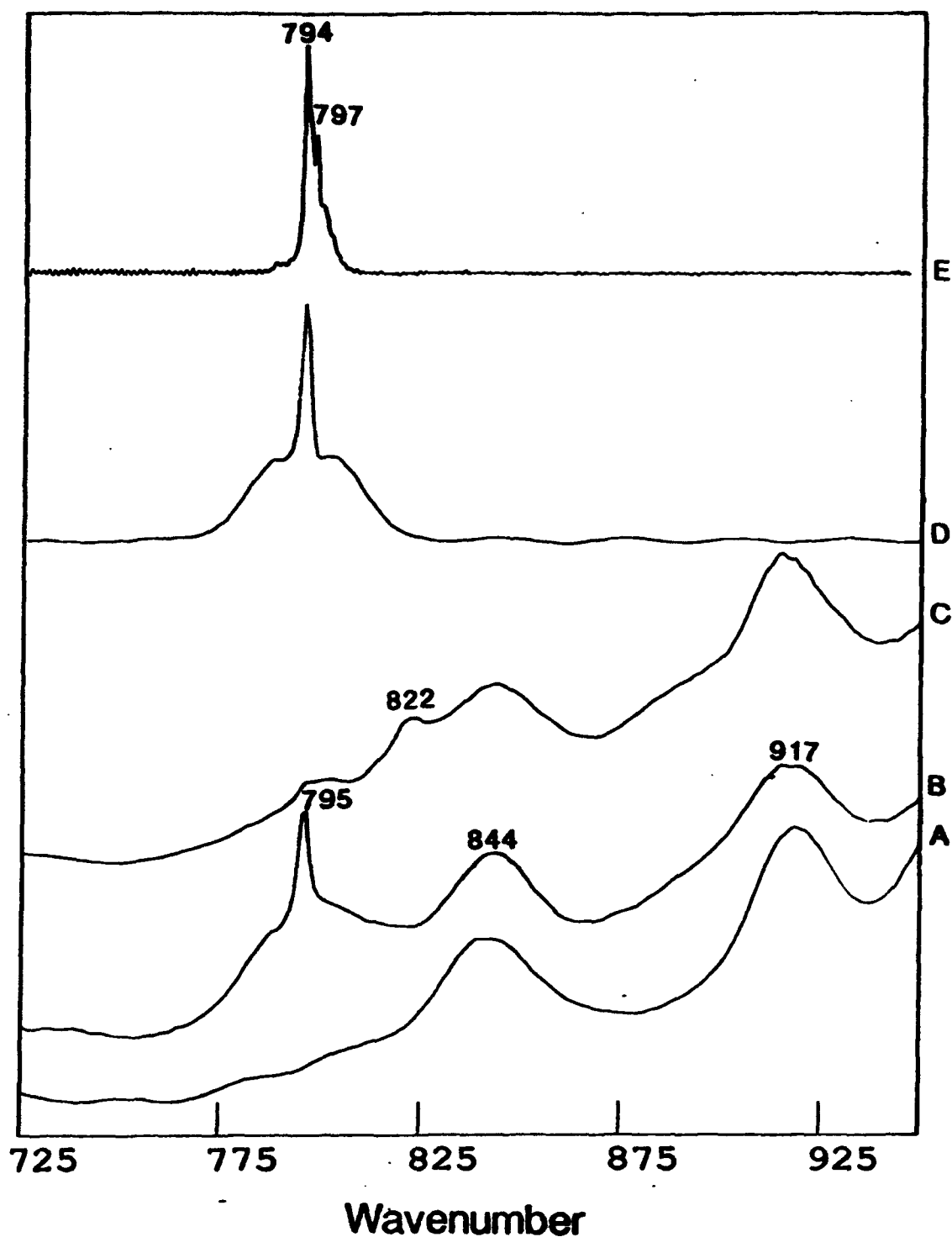


**Figure 15.** FTIR Spectra in the 725 - 950  $\text{cm}^{-1}$  Region of a Self-Supporting Film of Cu-Exchanged SAz-1 Montmorillonite (CuX) (A), CoX Film Exposed to p-Xylene Vapor (B), and CuX Film Exposed to p-Xylene Vapor (C) Obtained in the FTIR/Gravimetric cell in the Presence of  $\text{P}_2\text{O}_5$ . The Vapor-Phase (D) and Matrix Isolation Spectra of p-Xylene (E) are Shown for Comparison

xylene complex (Reference 43), the 1502  $\text{cm}^{-1}$  band was assigned to a red-shifted ring C-C ring mode. However, the other bands which appear upon dehydration at 1223, 1246, 1285, 1304, 1324, 1355, 1424, 1550, and 1596  $\text{cm}^{-1}$  have not been reported previously. Analogous shifts have been observed for a number of aromatic hydrocarbons sorbed on Cu- and Fe-exchanged montmorillonites. In the case of p-dimethoxybenzene, for example, Johnston et al. (Reference 34) showed that the  $\nu_{19}$  band shifted from 1509 to 1502  $\text{cm}^{-1}$  upon formation of a chemisorbed species. This band was assigned (Reference 34,46) to the formation of the radical organic cation (PDMOB<sup>+</sup>) upon dehydration. In a related Raman study of the PDMOB<sup>+</sup> cation in solution, a net decrease in the ring C-C force constants was suggested to account for the observed decrease in frequency of this mode upon oxidation which is consistent with the observed increase in the out-of-plane C-H deformation mode and strong color change.

#### d. UV-Visible Spectra

In addition to the perturbed vibrational modes, the color of the p-xylene-CuX complex changed from pale-blue to dark orange-brown. Using a tandem UV-visible/FTIR cell, a set of FTIR and UV-visible spectra were obtained for the sorption p-xylene on CuX as a function of time. This cell permitted the changes in the IR spectra to be correlated directly with those in the UV-visible in that the same sample could be analyzed using the two techniques at nearly the same time. The initial UV-visible spectrum of the dry Cu-montmorillonite clay without p-xylene present is characterized by an asymmetric absorption band at 240 nm with a shoulder at approximately 300 nm (Figure 16a). There is a broad, asymmetric tail on the the 240 nm feature which gradually loses intensity extending out to 800 nm. A strong band at 455 nm appears and increases in intensity upon exposure of the CuX film to p-xylene vapor (Figures 16b-d). The observed position of new band in the

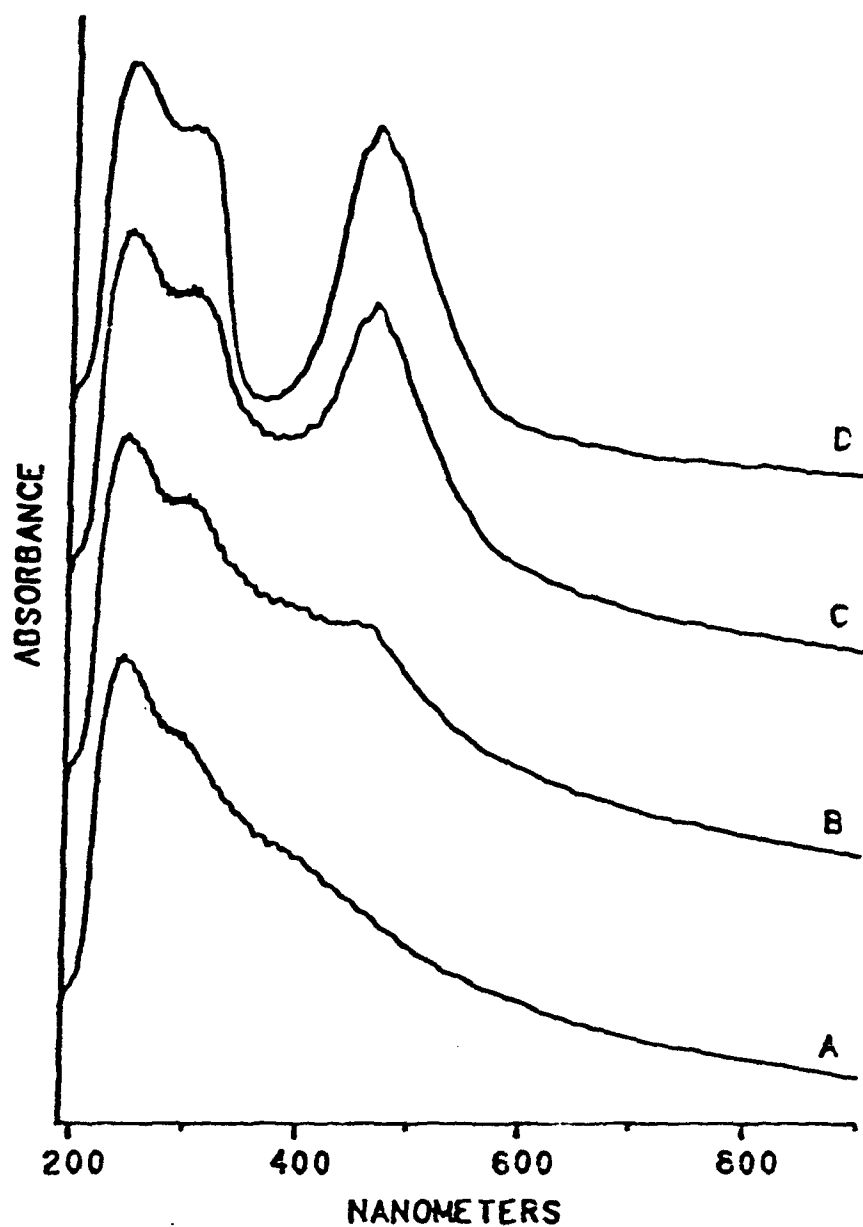


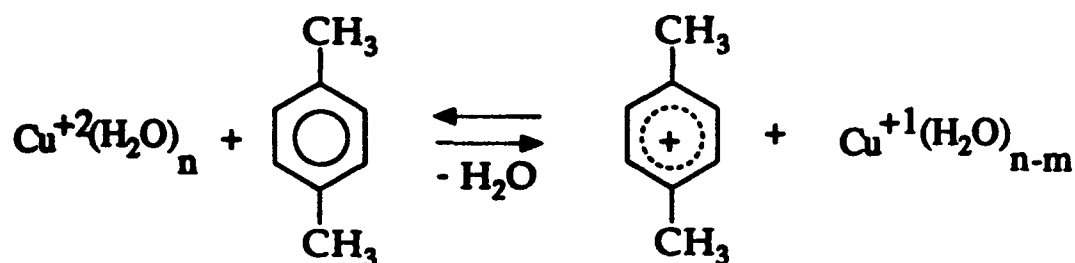
**Figure 16.** Ultraviolet-Visible Spectra of a Self-supporting Film of Cu-montmorillonite Exposed to p-Xylene Vapor for  $t =$  (A) 0.0, (B) 0.2, (C) 0.5, and (D) 1.0 hour Spectra were Obtained in the Tandem UV-Visible/FTIR Cell.

Cu-montmorillonite - p-xylene complex is in reasonable agreement with the value reported by Pinnavaia and Mortland (Reference 43) at 460 nm. They assigned the 460 nm band to the formation of a charge-transfer complex between the adsorbed p-xylene species and the transition metal cation.

The amount of p-xylene sorbed onto the dry CoX self-supporting clay film shown in Figures 9-10 was 0.924 mmol/g which corresponds to a fractional surface coverage of p-xylene on Co-montmorillonite of  $\Theta = 0.28$  monolayers (assuming a molecular surface area of p-xylene of 0.38 nm<sup>2</sup>/molecule). Comparable surface loadings of p-xylene have been reported for Y (Reference 99), and ZSM-5 (References 100,101) zeolites. A value of 0.11 mmol/g was reported by Rhue et al. (Reference 68) for p-xylene sorption on bentonite at a p-xylene P/P<sub>0</sub> concentration of 0.5. The significantly larger amount of p-xylene sorbed found in this study compared to the previous study (Reference 68) is attributed to the use of the desiccant P<sub>2</sub>O<sub>5</sub>. Reducing the amount of water present imparts the surface with a more hydrophobic character which enhances the sorption of p-xylene (Reference 71). The use of the FTIR/gravimetric cell provided a novel method to determine the separate contributions of water and p-xylene to the total mass of the sample (Figures 9-10).

No chemisorption was expected in the case of the CoX-p-xylene complex due to the unfavorably high reduction potential of Co<sup>+2</sup>, and due to negative result obtained for the CoX-benzene complex. In the case of Cu<sup>+2</sup>, however, previous studies have shown that p-xylene was chemisorbed on the surface of the Cu-exchanged montmorillonite which was attributed to a favorable coupling of the reduction potential of the metal cation and a moderately low ionization potential of p-xylene. The vibrational and electronic results obtained in this study for p-xylene sorbed on CuX are in good agreement with the earlier study of Pinnavaia and Mortland (Reference 43). They observed vibrational bands at 1503 and 817 cm<sup>-1</sup>, and

an electronic transition at 460 nm for the dry p-xylene-CuX complex which were assigned to perturbed  $\nu_{19a-b}$  ( $\nu(\text{C-C})$ ) and  $\nu_{11}$  ( $\delta_{oop}(\text{C-H})$ ) bands of p-xylene resulting from a single-electron-transfer reaction between p-xylene and the exchangeable  $\text{Cu}^{+2}$  metal cations of the montmorillonite as illustrated below:



The bands at 880, 1223, 1247, 1285, 1304, 1325, 1355, 1383, 1424, 1450-60, and 1596  $\text{cm}^{-1}$  have not been reported previously. However, the increase in intensities of these bands with time is very similar to that of the 1502  $\text{cm}^{-1}$  band (Figure 16) and on the basis of this agreement we assign these bands to the chemisorbed species.

The clay-mediated SET reaction shown above requires that p-xylene must first coordinate with the transition metal cation by assuming a direct ligand position. Under hydrated conditions, p-xylene has little, if any, affinity for the hydrophylic, interlamellar environment of the clay. Thus, minimal sorption of the p-xylene occurs on hydrated clay, oxide, or soil colloid surfaces (Reference 67,71). Dehydration of the Cu-exchanged montmorillonite, however, enhances p-xylene sorption by removal of the interlamellar water molecules which strongly compete for coordination sites around the  $\text{Cu}^{2+}$  cation which, in turn, allows the reaction to proceed to the right. Apparently, the formation of the radical p-xylene cation is stabilized on the surface of montmorillonite by the negatively charged siloxane ditrigonal cavities resulting from isomorphic substitution. Furthermore, the

presence of the methyl groups at the 1 and 4 positions on the ring serve as blocking groups which hinder subsequent dimerization and polymerization reactions (Reference 34).

Exposure of the dry chemisorbed complex to water vapor immediately lightens the color of the clay film to a light orange color and the vibrational bands (due to the chemisorbed species) are almost completely removed. This result is consistent with the formation of the radical organic cation under dry conditions. Similar to the chemisorption reaction of 1,4-dimethoxybenzene on Cu-montmorillonite (Reference 34), the methyl groups at the 1 and 4 positions hinder subsequent dimerization and polymerization reactions which are known to occur for benzene, toluene, thiophene and anisole. Addition of water vapor to the chemisorbed complex then drives the reaction to the left resulting in the formation of the neutral p-xylene species and the re-oxidation of  $\text{Cu}^{+1}$  to  $\text{Cu}^{+2}$ . The hydration of the metal cation, in turn, displaces the volatile surface species from the interlamellar region of the clay which is responsible for the nearly complete removal of p-xylene. Some residual intensity of the IR bands remain after exposure to water vapor. Similarly, the color of the clay film is not restored to its original pale-blue color but remains a light yellow-orange color. Thus, a small amount of the chemisorbed p-xylene can undergo further dimerization or polymerization.

## 2. PDMOB

The amount of water and PDMOB sorbed by Cu-montmorillonite was determined using an in-situ gravimetric FTIR cell. The surface loadings of PDMOB and water sorbed on Cu-montmorillonite, expressed as molecules/unit-cell, are plotted as a function of time in Figure 17. A three-dimensional plot of the FTIR spectra of the PDMOB-CuX complex in 1200 to 1800  $\text{cm}^{-1}$  region obtained as a function of time are shown in the lower portion of Figure 17. The offset of each

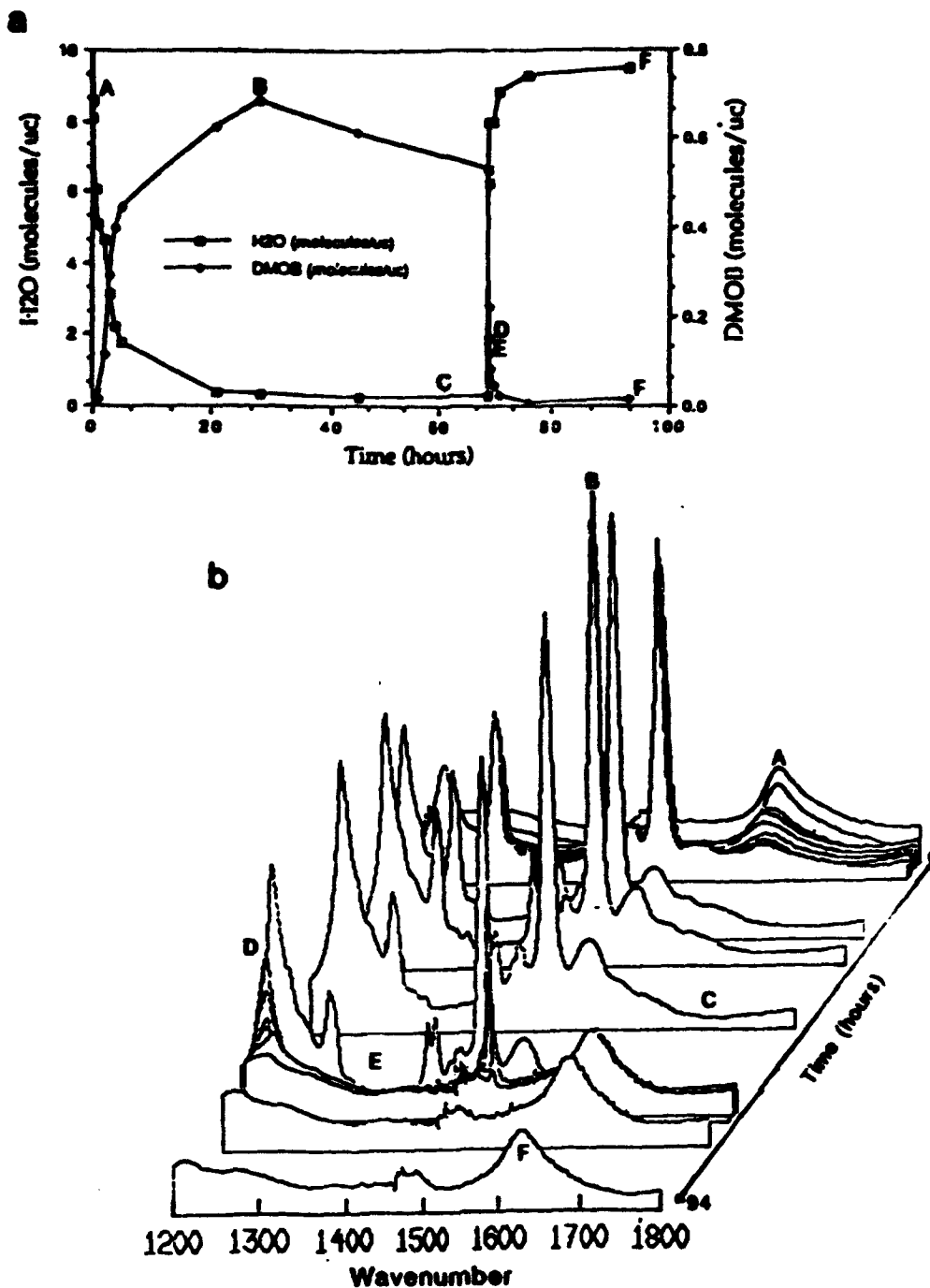


**Figure 17.** Surface Loading of H<sub>2</sub>O and PDMOB on the Cu-montmorillonite Film Expressed as Molecules Per Unit Cell (H<sub>2</sub>O Scale Shown on the Right; PDMOB on the left) as a Function of Time. (b) Three-Dimensional Plot of the FTIR Spectra in the 1200 - 1800 cm<sup>-1</sup> Region Presented as a Function of Time. The offset of Each Spectrum Along the z Axis Corresponds to the Time of Exposure to PDMOB and P<sub>2</sub>O<sub>5</sub> (0 hour < t < 69 hours) or to Water Vapor (t > 69 hours)

spectrum along the z-axis corresponds to the time at which the spectrum was collected. Initially, the high surface loading of water ( $\approx 9$  molecules/u.c.) is reflected by the strong OH bending band of water at  $1630\text{ cm}^{-1}$  (Point 17a). Upon dehydration over  $\text{P}_2\text{O}_5$  and exposure to PDMOB, the surface loading of PDMOB increased to approximately 0.7 molecules PDMOB/u.c. (Point 17b), whereas the intensity of the  $1630\text{ cm}^{-1}$  band was strongly diminished (Point 17c). Upon exposure to water vapor, the surface loading of PDMOB is rapidly lowered (Points 17d-e) with a concomitant increase in the amount of water sorbed (Point 17f). Several of the vibrational bands of the chemisorbed complex are completely eliminated after 6 minutes of contact (Point 17e) to water vapor, whereas other bands, although reduced in intensity, remain present for  $\approx 7$  hours (Point 17d). After 24 hours or exposure to PDMOB vapor, the water band at  $1630\text{ cm}^{-1}$  was restored to its original intensity (Point 17f) and no PDMOB bands remained.

**a. FTIR Spectra of PDMOB Sorbed on Cu-montmorillonite**

Representative FTIR spectra from the entire data set shown in Figure 17 are plotted in Figure 18b-h. The spectrum shown at the bottom (Fig. 18a) corresponds to that of the Cu-montmorillonite clay film exposed to ambient air (relative humidity  $\approx 50$  percent) prior to the addition of PDMOB to the cell. A moderate amount of water is present on the clay as evidenced by the intensity of the  $\delta(\text{O-H})$  band of adsorbed water at  $1630\text{ cm}^{-1}$  (Fig. 18a). Aside from the  $\delta(\text{O-H})$  band of water, there are no significant IR-active bands in the  $1200$  to  $1800\text{ cm}^{-1}$  region. Although self-supporting films of montmorillonite can be prepared, such a film could not be prepared in this study which was thin enough to permit both the UV-visible and FTIR absorption bands to be measured accurately. Thus, it was necessary to deposit the clay on a thin sheet of polyethylene which permitted extremely thin clay films to be prepared. The polyethylene spectrum (Fig. 18i) was subtracted from

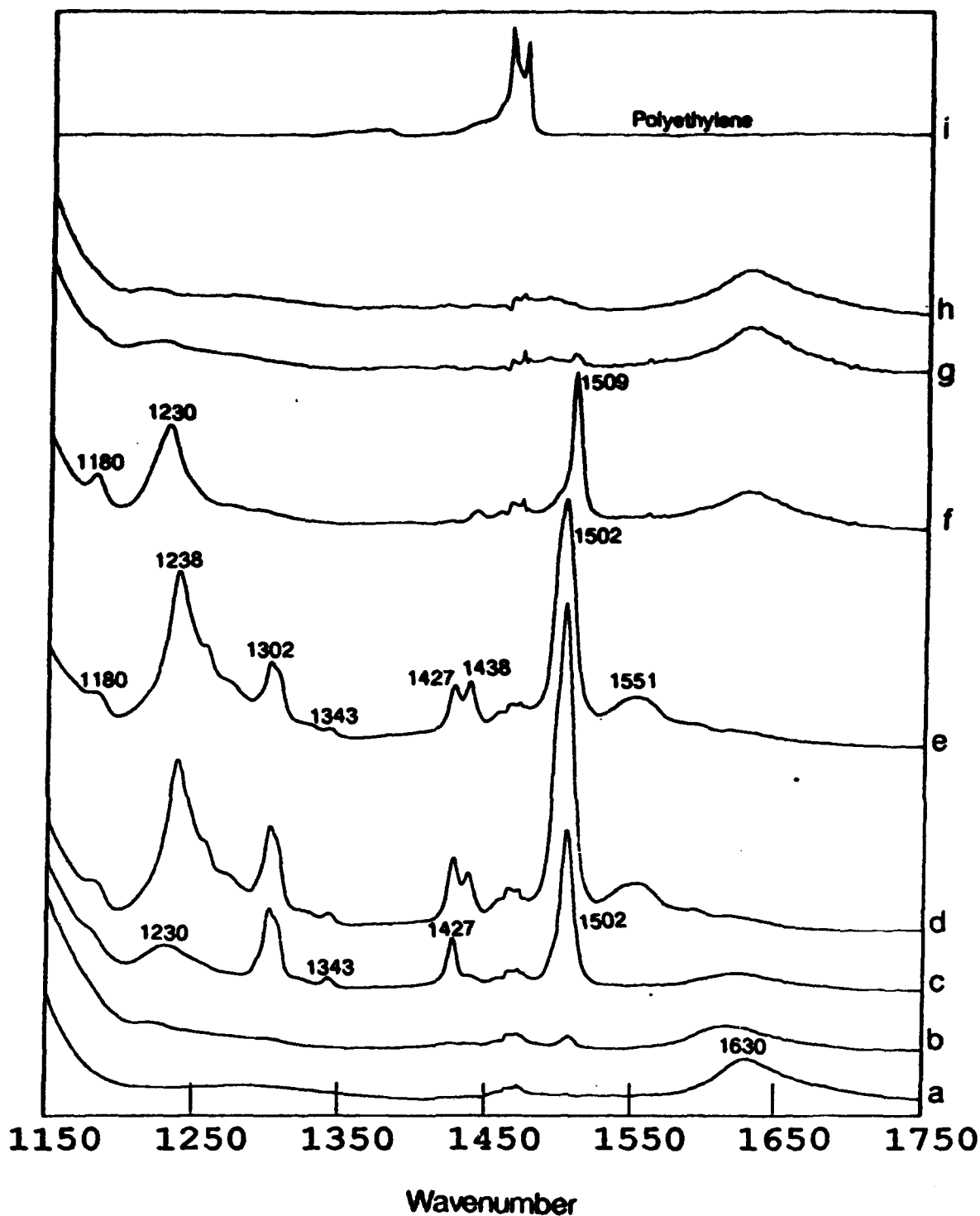


**Figure 18.** FTIR Spectra of Cu-montmorillonite Deposited onto a Sheet of Polyethylene (a) and of PDMOB on Cu-montmorillonite after 1.0 (b), 3.0 (c), 28 (d), and 69 hours (e) of Exposure to PDMOB and P<sub>2</sub>O<sub>5</sub>. at t = 69 hours the P<sub>2</sub>O<sub>5</sub> was Removed and the Complex was Exposed to Water Vapor. Spectra were Collected at 0.1 (f), 2.0 (g), and 24 hours (h) after Exposure to Water Vapor. The Spectrum of the Polyethylene (i) has been Subtracted From All of the Clay and Clay-Organic Spectra (a-h)

the spectra shown in Figures 3a-h. The polyethylene bands provided a slight interference in the 1450 - 1475  $\text{cm}^{-1}$  region (Figure 18i).

Upon exposure of the Cu-montmorillonite clay film to PDMOB and  $\text{P}_2\text{O}_5$ , the intensity of  $\delta(\text{O-H})$  water band at 1630  $\text{cm}^{-1}$  begins to diminish in intensity, whereas the intensities of the DMOB bands increase. The  $\delta(\text{O-H})$  water band has little of its original intensity, and the bands at 1180, 1230, 1302, 1343, 1427, 1438 and 1502  $\text{cm}^{-1}$  have increased significantly in intensity (Fig. 18c) after 3 hours of exposure to PDMOB and  $\text{P}_2\text{O}_5$ . After 69 hours (Fig. 18e), the intensities of the PDMOB bands have continued to increase and the 1630  $\text{cm}^{-1}$  water band is no longer present. In addition to the PDMOB bands listed above, "new" bands have appeared at 1438 and 1551  $\text{cm}^{-1}$  in the 69 hour spectrum (Fig. 18e).

A dramatic change in the intensities of the PDMOB/PDMOB<sup>+</sup> bands occurs upon exposure of the complex to water vapor. The spectrum shown in Figures 18f and 19 (t=69 hours) was collected 6 minutes after the PDMOB : Cu-X complex was exposed to water vapor. The bands at 1302, 1427, 1438 and 1551  $\text{cm}^{-1}$  are no longer present; in contrast, the PDMOB bands at 1180, 1230 and 1509 still have reasonable intensity. Upon further exposure of the complex to water vapor, the PDMOB bands are almost entirely diminished (Fig. 18g). Upon prolonged exposure of the complex to water vapor, there is no trace of sorbed PDMOB indicating that water has completely displaced the sorbed PDMOB. This spectrum (Fig 18h) is very similar to the clay spectrum prior to the addition of PDMOB and  $\text{P}_2\text{O}_5$  (Fig. 18a). The positions of the observed IR bands are compared to the literature values for PDMOB (IR and Raman), PDMOB<sup>+</sup> (Raman), and PDMOB sorbed on Cu-montmorillonite (Raman) in Table 4.

**Table 4** Infrared and Raman frequencies of DMOB, DMOB<sup>+</sup>, DMOB sorbed on Cu-montmorillonite

Lit <sup>a</sup> IR+R DMOB	Vapor IR DMOB	Matrix IR DMOB	Lit <sup>a</sup> R DMOB <sup>+</sup>	Lit <sup>a</sup> R DMOB	Obs. IR dry	Obs. IR wet	Symmetry	Assignment
			1647	1641		1630		water
1610	1600	1600	1638	1622			a <sub>g</sub>	8a
1588			1584				a <sub>g</sub>	8b
1515	1515	1518	1510	1495	1551	1509	b <sub>g</sub>	19 a/b
	1475	1511			1502			
		1477	1477	1460				
1470								
1462							a <sub>g</sub>	as δ(CH <sub>3</sub> )
1462		1460					b <sub>g</sub>	as δ(CH <sub>3</sub> )
1462							b <sub>g</sub>	as δ(CH <sub>3</sub> )
1462							a <sub>g</sub>	as δ(CH <sub>3</sub> )
1452	1450	1445					a <sub>g</sub>	symm δ(CH <sub>3</sub> )
	1445	1442			1438	1441		
1420	1418	1415			1427		b <sub>g</sub>	symm δ(CH <sub>3</sub> )
			1382					
					1343			
					1326			
1307	1310	1305	1375	1322	1308		a <sub>g</sub>	7a (X sens)
1292	1295	1299			1302	1293	b <sub>g</sub>	14
1264	1255	1270	1278		1270	1273	a <sub>g</sub>	3 [β(CH)]
					1256			
1240	1242	1240			1238	1230	b <sub>g</sub>	13 (X sens)
1180			1198				a <sub>g</sub>	9a [β(CH)]
1178			1186	1179			b <sub>g</sub>	ρ(CH <sub>3</sub> )
1178	1185	1188			1183	1181	a <sub>g</sub>	ρ(CH <sub>3</sub> )
1150	1158	1158	1124				b <sub>g</sub>	ρ(CH <sub>3</sub> )
					1113	1115		mont
	1112	1114						
1104	1104	1108					b <sub>g</sub>	15 [β(CH <sub>3</sub> )]
	1060	1065						
1042		1059	979	989			b <sub>g</sub>	18a [β(CH <sub>3</sub> )]
				974	990 - 1090			mont Si-O str
1030		1048					a <sub>g</sub>	O-CH <sub>3</sub> stretch
1019		1035					b <sub>g</sub>	O-CH <sub>3</sub> str
937							a <sub>g</sub>	17a γ(CH)
					917	917		mont δ(OH) def
845							b <sub>g</sub>	10a γ(CH)
					838	836		mont δ(OH) def
827	830	827					a <sub>g</sub>	11
820	822	820		819			a <sub>g</sub>	1 (X sens)
798	792						b <sub>g</sub>	5 [γ(CH)]
	789	789						
								mont
								mont
710		725			717	718	b <sub>g</sub>	4
709	720	718				712	b <sub>g</sub>	12 (X sens)
					673			
635			615	624	625	625	a <sub>g</sub>	6b
								mont
				609	617	617		
550			550	543			a <sub>g</sub>	9b (X sens)
517			530	522			a <sub>g</sub>	16a
472							b <sub>g</sub>	18b (X sens)
419							a <sub>g</sub>	17b (X sens)
406			404	405			a <sub>g</sub>	6a

#### **b. Electronic Spectra of PDMOB Sorbed on Cu-montmorillonite**

Sorption of PDMOB on dry Cu-montmorillonite results in a large color change with the clay film turning from light blue to green. A cell was designed to permit both FTIR and UV-visible spectra to be obtained on the same sample. The UV-visible spectra shown in Figure 19 were obtained on the same PDMOB : Cu-X sample and at nearly the same times as the FTIR spectra shown in Figures 17-18. This permitted the FTIR spectra to be correlated directly to the electronic absorption spectra. The most significant changes which occur in the UV-visible spectra are the appearance and subsequent growth of three bands at 325, 451 and 464 nm. In addition to these band maxima, there is a broad, underlying band at  $\approx 400$  nm with considerable intensity. The intensities of these bands are strongly reduced upon addition of water vapor to the cell at  $t=69$  hours (Fig. 19f). In addition to the 400, 451 and 464 nm bands, the broad band at 295 nm corresponds to the [0,0] band for PDMOB and agrees with published UV-visible spectra of PDMOB (Reference 102). The intensity of the 295 nm band, however, is diminished considerably more slowly than the 400, 451 and 464 nm bands. In addition to the 400, 451 and 464 nm bands, a low energy electronic transition above 900 nm appears to grow in intensity upon dehydration. The presence of this low-energy band is reflected by the appearance of a high frequency shoulder in the UV-visible spectrum of the dehydrated PDMOB : Cu-X complex (Figure 19d,e), and by the increased baseline in the FTIR spectra in the high-frequency region  $3000 - 4000\text{ cm}^{-1}$  (not shown).

#### **c. Discussion**

Upon dehydration of the Cu-montmorillonite: PDMOB complex, an electron transfer reaction occurs where  $\text{Cu}^{+2}$  is reduced to  $\text{Cu}^+$  or  $\text{Cu}^0$  resulting from the oxidation of PDMOB to  $\text{PDMOB}^+$ . Formation of the radical organic cation on the interlamellar surface is evidenced by the large color change

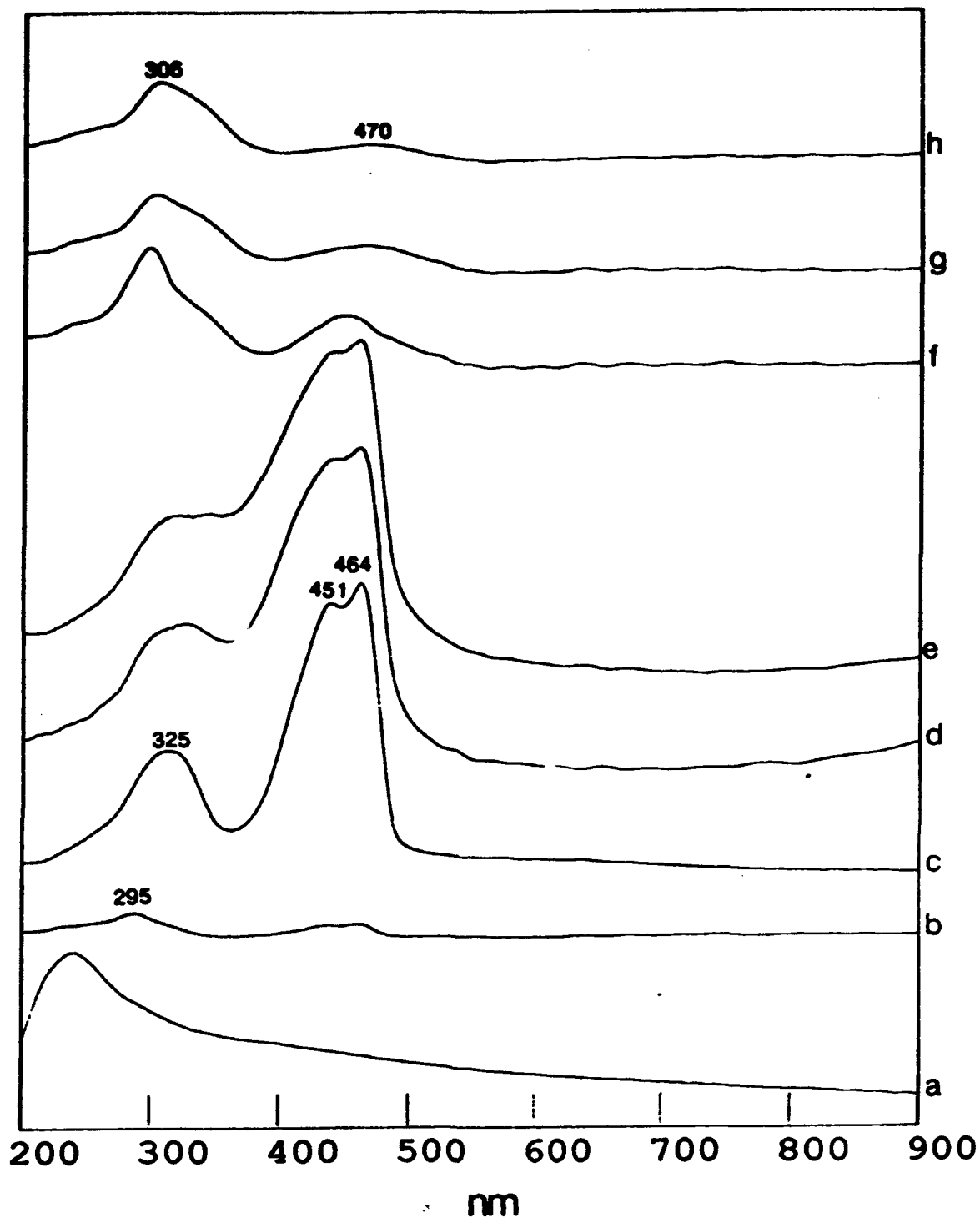


**Figure 19.** UV-Visible Spectra of Cu-montmorillonite Deposited onto a Sheet of Polyethylene (a) and of PDMOB Sorbed onto Cu-montmorillonite After 1.0 (b), 3.0 (c), 28 (d), and 69 hours (e) of exposure to DMOB and  $P_2O_5$ . at  $t = 69$  hours the  $P_2O_5$  was Removed and the Complex was Exposed to Water Vapor. Spectra were Collected at 0.1 (f), 2.0 (g), and 24 hours (h) after Exposure to Water Vapor. The Spectrum of the Cu-montmorillonite Film (a) was Subtracted From all of the Clay-Organic Spectra (b-h).

(Fig. 19), formation of new bands in the FTIR spectra (Fig. 17-18), loss of the ESR signal from the paramagnetic  $\text{Cu}^{2+}$  species, and the subsequent growth of a new ESR band at  $g=2.005$  which has been assigned the  $\text{PDMOB}^+$  radical (Reference 46). Similar to other clay mediated electron transfer reactions, the reaction only proceeds under dry (e.g.,  $\text{P}_2\text{O}_5$ ) conditions as shown in Reaction (1). As this reaction proceeds to the right, the two prominent bands at 451 and 464 nm increase in intensity. The position of these bands is in good agreement with published UV-vis absorption spectra of the  $\text{PDMOB}^+$  cation (References 96,103,104). Tadamasa et al. (Reference 96) reported bands at 429, 443, and 475 nm for  $\text{PDMOB}^+$  in butyl chloride, whereas Ernstbrunner et al. (Reference 103) observed bands at 433 and 458 nm in aqueous suspension using  $\text{Ce}^{4+}$  to oxidize  $\text{PDMOB}$ . The 400 nm band observed here (Figure 19) has not been reported in the literature; however, the electronic spectra of  $\text{PDMOB}$  sorbed on Cu-montmorillonite reported by Soma et al. (Reference 46) contains a lower-energy shoulder in this region.

The electronic spectra indicate that the  $\text{PDMOB}$  radical cation is stabilized on the clay surface in the absence of water. This agrees well with the ESR data of Soma et al. (Reference 46) who reported that 25 percent of  $\text{Cu}^{2+}$  spins lost upon reduction of  $\text{Cu}^{2+}$  are recovered as organic free radicals. For most other aromatic hydrocarbons adsorbed on Cu-montmorillonite, a much smaller proportion of free radicals are recovered from the loss of  $\text{Cu}^{2+}$ . In the case of benzene, for example, less than 5 percent of the  $\text{Cu}^{2+}$  spins lost are recovered as free radicals (Reference 44,45,78,80). The observed stability of the  $\text{PDMOB}$  radical cation is attributed to the fact that the methoxy substituents on the para positions of the ring stabilize the radical cation. Additional stability for the  $\text{PDMOB}^+$  species is provided by the negatively charged interlamellar clay surface. The SAz-1 montmorillonite clay used in this study has a cation exchange capacity of 1.20 meq/g resulting from isomorphous substitutions within the clay lattice. The ethylene glycol surface area of this clay is  $710 \text{ m}^2/\text{g}$ ; the

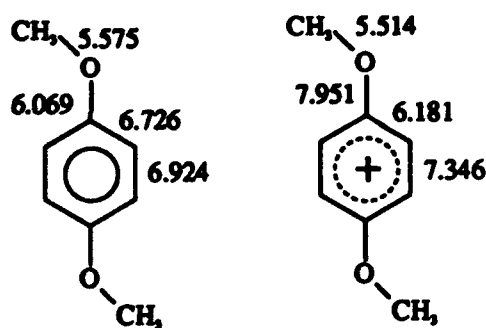
corresponding density of exchange sites for this clay is 1.01 (exchange sites)/nm<sup>2</sup>. Thus, the high density of negatively charged exchange sites can provide additional stabilization for the radical cation.

The PDMOB bands in the vibrational spectra of the PDMOB : Cu-X complex were no longer present (Figures 17-18) after exposure to water vapor for 24 hours. Thus, little, if any, polymerization of PDMOB occurred. In contrast, many other electron transfer reactions which have been observed on montmorillonite are accompanied by polymerization reactions. Chemisorption of benzene, for example, on transition-metal-exchanged montmorillonite is known to proceed initially through an electron transfer reaction which is followed by subsequent polymerization reactions. Since polymerization of PDMOB is minimal, the observed changes in the UV-visible and infrared spectra are assigned to the formation of free radicals in the interlayer region of the clay.

Upon dehydration of the clay-organic complex, the surface Lewis acidity of the interlamellar cation is strongly increased (Reference 50). In the case of PDMOB, the loss of water from the hydration sphere of interlamellar Cu<sup>2+</sup> ions permits the PDMOB species to approach the interlamellar Cu<sup>2+</sup> ions. When combined with the low ionization potential of PDMOB (7.9 eV (Reference 105)), the surface enhanced Lewis acidity results in favorable conditions for the charge transfer reaction. Based upon the gravimetric data, the presence of water precludes the sorption of PDMOB (Figure 17). The high concentration of water molecules in the interlamellar region (9 molecules/unit cell) apparently creates a predominantly hydrophilic environment in the interlamellar region. Typical of hydrophobic organic solutes, sorption of PDMOB on montmorillonite is insignificant under moist conditions. Removal of water from the interlamellar region, however, allows PDMOB molecules an opportunity to compete for sites in the interlamellar region as

evidenced by the pronounced increase in the surface loading of PDMOB under dry conditions.

Several of the infrared-active bands are strongly influenced by the oxidation state of PDMOB. Typical of aromatic hydrocarbons undergoing electron transfer reactions, the  $\nu_{19}$  (following Wilson's notation (Reference 106) ) band of PDMOB is shifted to a lower frequency by  $8\text{ cm}^{-1}$  from  $1509$  to  $1502\text{ cm}^{-1}$  upon dehydration. For comparison, Pinnavaia and Mortland (Reference 43) observed dehydration induced red-shifts of  $7$  to  $13\text{ cm}^{-1}$  for benzene, toluene and related arene compounds adsorbed onto dry Cu montmorillonite relative to their physisorbed positions. According to a Raman study and normal coordinate analysis (Reference 103) of PDMOB and PDMOB<sup>+</sup>, several of the C-C and C-O stretching force constants were determined (shown below).



Upon oxidation, the average C-C force constant for the aromatic ring is decreased. This calculated decrease is in qualitative agreement with the observed red-shift of the  $\nu_{19}$  mode from  $1509$  to  $1502\text{ cm}^{-1}$ .

In contrast, a shift to higher frequency is observed for the  $\nu_{13}$  mode which increases from  $1230$  to  $1238\text{ cm}^{-1}$  upon oxidation. The potential energy distribution for the  $\nu_{13}$  mode (Reference 103) was shown to contain a significant percentage of C-O stretch ( $C_{\text{ring}}$ ). Furthermore, the calculated force constants for the  $C_1$ -O and  $C_4$ -O bonds of the PDMOB radical cation were shown to increase from  $6.069$  to  $7.951\text{ mdyn \AA}^{-1}$  upon oxidation. The observed blue-shift of this band is in qualitative

agreement with the calculated force constants. for the PDMOB radical cation. In addition to the blue shift, this band increases in intensity relative to other PDMOB modes as the water content is decreased. This band immediately loses its 'extra' intensity gained upon oxidation and shifts back to its preoxidized position of  $1230\text{ cm}^{-1}$  upon exposure of the complex to water vapor.

The  $1302$ ,  $1308$ ,  $1343$ ,  $1427$ ,  $1438$  and  $1551\text{ cm}^{-1}$  bands all disappear within 6 minutes of exposure to water vapor. In contrast, the  $1230\text{-}8$  and the  $1502\text{-}9$  bands were found to remain on the clay for 7 hours. The integrated intensities of the  $1230\text{-}8$  and  $1502\text{-}9$  bands are plotted as a function of time in Figure 20. These bands appear to be associated with both the neutral PDMOB and with the  $\text{PDMOB}^+$  species. The growth and reduction of the integrated intensities as a function time of these bands are quite similar. The behavior of the  $1302$ ,  $1308$ ,  $1427$  and  $1551$  are distinct from the  $1230\text{-}8$  and  $1502\text{-}9$  bands as shown in Figure 20. Whereas a 'slower' growth in intensities for  $1230\text{-}8$  and  $1502\text{-}9$  bands occurs (Fig. 20), the growth of the  $1302$ ,  $1308$  (integrated as one band),  $1426$ , and the combined area of the  $400$ ,  $451$ , and  $464\text{ nm}$  bands in the UV-visible spectrum is more rapid. Thus, these data indicate that the  $1302$ ,  $1308$ , and  $1426\text{ cm}^{-1}$  bands in the infrared and the  $400$ ,  $451$  and  $464\text{ nm}$  bands in the electronic spectra are associated primarily with the  $\text{PDMOB}^+$  radical cation. In addition, two new bands at  $1438$  and  $1551\text{ cm}^{-1}$  exhibit a slower growth in intensity than the  $1302$ ,  $1308$ , and  $1426\text{ cm}^{-1}$  bands. Similar to the other  $\text{PDMOB}^+$  bands, however, they are quickly annihilated by the presence of water (Fig. 20). These data suggest that two different surface species related to the  $\text{PDMOB}^+$  are present upon prolonged exposure of the complex to the PDMOB and  $\text{P}_2\text{O}_5$ .

The strong agreement of the observed UV-visible to published UV-visible and ESR spectra indicate that the  $\text{PDMOB}^+$  radical species is the predominant surface species under dry conditions. Several of the IR bands associated with the radical cation appear to correlate with PDMOB bands in the matrix-isolation (MI) and/or

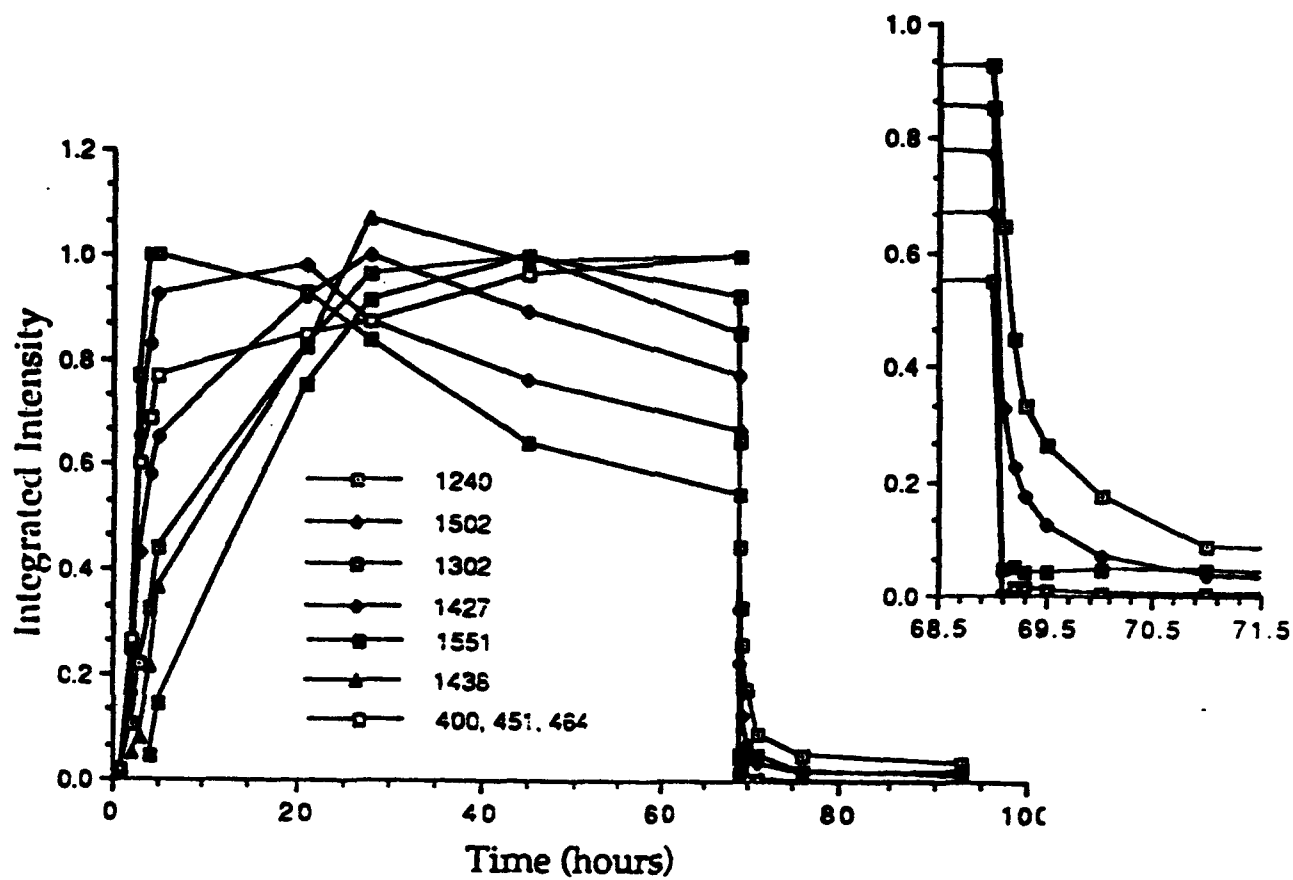


**Figure 20.** Plot of the Integrated Intensities of Selected IR and UV-Visible Bands as a Function of Time of Exposure of the Cu-montmorillonite Clay film to  $P_2O_5$  and PDMOB ( $0 < t < 69$  h) and Water Vapor ( $t > 69$  h)

vapor-phase spectra of PDMOB (Table 4). The 1295 and 1445-50  $\text{cm}^{-1}$  vapor phase bands, for example, have comparable intensity to those in the  $\text{PDMOB}^+ : \text{Cu-X}$  spectrum. Possible explanations to account for the appearance of these bands in the dry (oxidized) state and their absence in the presence of water vapor include (1) a re-orientation of the complex under dry conditions, and (2) enhanced intensity associated with the formation of the radical cation.

The self-supporting Cu-montmorillonite clay films used in this study had a preferred orientation of the 001 planes of the montmorillonite particles aligned perpendicular to the incident IR beam. Possible orientations of the aromatic ring of intercalated PDMOB include: (1) laying 'flat' on the siloxane surface (parallel to the 001 plane), (2) standing on edge (perpendicular to the 001 plane), or (3) with the plane of the ring making an intermediate angle of 0 (1) and  $90^\circ$  (2) with the 001 plane. Given the length of the PDMOB molecule from end-to-end, it is highly unlikely that the PDMOB molecules stand on end in the interlamellar environment which would result in an unfavorably large basal spacing. The two PDMOB IR-active fundamental vibrations which are most sensitive to the dehydration state of the clay are the 1238, 1302, 1308, 1427 and 1438  $\text{cm}^{-1}$  bands. Upon examination of the potential energy distribution of these bands among the symmetry coordinates (Reference 103), there does not appear to be a consistent grouping of these modes into either in-plane or out-of-plane modes which could account for the preferred orientation hypothesis.

The observed increase in intensity of the 1238, 1302, 1308, and 1438  $\text{cm}^{-1}$  bands, as well as the appearance of the two new bands at 1427 and 1551  $\text{cm}^{-1}$ , appears to be associated with the oxidation of the neutral molecule to  $\text{PDMOB}^+$ . This is consistent with a previous vibrational study of the PDMOB sorbed on Cu- and Ru-montmorillonites (Reference 46), where large changes in the relative intensities of

PDMOB bands were reported. We assign the 1238, 1302, 1308, 1427, 1438, and 1551  $\text{cm}^{-1}$  bands, therefore, to the PDMOB<sup>+</sup> species.

#### D. CONCLUSIONS

Physisorption of p-xylene on Co-montmorillonite resulted in a shift of the  $\nu_{19}$  mode (C-C ring stretch) mode from 1520 to 1516  $\text{cm}^{-1}$  as well as a loss of the P-Q-R lineshape of vapor phase band due to a sorption induced loss of translational and rotation freedom. This shift was sufficient to permit discrimination of the sorbed species from the vapor phase component. Correlation of the FTIR spectra with the gravimetric data provided a direct method to determine the individual masses of p-xylene and water sorbed whereas the gravimetric data alone could only provide the composite change. No evidence for chemisorption was found in the case of p-xylene sorption on Co-montmorillonite; however, chemisorption was readily apparent for sorption on Cu-montmorillonite. Chemisorption of p-xylene on Cu-montmorillonite was reflected by the dramatic color change of the sample from a pale yellow to dark orange, by the growth of an intense band in the UV-visible spectrum at 455 nm, and by the appearance and growth of set of new bands in the FTIR spectra which could not be assigned to p-xylene or to the clay. These new bands are assigned to formation of a radical organic cation of p-xylene resulting from a single electron transfer reaction on the surface of the clay. The fact that chemisorption was observed for Cu-montmorillonite but not in the case of  $\text{Co}^{+2}$  was related to the difference in the reduction potentials of the two metal cations.

## SECTION V

### MATRIX ISOLATION STUDIES OF ORGANIC CATIONS

#### A. INTRODUCTION

The spectroscopic study of organic molecular ions has received a considerable amount of attention recently (References 107-114). While good techniques have been developed to study the electronic spectra of aromatic and other organic ions (Reference 115-124), suitable approaches to produce quantities of these cations sufficient for observation of infrared and Raman spectra have not been widely reported (References 125-127). However, in clays such as montmorillonite and kaolinite, whose cations have been (partially) exchanged with specific transition metals such as Cu or Fe, certain aromatics readily form radical cations by an electron transfer between the aromatic and the metal. Mortland and Pinnavaia were among the first to experimentally delineate this process (References 44,75,90,128). Soma and co-workers showed (References 46,79,91) that if the para positions were blocked by a suitable group the radical cation was stabilized on the clay, but in the absence of such groups dimerization and polymerization reactions occurred. Johnston and co-workers have recently observed (Reference 34), as discussed in this report, the growth of a number of infrared bands in Cu-exchanged montmorillonite after adsorption of para-dimethoxybenzene (as well as other aromatics) under anhydrous conditions. Part of this study was to determine the vibrational frequencies of the radical cations of a number of aromatic molecules in a nonperturbing environment such as a rare gas matrix for comparison with the clay medium.

No studies of the infrared spectra of aromatic radical cations isolated in rare gas matrices have been reported. Although a number of articles have been published dealing with the electronic (or vibronic) spectra of the cations of some

aromatics (Reference 115-124). The methods usually employed to produce the cations included vacuum ultraviolet photolysis (Reference 118-122), pulsed radiolysis (References 115-117), x-ray photolysis (References 115-117) and electron bombardment (Reference 124). Apparently none of these methods is capable of producing sufficient quantities of the desired cation in a cryogenic matrix to be able to observe the inherently weaker infrared transitions. Thus, this report details our attempts to develop a method to do this and shows the techniques utilized to ensure that the vibrational bands observed belong to the desired aromatic parent radical cation.

## B. EXPERIMENTAL APPARATUS AND PROCEDURES

### 1. Matrix Isolation System

The stabilization and trapping of reactive ions and radicals in cryogenic rare gas matrices has been known since its introduction in the 1950s by Pimentel and co-workers (Reference 129). This technique requires that the species under study be formed in some fashion in the vapor phase and thence deposited with an excess of rare (Ne, Ar, Kr or Xe) or inert gas (e.g., N<sub>2</sub>) on a cold window at such a low temperature (usually 4K or 10K) that the rare/inert gas will condense and eventually form a solid film. The sample will then be surrounded in the solid by rare gas atoms and thereby prevented from diffusing to other sites and reacting with its neighbors. Thus the sample is isolated from its neighbors in the matrix, i.e., matrix-isolated.

The heart of the matrix isolation apparatus is a closed-cycle helium refrigerator (APD, Displex 202) capable of reaching temperatures of 10K at its cold finger tip. Cooling is achieved by expansion of compressed helium gas in a two-stage process. Obviously, the space surrounding the cryogenic sample tip must be

evacuated of all air and water and other condensibles: this is accomplished easily by a pumping station (Alcatel PDR250) comprised of diffusion and mechanical pumps plus assorted gauges, valves and vacuum tubing. A sample window held in a copper holder is attached to the cold finger of the cryostat. The temperature of the sample window is measured by a gold-chromel-iron thermocouple mounted near the middle of the sample window holder. Pressures inside the sample chamber were monitored by an ion gauge (Lesker, Model 4336P). For the infrared and UV/visible measurements the plasma mixture was trapped on a BaF<sub>2</sub> window, while for the resonance Raman and fluorescence runs the mixture was deposited on an angled, polished aluminum block attached to the closed-cycle cryostat tip.

## 2. Spectroscopic Instruments

Infrared spectra were run on a Nicolet 7199 Fourier transform infrared spectrometer (usually with 300 scans and 1 or 2 cm<sup>-1</sup> resolution), while the UV/visible scans were performed on a Cary 17 spectrophotometer (0.2 to 0.6nm resolution over the 240-700 nm range). In the later experiments the sample cryostat was positioned in a specially-constructed sample housing for the Cary 17. This housing allowed the IR beam exiting the FTIR to pass through KBr windows in the cryostat's outer shroud, reflect off a set of curved and plane mirrors and focus onto an IR detector (DTGS or MCT) located beneath the cryostat. Nitrogen gas purging of the entire IR beam path from the FTIR exit hole to the special compartment was effected within glass connecting tubes. This "cross beam" arrangement permitted sample scans in the UV/visible followed by IR on the same sample matrix. To change from the UV/visible to IR ranges a simple 90-degree rotation of the sample cryostat is all that is necessary. The BaF<sub>2</sub> sample window is transparent over the 210 nm to 14 micron range and is thus usable in both the IR and UV/visible regions.

### **3. Ionization Sources**

Four different approaches were investigated in our attempts to produce cations of the aromatic hydrocarbons. These will be discussed briefly with the major emphasis on the last and best approach.

#### **a. Photoionization**

Boric acid is a solid at room temperature and has been used as a "solvent" for the aromatic hydrocarbons previously (Reference 123). Two experiments using boric acid with anthracene and with pyrene were tried. By heating the boric acid up to its melting point (236 °C), mixing in the aromatic compound and casting on a flat surface it was possible to create relatively clear films. Photolysis of these films for from 4 hours (for pyrene) to 15 hours (for anthracene) with a low-pressure Hg lamp (254 nm line) produced samples containing the cations of the PAHs. Figures 21 and 22 show the visible/ultraviolet (vis/UV) spectra of the pyrene and anthracene samples. It can be seen that upon irradiation new bands appear in the visible region of both spectra. These bands are assignable to the cations of the PAHs. This approach while simple in practice was abandoned for several reasons: low resolution, low concentration of cationic species, highly perturbing medium and interfering medium background lines expected in the infrared. Since the goal of this research was the vibrational spectroscopy of the PAH cations in a medium with little or no perturbation, the present approach was dropped in favor of gas-phase ionization followed by trapping in cryogenic rare gas matrices.

#### **b. Conical Pulse Glow Discharge**

Our initial attempts at gas phase ionization utilized a continuous flow glow discharge. A continuous stream of argon gas, into which was sublimed the PAH under study, flowed through a chamber containing two electrically isolated, sharpened rods in close proximity which were held at a couple

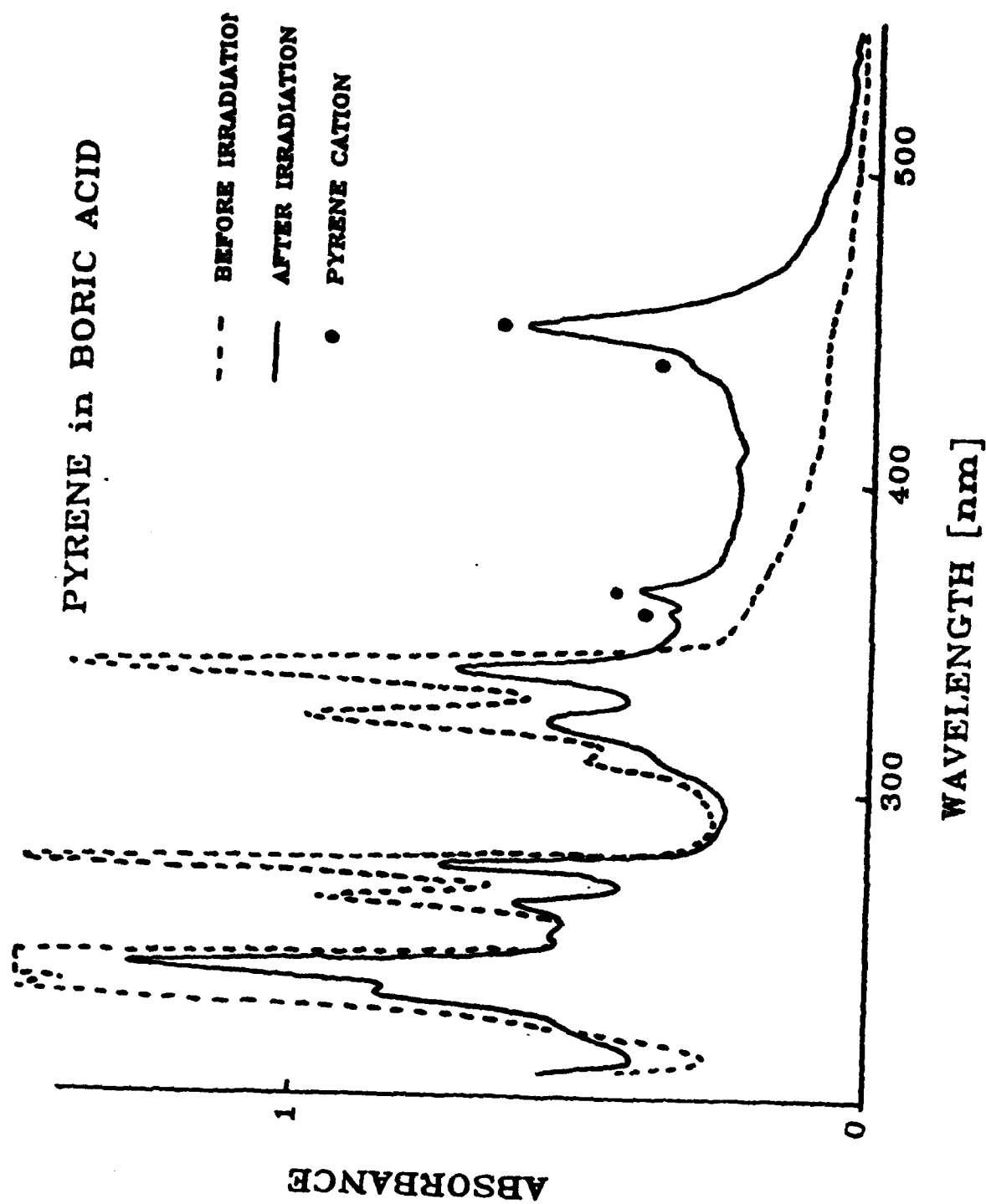


Figure 21. Visible-Ultraviolet Spectrum of Pyrene in Boric Acid Matrix at Room Temperature

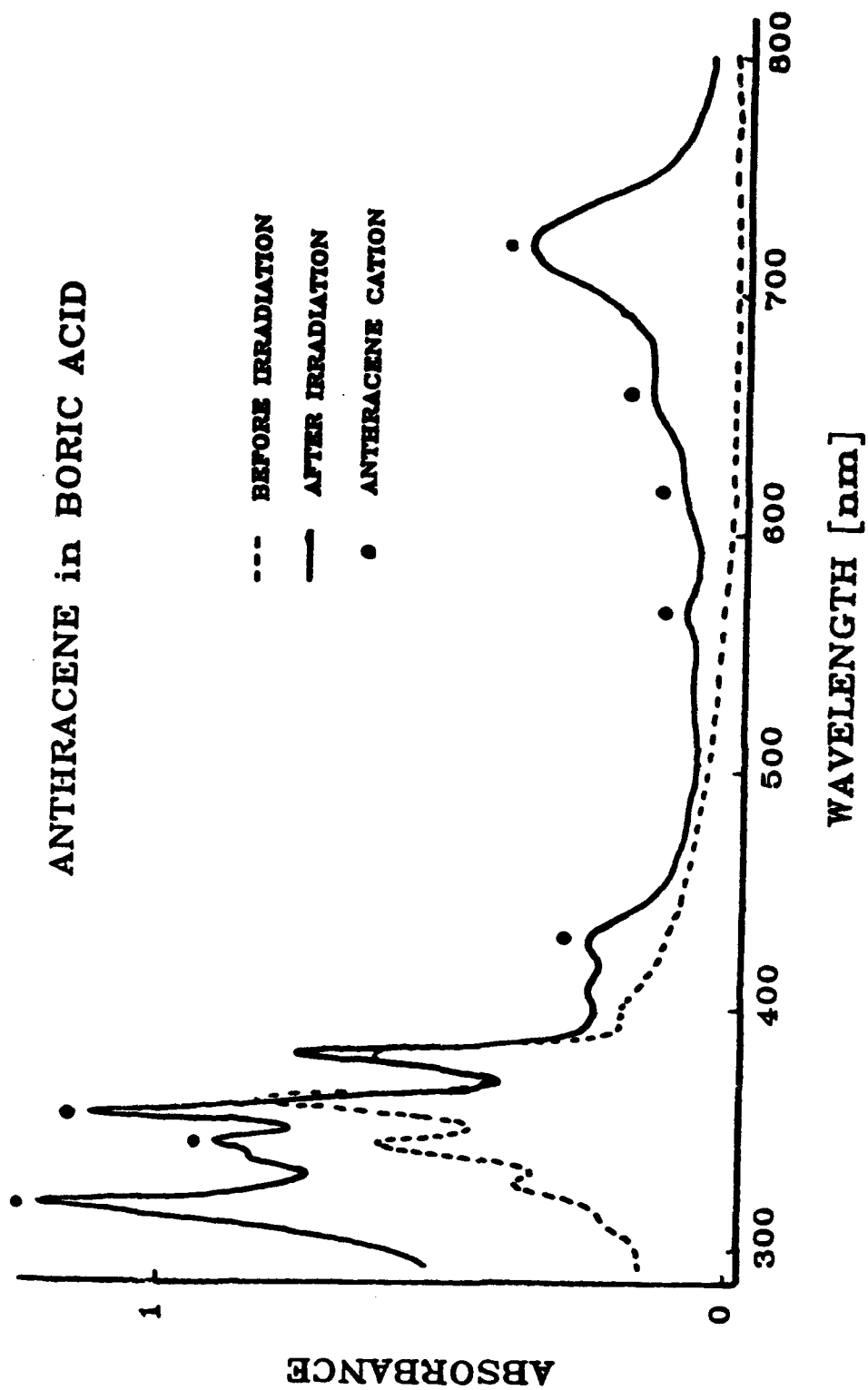


Figure 22. Visible-Ultraviolet Spectrum of Anthracene in Boric Acid Matrix at Room Temperature

kilovolts potential difference. The chamber was attached to the shroud of the closed cycle cryostat. Reasonably high pressures (several torr range) were necessary to sustain the discharge, but such high pressures, even when decreased by effusion through a small orifice, led to thick, optically opaque matrices. It became clear that it would be necessary to pulse the sample/rare gas mixture into the chamber, resulting in a short burst of moderate pressure gas which could sustain a short discharge yet form a matrix slowly and therefore clearly.

A pulsed valve (General Valve, Series 9, 2ms open time) was installed on the above apparatus and experiments on naphthalene tried. The backing pressure of the argon was approximately 400 torr. With no potentials on the rods, clear matrices displaying good ultraviolet spectra of neutral naphthalene in Ar were produced. However, in the experiments with the high potentials (several kilovolts) no clear evidence of ions was found. Not even for the neutral naphthalene was seen. Presumably the naphthalene was completely destroyed by the discharge. A gentler discharge technique was obviously called for.

In the next version of the discharge device the pointed rods were replaced by a glass cone with four pairs of parallel metal wire electrodes running down the interior of the cone. The apparatus is sketched in Figure 23. The base of the cone was glued to a brass block to which the pulsed valve was attached. A potential of 1-3 kV was applied between the electrodes. When a mixture of naphthalene and argon was pulsed through this device a bright bluish-purple discharge was observed. Readily discernible visible bands at 675nm, 652nm, 615nm and 598nm revealed that cations of naphthalene were indeed produced. To enhance the intensity of these bands,  $\text{CCl}_4$  was added to the argon stream to act as an electron trap in the matrix for those electrons produced in the discharge and isolated in the matrix. While this addition led to a markedly enhanced yield of naphthalene cations, the mechanism of this process turned out to be much more complex than the  $\text{CCl}_4$  merely acting as an

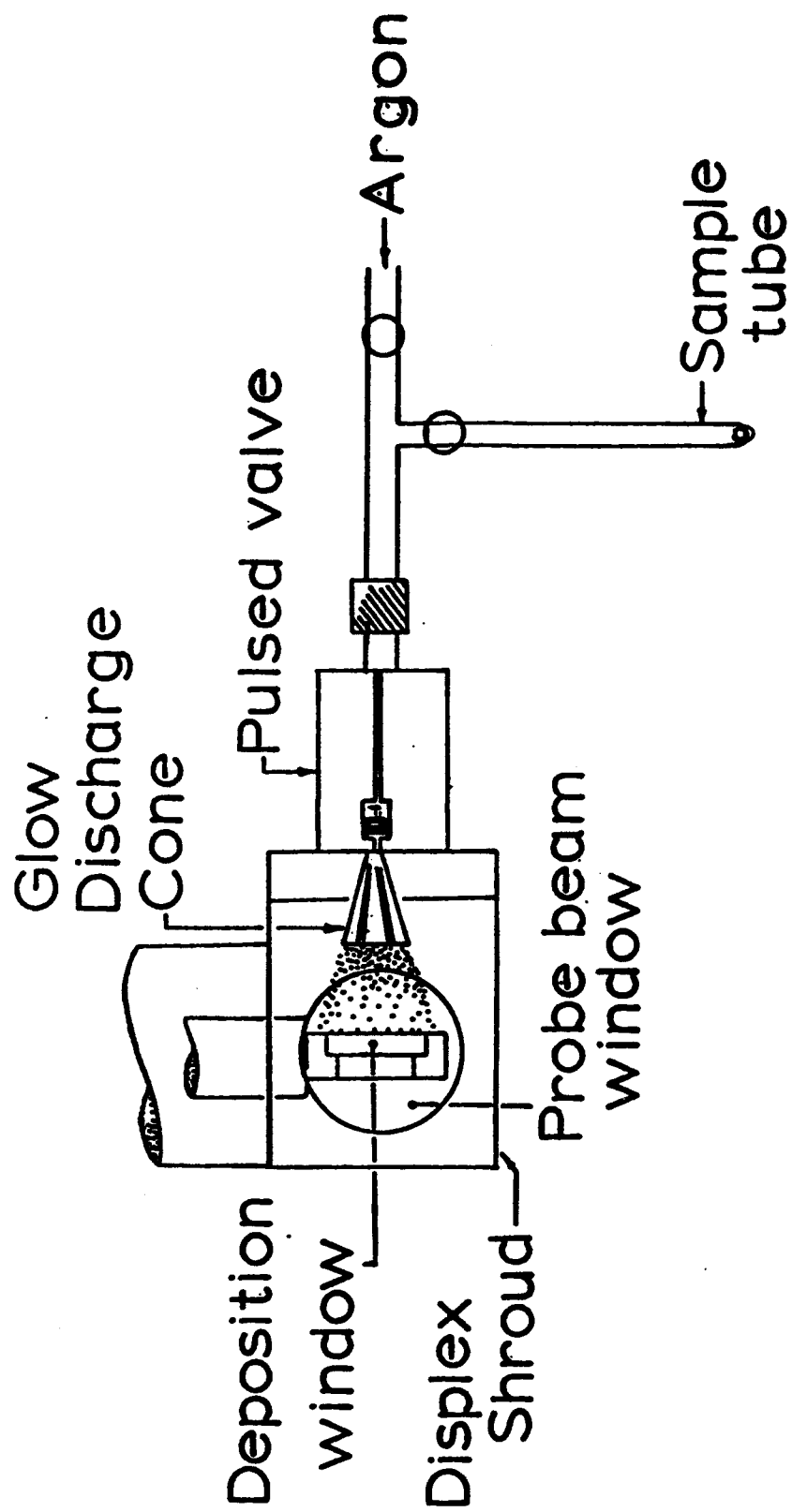


Figure 23. Conical Pulsed Glow Discharge Apparatus

electron trap (vide infra). This approach was dropped due to insufficient concentration of cations produced to observe the IR spectrum.

**c. Electron Bombardment**

It is well known that electron bombardment of a gaseous molecular beam results in the ionization of a fraction of the beam. To explore this approach and compare it to the pulsed glow discharge, the apparatus in Figure 24 was constructed. A tungsten filament (0.1mm diameter wire) was heated by 1.5 amperes current with resultant electron emission. The electron beam was accelerated by 100 volts on the anode. At a copper ring, situated immediately in front of the cold sample window, an electron current of 50 microamps was measured without any argon flowing. For the deposition the Ar was doped with a small amount of  $\text{CCl}_4$  and the naphthalene was sublimed from a side tube directly into the flowing Ar stream. It was intersected by the ionizing electron beam and deposited on the cold  $\text{BaF}_2$  sample window.

After only one hour of deposition, a strong spectrum (absorbance of 0.16 at 675 nm) of the naphthalene cation was measured. The infrared spectrum was then run on the same sample/matrix: new peaks, not due to neutral naphthalene, were noted. While it was tempting to conclude that these new peaks were due to the naphthalene cation, further tests were necessary before this could be done. Specifically, it was feared that the electron bombardment procedure also resulted in molecular fragmentation. This was tested and found not to be important. This method of ionization was used in the naphthalene results described in Sec. IIIA. Another ionization technique was tried also and is described next.

**d. Hemispherical Pulse Glow Discharge**

The major features of the hemispherical pulsed glow discharge device are shown in Figure 25. The precursor molecule is sublimed from a room temperature or slightly warmed side arm into a stream of argon gas. The argon

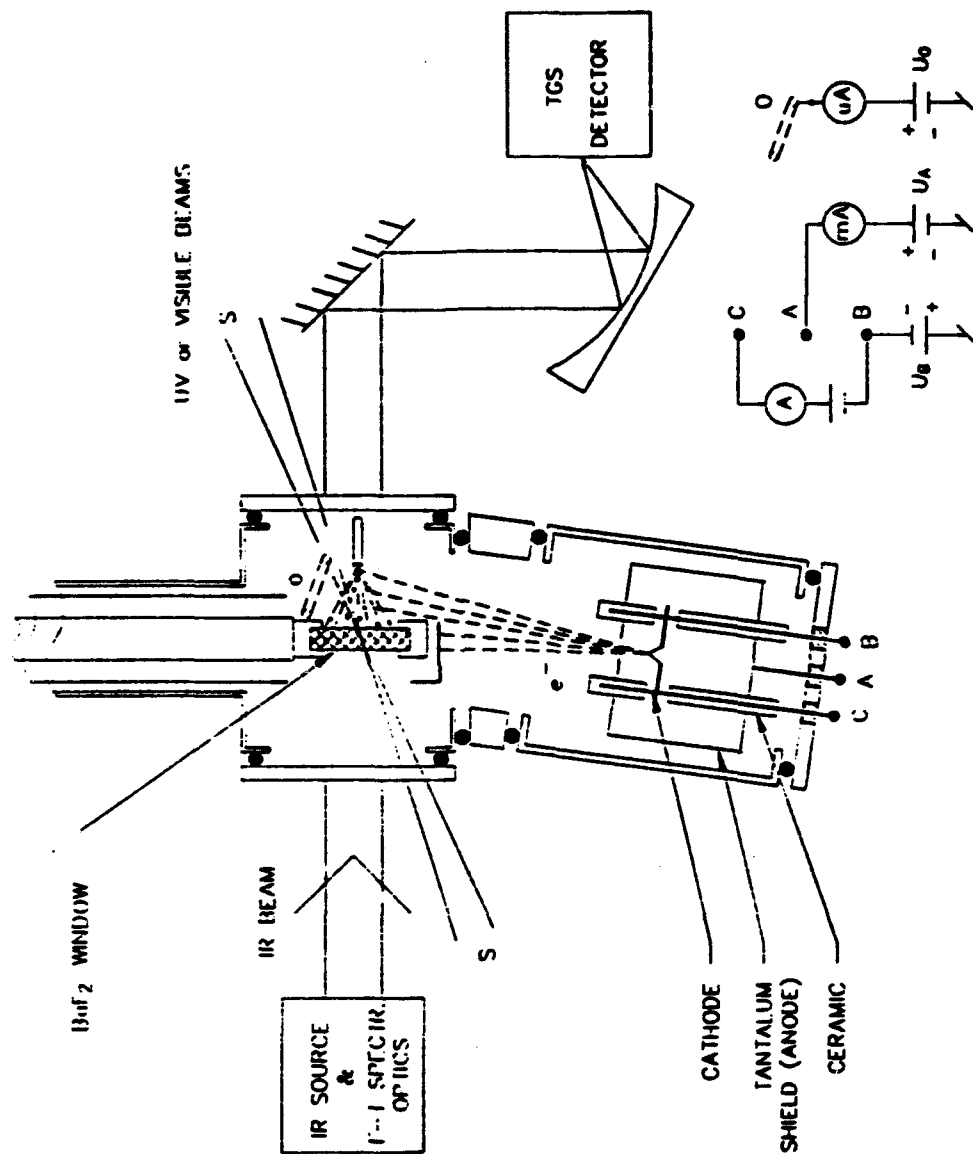


Figure 24. Electron Bombardment Source

serves as both the discharge gas and the matrix isolant gas. The sample/gas mixture is introduced via the pulsed valve with a backing pressure of approximately 100 torr. It enters the plasma generation region through a small (0.8mm ID) stainless steel tube insulated by a surrounding glass tube. The stainless tube is held at ground potential. A thin copper wire which is attached at one end to a hemispherical copper wire mesh grid held at +3 kilovolts is positioned approximately 2 mm from the tip of the SS inlet tube. The primary "cold" plasma is generated between the SS tube tip and the 3 kV wire and a secondary plasma is formed in the space between the grid and the cylindrical electrode held at +200 volts. The positive ions which are produced in the discharge sense the positive 3 kV potential and are repelled downstream toward the cold (12K) sample window. Argon ions and excited argon atoms are presumably formed in the plasma and probably result in charge transfer and Penning ionization processes which account for the enhanced yield of PAH cations. (An estimate of the actual number produced and trapped in the matrix is given later.) The plasma is confined in its flow toward the window by the +200 volt potential on the cylindrical lens between the grid and the cold window. As will be seen below good visible/ultraviolet and infrared spectra of the aromatic ions in argon matrices have been achieved with this apparatus.

#### **4. Mass Spectrometer**

##### **a. Interfacing**

To monitor the species produced in the various ionization sources and to determine their relative efficiencies, a quadrupole mass spectrometer (Finnigan 3500) was employed. Since its data collection system was obsolete, the apparatus was interfaced to a PC clone (286 AT) via an IBM Data Acquisition and Control Adapter (DACA) Card (cf. Figure 26). This interface board includes two analog output ports with 12 bit resolution, switch-selectable ranges of 0 to +10 volts,

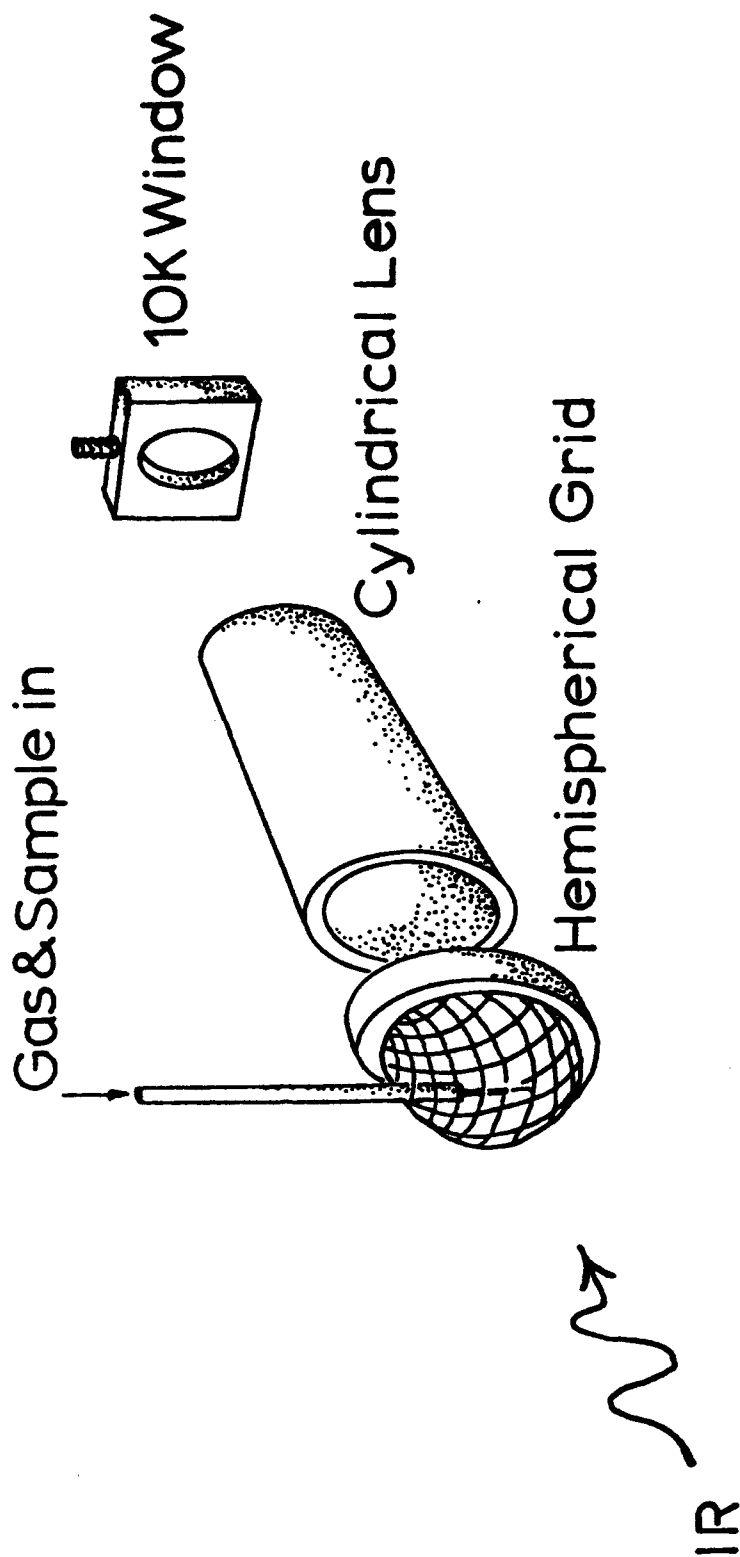


Figure 25. Hemispherical Pulsed Glow Discharge Source

-5 to +5 volts, and - 10 to +10 volts and can perform a minimum of 25,000 conversions per second with a settling time of 10 microseconds. Additionally, the board contains 4 differential, 12 bit input AD channels each with a conversion time of 35 microseconds. It also contains a 16 bit timer/counter device.

The quadrupole mass spectrometer can scan over the 1 to 800 amu range. External control of the mass range scanning was provided by supplying a 0-to 10-volt analog signal from the analog output port of the DACA board. Because the port is limited to 12 bits (4096 points), a full range scan restricts the resolution to 5 points/amu. Smaller range scans would, of course, enable higher resolution. It will be shown later that despite this low resolution reasonable mass spectra may be obtained. This low resolution has one distinct advantage for the present work: the size of the data files is limited thereby allowing very fast scans of the mass range. This is critical for use of the apparatus in the pulsed mode.

#### b. Programs

Interfacing the mass spectrometer to the computer required that new software be written. Initially the Microsoft C language was used but later the programs were transcribed into Turbo C because of its versatility, speed and ease of use. Three different programs were written. The first, entitled Massspec.C, is used to run the spectrometer in an ordinary manner, i.e., when the sample source is continuous. The second, called Mastrack.C, is employed when a pulsed sample source is attached and the third, Pulse.C, is a variation of the second which synchronizes a laser pulse or pulsed valve with the acquisition of data from the mass spectrometer. Each will be described briefly below. The program listings may be found in the Appendix.

##### (1) Masspec.C

With this program it is possible to scan any segment or the whole of the 1 to 800 amu range. It also provides for a scan accumulation

# Computer-controlled mass spectrometer

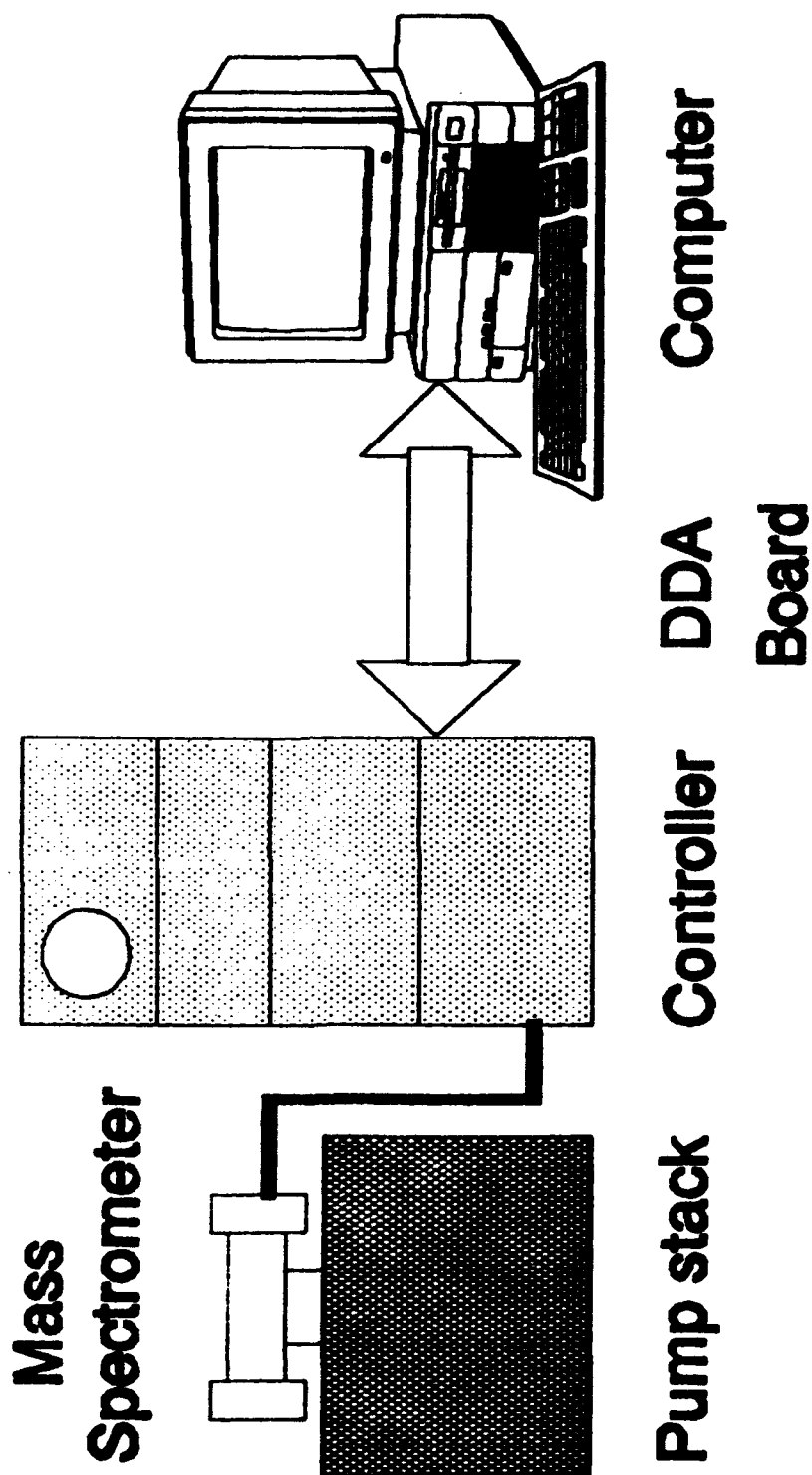


Figure 26. Schematic of Mass Spectrometer, Controller, Digital Data Acquisition (DDA) Board and Computer

routine in order to increase the signal-to-noise (S/N) ratio. A single scan provides an acceptable S/N ratio. To illustrate this, Figure 27 shows a background scan (presumably of pump oil, air, etc.) in the range 1 to 500 amu for only one scan. Figures 28 to 31 show the same spectrum for 10, 100, 1000 and 10,000 accumulated scans, respectively. It is readily apparent that the baseline noise decreases with 10 and 100 scans but interestingly no further improvement is discernable with the higher accumulations of 1000 and 10,000 scans.

It is still possible to obtain a mass spectrum under local (i.e., console) control without using the computer. Indeed the resolution obtainable under local control is superior to that obtainable with the computer for scans over the full 800 amu range. However, optimizing different parameters such as ionizing voltages or internal signal filters results in spectral resolution which is quite acceptable. Figure 32 illustrates the effect of varying the signal filters on scans over the 10-36 amu range. For a filter setting of 30 the peaks due to water (18 amu), nitrogen (28 amu) and oxygen (32 amu) are easily distinguishable.

## (2) Mastrack.C

In order to alter the mass spectrometer (MS) to run in the pulsed mode, it was necessary to determine the relative speeds of the mass spectrometer versus the analog-to-digital conversion and storage. By introducing various time delays in the program, it was found that the mass spectrometer response was faster than the A/D conversion. The duration of a scan could be measured by installing an oscilloscope in parallel with the MS controller. The scanning speeds are tabulated in Table 5.

An average of 0.29 ms/amu was found. Since the repetition rate of a typical pulsed source (ablation laser or pulsed valve) is 10 Hz, it is straightforward to calculate that 350 amu points may be scanned in each cycle as the sample source is pulsed on. It is not possible to scan the entire mass range using a 10 Hz sample

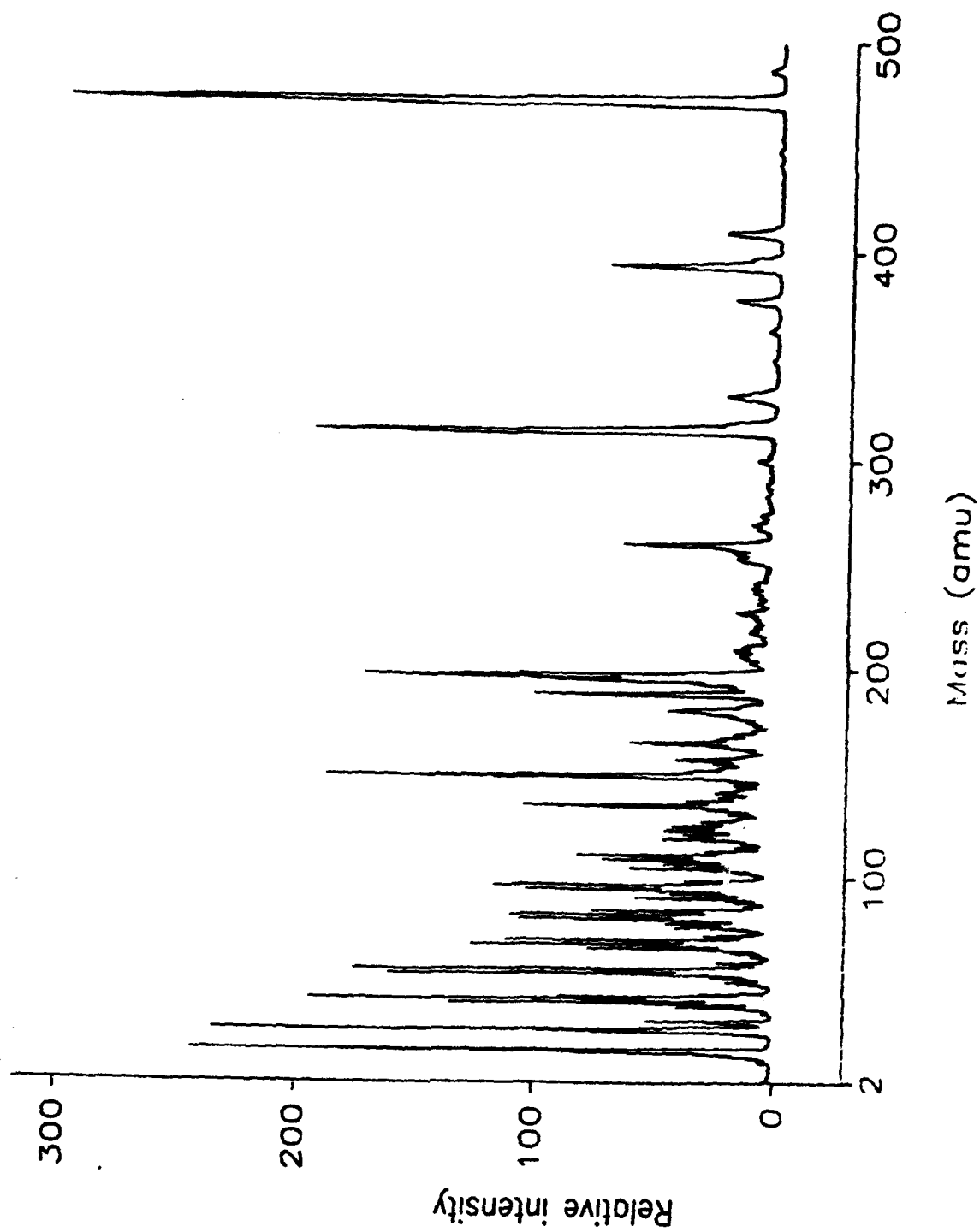
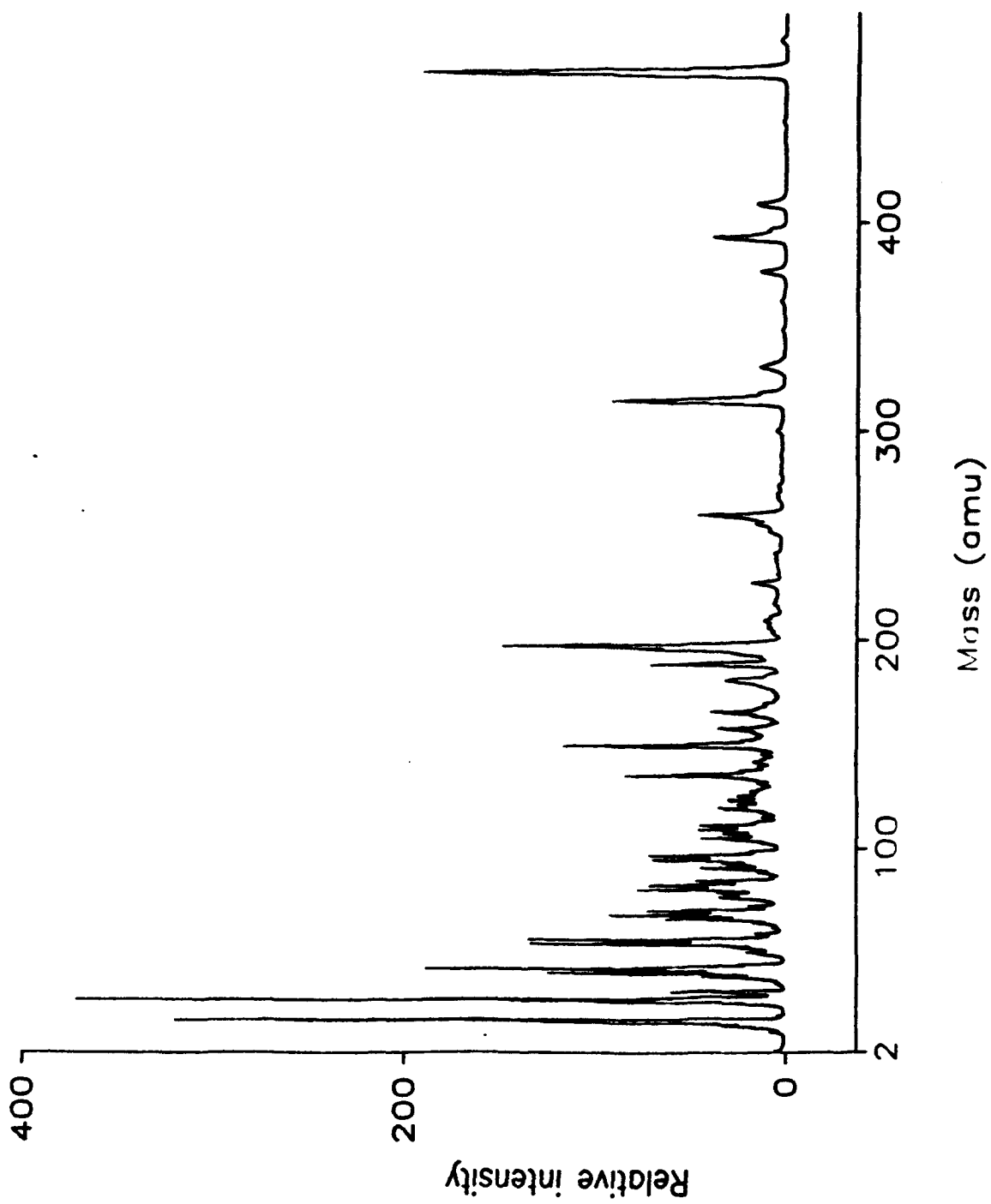


Figure 28. Ten Accumulated Mass Spectrometric Scans



**Figure 29. One Hundred Accumulated Mass Spectrometric Scans**



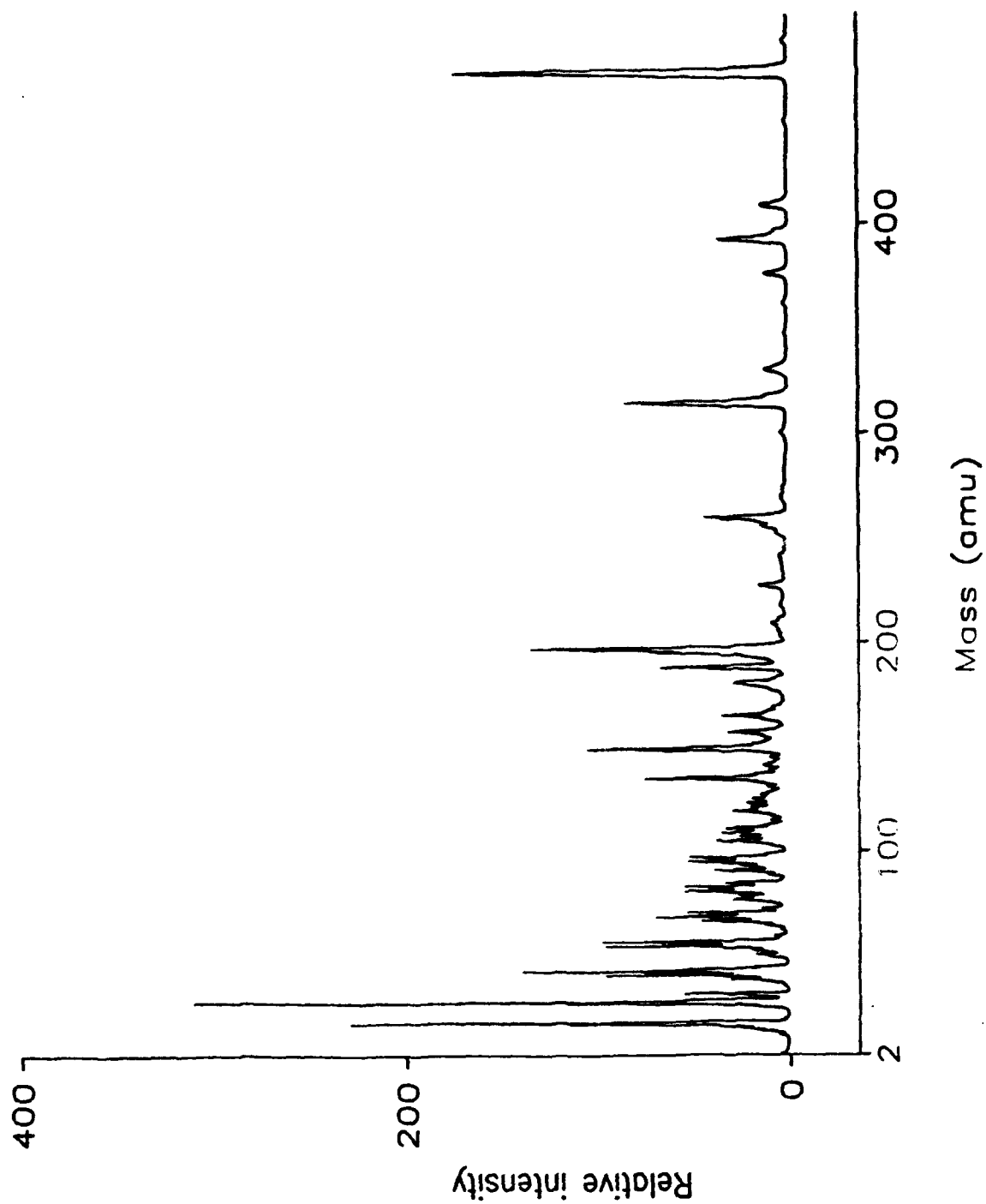


Figure 31. Ten Thousand Accumulated Mass Spectrometric Scans

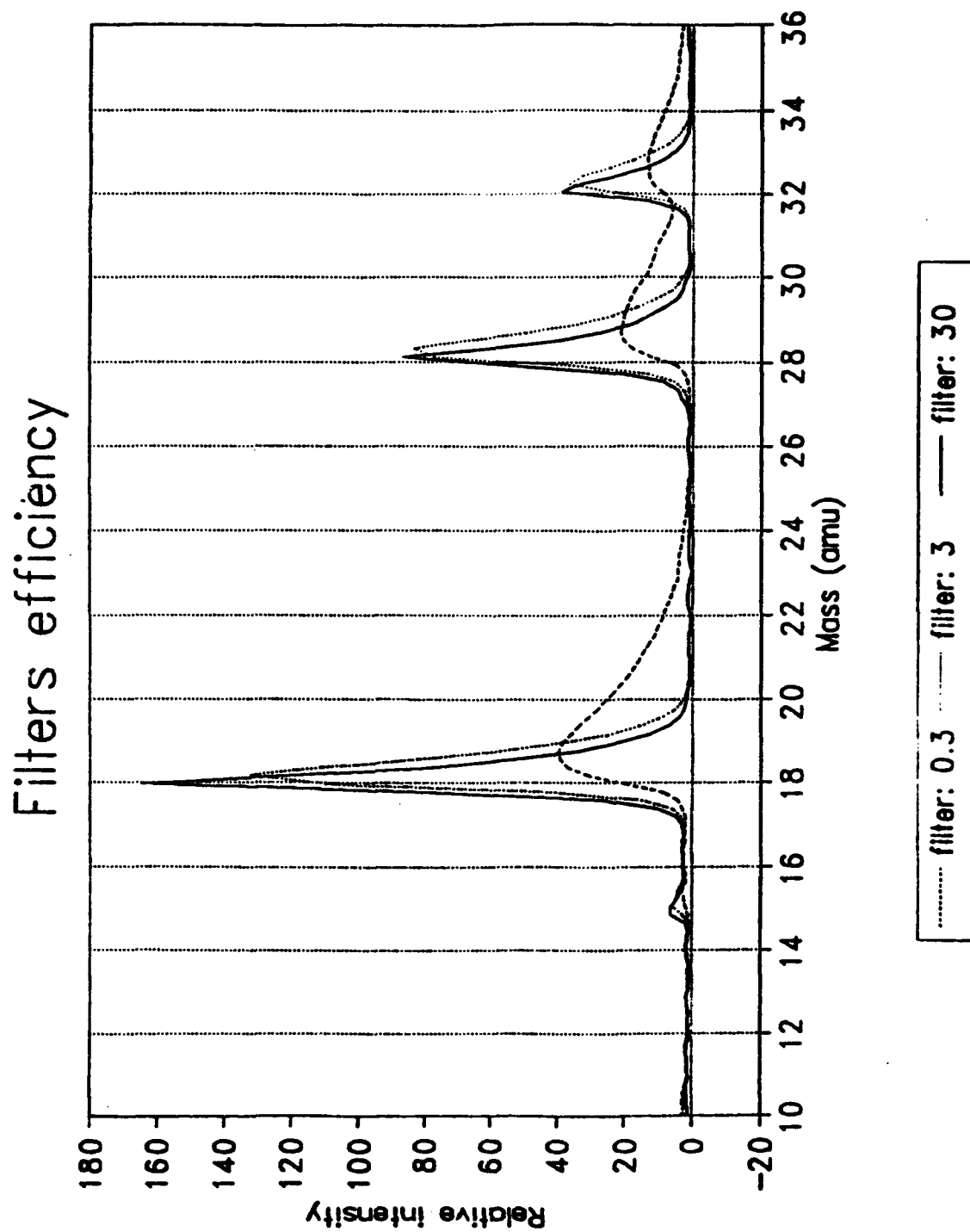


Figure 32. Effect on Mass Spectrum (10 - 36 amu range) of Varying Signal Filters

**TABLE 5 MASS SPECTROMETRIC SCANNING SPEEDS**

Mass Range (amu)	Voltage Range (volts)	Time of Scan (ms)	Time per amu ms/amu
1-800	0-10	230	0.287
1-400	0-5	116	0.290
400-800	5-10	116	0.290
300-350	---	14.8	0.296

source. In this program one mass is monitored as a function of time. (It will be easy in the future to scan and accumulate over a small mass range if desired.) A point is recorded every 5.6 ms and a variable number of accumulations is taken. To test the software a pulsed valve (General Valve, Series 9, 2 ms open time) was installed on the mass spectrometer. A needle valve between the pulsed valve and the mass spectrometer was used to ensure that the pressure in the mass spectrometer did not exceed  $10^{-5}$  torr. The gas was a mixture of nitrogen and argon; the evolution of the Ar peak was followed. Figure 33 shows the response of the system with the needle valve closed and the pulsed valve operational. The pulsed valve was found to leak slightly when closed which accounts for the nonzero "baseline" value. In this figure 5000 successive data points per pulsed valve period were recorded with a total of 10 accumulations. In Figures 34 and 35, a similar experiment was performed but with 500 and 50 successive data points and 100 and 1000 accumulations, respectively. The noise is substantial in the 5000/10 experiment as expected (but the mass spectrometer sensitivity is also high here,  $10^{-7}$  scale). The noise decreases as the number of accumulations increases. In Figures 36 to 38, similar sets of data points and number of accumulations are shown but with the needle valve open. Note the difference in scale on the y axis. For each the total time of the scan is about 6 seconds; the pulsed valve repetition rate was set to 1 Hz. Each pulse is about 300ms in width which far exceeds the pulsed valve open time of 2ms. Presumably this width depends on the ability of the diffusion pump to keep pace with the sudden increase in pressure and the distance between the valve and the ionization chamber in front of the quadrupole rods. The noise that is evident in Figure 33 has been suppressed in Figure 36 because of the less sensitive scale used.

### (3) Pulse.C

This program is designed to synchronize the acquisition of temporal data on one mass peak with the firing of a laser pulse or pulsed valve.

Mass tracking : ARGON  
needle valve closed / 5000 \* 10 acc

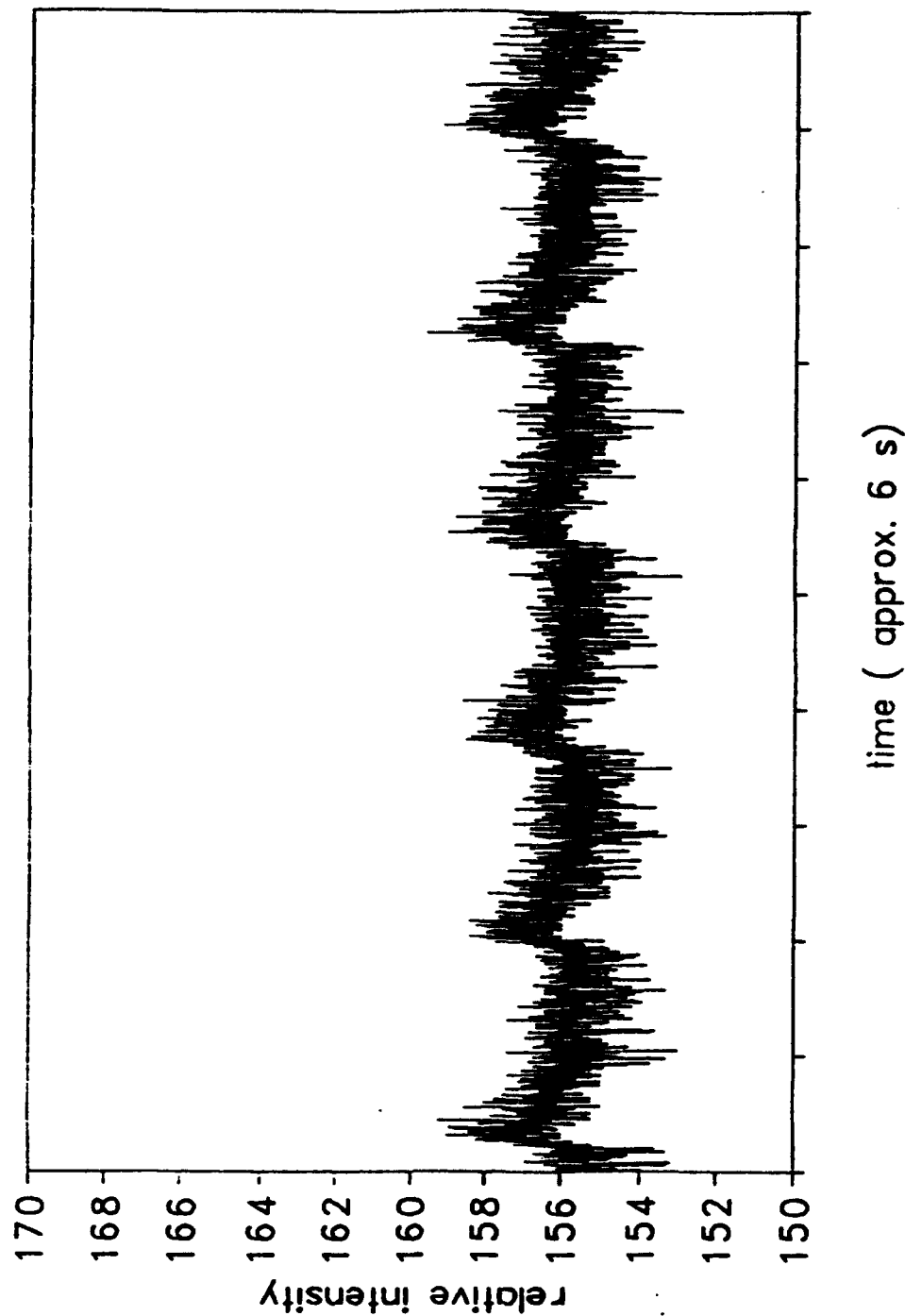


Figure 33. Time Response of Mass Spectrometer Set on 40 amu (for Argon) with Needle Valve Closed and Pulsed Valve Operational. 5000 Data Points Per Accumulation; 10 Accumulations

Mass tracking : ARGON  
needle valve closed / 500 \* 100 acc

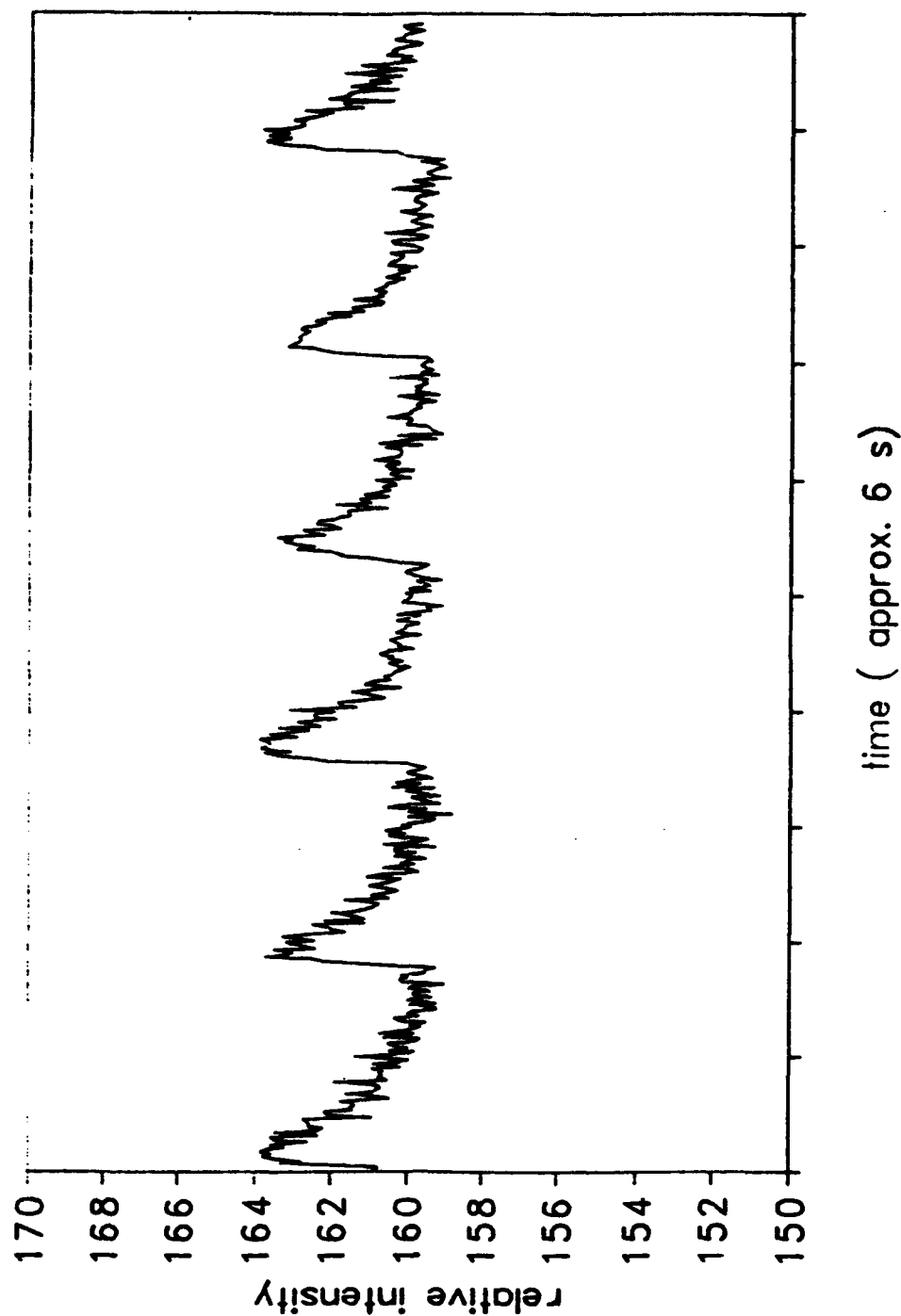


Figure 34. Time Response of Mass Spectrometer Set on 40 amu (for Argon) with Needle Valve Closed and Pulsed Valve Operational. 500 Data Points Per Accumulation; 100 Accumulations

Mass tracking : ARGON  
needle valve closed / 50 \* 1000 acc

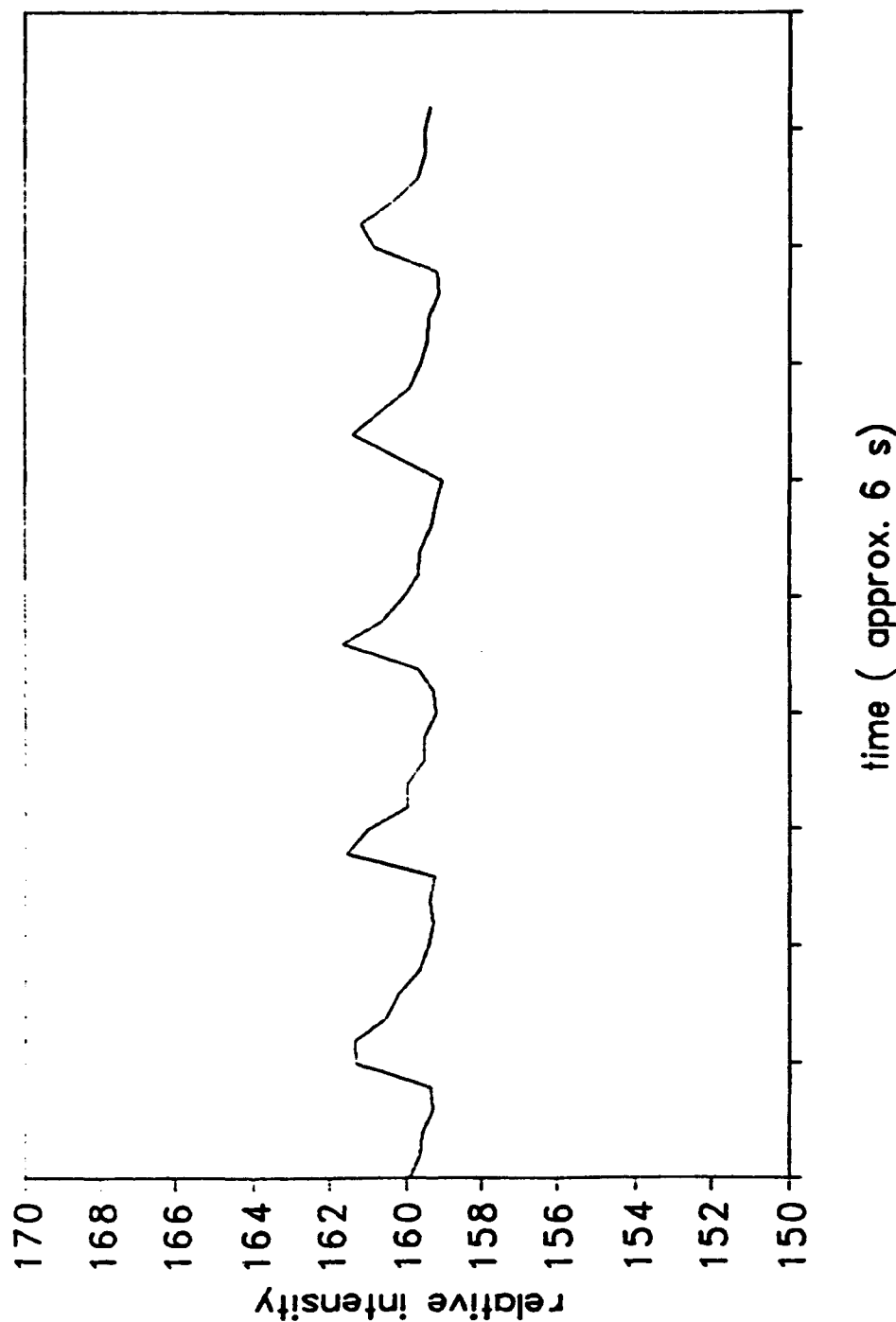


Figure 35. Time Response of Mass Spectrometer Set on 40 amu (for Argon) with Needle Valve Closed and Pulsed Valve Operational. 50 Data Points Per Accumulation; 1000 Accumulations

Mass tracking : ARGON  
Mean pres. 2 10-5 Torr / 5000 \* 10 acc.

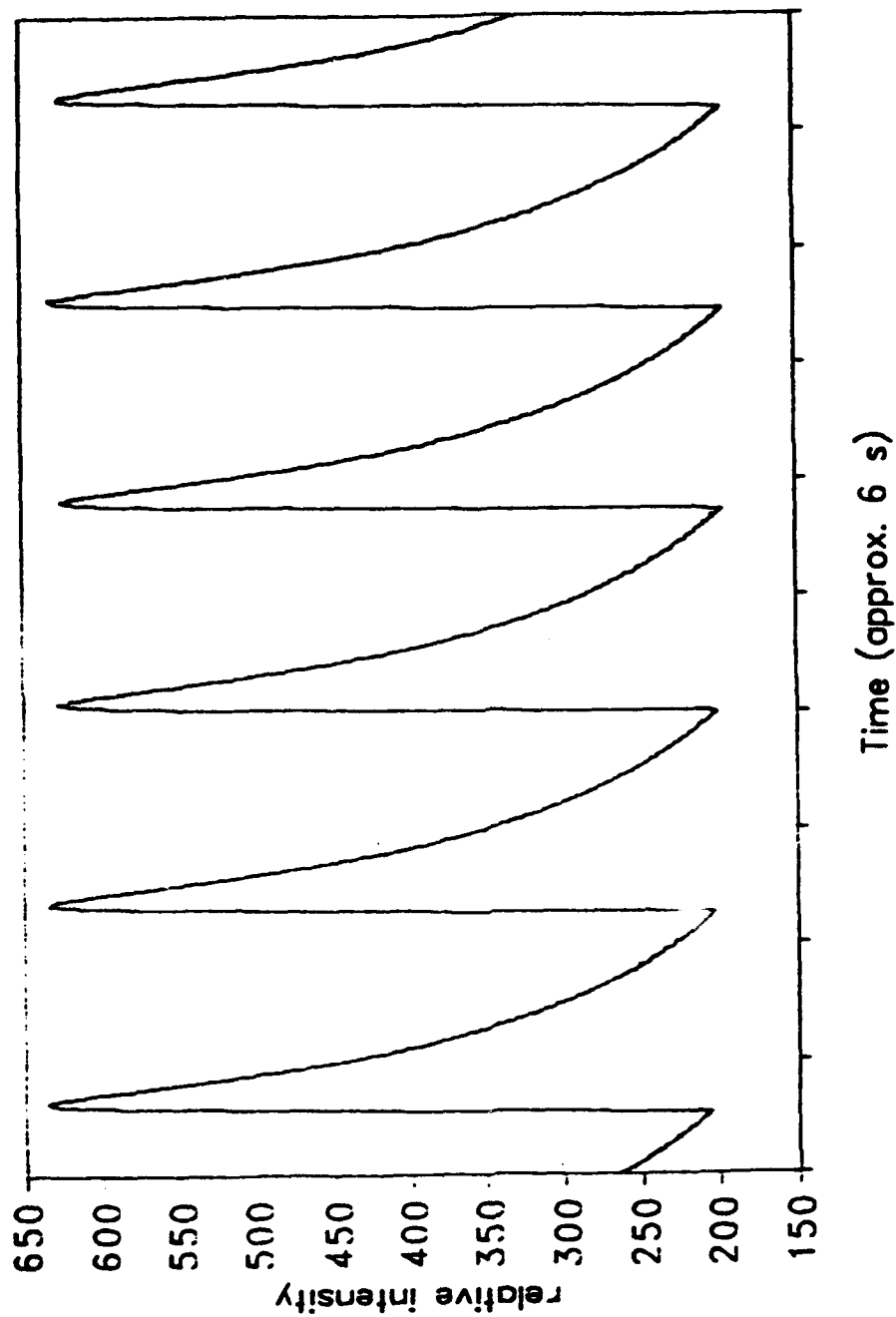


Figure 36. Time Response of Mass Spectrometer Set on 40 amu (for Argon) with Needle Valve Open and Pulsed Valve Operational. 5000 Data Points Per accumulation; 10 Accumulations

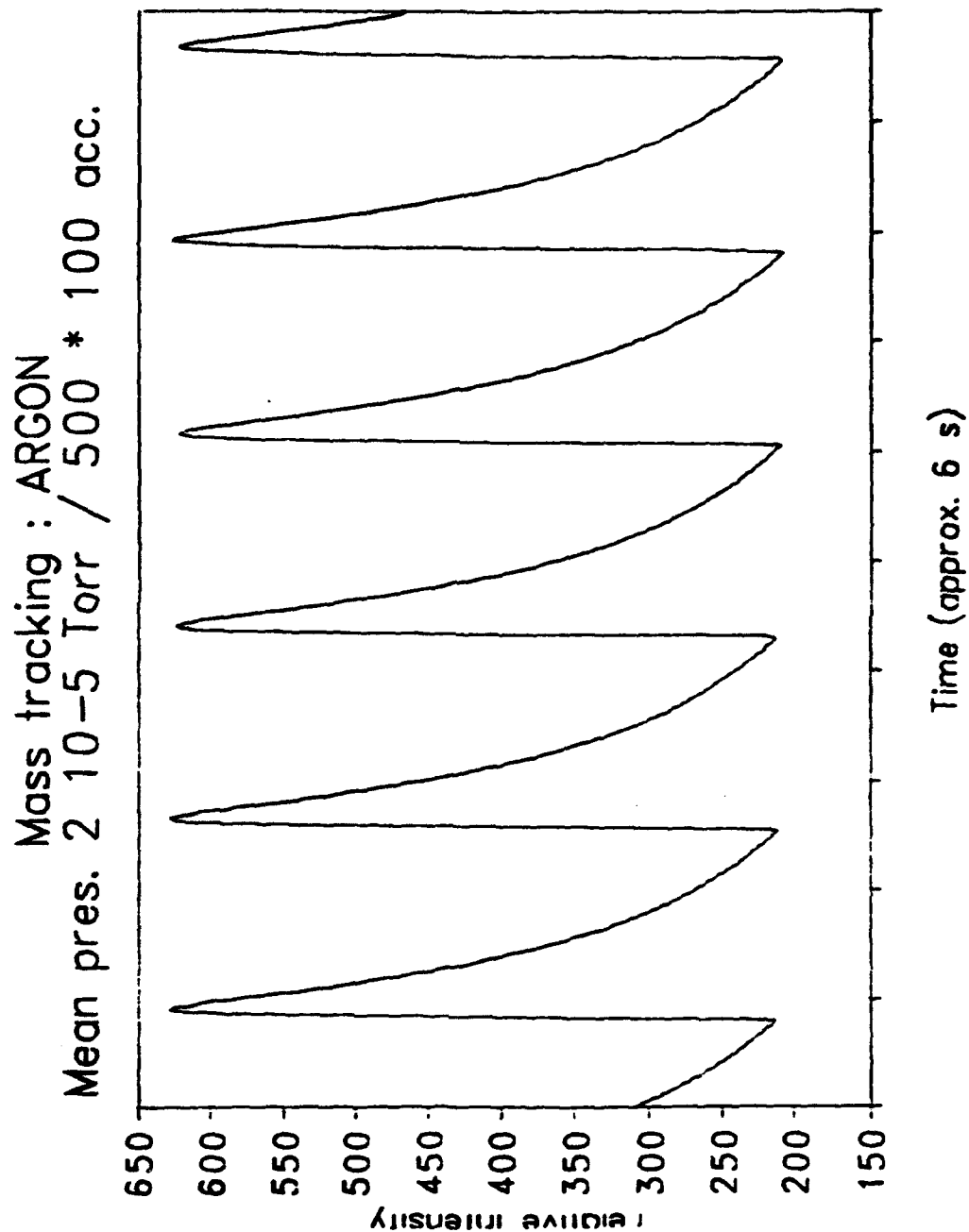


Figure 37. Time Response of Mass Spectrometer Set on 40 amu (for Argon) with Needle Valve Open and Pulsed Valve Operational

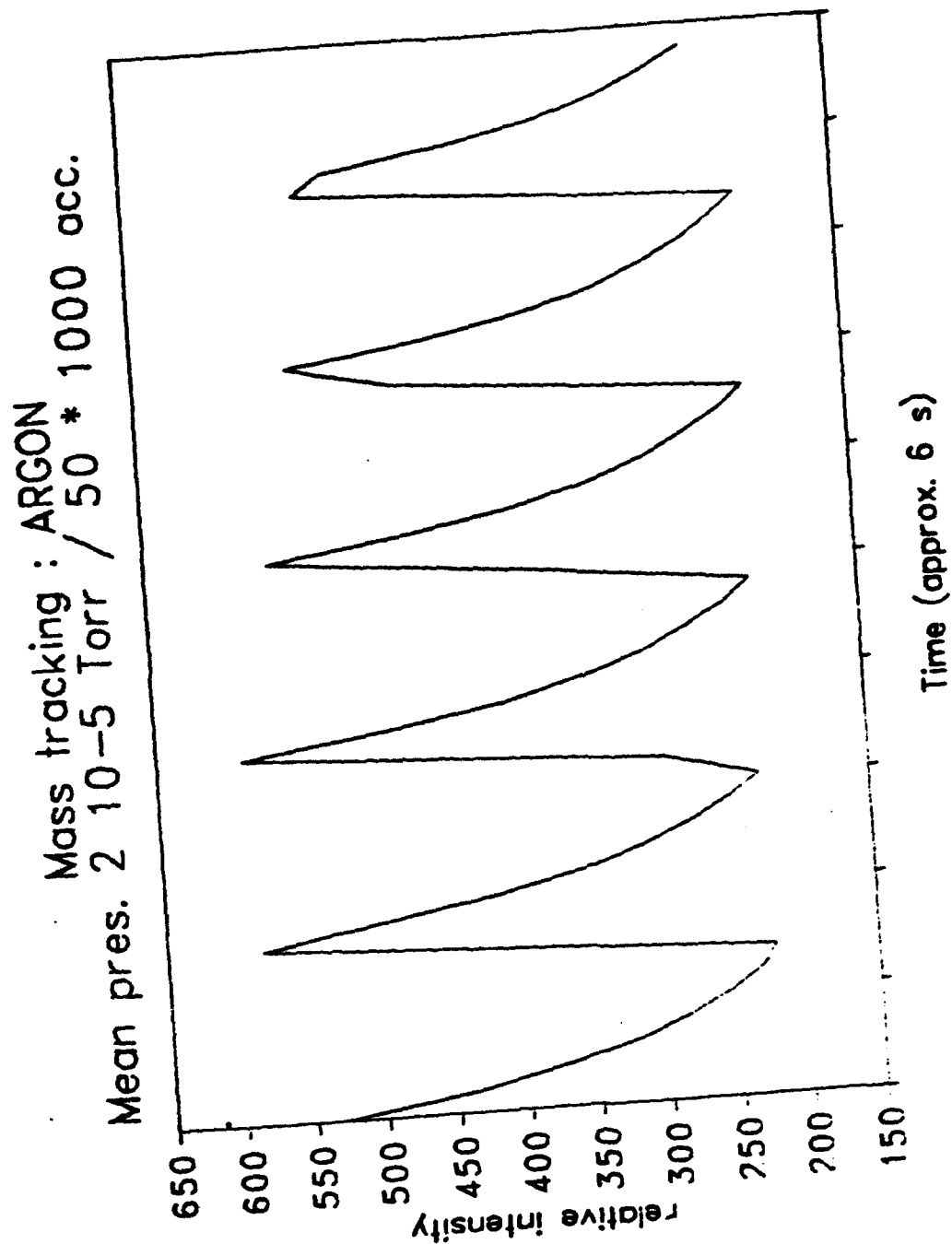


Figure 38. Time Response of Mass Spectrometer Set on 40 amu (for Argon) with Needle Valve Open and Pulsed Valve Operational

The sequence of commands is: set the mass spectrometer voltage for one particular mass, initialize the counter/timer of the DACA board, initialize the analog input of the board, start the countdown of the clock, start the acquisition loop as the countdown finishes and, finally, trigger the laser or pulsed valve. The number of points and accumulations is specified by the operator along with the delay time before event triggering.

## 5. Ion Quadrupole Deflector

A Quadrupole Ion Deflector has been constructed in our laboratory for use with the Finnigan 3500 Mass Spectrometer. A quadrupole deflector was first described by Zeeman (Reference 130); our device was adapted from a design developed by Yost and Pedder (Reference 131) working with Finnigan Instruments. The design is shown in Figure 39. It is basically a quadrupole mass spectrometer rotated on end with a series of focusing electrical lenses. In our application the device will be used first to monitor and optimize the ions formed in the source region by deflecting them 90 degrees into the quadrupole mass spectrometer and then, by deflecting them -90 degrees, to isolate them in a cryogenic matrix for interrogation via various spectroscopic measurements (infrared, visible/UV, etc.)

Ions generated by electron bombardment from an electron gun at right angles to the inlet flow of the atomic/molecular species of interest are accelerated into the Ion Deflector, where the potential field generated by differential DC voltages on the two pairs of quadrupoles deflects the ionic species away from the noncharged neutral atoms/molecules. Proper adjustment of the voltages on the quadrupoles, the inlet accelerating plates, and the outlet focusing lens is critical to acquiring effective separation of the ionic species, and maximization of the output ionic beam. Production of ionized species and the extent of fragmentation by the electron beam are a function of the ion gun filament current and anode potential, i.e., the kinetic

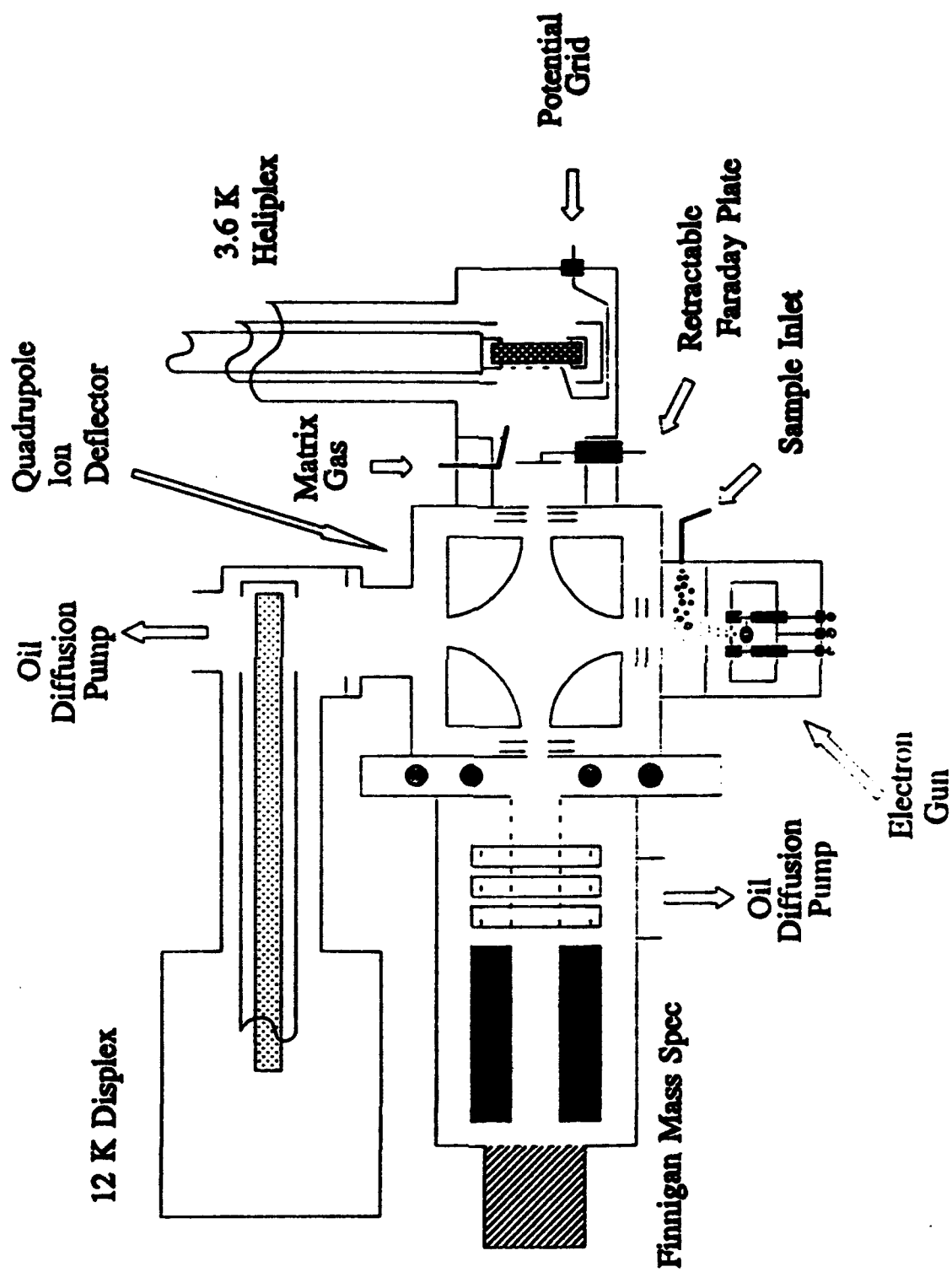


Figure 39. Quadrupole Ion Deflector

energy of the ionizing electrons. The anode of the electron gun also repels the positive ions formed and increases the amount of kinetic energy they have when entering the Ion Deflector. Proper control of these parameters is essential to obtaining the ideal yields of output ionic species.

An effective means of monitoring the output and effectiveness of the Ion Deflector is to couple the output beam from the deflector to the mass spectrometer. The Ion Deflector has a mirror plane of symmetry along its inlet path so that ions can be deflected out of either of two identical exit paths, both perpendicular to the inlet path. Simply reversing the DC potential voltages on the quadrupole rods of the deflector then permits us to choose the exit path of the deflector. Utilizing this option, it is possible to direct the generated ion beam into the mass spectrometer for analysis of the beam contents, then output through the other port for experimental use, i.e., deposition in a matrix. The ionization assembly of the mass spectrometer has been removed, so that any species being detected would have to be generated by the electron gun assembly at the Ion Deflector inlet port. A series of electrostatic lenses has been installed in this region to focus the ion beam toward the mass spectrometer quadrupoles.

The Ion Deflector is connected to an oil diffusion pump on the opposite side of the inlet port. Inserted just in front of the diffusion pump outlet is the cold finger of a closed cycle helium cryostat (APD products) which is maintained at approximately 12 K as a cryopump. The cryopump/diffusion pump combination should effectively remove substantial residual and neutral species not deflected. The mass spectrometer itself is pumped directly by a separate oil diffusion pump.

Initial quadrupole and plate voltages for the Ion Deflector and focusing lenses were determined from simulations of the ion trajectories utilizing program SIMION PC/PS, an electrostatic lens analysis and design program originally developed by D.C. McGilvery and extensively revised for use on PC and PS2

computers by D.A. Dahl and J.E. Delmore (Reference 132). The design of our Quadrupole Ion Deflector had its origin in simulations utilizing SIMION. These simulations proved fairly accurate, as on initial startup of the Ion Deflector, ion peaks of air contaminant were observed immediately in spite of the fact that the quadrupole voltage range over which peaks could be detected was not large (i.e., SIMION simulated voltages were within that narrow range).

The Finnigan mass spectrometer has been used to maximize the parameters for the Ion Deflector (i.e., quadrupole potentials, inlet/outlet focusing lens potentials) as well as the electron beam kinetic energy coming from the ionizing electron gun. The initial experiment was conducted with argon gas. The generated ion beam was deflected into the mass spectrometer utilizing the Ion Deflector. An excellent Ar peak was easily obtainable and quickly maximized. The next experiment was run with p-dimethoxybenzene inlet as a vapor sublimed from the solid at room temperature. A parent ion peak at 138 amu was readily apparent, along with a fragmentation pattern expected for this compound. The intensity of this peak was then maximized utilizing the ion deflector voltages. Next, the intensity of the fragments was then manipulated by varying the electron gun filament voltage and the anode potential (i.e., varying the ionizing electron beam kinetic energy). The ratios of fragments to parent ion could be varied quite dramatically. The present intent for use of the Ion Deflector is to maximize the parent ion concentration, minimizing fragment formation. Similar results were obtained with naphthalene as the inlet species.

The scope of experimental interest in this lab is to now focus these generated ion beams which are essentially free of neutral molecular species on a surface for deposition so that the ionic species can be studied spectroscopically without interference from the neutral species. Once the parameters for parent ion generation have been maximized utilizing the mass spectrometer, the deflection of

the ion beam is altered 180 degrees by reversing the potentials on the Ion Deflector quadrupoles. Thus the ion beam is deflected out the exit port opposite the Finnigan. To this port is coupled a small block containing a removable Faraday plate for detecting the level of ion current and a gas inlet port for allowing the input of other species, in this case the nonreactive noble gases xenon, krypton, argon, and neon for co-deposition. Beyond this block is another dispex coldfinger containing a  $\text{CaF}_2$  window to permit collection of the ionic species co-condensed in dilute solution in the rare gas matrix. In the present apparatus, a closed-cycle helium cryostat is being utilized, permitting attainment of temperatures as low as 3.6 K ideally. The actual window temperature is approximately 1.5 K warmer (about 5 K). This permits condensation of neon.

The present experiments are attempting to isolate naphthalene cation in rare gas matrix free of molecular naphthalene. Naphthalene cation has been isolated in argon previously in this laboratory utilizing pulse discharge methods. The cation species is of course present simultaneously with molecular naphthalene. Isolation of naphthalene ion in argon matrix utilizing the Ion Deflector has not yet been successful, although intuitively it should be achievable since it has been accomplished via pulse discharge. Several other parameters have been introduced utilizing the ion deflector, a significant one which seems to be the kinetic energy of the ion leaving the deflector. Ions of too high kinetic energy would most likely abstract an electron from Argon on condensation on the  $\text{CaF}_2$  window and neutralize themselves. Argon has a reasonably low ionization potential, thus the ion energies may be very critical. Experiments with neon have just now been initiated, since the higher ionization potential of neon should reduce this problem. However, the ion kinetic energies still need to be reasonably reduced prior to collision with the matrix, and control of the exiting plate potentials, distance of

travel to the matrix window, pressure of the matrix gas at the window surface, and electrostatic potential at the window surface are now being examined closely. The buildup of positive charge in a matrix of course would eventually result in a repulsive force impeding positive ions from approaching the window. To compensate this, an electrical grid has been installed just above the  $\text{CaF}_2$  window surface to maintain an opposing negative voltage in the matrix region. The grid had been utilized on the window surface in recent experiments with resultant periodic (circa 20-30 secs) blue electrical discharges occurring between the grid and the window surface at potentials around -125 V DC and greater (more negative). Fine tuning the potential field in this region to control the incoming ion kinetic energy while balancing the charge buildup seems to be the chief factor in obtaining matrix isolated ions at present. Excellent ion currents are measured utilizing the insertable Faraday plate just prior to the window -- 10 nA to 50 nA.

## C. RESULTS AND DISCUSSION

### 1. Naphthalene

#### a. Experimental Results

The use of the crossed IR/UV-visible beam apparatus is a powerful method for the determination of which new IR bands are due to the parent naphthalene radical cation. This approach has been used previously for the investigation of the IR spectra of para-dichlorobenzene (Reference 133) and para-dimethoxybenzene (Reference 134) radical cations, and in the study of the visible/UV spectra of certain carbon clusters (References 135,136). The method depends on a priori knowledge of either the visible/UV spectrum or IR spectrum of the sought-after species. By varying the conditions under which the species is produced, a variety of concentrations of this species is obtained. The IR and UV/visible spectra are then run on the same matrix and a correlation between the

band intensities in the IR and UV/visible is sought. If a good correlation is found, it is strong evidence that the species giving rise to the one spectrum is also responsible for the other.

In the present case, the visible spectrum of the naphthalene cation is well-known, having been studied by Andrews and co-workers in Ar matrices (References 119,120,137), Shida and co-workers in sec-butylchloride and freon matrices (References 116,117,138), and very recently by Salama and Allamandola in argon and neon matrices (Reference 139). It is characterized by a well-developed series of vibronic bands commencing at 675nm (in Ar). The visible spectrum obtained in the present work, shown in Figure 40, matches closely that obtained by the above authors. We have found that the addition of  $\text{CCl}_4$  to the Ar isolant gas greatly enhances (by a factor of 5 to 8) the intensity of the visible bands due to the naphthalene cation. A maximum absorbance of 1.4 was obtained for the 675nm band after 6 hours deposition. The possible reasons for this enhancement are discussed later. (Remember that the ionization process (via electron bombardment) occurs in the vapor phase prior to deposition and is not a solid state irradiation as in the previous studies).

The IR spectrum of the same sample which gave rise to the 675nm visible band system is shown in Figure 41, together with a spectrum obtained when the intensity of the 675nm system was absent. The latter is obviously due to neutral naphthalene. In the former spectrum a number of new bands are observed: at 1537, 1525, and 1519, 1401, 1218, 1215, 1037, 1023, 927, and 898  $\text{cm}^{-1}$ . Previous studies have identified the band at 898  $\text{cm}^{-1}$  as due (Reference 140) to  $\text{CCl}_3$ , the one at 927  $\text{cm}^{-1}$  as due (Reference 141) to  $\text{CCl}_4^+$  and the one (Reference 141) at 1037  $\text{cm}^{-1}$  belonging to  $\text{CCl}_3^+$ . A recent study (References 142,143) ascribes a band at 929  $\text{cm}^{-1}$  to the unusual species  $\text{CCl}_3 \cdot \text{Cl}$ . Although these authors believe previous assignments of the 927  $\text{cm}^{-1}$  band to  $\text{CCl}_4^+$  should now be ascribed to  $\text{CCl}_3 \cdot \text{Cl}$ , a 2  $\text{cm}^{-1}$  shift is easily

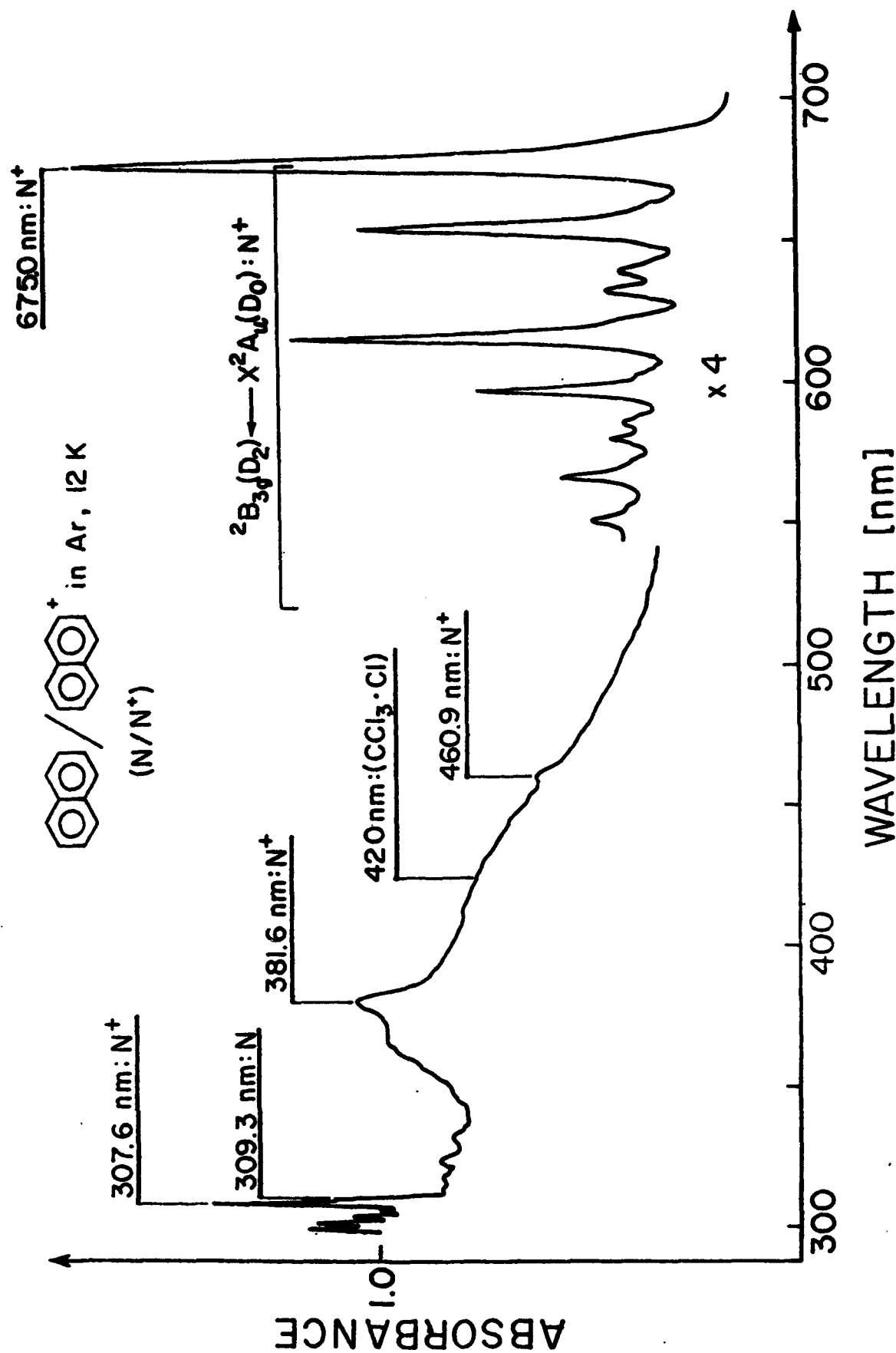


Figure 40. Visible-Ultraviolet Spectra of Neutral and Cationic Naphthalene in Ar at 12 K Between 290 and 700 nm

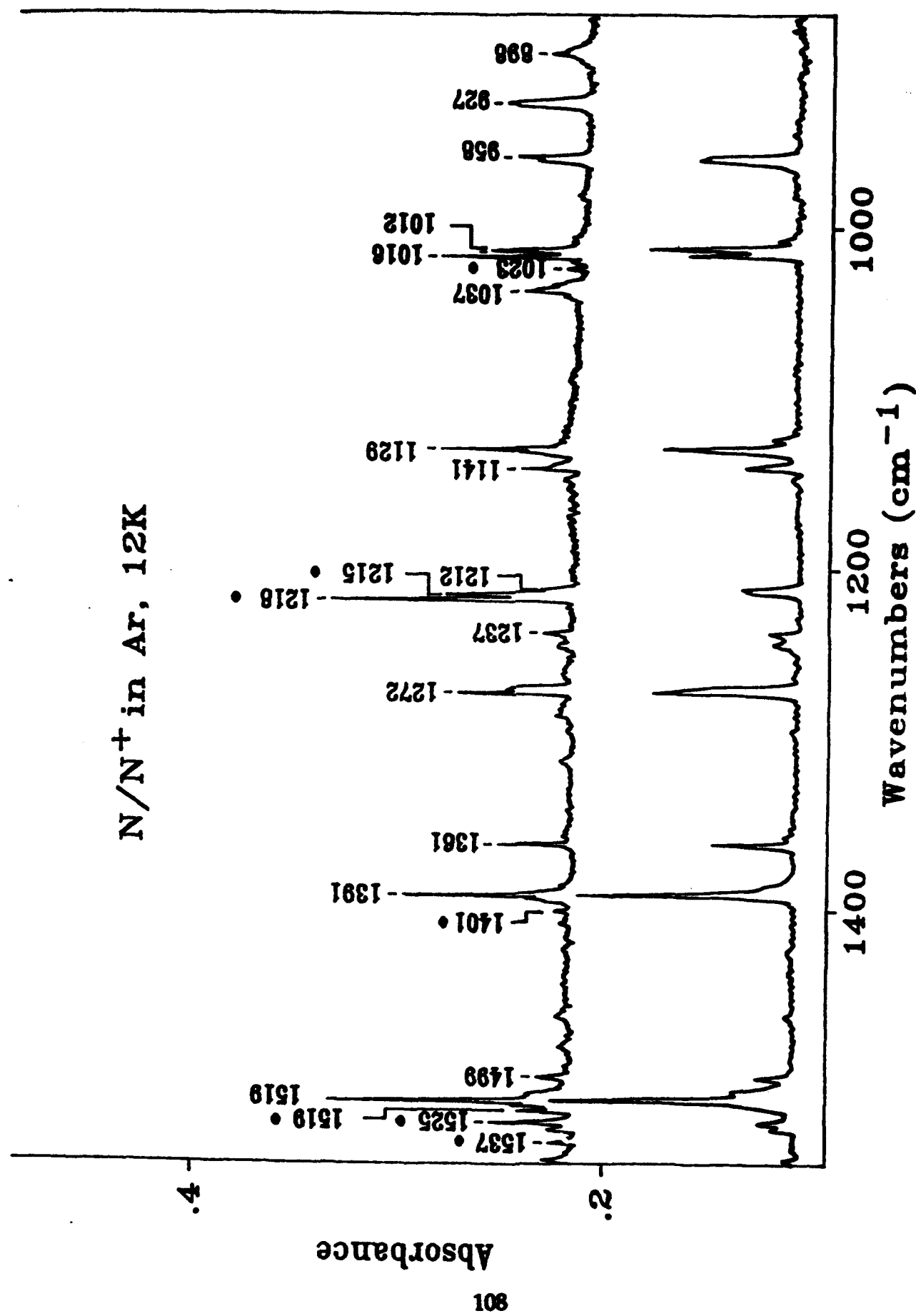


Figure 41. Infrared Spectra of Neutral (bottom) and Neutral and Cationic (top) Naphthalene in Ar at 12 K. New Peaks Due to the Cation are Marked with Solid Circles

discernible and, given the asymmetry of the band observed in this region in our spectrum, it is possible that both species are present in our matrix.

Of the remaining bands the most intense band at  $1218\text{ cm}^{-1}$  was subjected to a correlation analysis. The results are sketched in Figure 42. The experimental points represent ten different experiments in which the absorbance of the visible (675 nm) band varied (via length of deposit, intensity of ionizing electron beam, and concentration of  $\text{CCl}_4$  and naphthalene) from a low of 0.16 to a high of 1.4. It can be seen that the correlation between the visible band and the  $1218\text{ cm}^{-1}$  IR band is excellent (slope is 8). This provides strong evidence that the  $1218\text{ cm}^{-1}$  band is caused by to a vibration of the naphthalene radical cation. It was not possible to perform such an analysis on the remaining bands because of their weakness; however, it was apparent that these bands tracked the intensity of the  $1218\text{ cm}^{-1}$  band. Thus, we believe that these bands also arise from the naphthalene radical cation.

#### b. Discussion

##### (1) Are the new bands due to naphthalene radical cation?

The strongest piece of evidence identifying the new bands with the naphthalene cation is their intensity correlation with the 675 nm visible peak, previously ascribed (References 116,117,119,120,137-139) to this species. Other pieces of evidence were obtained also. First, because electron impact ionization was used here it is possible that the new peaks result from naphthalene fragments. Using the same electron bombardment source under the same conditions as used in these experiments, mass spectra were run on a modified quadrupole mass spectrometer whose own ionizer had been removed. It was found that the intensity and distribution of the naphthalene fragments was sensitively dependent on the electron impact energies. Since similar electron energies had also been used in the spectroscopic measurements, the fact that the new bands tracked the 675 nm cation

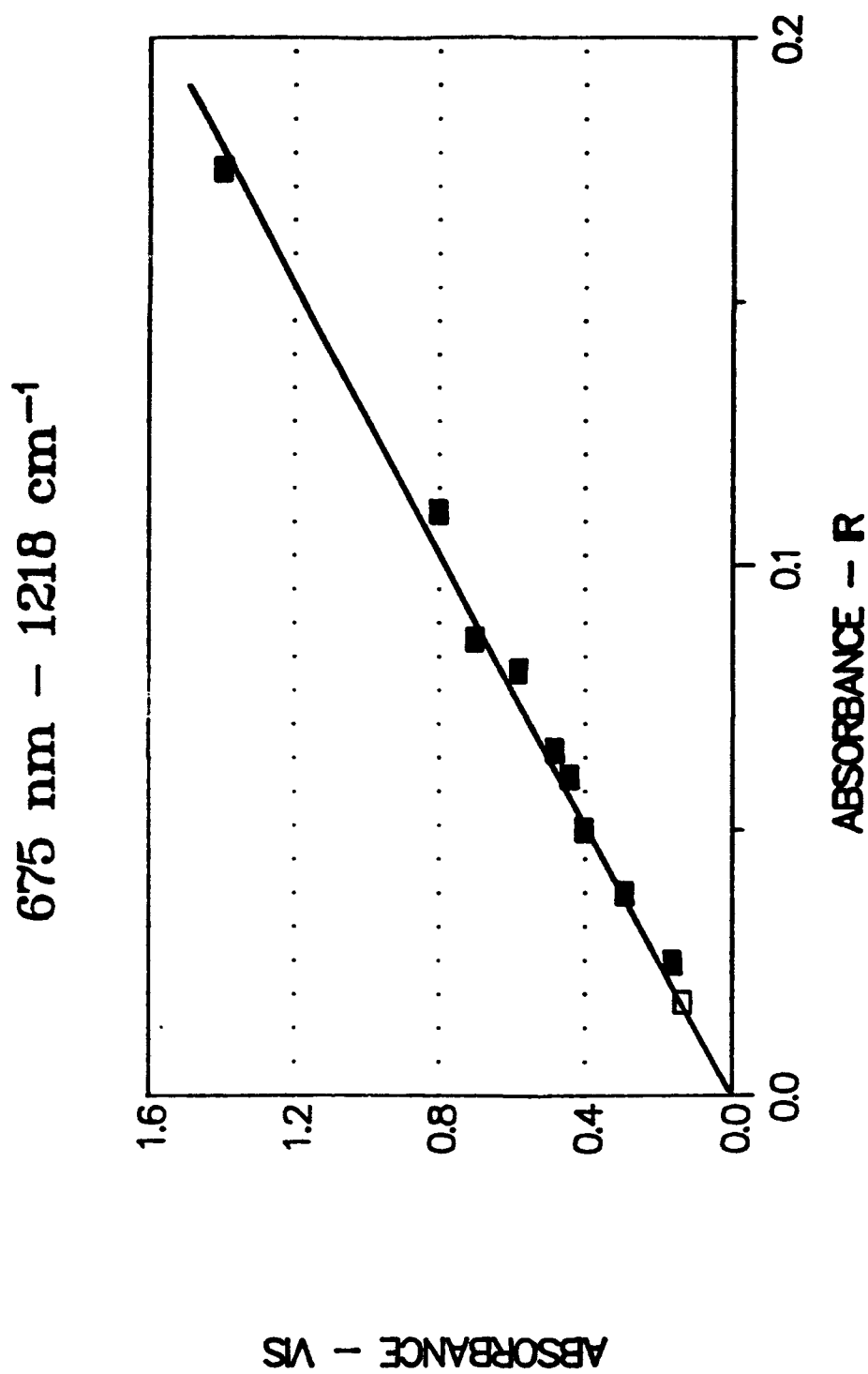


Figure 42. Correlation of 675 nm Visible Band Absorbance of Naphthalene Cation with 1218  $\text{cm}^{-1}$  IR Band Absorbance

peak well argues against their arising from naphthalene fragments. Conversely, it appears that the smaller fragments did not contribute any observable peaks in the infrared. However, the real experimental situation is difficult to check using mass spectrometric detection for the following reasons. First the matrix experiment, the naphthalene/Ar/CCl<sub>4</sub> mixture pressure in the ionization region, close to the cold window and electron gun, is higher than the pressure of naphthalene in the same region when using the mass spectrometer. Thus, the average electron kinetic energy was probably lower in the matrix experiment, with the result that fragmentation processes may not have been as prevalent. Second, the new bands cannot be due to the CCl<sub>4</sub> molecule or its fragments or to fragments created from naphthalene and CCl<sub>4</sub>, since the new bands were also observed, although much more weakly, in experiments with CCl<sub>4</sub> absent.

## (2) Comparison to theoretical frequencies

Using a SCF Hartree-Fock approach with a 3-21G basis set, DeFrees and co-workers calculated the frequencies and intensities of neutral and monocationic naphthalene (Reference 144). Table 6 gives the results of this calculation (only those vibrations displaying nonzero intensities are included). The calculated frequencies were scaled by a factor of 0.89; both scaled and unscaled values are presented in the table. A tentative matchup of the experimental and calculated frequencies is also given in the table. Several interesting observations can be made from this comparison. (1) The band calculated to be most intense, the 1210 cm<sup>-1</sup> band (unscaled), is very close (probably fortuitously so) to the observed major cation peak at 1218 cm<sup>-1</sup>. (2) After the 1210 cm<sup>-1</sup> band, the three next-most intense bands calculated are at 1058, 1660 and 1658 cm<sup>-1</sup>. These correspond reasonably well with the observed bands at 1033, 1537 and 1525 cm<sup>-1</sup>, respectively. (Scaling factors of only 0.976, 0.926 and 0.92 are needed.) (3) The observed 1519 cm<sup>-1</sup> band corresponds well with the 1583 cm<sup>-1</sup> calculated value (0.96 scaling factor) but the calculated intensity

TABLE 6 THEORETICAL<sup>a</sup> AND EXPERIMENTAL<sup>b</sup> IR BANDS FOR NAPHTHALENE

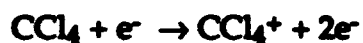
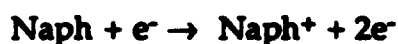
Neutral				Cation			
Sym	$\tilde{\nu}^e/\text{cm}^{-1}$	$\tilde{\nu}^d/\text{cm}^{-1}$	Int. km/mole	Sym	$\tilde{\nu}^e/\text{cm}^{-1}$	$\tilde{\nu}^d/\text{cm}^{-1}$	Int. km/mole
$b_{2u}$	3381	3009	46	$b_{2u}$	3406	3031	1
$b_{1u}$	3364	2997	54	$b_{1u}$	3393	3020	1
$b_{2u}$	3348	2980	1	$b_{1u}$	3376	3005	2
$b_{1u}$	3346	2979	2	$b_{2u}$	3375	3004	11
$b_{1u}$	1784	1588	12	$b_{2u}$	1660	1477	180
$b_{2u}$	1664	1481	15	$b_{1u}$	1658	1476	147
$b_{1u}$	1566	1394	4	$b_{1u}$	1583	1409	19
$b_{2u}$	1481	1318	3	$b_{2u}$	1465	1304	3
$b_{1u}$	1409	1254	8	$b_{1u}$	1430	1273	5
$b_{1u}$	1265	1126	4	$b_{2u}$	1299	1156	31
$b_{2u}$	1209	1076	3	$b_{2u}$	1210	1077	1123
$b_{3u}$	1154	1027	6	$b_{1u}$	1207	1074	22
$b_{2u}$	1070	952	3	$b_{3u}$	1164	1036	1
$b_{3u}$	916	815	168	$b_{2u}$	1058	942	662
$b_{1u}$	884	787	1	$b_{3u}$	898	799	162
$b_{2u}$	706	628	4	$b_{2u}$	635	565	324
$b_{3u}$	548	488	33	$b_{3u}$	483	430	48
$b_{1u}$	401	357	2	$b_{3u}$	178	158	5
$b_{3u}$	192	171	3				

<sup>a</sup>Theoretical values from DeFrees and coworkers, (Reference 144).<sup>b</sup>Present work.<sup>c</sup>Unscaled, from (Reference 144).<sup>d</sup>Scaled by factor 0.89, from (Reference 144).

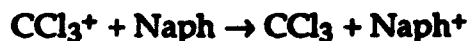
appears to be too low. (4) Two other bands are predicted to have intensities comparable to the above ones; however, the  $898\text{ cm}^{-1}$  band may be overlapped by the  $\text{CCl}_3$  band while the  $635\text{ cm}^{-1}$  band is out of range due to the use of the  $\text{BaF}_2$  window. In conclusion, the calculated and experimental frequencies match reasonably well. At this level of theory, scaling factors of between 0.92 and 0.98 are needed for a good match.

### (3) Mechanism of Enhanced Ionization and Matrix Stabilization

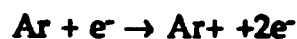
The fact that the carbon tetrachloride fragments,  $\text{CCl}_4^+$ ,  $\text{CCl}_3^+$  and  $\text{CCl}_3$  (plus  $\text{Cl}$  and/or  $\text{Cl}^-$ , by deduction) are observed in the matrix points to the following processes occurring under electron bombardment:

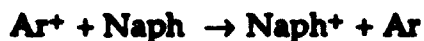


Because of the high electron affinity of chlorine, carbon tetrachloride is often added to matrices as an electron trap to provide charge balance for the cations under study. In the present work, however,  $\text{CCl}_4$  and argon gas appear to behave additionally as ionization enhancers. We believe this may occur via the following charge transfer processes:



This may also occur via Penning ionization. Argon, as the dominant gas in the  $\text{Ar}/\text{CCl}_4/\text{naphthalene}$  mixture, is ionized and excited by electron impact. Since the energy of the excited metastable  $\text{Ar}$  is higher than the IP of naphthalene, Penning ionization of naphthalene is possible:





The presence of the ring electrode (with a +50-volt potential) close to the deposition window serves as a negative ion and electron trap. The electron current monitored at this electrode was observed to increase five-fold when the Ar/CCl<sub>4</sub>/naphthalene gas mixture was admitted to the deposition chamber.

In addition to the above vapor phase processes, the addition of CCl<sub>4</sub> to the gas stream plays an important role in the matrix. Electron impact with Ar atoms produces low-energy electrons; these slow electrons can be captured by Cl atoms (from CCl<sub>4</sub> dissociation) to produce Cl anions. These anions (plus perhaps other impurity ions such as OH<sup>-</sup>) act to balance the excess charge created by the deposited naphthalene cations. To emphasize this point, it is instructive to calculate the potential created by a matrix whose cationic absorbance is 1.0. At a point 1 cm in front of the matrix, the potential is approximately a megavolt. Clearly, such a matrix would explode coulombically; thus the presence of negative balancing charges (preferably infrared-invisible) is mandated for the successful spectroscopic interrogation of cationic species.

#### (4) Cation yield and absolute infrared band intensities

The molar absorption coefficient of the naphthalene cation in the visible was determined by Kelsall and Andrews (Reference 120) (KA) as  $\epsilon^+_{\text{max}}(675\text{nm})=24900 \text{ M}^{-1}\text{cm}^{-1}$  (in Ar) and recently by Salama and Allamandola (Reference 139) (SA) as  $\epsilon^+_{\text{max}}(675\text{nm})=1130 \text{ M}^{-1}\text{cm}^{-1}$  (in Ar). To calculate the yield of cations-to-neutrals ( $c^+/c^0$ ) in the matrix the following absorbance formulas are applicable:

$$A^+(675\text{nm}) = \epsilon^+_{\text{max}}(675\text{nm})c^+l$$

$$A^0(309.2\text{nm}) = \epsilon^0_{\text{max}}(309.2\text{nm})c^0l$$

The yield of cations is thus:

$$c^+/c^0 = A^+(675\text{nm})/A^0(309.2\text{nm}) \cdot \epsilon^0_{\text{max}}(309.2\text{nm})/\epsilon^+_{\text{max}}(675\text{nm})$$

The absorbance ratio (first on the RHS) is 1.46 based on our spectra (cf. Figure 40), while the molar absorption coefficient ratio (second on the RHS) is 0.185, using the results of SA. From this, the percentage of cations (to neutrals) is determined to be 27 percent. On the other hand, using KA's results leads to a percentage yield of 1.2%. Given the extremely high potentials expected to be built up by a large excess of charge in a matrix, the 27 percent calculated from SA's results appears unrealistically high. The implication is that their molar absorption coefficient is too low. Indeed, allowed electronic transition in PAH's are known (Reference 145) to be in the  $10^4$  to  $10^5$  range. The 1.2 percent yield deduced from KA's results is reasonable.

One of the advantages of the crossed IR/UV-visible beam approach is the possibility of obtaining absolute band intensities for IR bands when the corresponding quantities are known for the UV-visible bands. From Beer's law, the simple relation:  $\epsilon(\text{IR}) = \epsilon(\text{UV-vis}) \cdot A(\text{IR})/A(\text{UV-vis})$  holds, since the concentration and path length are the same in both measurements and thus cancel.

Accepting the KA molar absorption coefficient of  $24,900 \text{ M}^{-1}\text{cm}^{-1}$  for the 675 nm peak and using our result that the  $1218 \text{ cm}^{-1}$  IR band is 8 times weaker than the 675 nm band (cf slope of the correlation plot in Figure 42) leads to a value for  $\epsilon^+_{\text{max}}(1218\text{cm}^{-1}) = 3112.5 \text{ M}^{-1}\text{cm}^{-1}$ . To compare with theoretical values the integrated band intensity is needed:

$$\int \epsilon(\nu) d\nu = \epsilon_{\text{max}} \frac{\Delta\nu_1}{2} = \epsilon^+_{\text{max}}(1218 \text{ cm}^{-1}) \cdot \frac{\Delta\nu_1}{2} = 62.25 \text{ km mol}^{-1}$$

This value is considerably smaller (about 18 times) than the theoretical value of 1123 km/mole of DeFrees and co-workers (Reference 144). Our experimental value of 62 km/mole is dependent on the value used for the 675nm band intensity. A higher value for  $\epsilon(675\text{nm})$  would lead to better agreement; a value equal to  $4.5 \times 10^5$

$M^{-1} cm^{-1}$  would be necessary for a match. However, KA point out (Reference 120) that their 675 nm band value is probably uncertain to only 20 percent. Their method entails the measurement of the intensity decrease of the neutral parent and the increase of the cationic product upon photolysis. It assumes that all neutral parent lost is converted to ionic product. If this is not the case, the values determined represent lower limits. Thus, if a nonionizing process such as fragmentation were occurring, the molar absorption coefficient for the IR band would be higher than found here. While possible, we believe this is unlikely.

The discrepancy may result from the level of theory (HF/3-21G) employed to calculate the intensities. DeFrees and co-workers state (Reference 144) that higher level theory (MP2/6-31G\*) on pyridine and its cation do not greatly affect the conclusion that ionization strongly enhances the intensities of certain vibrational bands, and decreases others. It would be of interest to test this conclusion on the larger PAHs in light of the results presented here.

Finally, DeFrees et al. predict (Reference 144) that the intensities of the CH stretch modes should decrease dramatically (factor of about 50) upon ionization. It would have been interesting to verify this but spectral congestion from the CH stretches of the neutral parent, prevent location of new bands in this region. Verification of this prediction may prove difficult because of the congestion, the low concentration of the cationic species present, and the expected low molar absorption coefficients of these vibrations.

## 2. Para-dichlorobenzene

### a. Experimental results

The UV spectrum of the precursor parent, PDCB, isolated in an argon matrix at 12 K is shown in Figure 43; the lowest energy band lies at 280 nm. After deposition of the pulsed-glow discharge plasma mixture two apparent band

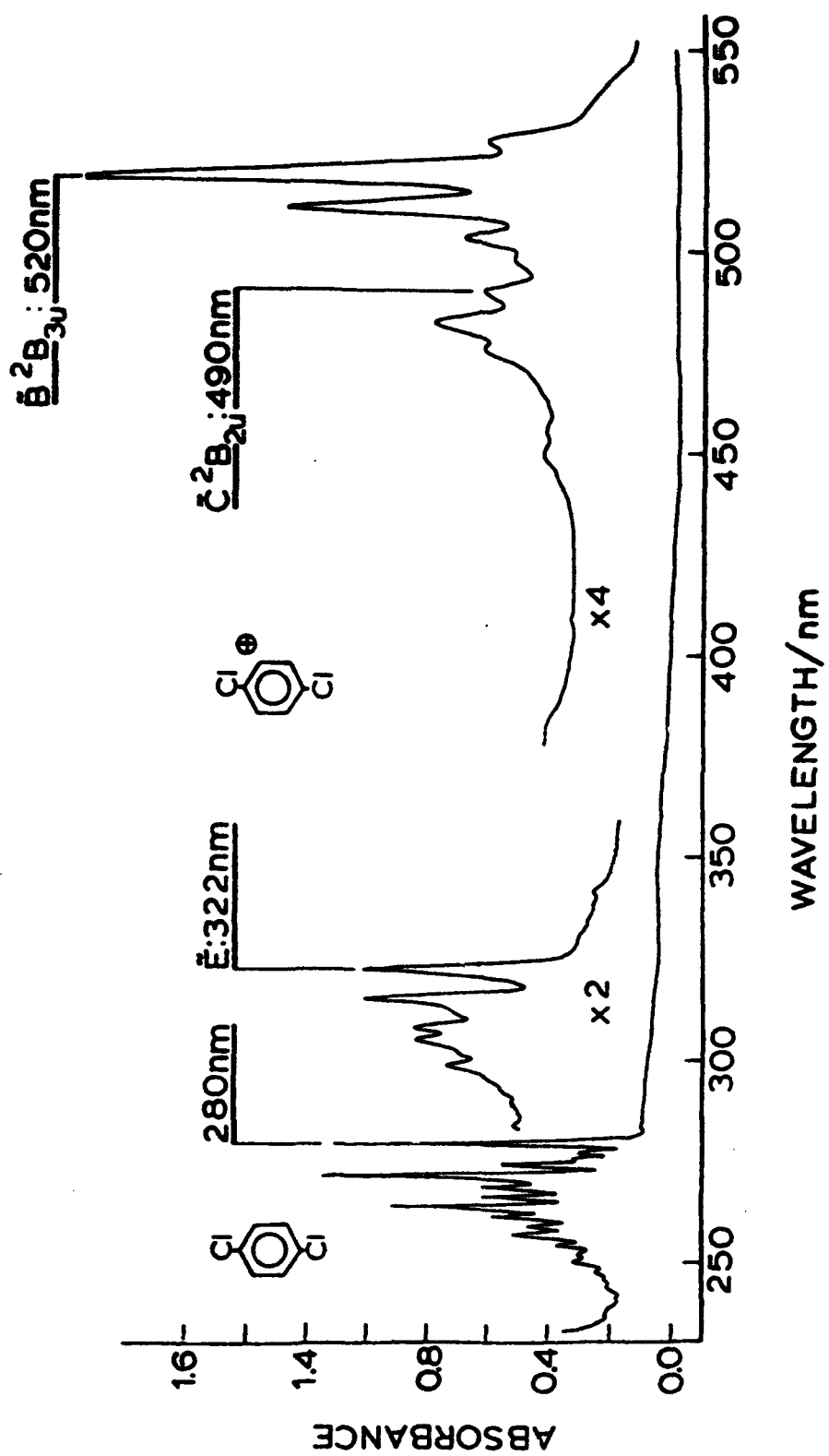


Figure 43. UV Spectrum of Neutral para-Dichlorobenzene (PDCB) in Ar Matrix at 12 K, Showing Band System at 280 nm

systems appear between 550 nm and 280 nm. These systems, with prominent bands at 520 nm and 322 nm, correspond very closely to those observed previously by Friedman, Kelsall and Andrews (Reference 122) (FKA) and attributed by them to the PDCB cation. The 520nm system was ascribed to the  $\tilde{B}^2B_{3u} \leftarrow \tilde{X}^2B_{2g}$  allowed transition. (Reference 122,146). We differ from FKA in the assignment of the vibronic bands of the cation. While FKA assign all the vibronic bands in the 520-440 nm region to one electronic transition and the bands in the 322-283 nm range to another, we prefer to assign the bands in 520-440 nm region to two electronic transitions. Table 7 lists the vibronic bands of the PDCB cation and their attribution. The present assignment to two electronic transitions is consistent with the known photoelectron spectrum of PDCB (Reference 146). Table 8 compares the optical absorption bands and the photoelectron bands. Energies close to the observed optical bands by subtraction of the ionization energies of the ground and excited states of PDCB.

The infrared spectrum of neutral PDCB (in an Ar matrix at 12 K) is shown in Figure 44. Prominent bands are observed at 820, 1012, 1090 and 1480  $\text{cm}^{-1}$ . The IR spectrum of the same sample matrix exhibiting the cation visible bands (520 nm, 322 nm) discussed above is shown also in Figure 44; new bands are observed at 843, 986, 1110 and 1429  $\text{cm}^{-1}$ . Over a series of experiments, the ratio of the 520 nm band absorbance to the 1429  $\text{cm}^{-1}$  band absorbance was consistently found to be ~16. A series of experiments were performed with varying deposition times, pulsed-glow discharge pulse rates, and discharge configurations to prepare samples containing different concentrations of PDCB cations. If the 520 nm visible band and the above four IR bands all originate in the PDCB cation, their relative intensities should vary linearly. Figure 45 displays the correlation for eight different experiments: an excellent correlation is found between the four IR band absorbances and the 520 nm

**TABLE 7 VISIBLE/UV ABSORPTION BANDS OF  
PARA-DICHLOROBENZENE CATION IN Ar, 12 K.**

$\lambda/\text{nm}$	$\bar{\nu}/\text{cm}^{-1}$	$\Delta\bar{\nu}/\text{cm}^{-1}$	Assignment
528.0	18939	-273	site
520.5	19212	0	origin: $\tilde{\text{B}}^2\text{B}_{3u}$
511.7	19543	331	$\nu_6$
503.8	19849	637	$2\nu_6$
498.5	20056	844	
490.6	20383	0	origin: $\tilde{\text{C}}^2\text{B}_{2u}$
482.6	20721	338	$\nu_6$
475.9	21013	630	$2\nu_6$
467.8	21376	993	$3\nu_6$
456.0	21930	1547	$\nu_2$ ; $\tilde{\text{D}}^2\text{B}_{3g}(\text{?})$
449.6	22242	1859	$\nu_2 + \nu_6$
322.4	31017	0	origin: $\tilde{\text{E}}$
315.0	31746	729	$\nu_5$
311.5	32102	1085	$\nu_4$
308.1	32457	1440	$2\nu_5$
305.0	32787	1770	$\nu_5 + \nu_4$
301.3	33189	2172	$3\nu_5$
298.5	33501	2484	$\nu_4 + 2\nu_5$
295.2	33875	2858	$4\nu_5$
292.3	34602	3585	$5\nu_5$ or $2\nu_4 + 2\nu_5$
283.5	35273	4256	$6\nu_5$

**TABLE 8 COMPARISON OF THE PDCB CATION OPTICAL ABSORPTION TRANSITIONS WITH THE PHOTOELECTRON BANDS**

State <sup>a</sup>	IE <sub>i</sub> /eV <sup>a</sup>	IE <sub>i</sub> - IE( <sup>2</sup> B <sub>2g</sub> )	Optical Transition in Ar Matrix
$\tilde{X}^2B_{2g}$	8.98	0.0	--
$\tilde{A}^2B_{1g}$	9.87	0.89 eV (1393nm, 7178 cm <sup>-1</sup> )	not obs.: forbidden
$\tilde{B}^2B_{3u}$	11.36	2.38 eV (520.9nm, 19195 cm <sup>-1</sup> )	520.5nm. 19212 cm <sup>-1</sup>
$\tilde{C}^2B_{2u}$	11.49	2.51 eV (494.0nm, 20243 cm <sup>-1</sup> )	490.6nm. 20383 cm <sup>-1</sup>
$\tilde{E}$	12.8	3.82 eV (324.6nm, 30808 cm <sup>-1</sup> )	322.4nm. 31017 cm <sup>-1</sup>

<sup>a</sup> From Reference 146

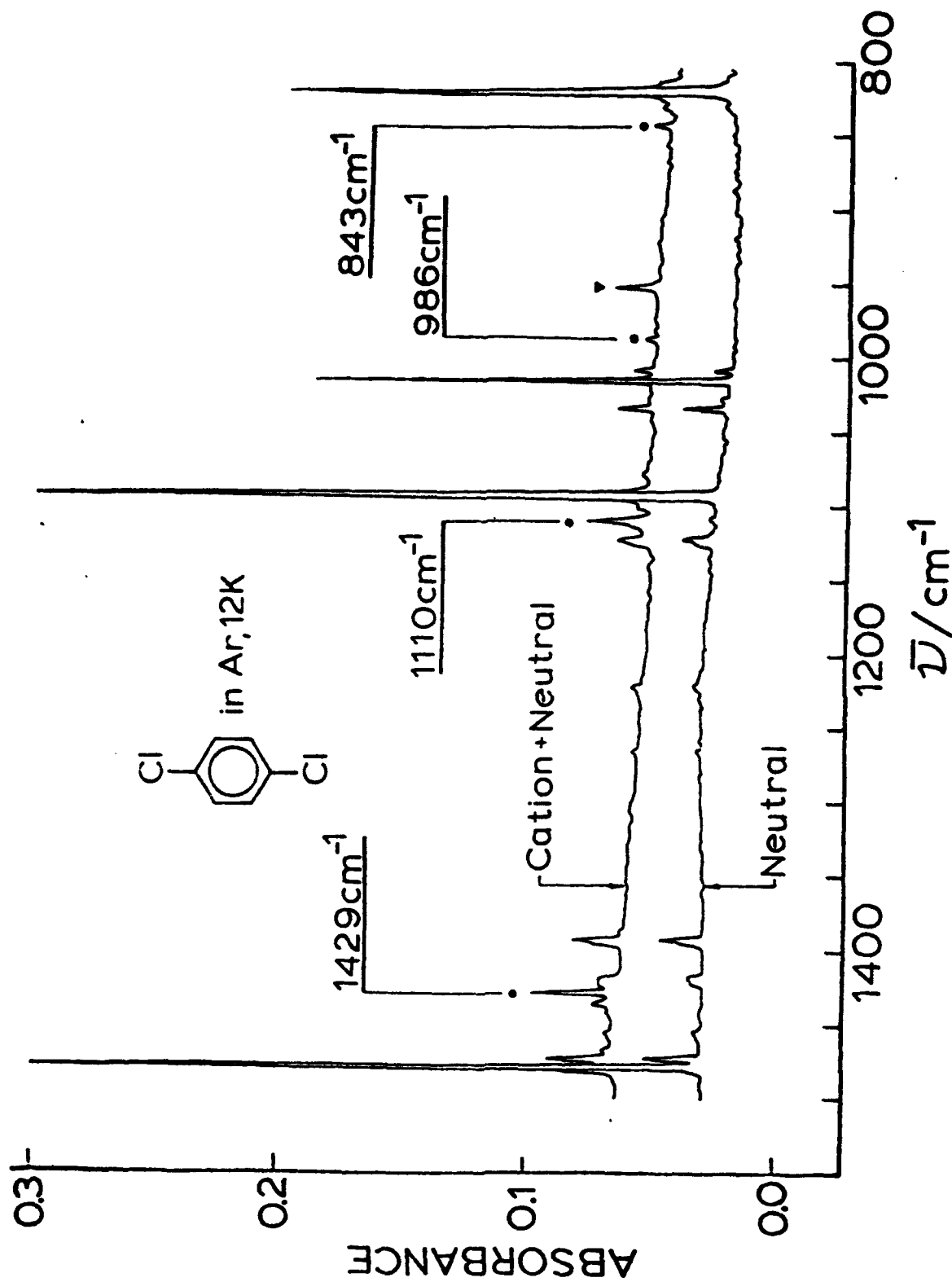


Figure 44. Fourier Transform Infrared Spectrum of Neutral PDCB (bottom) and Neutral Plus Cation PDCB (top) in Ar Matrix at 12 K

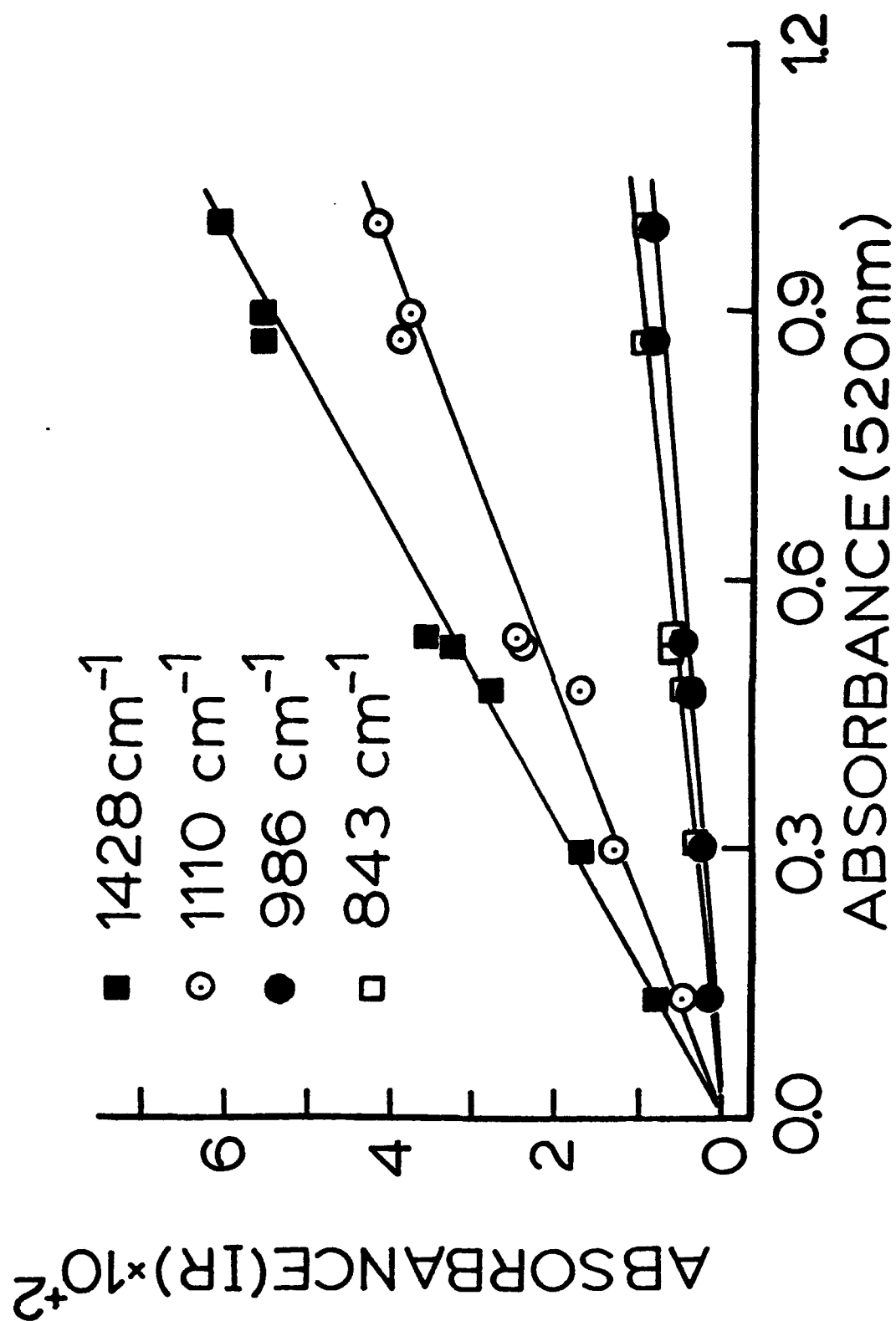


Figure 45. Correlation of 520 nm Visible Absorption Band Absorbance of PDCB Cation with Four IR Band Absorbances

band absorbance. The correlation of the neutral PDCB IR intensities to the intensity of the 520 nm band was poor for the same set of experiments. A new band at 951  $\text{cm}^{-1}$  (marked with an inverted triangle in Figure 45) was observed upon deposition of the pulsed-glow discharge mixture. This band does not correlate with the 520 nm PDCB cation band and therefore does not arise from this species. Its origin is unknown at present.

Confirmatory correlation between the 520 nm and new the IR bands was sought via a photolysis experiment. Using a medium pressure Hg lamp (with a filter whose cutoff  $\lambda < 420$  nm) for 20 minutes resulted in a twofold decrease in the 520 nm band system while the intensity of the neutral 280 nm band was practically constant. The intensity of the IR peaks at 843, 986, 1110 and 1429  $\text{cm}^{-1}$  also decreased by a factor of  $\sim 2$ . Thus, we conclude that these four IR frequencies belong to the PDCB radical cation.

The results of the fluorescence/resonance Raman measurements are shown in Figures 46 and 47. The spectrum in Figure 46 (excited by 10 mW, 514.5 nm Ar laser radiation) shows both sharp and broad features. The broad features are fluorescence from the  $\tilde{B}^2B_{3u}$  state, whereas the sharp features are resonance Raman lines. An analysis of the sharp lines is given in Table 9 where the observed bands are also compared to previous work by Kato, Muraki and Shida (Reference 125). An analysis of the broad bands from Figure 46 is presented in Table 10. It can be seen that the vibrational intervals mimic each other quite closely. Excitation with 488 nm laser radiation (cf. Figure 47) results only in broad spectral bands; cf. Table 10 for an analysis of the bands. The highest energy peak observed for 488 nm and 514 nm excitation appears at 19089  $\text{cm}^{-1}$  and 19052  $\text{cm}^{-1}$ , respectively. Since this energy is identical within experimental error (these two peaks differ by only  $\sim 1.0$  nm), the broad bands are fluorescence in origin. The spectrum in Figure 47 shows "extra"

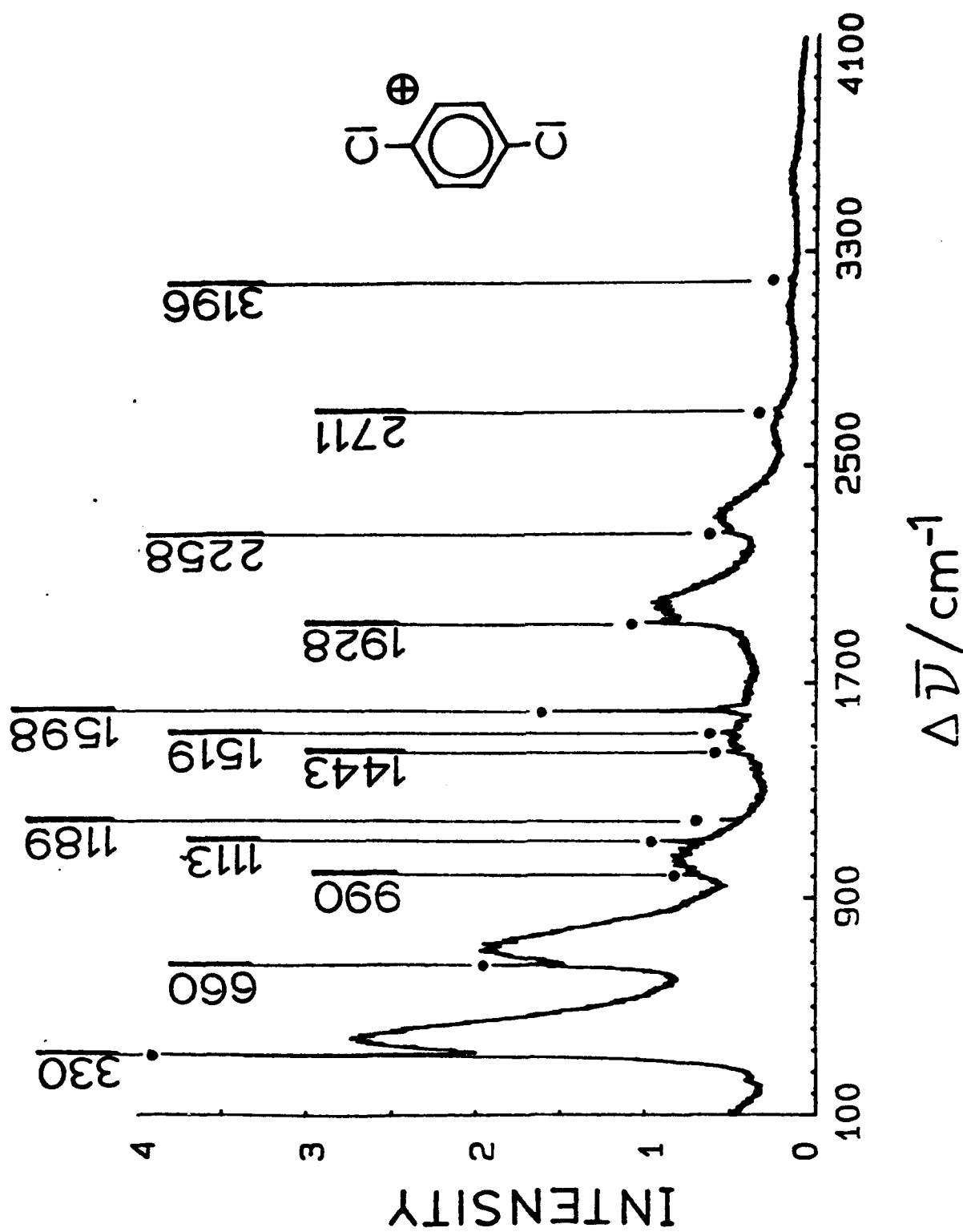


Figure 46. Fluorescence and Resonance Raman Bands of PDCB Cation (Ar Matrix, 12 K) Excited by 514.5 nm Ar Ion Laser Radiation

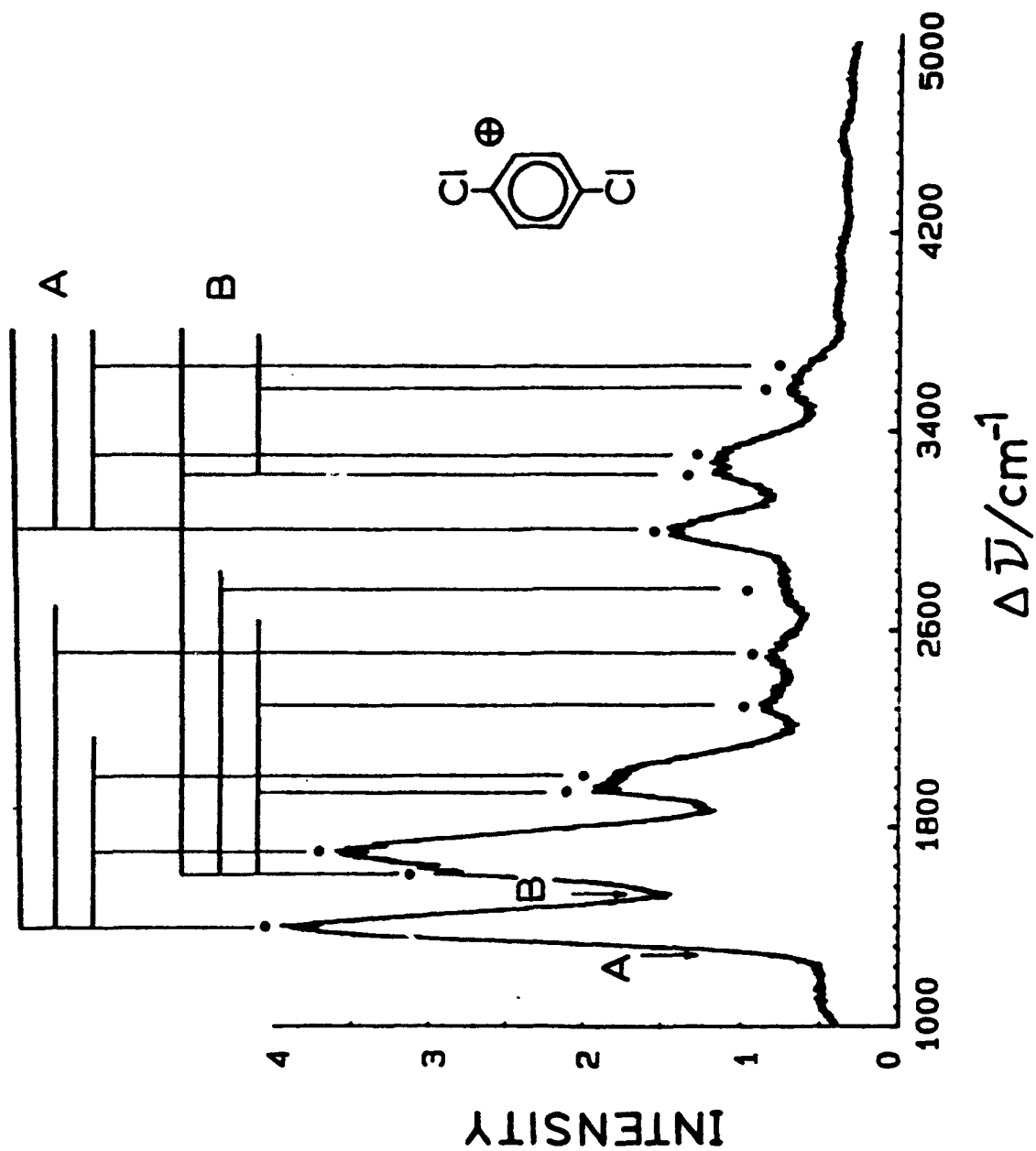


Figure 47. Fluorescence of PDCB Cation (Ar Matrix, 12 K) Excited by 488.0 nm Ar Ion Laser Radiation

**TABLE 9 RESONANCE RAMAN BANDS OF THE PARA-DICHLOROBENZENE CATION**

<u>In Freon Mixture, 77 K. <math>\gamma</math>-irradiation<sup>a</sup> <math>\bar{\nu}/\text{cm}^{-1}</math></u>	<u>In Argon Matrix, 12 K. Pulsed-Glow Discharge<sup>b</sup> <math>\bar{\nu}/\text{cm}^{-1}</math></u>	<u>Assignment</u>
--	330	$\nu_6$
666	660	$2\nu_6$
990	990	$3\nu_6$
1115	1113	$\nu_4$
1195	1189	$\nu_3$
1447	1443	$\nu_4 + \nu_6$
1601	1598	$\nu_2$
1932	1928	$\nu_2 + \nu_6$
--	2258	$\nu_2 + 2\nu_6$
2714	2711	$\nu_2 + \nu_4$
--	3196	$2\nu_2$

<sup>a</sup> 538.27nm laser excitation; Reference 125

<sup>b</sup> 514.5nm laser excitation; present work.

TABLE 10 FLUORESCENCE BANDS OF PDCB RADICAL CATION IN Ar/12K.

514.5nm Laser Excitation				488.0nm Laser Excitation					
A Series				B Series					
$\Delta\bar{\nu}^a/\text{cm}^{-1}$	$\bar{\nu}/\text{cm}^{-1}$	$\Delta\bar{\nu}^b/\text{cm}^{-1}$	$\Delta\bar{\nu}^c/\text{cm}^{-1}$	$\bar{\nu}/\text{cm}^{-1}$	$\Delta\bar{\nu}^d/\text{cm}^{-1}$	$\bar{\nu}/\text{cm}^{-1}$	$\Delta\bar{\nu}^e/\text{cm}^{-1}$	Assign <sup>f</sup>	
384	19052	0	1402	19089	0	1619	18873	0	--
716	18720	332	1704	18789	300	1947	18545	328	$\nu_6$
1040	18396	332 + 324	2027	18465	300 + 324	2294	18198	328 + 347	$2\nu_6$
1485	17951	1101	2508	17984	1105	2766	17726	1147	$\nu_4$
1988	17448	1604	2989	17503	1586	3231	17260	1612	$\nu_2$
2318	17124	1604 + 324	3304	17188	1586 + 318	3564	16928	1612 + 332	$\nu_2 + \nu_6$
2643	16793	1604 + 324 + 331	3632	16860	1586 + 318 + 328	--	--	--	$\nu_2 + 2\nu_6$
3094	16342	1604 + 1106	--	--	--	--	--	--	$\nu_2 + \nu_4$

<sup>a</sup> Displacement from laser excitation line at 514.5nm (19,436  $\text{cm}^{-1}$ ).<sup>b</sup> Displacement from 19052  $\text{cm}^{-1}$  (0-0) band.<sup>c</sup> Displacement from laser exc. line at 488.0nm (20,492  $\text{cm}^{-1}$ ).<sup>d</sup> Displacement from 19089  $\text{cm}^{-1}$  (0-0) line (A series origin).<sup>e</sup> Displacement from 18873  $\text{cm}^{-1}$  (0-0) line (B series origin).<sup>f</sup> Assignment for all three columns: 514.5nm excitation, 488.0nm excitation, series A and B.

broad bands compared to those in Figure 46 (labelled as Series B). We believe this results from a concurrent excitation of both those molecules, giving rise to the 520.5 nm absorption band origin (A series) and those molecules in another (undefined) site giving rise to the 528.0 nm band (B series) (cf. Table 7). FKA assign the 528.0 nm band as a "site" band also. The 488 nm excitation is into the  $\tilde{C}^2B_{2u}$  second excited state whose vibrational structure is broad and congested with overlap of bands from the lower  $\tilde{B}^2B_{2u}$  state. In Figure 47, the peak maxima of the 520.5 nm (A) and 528.0 nm (B) absorption origins are marked by arrows. The placement of the A and B series fluorescence bands is compatible with emission from the two A and B origins. Presumably with 514 nm irradiation, excitation of the B site molecules is much less probable, although a hint of a B series can be discerned in the broad bands in Figure 46.

#### b. Theoretical Results

Theoretical calculations on the excited electronic states of PDCB radical cation were performed in order to confirm, where known, and assign, where unknown, the optical bands observed (cf. Figure 43). Initially, we optimized the geometrical structure using the INDO/1 method (References 147,148) and obtained:  $r_{C-H} = 1.093 \text{ \AA}$  (1.101  $\text{\AA}$ ),  $r_{C-Cl} = 1.777 \text{ \AA}$  (1.738  $\text{\AA}$ ),  $r_{C-C} = 1.381 \text{ \AA}$  (1.408  $\text{\AA}$ ) for the C-C bonds adjacent to the C-Cl bonds and  $r'_{C-C} = 1.395 \text{ \AA}$  (1.357  $\text{\AA}$ ) for the central C-C bonds (values given are for neutral PDCB with radical cation in parenthesis).

We have used the INDO/S model (References 149,150) to examine the electronic spectra of both neutral and cationic PDCB. Calculations on the neutral yield a  $^1B_{2u}$  ( $3 \times 10^{-4}$ ) state at 37,500  $\text{cm}^{-1}$ , a  $^1B_{2u}$  state at 39,100  $\text{cm}^{-1}$  and a  $^1B_{3u}$  (0.0177) state at 40,200  $\text{cm}^{-1}$ , where the numbers in parentheses are calculated oscillator strengths. Since the calculation (which includes configuration interaction) refers to the geometry of the  $^2B_{2g}$  ground state, the calculated values should be compared with the band maxima of Figure 43. The calculated energy of the weakly allowed

$^1B_{2u}$  state is in reasonably good accord with the  $\lambda_{\text{max}} = 272 \text{ nm} (= 36,760 \text{ cm}^{-1})$  peak of Figure 43. The calculated spectrum of the cation is given in Table 11. The order of the lower-lying states is in general accord with an earlier suggestion (Reference 146). The first excited state of the cation seen in the ionization spectrum, but not absorption, is a  $^1B_{1g}$  calculated at 0.68 eV. The  $^2B_{3u} \leftarrow ^2B_{2g}$  allowed transitions calculated at 2.89 eV is some 0.5 eV higher in energy than that observed. This then leads to two possible assignments for the higher-lying transitions. The first of these is that suggested in the table, in the order calculated. The assignment of the  $\tilde{A}$  through  $\tilde{D}$  is in good agreement with previous assignments (Reference 146). The observed feature at 2.72 eV is assigned to  $^2B_{3g}$ , and  $\tilde{E}$  to the  $^2B_{3u}$  transition calculated at 3.41 eV. This also agrees with the general order of intensities observed in Figure 43. The second suggested assignment comes from the observation that both  $^2B_{3u}$  at 2.89 eV and  $^2B_{2u}$  at 3.14 eV are calculated about 0.5-0.6 eV higher in energy than they are observed. If this is a systematic trend, the  $\tilde{E}$  state might be assigned to the third calculated  $^2B_{3u}$  at 4.26 eV and the second  $^2B_{3u}$  associated with the broad, structureless feature observed at 2.72 eV. Polarization data would be helpful in deciding between these two alternatives.

To determine the effect of ionization on the vibrational force constants of specific bonds in PDCB, an *ab initio* Hartree-Fock SCF level calculation (6-31 G\* basis) was performed. Initially, the geometries of the neutral parent and the radical cation were optimized using the GAMESS program (References 151,152). The optimized geometries found are (radical cation figures in parentheses):  $r_{\text{C-H}} = 1.070 \text{ \AA}$  (1.070  $\text{\AA}$ ),  $r_{\text{C-Cl}} = 1.805 \text{ \AA}$  (1.742  $\text{\AA}$ ),  $r_{\text{C-C}} = 1.380 \text{ \AA}$  (1.419  $\text{\AA}$ ) for the C-C bonds "adjacent" to the C-Cl bonds, and  $r'_{\text{C-C}} = 1.388 \text{ \AA}$  (1.359  $\text{\AA}$ ) for the "central" C-C bonds. The values are in good agreement with those found using the INDO/1 method. The relative decrease of the  $r_{\text{C-Cl}}$  and  $r'_{\text{C-C}}$  lengths and the increase of the  $r_{\text{C-C}}$  adjacent bonds is consistent with the removal of an electron from the HOMO of

TABLE 11 CALCULATED AND OBSERVED ELECTRONIC SPECTRA OF PDCB CATION (ENERGIES IN eV).

Observed (cf. Table 8)			Calculated (INDO/S)		
	$\Delta IE^a$	Opt. (Ar Matrix <sup>b</sup> )	$\epsilon$ (Koopmans) Neutral <sup>c</sup>	CI Cation <sup>e,d</sup>	Assignment
$\tilde{X}^2B_{2g}$	--	--	--	--	--
$\tilde{A}^2B_{1g}$	0.89	--	0.20	0.68	$^2B_{1g}$
$\tilde{B}^2B_{3u}$	2.38	2.40	2.65	2.89(0.156)	$^2B_{3u}$
$\tilde{C}^2B_{2u}$	2.51	2.58	2.45	3.14	$^2B_{2u}$
$\tilde{D}^2B_{3g}$		2.72(?)	2.55	3.23	$^2B_{3g}$
$\tilde{E}$	3.82	3.97	3.35	3.41(0.081)	$^2B_{3u}$
				3.52	$^2A_g$
				4.26(0.054)	$^2B_{3u}$
				4.87(0.185)	$^2A_u$
				4.88(0.000)	$^2B_{1u}$
				5.31(0.094)	$^2A_u$

<sup>a</sup>The first IE of  $\tilde{X}^2B_{2g}$  is 8.98 eV. All others are relative to this, see Reference 146

<sup>b</sup>See Figure 45 These are estimated  $v_{max}$ .

<sup>c</sup>Relative to the first M.O. eigenvalue of 9.74 eV.

<sup>d</sup>The numbers in parentheses are calculated oscillator strengths from the  $^2B_{1g}$  ground state of the cation.

<sup>e</sup>The first IE is calculated at 9.00 eV. All others are relative to this.

PDCB. This  $\pi$  molecular orbital (cf. Figure 48) is antibonding with respect to the C-Cl and central C-C bonds and bonding with respect to the adjacent C-C bonds.

Harmonic vibrational frequencies for PDCB neutral and radical cation species were calculated using the GAMESS program. Vibrational frequencies calculated at the SCF level are typically overestimated by ~10 percent because of the harmonic approximation used and the neglect of electron correlation effect (Reference 153). To account for this, a scaling factor of 0.9 has been adopted to adjust the calculated frequencies. Previous experience has shown (Reference 154) that the match with experimental vibrational frequencies using such a scaling factor is usually within  $\pm 50 \text{ cm}^{-1}$ . Calculated, scaled and experimental frequencies for neutral PDCB and its radical cation are given in Table 12 and 13, respectively. Good agreement is found between the scaled and experimental frequencies for both species. The observation that the lower frequency modes need not be scaled as severely as the higher frequency modes is in agreement with an SCF calculation (6-31 G\* basis) done by Rohlfing, et al (Reference 155). The presence of polarization functions (d orbitals) on carbon and chlorine in 6-31 G\* generally decreases the calculated out-of-plane mode frequencies ( $a_u$ ,  $b_{1g}$ ,  $b_{2g}$  and  $b_{3u}$ ) relative to the values obtained with 6-31 G. This may be due to the ability of the polarization functions to better accommodate charge build-up in the  $\pi$ -system during out-of-plane motion. Interestingly, the calculated IR intensities indicate that the two  $b_{1u}$  modes ( $1429$  and  $1110 \text{ cm}^{-1}$ ) of the ionic form should be the most intense and indeed these are the most prominent experimental ionic bands.

In attempting a mode-by-mode comparison between the neutral and ionic species, problems arise. One expects a simple inverse relationship between bond lengths and stretching force constants. However, normal coordinate frequency shifts cannot be so simply described because coupling of various internal coordinates varies as a function of the geometry changes and the force constant changes which

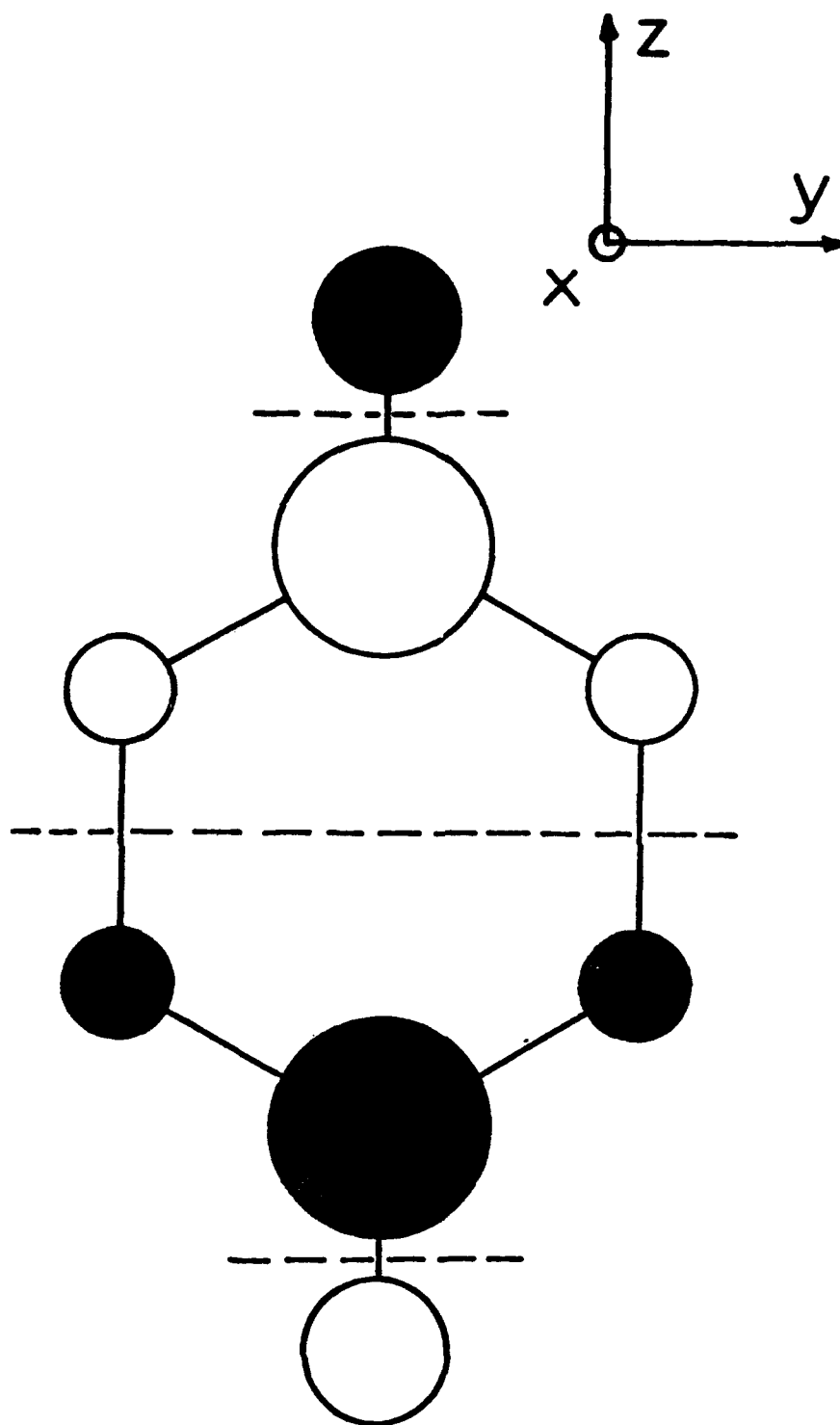


**Figure 48.** Schematic of HOMO (Highest Occupied Molecular Orbital) of PDCB Cation (Adapted from Reference 36)

**TABLE 12 CALCULATED AND OBSERVED VIBRATIONAL FREQUENCIES  
(cm<sup>-1</sup>) FOR NEUTRAL PDCB.**

Mode	Sym.	Calc.	Scaled (0.9)	Expt. <sup>a</sup>
1	a <sub>g</sub>	3403	3063	3072
2		1777	1599	1574
3		1329	1196	1169
4		1186	1067	1096
5		804	724	747
6		344	310	328
7	a <sub>u</sub>	1169	1052	951
8		478	430	405
9	b <sub>1g</sub>	987	888	815
10	b <sub>1u</sub>	3385	3046	3078
11		1668	1501	1477
12		1208	1087	1090
13		1135	1021	1015
14		554	499	550
15	b <sub>2g</sub>	1168	1051	934
16		826	743	687
17		333	300	298
18	b <sub>2u</sub>	3400	3060	3087
19		1533	1398	1394
20		1331	1198	1220
21		1228	1105	1107
22		223	201	226
23	b <sub>3g</sub>	3386	3047	3065
24		1783	1605	1577
25		1479	1331	1290
26		712	641	626
27		375	337	350
28	b <sub>3u</sub>	998	898	819
29		577	519	485
30		112	101	122

<sup>a</sup> References

result from ionization. Nevertheless, comparisons can be made by first coupling calculated neutral and ionic vibrational frequencies by symmetry and then by energy, within each symmetry block. Finally, after scaling, the energy shifts can be compared to the experimental values.

Calculated and scaled neutral-to-ionic frequency shifts are compared in Table 14. The direction of the frequency shift is correctly predicted for all observed bands except for the  $b_{3u}$  mode. This mode differs from the others since it is the only out-of-plane mode observed. The shifts for the Raman-active totally symmetric modes match better than the IR-active modes. This may be due to the greater interaction with the host matrix of transitions involving a dipole moment change with subsequent polarization of the matrix.

To discuss the effect of ionization on specific bonds, it is necessary to transform the normal coordinates to internal coordinates. Boatz and Gordon have introduced (Reference 156) such a vibrational decomposition scheme in which symmetry-adapted normal coordinate frequencies are transformed into intrinsic frequencies. These latter represent the sum of the contributions of all normal modes of a vibration to a particular internal coordinate. Calculated intrinsic frequencies may vary depending on the specific internal coordinates used, but usually do not differ by more than  $\sim 10 \text{ cm}^{-1}$ , particularly for bond stretches. Only intrinsic stretching frequencies and force constants are presented here. The quantities calculated for PDCB, using the method of Boatz and Gordon, are given in Table 15. It may be seen that, upon ionization the C-Cl force constant rises from  $2.509 \text{ mdyne/\AA}$  to  $3.237 \text{ mdyne/\AA}$ , the central C-C force constants also rise from  $6.002 \text{ mdyne/\AA}$  to  $7.289 \text{ mdyne/\AA}$ , while the adjacent C-C force constants drop from  $6.237 \text{ mdyne/\AA}$  to  $4.577 \text{ mdyne/\AA}$ . From the optimized geometries, described previously, it has already been noted that, upon ionization, an increase in the C-Cl and central C-C and decrease in the adjacent C-C bond strengths is expected. This

**TABLE 13. CALCULATED AND OBSERVED VIBRATIONAL FREQUENCIES (cm<sup>-1</sup>) FOR THE RADICAL-CATION OF PDCB.**

Mode	Sym.	Calc.	Scaled (0.9)	Expt. <sup>a</sup>
1	a <sub>g</sub>	3417	3075	--
2		1814	1633	1598
3		1354	1219	1189
4		1204	1084	1113
5		801	721	--
6		346	311	330
7	a <sub>u</sub>	1190	1071	--
8		419	377	--
9	b <sub>1g</sub>	947	852	--
10	b <sub>1u</sub>	3402	3062	--
11		1596	1436	1429
12	b <sub>2g</sub>	1247	1122	--
13		1178	1060	1110
14		575	517	--
15		1181	1063	--
16		796	716	--
17		273	246	--
18	b <sub>2u</sub>	3415	3073	--
19		1624	1462	--
20		1423	1281	--
21		1070	963	986
22	b <sub>3g</sub>	238	214	--
23		3402	3062	--
24		1553	1398	--
25		1336	1239	--
26		622	560	--
27	b <sub>3u</sub>	385	346	--
28		997	897	843
29		558	502	--
30		89	80	--

<sup>a</sup> Present work.

**TABLE 14** CALCULATED AND OBSERVED VIBRATIONAL  
FREQUENCY SHIFTS UPON IONIZATION OF PDCB.

Mode	Sym.	Shift ( $\nu_{\text{ion}} - \nu_{\text{neutral}}$ ; $\text{cm}^{-1}$ )		
		Calc.	Scaled (0.9)	Expt.
2	$a_g$	+37	+33	+24
3		+25	+22	+20
4		+18	+16	+17
6		+2	+2	+2
11	$b_{1u}$	-72	-65	-48
13		+43	+39	+95
21	$b_{2u}$	-158	-142	-121
28	$b_{3u}$	-1	-1	+24

**TABLE 15** CALCULATED INTRINSIC STRETCHING FREQUENCIES  
AND FORCE CONSTANTS FOR NEUTRAL AND RADICAL  
PDCB (IN PARENTHESES)

Bond	Frequency ( $\text{cm}^{-1}$ )		Force Constant ( $\text{mdyn}/\text{\AA}$ )	
	Calc.	Scaled (0.9)	Calc.	Scaled (0.9)
C-H	3388(3401)	3049(3061)	6.287(6.335)	5.658(5.701)
C-Cl	728(827)	655(744)	2.788(3.597)	2.509(3.237)
C-C <sup>a</sup>	1373(1514)	1236(1363)	6.669(8.099)	6.002(7.289)
C-C	-1400(1198)	1260(1078)	-6.930(5.086)	6.237(4.577)

<sup>a</sup> The central C-C bonds.

expectation is fully borne out by the calculated intrinsic frequencies and force constants described here.

A similar trend was also found by Ernstbrunner and co-worker (Reference 103) in a normal coordinate analysis of neutral and cationic para-dimethoxybenzene. They found the ring C-O force constant increased 25 percent (compared to 29 percent for C-Cl in PDCB), while the central C-C bond force constant increased 6 percent (20 percent for PDCB), and the adjacent C-C bond force constant decreased 10 percent (compared to 25 percent for PDCB).

The above intrinsic frequency analysis makes clear why certain bands blue-shift and others red-shift upon ionization. Consider modes 2 and 11: examination of the eigenvectors for neutral PDCB indicate they are associated primarily with central C-C and adjacent C-C bond stretching motions, respectively. Since the force constant for the former increases and for the latter decreases, the blue shift of  $24\text{ cm}^{-1}$  for Mode 2 and the red shift of  $-48\text{ cm}^{-1}$  for Mode 11 is expected. The ratio of the absolute magnitudes of the frequency shifts for Modes 11 and 2 is two and this tracks exactly the number of C-C bond stretches involved in each mode, i.e., there are twice as many adjacent as there are central C-C bonds. This is also consistent with the removal of an electron from the HOMO which is bonding with respect to the adjacent C-C bonds but antibonding with respect to the central C-C bonds (Fig. 48).

### c. Discussion

The use of the pulsed-glow discharge technique with matrix isolation for production and trapping of organic molecular ions has been shown by the present work to be an effective approach. Although sufficient concentrations of the ionic species can be produced and stabilized in the matrix, two important questions remain: (1) Is the ion generation method gentle enough to produce only the parent ion and not unwanted degradation products? And, (2) is the generation and trapping more efficient than other methods reported previously?

To answer the first, we contrast our visible absorption spectrum of PDCB cation to those shown by FKA (Reference 122). Produced either by filtered high-pressure Hg arc photolysis after deposition of the parent precursor or by irradiation via microwave-powered discharge of flowing argon aimed at the sample window during deposition, both methods used by FKA yielded virtually identical spectra (albeit with different intensities). Our spectrum is indistinguishable from their two.

Further support for the production of only the PDCB cation comes from a comparison of our resonance Raman spectrum (argon matrix, 12 K) with the results of Kato, Muraki and Shida (Reference 125) (freon mixture, 77 K,  $\gamma$ -irradiation). The bands observed are compared in Table 7. Despite different methods of ion production, different matrix media and different matrix temperatures, the results are similar.

Finally, a comparison of the gaseous emission spectrum reported by Maier and Marthaler (Reference 146) (produced by controlled electron impact) and our matrix fluorescence spectrum (their Figure 1 and our Figure 27) shows similar vibronic structure involving  $330\text{ cm}^{-1}$  and  $1600\text{ cm}^{-1}$  modes. The vapor phase origin is at  $19620\text{ cm}^{-1}$  while the matrix origin lies at  $19130\text{ cm}^{-1}$  (peak at  $19210\text{ cm}^{-1}$  in absorption and  $19050\text{ cm}^{-1}$  in emission; difference is probably due to self-absorption). A  $490\text{ cm}^{-1}$  red gas-to-matrix shift is not unreasonable for the solvation of the ion. On the basis of these three comparisons, we conclude that the PDCB cation is the predominant, if not the sole, species produced by our pulsed-glow discharge method.

The second question concerning the efficiency of the pulsed-glow discharge/matrix isolation technique can best be answered by a comparison of relative intensities of absorption bands. FKA report (Reference 122) a maximum relative intensity of the 520 nm PDCB cation band to the 280 nm PDCB neutral band of  $\sim 1$ . Our best results show a threefold increase in this ratio: the maximum

absorbance of our 520 nm band is ~1.6, while FKA report  $A = 0.60$ . It is informative to estimate the number of the radical cations actually trapped in the matrix. The  $\tilde{B}^2B_{2u} \leftarrow \tilde{X}^2B_{2g}$  transition at 520 nm is an allowed electronic transition; assuming a typical extinction coefficient value for an allowed transition of  $5 \times 10^4 \text{ l cm}^{-1} \text{ mole}^{-1}$ , and a matrix thickness of 5 microns, yields a cation number density of  $\sim 4 \times 10^{19}$  cations/cm<sup>3</sup>. For a cross-sectional area of 2.8 cm<sup>2</sup> (0.75 in. diam. sample irradiation area), gives  $\sim 5 \times 10^{16}$  radical cations trapped in the matrix. Our pulsed valve operates at 1 Hz, so over a typical 4 hour deposition the valve is pulsed  $1.44 \times 10^4$  times producing approximately  $4 \times 10^{12}$  PDCB ions per pulse.

Comparison of theoretically calculated oscillator strengths with observed absorbances for neutral and cationic IR bands provides an estimate of the relative concentrations of neutral to cationic PDCB present in the matrix. As an initial check of reliability the calculated intensity and observed absorbance ratios for the prominent 1477 and 1090 cm<sup>-1</sup> neutral bands were compared. The ratio was calculated to be equal to 1 and observed to be equal to 0.97 ( $= A_{1477}/A_{1090}$ ). For the prominent 1429 and 1110 cm<sup>-1</sup> cation bands the calculated ratio ( $I_{1429}/I_{1110}$ ) is 1.37 compared to 0.68 determined experimentally. The greater disparity for the cation is not unexpected since the observed absorbances for the ion are an order of magnitude less than those of neutral PDCB.

An estimate of the relative concentrations of neutral to ionic PDCB may be obtained from the theoretical neutral-to-ion intensity ratio ( $I$ ) for a pair of IR bands and the experimental neutral-to-ion absorbance ratio ( $A$ ) for the same two bands. The ratio ( $A/I$ ) gives the relative neutral-to-ion concentration, i.e., there are ( $A/I$ ) more neutral PDCB molecules than PDCB cations. To convert to a percentage we use  $x + (A/I)x = 100$  percent, where  $x$  is the percentage of cations present in the matrix. Comparing the prominent neutral and cationic bands mentioned previously, a 2 to 4 percent net conversion is estimated. Assuming that

experimental error is small compared with theoretical accuracy and that calculated intensities are correct within a factor of two (Reference 154), an upper limit of ~10 percent conversion is estimated.

### 3. para-Dimethoxybenzene

#### a. Experimental Results

Figure 49 shows the UV spectrum of neutral PDMOB (pulsed deposition, zero discharge potentials) in an Ar matrix at 12K. A strong band system commencing at about 300nm is observed. Figure 49 also shows the visible spectrum of the PDMOB radical cation produced in the discharge without  $\text{CCl}_4$  added; a vibrationally structured band system stretching from 460nm to 320nm is seen.

Figure 50 shows the infrared spectra of neutral PDMOB (bottom) and neutral plus radical cation (top), the latter obtained with the pulsed-glow discharge source and the hemispherical grid on. New bands appear in the pulsed-glow discharge scan. The addition of  $\text{CCl}_4$  to the argon (-3 percent) was found to enhance the intensities of the PDMOB cation IR bands substantially, and to give rise to a number of bands due (References 134,140,157-160) to various species emanating from the  $\text{CCl}_4$  seed; these are so marked in the figure. To determine which of the remaining bands are due to the PDMOB radical cation a correlation as a function of photolysis duration was sought between the peak intensity of the 460nm visible band and each of the IR peaks. If a true correlation exists, the intensity of the visible band and the intensity of the infrared band should increase (or decrease) in concert, and pass through the origin. A positive correlation was found for only four frequencies, viz., 1309, 1342, 1388, and  $1427\text{cm}^{-1}$  (all marked by blackened circles in Figure 50). No correlation was attempted for the shoulder at  $1304\text{cm}^{-1}$  since it is severely overlapped by the  $1309\text{cm}^{-1}$  band. Figure 51 shows a graph of the positive correlation of the 460 nm band and the above-mentioned IR bands. Six other bands

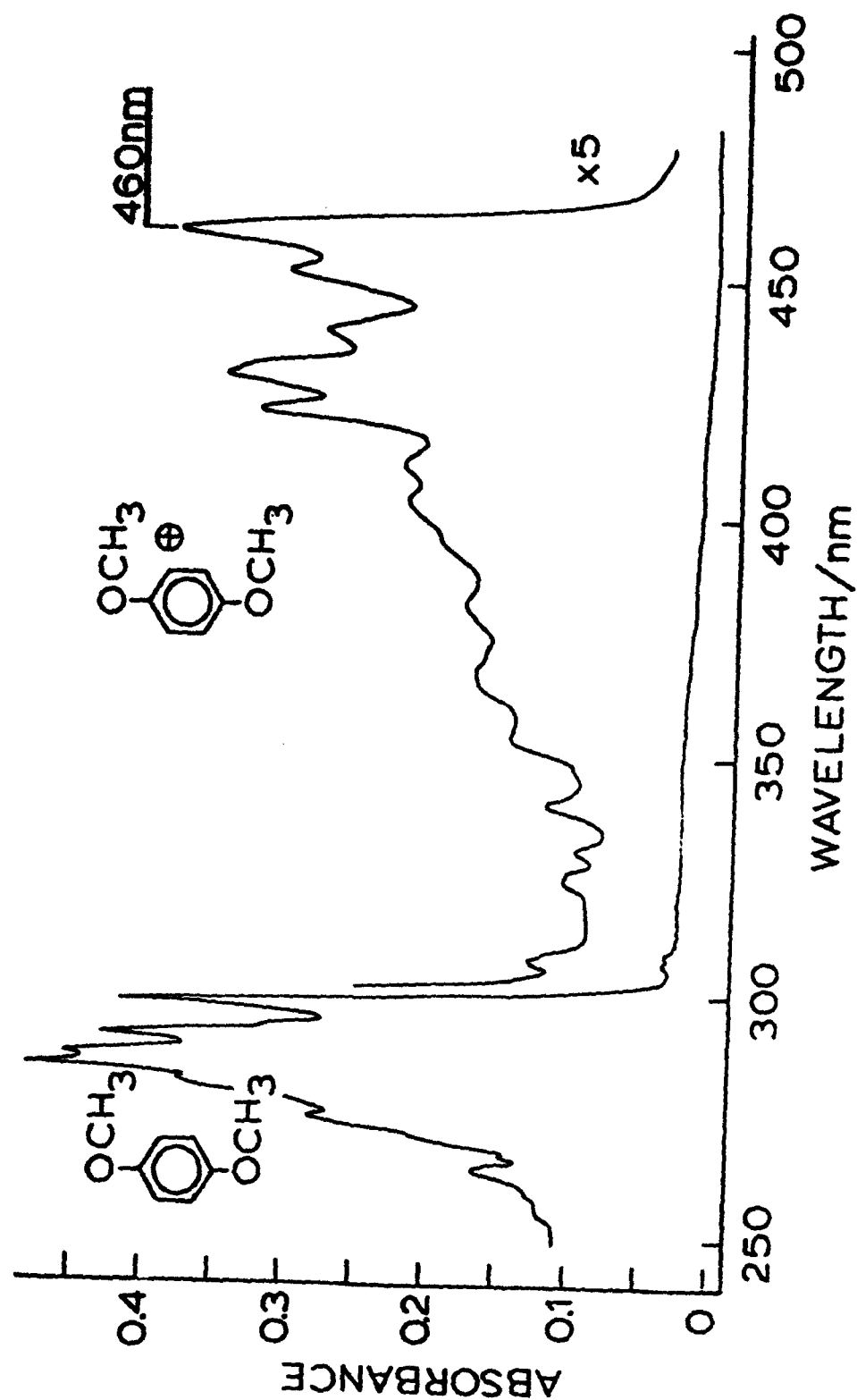


Figure 49. Visible/UV Spectra of PDMOB Neutral (< 300 nm) and Radical Cation (300 nm < 470 nm) in an Ar Matrix at 2 K

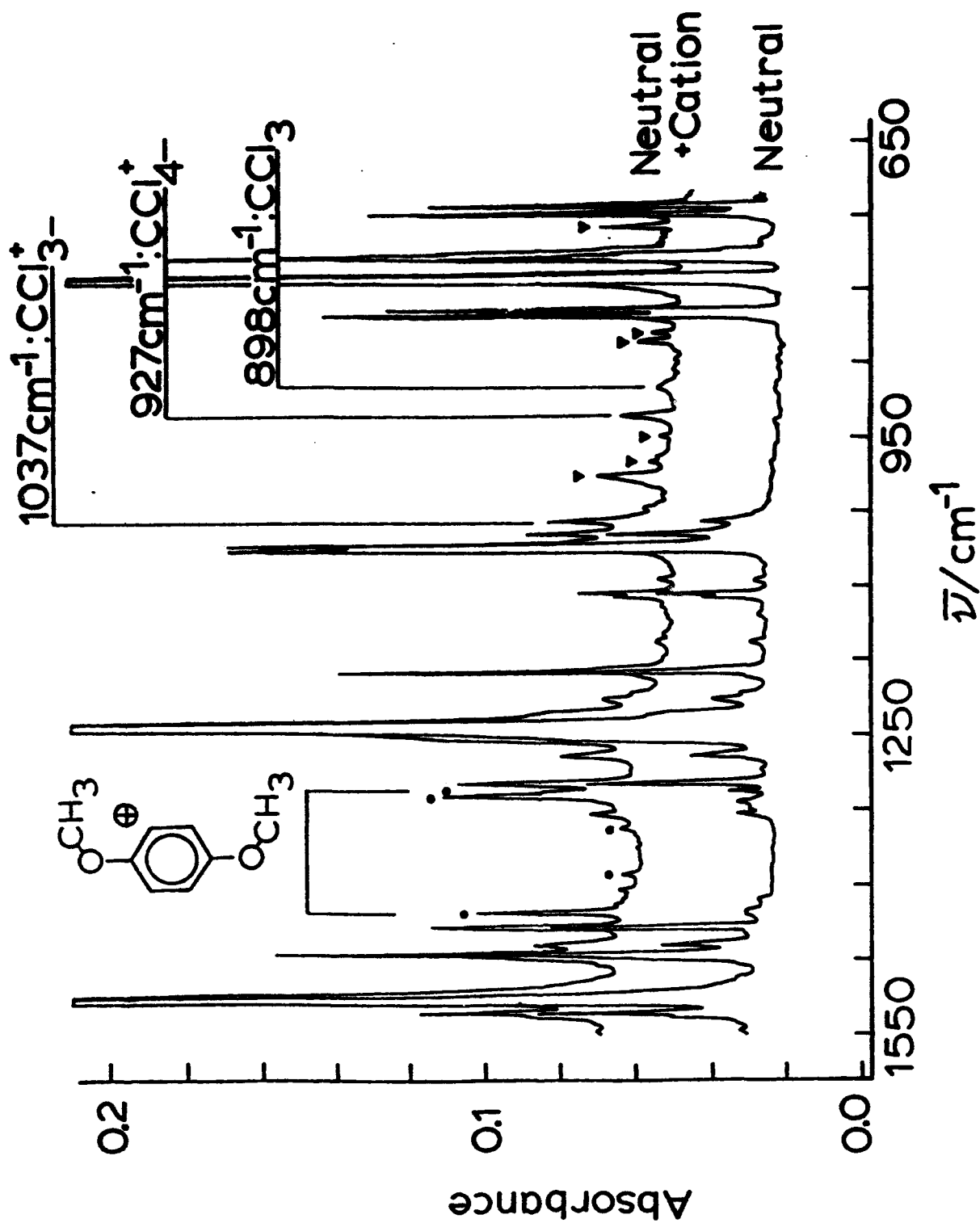


Figure 50. Infrared Spectra of Discharged PDMOB/ $\text{CCl}_4$ /Ar Mixture (top) Showing Neutral and Radical Cation (black circles) Bands and Neutral PDMOB Molecules in an Ar Matrix at 12 K.

at 737, 844, 852, 948, 974, and 987 $\text{cm}^{-1}$  (marked by black inverted triangles in Figure 50) do not correlate with the 460 nm band and remain unassigned. This points out an important aspect of this type of study: the appearance of new bands in the infrared cannot a priori be assumed to arise from the specific species under study. Some type of independent check is needed.

In Figure 52 shows spectra obtained before and after photolysis. This figure includes 1) the PDMOB radical cation with added  $\text{CCl}_4$  in Ar (cf. A and B) and 2) discharged  $\text{CCl}_4/\text{Ar}$  mixtures without PDMOB (cf. C and D). Spectrum A shows peaks commencing at 460 nm due to the PDMOB cation, plus a broad featureless band with a maximum at 375 nm. In spectrum B, obtained after twenty-five minutes photolysis of A, the broad maximum has been greatly reduced. In spectrum C, taken on a discharged Ar/ $\text{CCl}_4$  mixture before photolysis, a broad asymmetric band with maxima at 375 nm and 425 nm is observed. Upon photolysis for twenty-five minutes the 425 nm peak has diminished almost completely (cf. D). While it appears that the 375 nm component has been somewhat reduced, this is not certain since the two bands overlap substantially. Concomitantly with this behavior in the visible region, the infrared spectra taken on the same sample/matrix showed that the 927 $\text{cm}^{-1}$  band (previously assigned (Reference 157) to the  $\text{CCl}_4^+$  ion) disappears completely after twenty-five minutes photolysis, whereas the 1037 $\text{cm}^{-1}$   $\text{CCl}_3^+$  ion peak (References 158,159) remains unchanged. At the same time the neutral  $\text{CCl}_4$  peaks increase in intensity. Prolonged photolysis (up to 6 hrs) decreased the PDMOB cation IR and visible bands further without completely radiating them. From these observations we conclude that the 425 nm visible band is due to the  $\text{CCl}_4^+$  ion. This is in agreement with results previously reported by Andrews et al. (Reference 161). Furthermore, it seems clear that photolysis serves to release electrons from traps in the matrix which then

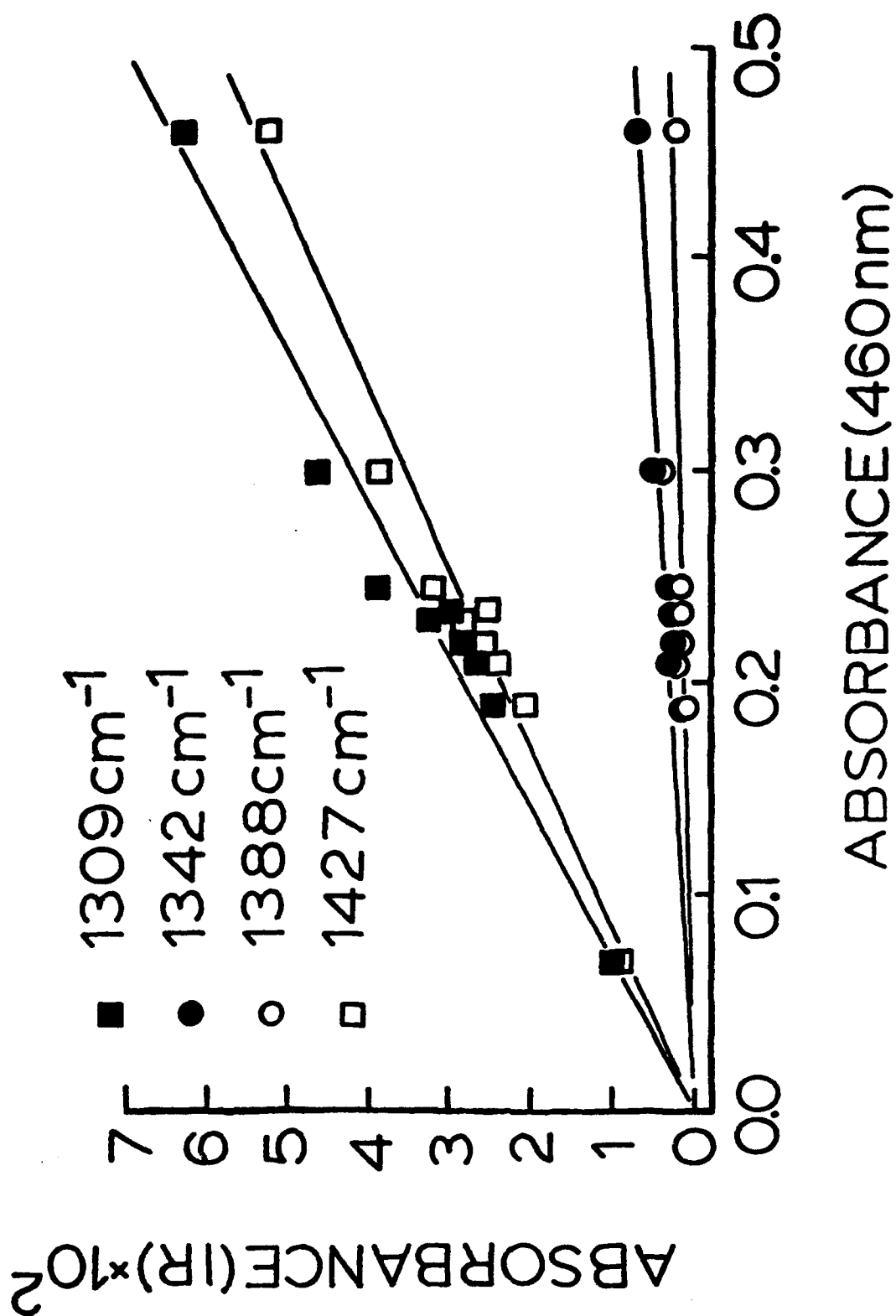
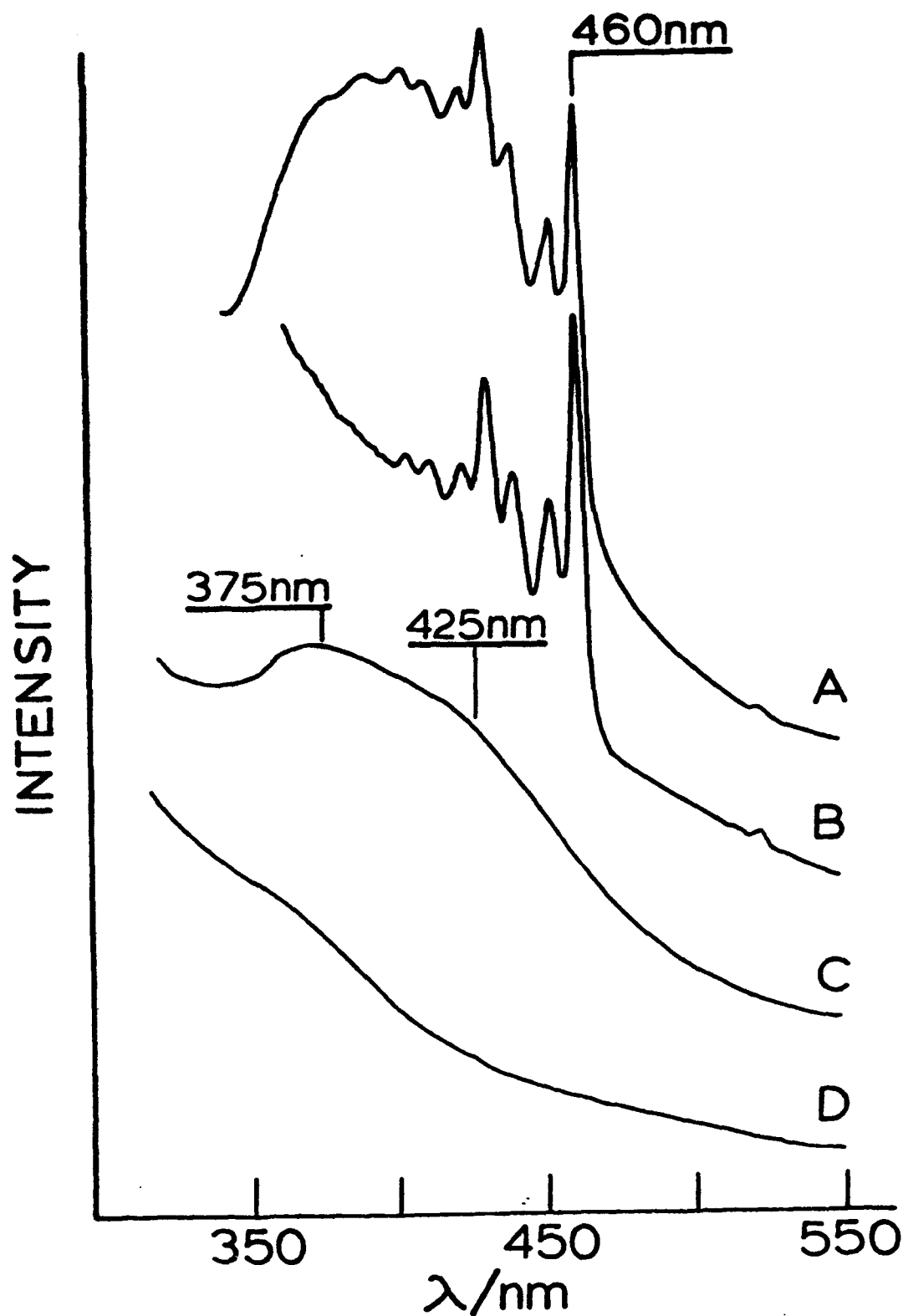


Figure 51. Correlation Diagram between 460 nm Visible Band and Four IR Peaks (Varying Absorbances Produced by Different Photolysis 7 Times)



**Figure 52.** Visible/UV Spectra of: A) Unphotolyzed PDMOB Radical Cation Formed From Discharged PDMOB/ $\text{CCl}_4$ /Ar Mixture; B) Spectrum A After 25 min. Photolysis; C) Discharged  $\text{CCl}_4$ /Ar Mixture Before Photolysis; D) Spectrum C After 25 min. Photolysis.

preferentially seek out and neutralize the  $\text{CCl}_4^+$  species over the  $\text{CCl}_3^+$  and  $\text{PDMOB}^+$  species.

#### b. Theoretical Results

An *ab initio* Hartree-fock SCF level calculation (6-31 G\* basis set) of the vibrational spectra of neutral p-dimethoxybenzene (PDMOB) and its radical cation was performed (Reference 51). First, however, the geometries (Figure 21) for the neutral and cation species were optimized using the GAMESS program (References 151,152); the relevant bond distances found are presented in Table 16. (Note that C-H bonds and their stretching frequencies were not considered.). From the optimized geometries it can be seen that certain bonds are lengthened while others are shortened upon ionization. A lengthening of the C-C and  $\text{C}_{\text{methyl}}\text{-O}$  bonds indicates that the electron is removed from a molecular orbital (MO) which is bonding with respect to these bonds, while a shortening of the  $\text{C}_{\text{ring}}\text{-O}$  and central C-C bonds indicates the anti-bonding character of the MO with respect to these bonds. This result is mimicked by the force constants and vibrational frequencies when the normal modes are decomposed into the intrinsic vibrational modes (vide infra).

Calculated infrared frequencies and relative intensities for neutral PDMOB are presented in Table 17. The experimental frequencies and qualitative band intensities are also given in the table. The agreement is quite good. The bands observed to be the strongest at  $1511\text{ cm}^{-1}$  and  $1240\text{ cm}^{-1}$  are predicted at  $1701\text{ cm}^{-1}$  and  $1396\text{ cm}^{-1}$  (unscaled). When scaled by a factor of 0.9 (acknowledged to be appropriate for Hartree Fock-level calculations) these bands fall close to the observed ones ( $1531\text{ cm}^{-1}$  and  $1257\text{ cm}^{-1}$ ); a scaling factor of 0.888 ensures an exact match. The remaining bands also are well-positioned by theory. This agreement lends confidence that the basis set and calculational approach are sufficiently good to expect reasonable agreement for the cationic species.

**TABLE 16 OPTIMIZED THEORETICAL BOND DISTANCES FOR NEUTRAL AND CATIONIC PDMOB.**

Bond	Distance/Å	
	Neutral	Cation
C-C	1.39	1.42
C <sub>methyl</sub> -O	1.43	1.46
C <sub>ring</sub> -O	1.38	1.31
C-C <sup>a</sup>	1.39	1.36

<sup>a</sup>The central C-C bonds.

**TABLE 17 THEORETICAL AND EXPERIMENTAL IR FREQUENCIES AND INTENSITIES FOR NEUTRAL PDMOB**

<u>Theoretical</u>			<u>Experimental<sup>b</sup></u>	
Frequency/cm <sup>-1</sup>	Relative Intensity <sup>a</sup>		Frequency/cm <sup>-1</sup>	Intensity
Calc. Scaled (0.9)				
1701	1531	56	1511	strong
1669	1504	19	1467	medium
1660	1494	4	1440	weak
1628	1466	6	1300	weak
1396	1257	100	1240	strong
1348	1213	20	1183	medium
1292	1164	3		
1235	1111	4	1060	medium
1150	1037	36	1031	medium
976	878	31	823	medium
752	676	13		

<sup>a</sup>Relative to calculated 1396 cm<sup>-1</sup> band.

<sup>b</sup>Isolated in Ar at 12K; present work.

Calculated and experimental frequencies and relative intensities for the PDMOB cation are presented in Table 18. Also included in the table are the experimental values obtained from studies using a clay substrate. Bands calculated at  $1518\text{ cm}^{-1}$  and  $1310\text{ cm}^{-1}$  are predicted to be the most intense. The strong band observed at  $1502\text{ cm}^{-1}$  in the clay correlates well with the  $1518\text{ cm}^{-1}$  prediction, while the  $1309(1304)\text{ cm}^{-1}$  matrix and  $1308(1302)\text{ cm}^{-1}$  clay bands correlate very well with the  $1310\text{ cm}^{-1}$  predicted band. The matrix analog to the  $1502\text{ cm}^{-1}$  band is not observed because of overlapping from neutral PDMOB's bands. The observed  $1427\text{ cm}^{-1}$  band matches well with the  $1451\text{ cm}^{-1}$  predicted one. The  $1342$  and  $1388\text{ cm}^{-1}$  cation bands have, however, no counterpart among the calculated bands, although the former is observed in the clay sample. The determination of shifts in vibrational frequencies between neutral and cationic species is difficult to ascertain. Because of the difference in internal coordinate composition of the normal modes for the two species. However, Boatz and Gordon (Reference 156) have reported a method which allows one to handle this difference and determine what they call "intrinsic" frequencies, i.e., frequencies localized in certain bonds or bond groupings. The results of this analysis applied to PDMOB are reported in Table 19. It is found that those bonds which elongate upon ionization show an increase in their respective frequencies and force constants while the opposite is found for those which contract. This behavior parallels perfectly what one expects qualitatively from a consideration of electron removal from the HOMO. Those bonds having bonding character in the HOMO are expected to decrease in frequency upon ionization while those having anti bonding character are expected to increase. Ionization of PDMOB, i.e. removal of an electron from the highest-lying pi molecular orbital, has a significant effect on the vibrational spectrum. This is perhaps somewhat surprising since the pi orbital is out-of-plane and therefore might be expected to influence vibrations involving only the C-C bonds. The changes in the intrinsic frequencies indicate that

**TABLE 18 THEORETICAL AND EXPERIMENTAL IR FREQUENCIES AND INTENSITIES FOR RADICAL CATION PDMOB**

Theoretical			Experimental		
Frequency/cm <sup>-1</sup>		Relative Intensity <sup>a</sup>	Frequency/cm <sup>-1</sup>		Intensity
Calc.	Scaled (0.9)		Matrix <sup>b</sup>	Clay <sup>c</sup>	
1689	1518	100	---	1550	medium
1653	1488	5	---	1502	strong
1640	1476	13	---	---	
1612	1451	26	---	1438	
			1427	1427	medium
			1388	---	
			1342	1342	
1456	1310	97	1309	1308	medium
			1304	1302	medium
1407	1265	9	---	1238	
1243	1119	1			
1087	978	27			
1051	947	17			
987	888	20			

<sup>a</sup>Relative to calculated 1689cm<sup>-1</sup> band intensity

<sup>b</sup>In Ar matrix at 12K; present work.

<sup>c</sup>Johnston and coworkers, Reference 34

**TABLE 19 CALCULATED INTRINSIC STRETCHING FREQUENCIES  
AND FORCE CONSTANTS FOR NEUTRAL PDMOB AND  
RADICAL CATION OF PDMOB (IN PARENTHESES)**

Bond	Frequency/cm <sup>-1</sup>		Force Constant	
	Calc.	Scaled (0.9)	Calc.	Scaled (0.9)
C-C	1355(1220)	1220(1098)	6.45(5.27)	5.80(4.74)
C <sub>methyl</sub> -O	1094(966)	985(869)	4.84(3.77)	4.84(3.77)
C <sub>ring</sub> -O	1194(1398)	1075(1258)	5.76(7.89)	5.13(7.10)
C-C*	1386(1522)	1247(1370)	6.81(8.19)	6.13(7.37)

\*The central C-C bonds.

<sup>b</sup>Units: mdynes/Å

stretching motions of the methoxy group are also affected by ionization. Conjugation beyond the phenyl ring is presumably the cause of this.

### **c. Discussion**

The pulsed-glow discharge/matrix isolation method has made it possible to produce and trap the PDMOB radical cation in Ar matrices in concentrations sufficient to observe (a portion of) its infrared spectrum. New IR bands due to the PDMOB cation were found at 1309, 1342, 1388, and 1427 $\text{cm}^{-1}$  and probably 1304  $\text{cm}^{-1}$ . These bands were shown to be correlated to the 460 nm visible absorption band previously assigned to this cation (References 103,138,162). This is an essential point in experiments of this type. Some means must be used by which the IR bands can be correlated with another physical measurement specific to the cation under study. Here we utilized photolysis degradation and monitored the visible absorption band at 460 nm as well as the IR bands. This approach has been applied to small carbon clusters generated by varying the conditions of laser ablation of graphite and monitoring their known IR bands and the to-be-assigned visible/UV bands (Reference 135).

The addition of  $\text{CCl}_4$  to the argon gas in the plasma was found to significantly enhance the number of radical cations trapped. It was initially assumed that this additive would act as an electron trap in the matrix, allowing a greater concentration of positive ions to be stabilized. However, the presence of several positive carbon tetrachloride product ions in the matrix led us to revise this idea. While the exact mechanism of operation is not yet fully understood, one or more of the following vapor phase ionization mechanisms must be operative: photoionization by the Ar plasma (Ar resonance lines at 11.83 eV and 11.67 eV lie above the 7.9 eV ionization potential of PDMOB.), electron impact, charge transfer from the aromatic to the discharge-formed  $\text{CCl}_4$  ionic product and Penning ionization of the aromatic by excited metastable Ar. Further effort will be required to establish which one(s) of

these (or other) effects play the predominant role(s). The short pulse plasma "soup" is a complex mixture as evidenced by the  $\text{CCl}_4$  ionic products and PDMOB cations formed plus the species formed which give rise to the unidentified IR bands. In the present approach, this complex mixture does not present any large disadvantages. The visible spectrum of the cation can easily be generated without added  $\text{CCl}_4$ , and the suspected aromatic cation IR bands can be correlated with any known visible bands. The major disadvantage of the present approach is the presence in the matrix of sufficient quantities of neutral PDMOB which obscure regions of the IR of the cation due to band overlap. Attempts are underway in our lab to circumvent this problem using a quadrupole ion deflector.

In addition to the above vapor-phase processes, attention should be drawn to a matrix-phase photoionization which occurs. The ratio of the intensities of the cation and neutral PDMOB band (visible and IR) increases slightly with deposition time. We believe the Ar resonance radiation from the pulsed plasma impinging on the matrix is probably responsible for this effect.

It would be informative to know the relative percentage of PDMOB molecules which exist as cations. This is difficult experimentally since extinction coefficients of neither the optical nor the infrared absorption bands are known. However, using ab initio SCF-level theoretical intensities and comparing experimental and theoretical intensities for neutral PDMOB with similar quantities for the cation we estimated (Reference 51) that 5-10 percent of the PDMOB present exists in the cation form in the matrix.

Finally, a comparison of our IR results with those obtained by Johnston and co-workers for the PDMOB cation in Cu-exchanged montmorillonite clay is instructive. Bands ascribed to the PDMOB cation in Cu-exchanged montmorillonite clay were found (Reference 34) at 1502, 1238, 1302, 1308, 1342, 1427, 1438, and 1550 $\text{cm}^{-1}$ . The growth of these bands in the clay appears simultaneously with a color change

from pale blue to dark green and the growth of three intense bands in the visible at 400 nm, 451 nm and 464 nm. Upon exposure to water vapor, the visible bands and all the IR bands with the exception of  $1502\text{ cm}^{-1}$  and  $1238\text{ cm}^{-1}$  disappear rapidly (in minutes). The latter two decayed in hours. This rate difference was interpreted (Reference 34) as a difference in the surface sites at which the PDMOB cations are positioned. The disappearance of the PDMOB radical cation is now known to be the result of a reversible one-electron transfer process between the hydrated  $\text{Cu}^{2+}$  ion and adsorbed aromatic. There is a good correspondence between the argon matrix bands at  $1304$ ,  $1309$ ,  $1342$ , and  $1427\text{ cm}^{-1}$  and the clay bands at  $1302$ ,  $1308$ ,  $1343$ , and  $1427\text{ cm}^{-1}$ . The  $1388\text{ cm}^{-1}$  matrix band and the  $1438\text{ cm}^{-1}$  and  $1550\text{ cm}^{-1}$  clay bands do not correspond well, however. Nevertheless, the close correspondence of four bands leads to the conclusion that one of the sites in the clay is minimally perturbed. This is consistent with Johnston's conclusion that the PDMOB radical cation is the predominant surface species of PDMOB chemisorbed on the Cu-montmorillonite clay.

## SECTION VI

### CONCLUSION

These studies have shown that water influences the sorption of organic solutes on mineral surfaces. In fact, water can compete for surface sites more effectively than the organic sorbents studied here. This is due to hydration of the exchangeable metal cations on the surface, thus, rendering the surface with an increased hydrophylic character. Upon removal of water from the system, chemisorption reactions of unsaturated organic sorbents may occur provided that Fe- or Cu- cations are present. The role of the cation is to accept an electron from the coordinated organic solute species forming a radical organic cation on the surface. Although  $\text{Cu}^{2+}$  cations are only present in trace amounts in soil and subsurface environments,  $\text{Fe}^{3+}$  is ubiquitous. Thus, the potential for chemisorption reactions in soil and subsurface environments will depend on the type of mineral surfaces present, amount of free  $\text{Fe}^{3+}$  available, and the water content.

## SECTION VII

### RECOMMENDATIONS

This research has provided molecular-level insight into a potentially significant means of attenuating the toxicity and concentration several organic compounds. The extent of SET reactions that could occur on natural sorbents would depend on the mineralogy, nature of exchangeable cations, and on the water content. The results obtained in this study have identified the diagnostic bands of the organic solutes and have shown how water influences the SET reactions. The data obtained in this research effort could be extended to include a broader class of Air Force related organic compounds and natural sorbents. One hypothesis that would be especially useful to test would be the ability of free  $\text{Fe}^{3+}$  to promote SET reactions. It is not clear how naturally occurring humic substances would effect SET reactions. One possibility is that the hydrophobic organic solutes would partition into the humic substances and would not be able to participate with mineral surfaces of interest. Finally, all of the chemisorption reactions required removal of water. It is not clear if the low water contents required to facilitate these reactions could be obtained in field conditions.

## SECTION VIII

### REFERENCES

1. Sposito, G. "Distinguishing adsorption from surface precipitation," In *Chemical processes at mineral surfaces*, Eds. J.A. Davis and K.F. Hayes. (American Chemical Society, 1986), pp. 217-228.
2. Johnston, C.T. and G. Sposito. "Disorder and early sorrow: progress in the chemical speciation of soil surfaces," In *Future developments in soil science research*, Ed. L.L. Boersma. (Madison, Wisconsin, USA: Soil Science Society of America, 1987), pp. 89-100.
3. Brown, G.E. "Spectroscopic studies of chemisorption reaction mechanisms at oxide-water interfaces," In *Mineral-water interface geochemistry*, Eds. M.F. Hochella and A.F. White. (Washington, D.C.: Mineralogical Society of America, 1990), pp. 309-363.
4. Hair, M.L. "Transmission infrared spectroscopy for high surface area oxides," In *Vibrational spectroscopies for adsorbed species*, Eds. A.T. Bell and M.L. Hair. (Washington D.C.: ACS Symposium Series No. 137, 1980), pp. 1-11.
5. Bell, A.T. "Applications of Fourier transform infrared spectroscopy to studies of adsorbed species," In *Vibrational spectroscopies for adsorbed species*, Eds. A.T. Bell and M.L. Hair. (Washington, D.C.: American Chemical Society Symposium Series 137, 1980), pp. 13-35.
6. Bell, A.T. "Infrared spectroscopy of high-area catalytic surfaces," In *Vibrational spectroscopy of molecules on surfaces*, Eds. J.T. Yates and T.E. Madey. (New York: Plenum Press, 1987), pp. 105-134.
7. Griffiths, P.R. and J.A. deHaseth. *Fourier transform infrared spectrometry*, (New York: John Wiley & Sons, 1986) pp. 1-656.
8. Buswell, A.M., K. Krebs and W.H. Rodebush. "Infrared studies. III. Absorption bands of hydrogels between 2.5 and 3.5 micrometers," *J. Am. Chem. Soc.* 59:2603-2605 (1937).
9. Little, L.H., A.V. Kiselev and V.I. Lygin. *Infrared spectra of adsorbed species*, (London: Academic Press, 1966) pp. 1-428.
10. Hair, M.L. *Infrared spectroscopy in surface chemistry*, (New York: Dekker, 1967).

11. White, J.L. "Proton migration in kaolinite," *9th Intl. Congr. of Soil Sci. Trans.* 701-707 (1968).
12. Delgass, W.N., G.L. Haller, R. Kellerman and J.H. Lunsford. *Spectroscopy in Heterogeneous Catalysis*, New York: Academic Press, 1988) pp. 1-341.
13. Nguyen, T.T., L.J. Janik and M. Raupach. "Diffuse reflectance infrared Fourier transform (DRIFT) spectroscopy in soil studies," *Aust. J. Soil Res.* 29:49-67 (1991).
14. McBride, M.B. and L.G. Wesselink. "Chemisorption of catechol on gibbsite, boehmite, and noncrystalline alumina surfaces," *Environ. Sci. Technol.* 22:703-708 (1988).
15. McBride, M.B. "Adsorption and oxidation of phenolic compounds by iron and manganese oxides," *Soil Sci. Soc. Am. J.* 51:1466-1472 (1987).
16. Hamadeh, I.M., D. King and P.R. Griffiths. "Heatable - evacuable cell and optical system for diffuse reflectance FT-IR spectrometry of adsorbed species," *J. Catal.* 88:264-272 (1984).
17. Culler, S.R., M.T. McKenzie, L.J. Fina, H. Ishida and J.L. Koenig. "Fourier transform diffuse reflectance infrared study of polymer films and coatings: A method for studying polymer surfaces," *Appl. Spectrosc.* 38:791-795 (1984).
18. Fuller, M.P. and P.R. Griffiths. "Diffuse reflectance measurements by infrared Fourier transform spectrometry," *Anal. Chem.* 50:1906-1910 (1978).
19. Bell, A.T. "Infrared spectroscopy of high-area catalytic surfaces," In *Vibrational spectroscopy of molecules on surfaces*, Eds. J.T. Yates and T.E. Madey. (New York: Plenum Press, 1987), pp. 105-134.
20. Bowen, J.M., S.V. Compton and M.S. Blance. "Comparison of sample-preparation methods for the Fourier-transform-infrared analysis of organo-clay mineralsorption mechanism," *Anal. Chem.* 61:2047-2050 (1989).
21. Baes, A.U. and P.R. Bloom. "Diffuse reflectance and transmission Fourier transform infrared (DRIFT) spectroscopy of humic and fulvic acids," *Soil Sci. Soc. Am. J.* 53:695-700 (1989).
22. Vidrine, D.W. "Photoacoustic Fourier transform infrared spectroscopy of solids and liquids," *Four. Trans. Inf. Spec.* 3:125-148 (1982).
23. Rockley, M.G. "Fourier Transform infrared spectroscopy using a photo acoustic detector," *FTS/IR Notes* 32 (1980).

24. Royce, B.S.H., S. McGovern and J.B. Benziger. "Analytical photoacoustic spectroscopy of catalysts," *Amer. Labor.* (1985).
25. Street, K.W., H.B. Mark, S. Vasireddy, R.A.L. Filio, C.W. Anderson, M.P. Fuller and S.J. Simon. "Cadmium(II) exchanged zeolite as a solid sorbent for the preconcentration and determination of atmospheric hydrogen sulfide II: Spectroscopic techniques," *Appl. Spectrosc.* 39:68-72 (1985).
26. Yang, C.Q. and W.G. Fateley. "The effect of particle size on peak intensities of FTIR photoacoustic spectra," *J. Mol. Struct.* 141:279-284 (1986).
27. Yang, C.Q. and W.G. Fateley. "The effect of particle size on Fourier transform infrared photoacoustic spectra," *J. Mol. Struct.* 146:25-39 (1986).
28. Rockley, M.G., D.M. Davis and H.H. Richardson. "Quantitative analysis of a binary mixture by Fourier transform infrared photoacoustic spectroscopy," *Appl. Spectrosc.* 35:185-186 (1981).
29. Donini, J.C. and K.H. Michaelian. "Low-frequency photoacoustic spectroscopy of solids," *Appl. Spectrosc.* 42:289-292 (1988).
30. Sperline, R.P., S. Muralidharan and H. Freiser. "In situ determination of species adsorbed at a solid-liquid interface by quantitative infrared attenuated total reflectance spectrophotometry," *Langmuir* 3:198-202 (1987).
31. Anderson, M.A. *A study of the physical-chemical mechanisms and variables which affect the transport of inorganic and organic microcontaminants in heterogeneous systems*, (1986) (UnPub)
32. Yost, E.C., M.I. Tejedor and M.A. Anderson. "In-situ CIR-FTIR characterization of salicylate complexes at the goethite/aqueous solution interface," *Environ. Sci. Technol.* 24:822-828 (1990).
33. Iskra, J. and M. Kielkowska. "Application of ATR technique to flourite-oleate-quebracho systems," *Institution of Mining and Metallurgy* c87-c90 (1980).
34. Johnston, C.T., T. Tipton, D.A. Stone, C. Erickson and S.L. Trabue. "Chemisorption of p-dimethoxybenzene on Cu-montmorillonite," *Langmuir* 7:289-296 (1991).
35. Sposito, G. and R. Prost. "Structure of water adsorbed on smectites," *Chem. Rev.* 82:553-573 (1982).
36. Giese, R.F. "Interlayer bonding in kaolinite, dickite, nacrite," *Clays and Clay Min.* 21:145-149 (1973).

37. Hartman, P. "Calculation of electrostatic interlayer bonding energy and lattice energy of polar phyllosilicates: kaolinite and chlorite," *Clays and Clay Min.* 31:218-222 (1983).
38. Hipps, K.W., E.A. Dunkle and U. Mazur. "Reactive adsorption of alpha,alpha-diphenyl-beta-picrylhydrazyl on alumina as studied by inelastic-electron-tunneling, FT-IR, and EPR spectroscopy," *Langmuir* 2:528-532 (1986).
39. Johnston, C.T. "Fourier transform infrared and Raman spectroscopy," In *Instrumental surface analysis of geologic materials*, Ed. D.L. Perry. (New York: VCH, 1990), pp. 121-155.
40. Russell, J.D. and V.C. Farmer. "Infra-red spectroscopic study of the dehydration of montmorillonite and saponite," *Clay Min. Bull.* 5:443-464 (1964).
41. Poinسیون, C., J.M. Cases and J.J. Fripiat. "Electrical-polarization of water molecules adsorbed by smectites. An infrared study," *J. Phys. Chem.* 82:1855-1860 (1978).
42. Zhang, Z.Z., P.F. Low, "Relation between the heat-of-immersion and the initial water-content of Li, Na, K montmorillonite," *J. Colloid Sci.* 133:461-472 (1989).
43. Pinnavia, T.J. and M.M. Mortland. "Interlamellar metal complexes on layer silicates. I. Copper(II) arene complexes on montmorillonite," *J. Phys. Chem.* 75:3957-3962 (1971).
44. Pinnavia, T.J., P.L. Hall, S.S. Cady and M.M. Mortland. "Aromatic radical cation formation on the intracrystal surfaces of transition-metal layer lattice silicates," *J. Phys. Chem.* 78:994-999 (1974).
45. Rupert, J.P. "Electron-spin-resonance spectra of interlamellar copper(II) - arene complexes on montmorillonite," *J. Phys. Chem.* 77:784-790 (1973).

46. Soma, Y. and M. Soma. "Raman spectroscopic evidence of formation of p-dimethoxybenzene cation on Cu- and Ru-montmorillonite," *Chem. Phys. Lett.* 94:475-478 (1983).
47. Mortland, M.M. "Clay-organic complexes and interactions," *Adv. Agron.* 22:75-117 (1970).
48. Voudrias, E.A. and M. Reinhard. "Abiotic organic reactions at mineral surfaces," In *Geochemical processes at mineral surfaces. ACS Symposium Series Vol 323*, Eds. J. Davis and K.F. Hayes. (Washington, D.C.: American Chemical Society, 1986), pp. 462-486.
49. Mortland, M.M. and S.A. Boyd. "Polymerization and dechlorination of chloroethenes on Cu(II)-smectite via radical-cation intermediates," *Environ. Sci. Technol.* 23:223-227 (1989).
50. Mortland, M.M. and K.V. Raman. "Surface acidities of smectites in relation to hydration, exchangeable-cation and structure," *Clays and Clay Min.* 16:393-398 (1968).
51. McBride, M.B. "Hydrolysis and dehydration reactions of exchangeable  $\text{Cu}^{++}$  on hectorite," *Clays and Clay Min.* 30(3):200-206 (1982).
52. Laszlo, P. "Catalysis of organic reactions by inorganic solids," *Acc. Chem. Res.* 19:121-127 (1986).
53. Grandjean, J. and P. Laszlo. "Multinuclear and pulsed gradient magnetic resonance studies of Na cations and of water reorientation at the interface of a clay," *J. Mag. Res.* 83:128-137 (1989).
54. Delville, A., J. Grandjean and P. Laszlo. "Order acquisition by clay platelets in a magnetic field. NMR study of the structure and microdynamics of the adsorbed water layer," *J. Phys. Chem.* 95:1383-1392 (1991).
55. Mooney, R.W., A.G. Keenan and L.A. Wood. "Adsorption of water vapor by montmorillonite. I. Heat of desorption and application of BET theory," *J. Am. Chem. Soc.* 74:1367-1374 (1952).
56. Mooney, R.W., A.G. Keenan and L.A. Wood. "Adsorption of water vapor by montmorillonite. II. Effect of exchangeable ions and lattice swelling as measured by X-ray diffraction," *J. Am. Chem. Soc.* 74:1371-1374 (1952).

57. Clementz, D.M., T.J. Pinnavaia and M.M. Mortland. "Stereochemistry of hydrated copper(II) ions on the interlamellar surfaces of layer silicates. An electron spin resonance study," *J. Phys. Chem.* 77:196-200 (1973).
58. Clementz, D.M., M.M. Mortland and T.J. Pinnavaia. "Properties of reduced charge montmorillonites: Hydrated Cu(II) ions as a spectroscopic probe," *Clays and Clay Min.* 22:49-57 (1974).
59. McBride, M.B. and M.M. Mortland. "Copper (II) interactions with Montmorillonite: evidence from physical methods," *Soil Sci. Soc. Am. Proc.* 38:408-415 (1974).
60. McBride, Murray B., T.J. Pinnavaia and M.M. Mortland. "Electron Spin Resonance Studies of Cation Orientation in Restricted Water Layers on Phyllosilicate (Smectite) Surfaces," *J Phys Chem* 79:2430-2435 (1975).
61. Prost, R. "Interactions between adsorbed water molecules and the structure of clay minerals: Hydration mechanism of smectites," *Proc. Int. Clay Conf.* 351-359 (1975).
62. Sposito, G., R. Prost and J.P. Gaultier. "Infrared spectroscopic study of adsorbed water on reduced-charge Na/Li montmorillonites," *Clays and Clay Min.* 31:9-16 (1983).
63. Bidadi, H., P.A. Schroeder and Thomas J. Pinnavaia. "Dielectric Properties of Montmorillonite Clay Films: Effects of Water and Layer Charge Reduction," *J Phys Chem Solids* 49:1435-1440 (1988).
64. Kogelbauer, A., J.A. Lercher, K.H. Steinberg, F. Roessner, A. Soellner and R.V. Dmitriev. "Type, stability, and acidity of hydroxyl groups of HNaK-erionites," *Zeolites* 9:224-230 (1989).
65. Fripiat, J.J., A. Jelli, G. Poncelet and J. Andre. "Thermodynamic properties of adsorbed water molecules and electrical conduction in montmorillonites and silicas," *J. Phys. Chem.* 69:2185-2197 (1965).
66. Van Olphen, H. and J.J. Fripiat. *Data handbook for clay materials and other non-metallic minerals*, (Oxford: Pergamon Press, 1979) pp. 1-346.
67. Rhue, R.D., K.D. Pennell, P.S.C. Rao and W.H. Reve. "Competitive adsorption of alkylbenzene and water vapor on predominantly mineral surfaces," *Chemosphere* 18:1971-1986 (1989).
68. Rhue, R.D., P.S.C. Rao and R.E. Smith. "Vapor-phase adsorption of alkylbenzenes and water on soils and clay," *Chemosphere* 17:727-741 (1988).

69. Rao, P.S.C., R.A. Ogwada and R.D. Rhue. "Adsorption of volatile organic compounds on anhydrous and hydrated sorbents: Equilibrium adsorption and energetics," *Chemosphere* 18:2177-2191 (1989).
70. Chiou, C.T., D.E. Kile and R.L. Malcom. "Sorption of vapors of some organic liquids on soil humic acid and its relation to partitioning of organic compounds in soil organic matter," *Environ. Sci. Technol.* 22:298-303 (1991).
71. Chiou, C.T. and T.D. Shoup. "Soil sorption of organic-vapors and effects of humidity on sorptive mechanism and capacity," *Environ. Sci. Technol.* 19:1196-1200 (1985).
72. Keenan, A.G., R.W. Mooney and L.A. Wood. "The relation between exchangeable ions and water adsorption on kaolinite," *J. Phys. Coll. Chem.* 55:1462-1474 (1951).
73. Prost, R. "Etude de l'hydratation des argiles: Interactions eau-mineral et mecanisme de la retention de l'eau," *Ann. Agron.* 26:401-461 (1975).
74. Voudrais E.A. and M. Reinhard, "Abiotic organic reactions at mineral surfaces," *ACA Symposium Series* 323:462-486 (1986).
75. Doner, H.E. and M.M. Mortland. "Intermolecular interaction in montmorillonite: NH-CO systems," *Clays and Clay Min.* 17:265-270 (1969).
76. Cloos, P., D. Vande Poel and J.P. Camerlynck. "Thiophene complexes on montmorillonite saturated with different cations." *Nature* 243:54-55 (1973).
77. Fenn, D.B., M.M. Mortland and T.J. Pinnavaia. "The chemisorption of anisole on Cu(II)-hectorite," *Clays and Clay Min.* 21:315-322 (1973).
78. Soma, Y., M. Soma and I. Harada. "Resonance Raman spectra of benzene adsorbed on Cu-montmorillonite. Formation of poly(p-phenylene) cations in the interlayer of the clay mineral," *Chem. Phys. Lett.* 99:153-156 (1983).
79. Soma, Y., M. Soma and I. Harada. "Reactions of aromatic molecules in the interlayer of transition-metal ion-exchanged montmorillonite studied by resonance Raman spectroscopy. 2. monosubstituted benzenes and 4,4'-disubstituted biphenyls," *J. Phys. Chem.* 89:738-742 (1985).
80. Eastman, M.P., D.E. Patterson and K.H. Pannell. "Reaction of benzene with Cu(II)- and Fe(III)-exchanged hectorites," *Clays and Clay Min.* 32:327-333 (1984).
81. Boyd, S.A. and M.M. Mortland. "Dioxin radical formation and polymerization on Cu(II)-smectite," *Nature* 316:532-535 (1985).

82. Govindaraj, N., M.M. Mortland and S.A. Boyd. "Single-electron-transfer mechanism of oxidative dechlorination of 4-chloroanisole on copper(II)-smectite," *Environ. Sci. Technol.* 21:1119-1123 (1987).
83. Mortland, M.M. "Soil surface chemistry: History and preview," *Future Development in Soil Science Research.* 75-88 (1987).
84. Sayed, M.B. and R.P. Cooney. "Raman spectra of benzene adsorbed at the aqueous / silica and vapor / silica interfaces," *J. Colloid Interface Sci.* 91:552-559 (1983).
85. Lau, C.L. and R.G. Snyder. "A valence force field for alkyl benzenes toluene, p-xylene, m-xylene, mesitylene, and some of their deuterated analogues," *Spectrochim. Acta, Part A* 27A:2073-2088 (1971).
86. Zielke, R.C., T.J. Pinnavaia and M.M. Mortland. "Adsorption and reactions of selected organic-molecules on clay mineral surfaces," In *Reactions and movement of organic chemicals in soils. SSSA Special Publication Number 22*, Eds. B.L. Sawhney and K. Brown. (Madison, WI: Soil Sci. Soc. Amer., 1989), pp. 81-98.
87. Sawhney, B.L. "Vapor-phase sorption and polymerization of phenols by smectite in air and nitrogen," *Clays and Clay Min.* 33(2):123-127 (1985).
88. Yamagishi, A. "Optical resolution and asymmetric syntheses by use of adsorption on clay minerals," *J. Coord. Chem.* 16:132-211 (1987).
89. Doner, H.E. and M.M. Mortland. "Benzene complexes with copper(II) montmorillonite," *Science* 166:1406-1407 (1969).
90. Mortland, M.M. and T.J. Pinnavaia. "Formation of copper(II) arene complexes on the interlamellar surfaces of montmorillonite," *Nature* 229:75-77 (1971).
91. Soma, Y., M. Soma and I. Harada. "The reaction of aromatic molecules in the interlayer of transition-metal ion-exchanged montmorillonite studied by resonance Raman spectroscopy. I. Benzene and p-phenylenes," *J. Phys. Chem.* 88:3034-3038 (1984).
92. Mortland, M.M. and L.J. Halloran. "Polymerization of aromatic molecules on smectite," *Soil Sci. Soc. Am. J.* 40:367-370 (1976).
93. Vande Poel, D., P. Cloos, J. Helsen and E. Jannini. "Comportement particulier du benzene adsorbe sur la montmorillonite cuivrique," *Bull. Groupe. franc. Argiles* 25:114-126 (1973).

94. Moreale, A., P. Cloos and C. Badot. "Differential behavior of Fe(III)- and Cu(II)-montmorillonite with aniline: I. Suspensions with constant solid:liquid ratio," *Clay Min.* 20:29-37 (1985).
95. Soma, Y. and M. Soma. "Adsorption of benzidines and anilines on Cu- and Fe-montmorillonites studied by Resonance Raman spectroscopy," *Clay Min.* 23:1-12 (1988).
96. Shida, T. *Electronic absorption spectra of radical ions. Physical Sciences data* 34, (New York, NY: Elsevier, 1988) pp. 1-446.
97. Alpert, N.L., W.E. Keiser and H.A. Szymanski. *IR Theory and practice of infrared spectroscopy*, (New York, NY: Plenum Publ., 1973)
98. Farmer, V.C. "The Layer Silicates," In *The infrared spectra of minerals*, Ed. V.C. Farmer. (London: Mineral Society, 1974), pp. 331-359.
99. Santacesaria, E., D. Gelosa, D. Picononi and P. Danise. "The effect of the exchanged cations in the adsorption of p- and m-xylene onto Y zeolite," *J. Colloid Interface Sci.* 98:467-470 (1984).
100. Richards, R.E. and L.V.C. Rees. "Sorption and packing of n-alkane molecules in ZSM-5; *Langmuir* 3:335-340 (1987).
101. Richards, R.E. and L.V.C. Rees. "The sorption of p-xylene in ZSM-5," *Zeolites* 8:35-39 (1988).
102. Marjit, D., P.K. Bishui and S.B. Banerjee. "Vibrational and electronic spectra of meta- and para-dimethoxybenzene," *Indian J. Phys.* 46:457-468 (1972).
103. Ernstbrunner, E., R.B. Girling, W.E.L. Crossman and R.E. Hester. "Free radical studies by resonance raman spectroscopy. Part 1. The 1,4-dimethoxybenzene radical cation," *J. Chem. Soc., Perkins Trans.* 2:177-184 (1978).
104. O'Neill, P., S. Steenken and D. Schulte-Frohlinde. "Formation of radical cations of methoxylated benzenes by reaction with OH radicals,  $Ti^{2+}$ ,  $Ag^{2+}$ , and  $SO_4^-$  in aqueous solution. An optical and conductometric pulse radiolysis and in situ radiolysis electron spin resonance study," *J. Phys. Chem.* 79:2773-2779 (1975).
105. Baker, A.D., D.P. May and D.W. Turner. "Molecular photoelectron spectroscopy. Part VII. The vertical ionisation potentials of benzene and some of its monosubstituted and 1,4-disubstituted derivatives," *J. Chem. Soc.* 22-34 (1968).

106. Wilson, E.B., J.C. Decius and P.C. Cross. *Molecular vibrations: The theory of infrared and Raman vibrational spectra*, (New York: Dover Publications, Inc., 1955) pp. 1-388.
107. Jacox, M.E. "The stabilization and spectra of free radicals and molecular ions in rare gas matrices," *Rev. Chem. Intermed.* 2:1 (1978).
108. Andrews, L. "Laser excitation matrix-isolated spectroscopy," *Appl. Spectros. Rev.* 11:125-120 (1976).
109. Andrews, L. "Spectroscopy of molecular ions in noble gas," *Ann. Rev. Phys. Chem.* 30:79-70 (1979).
110. Miller, T.A. and V.E. Bondybey. "Spectroscopy of molecular ions," *Appl. Spectros. Rev.* 18:105-100 (1982).
111. *Molecular Ions: Spectroscopy, Structure, and Chemistry*, (Amsterdam: North-Holland, 1983)
112. *Radical Ionic Systems*, (Norwell, Ma: Kluwer Academic Publishers, 1991).
113. *Molecular Ions: Geometric and Electronic Structure*, (N.Y.: Plenum Press, 1983).
114. *Ion and Ion Cluster Spectroscopy and Structure*, (Amsterdam: Elsevier Press, 1989).
115. Shida, T., E. Haselbach and T. Bally. "Organic radical ions in rigid systems," *Acc'ts Chem. Rsch.* 17:180 (1984).
116. Shida, T. and I. Iwata. "Electronic spectra of ion radicals and their molecular orbital interpretations. III. Aromatic hydrocarbons," *J. Am. Chem. Soc.* 95:3473-3470 (1973).
117. Shida, T. and W.H. Hamill. "Molecular ions in radiation chemistry. III. Absorption spectra of aromatic hydrocarbon cations and anions in organic gasses," *J. Chem. Phys.* 44:4372-4370 (1966).
118. Kelsall, B.J. and L. Andrews. "Surface electric discharge during sample condensation. A new method for producing and trapping molecular ions," *J. Phys. Chem.* 85:2938-2930 (1981).
119. Andrews, L., B.J. Kelsall and T.A. Blankenship. "Vibronic absorption spectra of naphthalene and substituted naphthalene cations in solid argon," *J. Phys. Chem.* 86:2916-2910 (1982).

120. Kelsall, B.J. and L. Andrews. "Two-color resonance photoionization of aromatic molecules in solid argon," *J. Chem. Phys.* 76:5005-5000 (1982).
121. Friedman, R.S. and L. Andrews. "Photochemical rearrangements of o- and m-dichlorobenzene cations to p-dichlorobenzene cation in solid argon," *J. Am. Chem. Soc.* 107:822-820 (1985).
122. Friedman, R.S., B.J. Kelsall and L. Andrews. "Vibronic absorption spectra of dichloro- and dibromobenzene cations in solid argon at 20K," *J. Phys. Chem.* 88:1944-1940 (1984).
123. Bennema, P., G.J. Hoijsink, J.H. Lupinski, L.J. Oosterhoff, P. Selier and J.D.W. van Voorst. "Photo-ionization of aromatic hydrocarbons in boric acid gasses," *Molecular Phys.* 2:431-430 (1959).
124. Allan, M., E. Kloster-Jensen and J.P. Maier. "Emission spectra of  $\text{Cl}=\text{C}=\text{C}=\text{H}^+$ ,  $\text{Br}=\text{C}=\text{C}=\text{H}^+$ , and  $\text{I}=\text{C}=\text{C}=\text{H}^+$  radical cations," *J. Chem. Soc. Faraday Trans. 2* 73:1406-1400 (1977).
125. Kato, T., N. Muraki and T. Shida. "Resonance raman spectra and excited state geometry of the radical cation of p-dichlorobenzene," *J. Chem. Phys. Letts.* 164:388-380 (1989).
126. Suzer, S. and L. Andrews. "Matrix isolation study of electron impact on  $\text{H}_2\text{O}$  infrared spectrum of  $\text{OH}^-$  in solid argon," *J. Chem. Phys.* 88:916-910 (1988).
127. Sheng, S. and G. Hug. "Single vibronic level resonant raman scattering of molecular ions in solid glass: PMDA anion and naphthalene cation," *Chem. Phys. Letts.* 57:168-160 (1978).
128. Pinnavaia, T.J. and M.M. Mortland. "Interlamellar metal complexes on layer silicates. I. copper(II)-arene complexes on montmorillonite," *J. Phys. Chem.* 75,no. 26:3957-3962 (1971).
129. Whittle, E., D.A. Dows and G.C. Pimentel. "Matrix isolation method for the experimental study of unstable species," *J. Chem. Phys.* 22:1943-1940 (1954).
130. Zeeman, H.D. "Deflection of an ion beam in the two-dimensional electrostatic quadrupole field," *Rev. Sci. Instr.* 48:1079-1070 (1977).
131. Yost, R.A. , (1992) (UnPub)
132. Dahl, D.A. and J.E. Delmore. *The Simion PC/PS2 User's Manual Version 4.0*, (Idaho Falls, Id: Idaho Nat'l Engineering Laboratory, EG&G Idaho Inc., 1988).

133. Szczepanski, J., W. Personette, R. Pellow, T.M. Chandraskhar, D. Roser, M. Cory, M. Zerner and M. Vala. "Vibrational and electronic spectra of matrix-isolated para-dimethylchlorobenzene radical cations," *J. Chem. Phys.* 96: 35 (1992).
134. Szczepanski, J., W. Personette and M. Vala. "Pulsed-glow discharge matrix isolation method for the production and trapping of organic ions: Application to para-dimethoxybenzene," *Chem. Phys. Lett.* 185: 324 (1991).
135. Szczepanski, J. and M. Vala. "Correlation of infrared and UV-visible bands of matrix-isolated carbon clusters," *J. Phys. Chem.* 95:2792-2790 (1991).
136. Kurtz, J. and D. Huffman. "Combined infrared and UV-visible spectroscopy matrix-isolated carbon vapor," *J. Chem. Phys.* 92:30 (1990).
137. Andrews, L. and T.A. Blankenship. "Vibrational spectra of naphthalene and naphthalene-d<sub>8</sub> cations in solid argon," *J. Am. Chem. Soc.* 103:5977-5970 (1981).
138. Shida, T. *Electronic Absorption Spectra of Radical Ions*, (Amsterdam: Elsevier Science Publ., 1988).
139. Salama, F. and L.J. Allamandola. "Electronic absorption spectroscopy of matrix-isolated polycyclic aromatic hydrocarbons. I. The naphthalene cation (C<sub>10</sub>Hg<sup>+</sup>)," *J. Chem. Phys.* 94:6964-6960 (1991).
140. Rogers, E.E., S. Abramowitz, M.E. Jacox and D.E. Milligan. "Matrix isolation studies of infrared spectra of free radicals CCl<sub>3</sub> and CBr<sub>3</sub>," *J. Chem. Phys.* 52:2198-2190 (1970).
141. Lulli, L., D. Bidini, B. Dabin and P. Quantin. "Study of two soils derived from volcanic rocks in southern Italy (Mount Roccamonfina and Vulture), with cryptopodzolic characteristics. 2. Forms of organic matter and phosphorous. General interpretation," *Cah. O. R. S. T. O. M., Ser. Pedol.* 20:45-61 (1983).
142. Maier, G., H.P. Reisenauer, J. Hu, L.J. Schaad and B.A. Hess. "Photochemical isomerization of dihalomethanes in argon matrices," *J. Am. Chem. Soc.* 112:5117-5110 (1990).
143. Maier, G., H.P. Reisenauer, J. Hu, B.A. Hess and L.J. Schaad. "Photomerisierung von tetrachlormethan in einer argon-matrix," *Tetrahedron Lett.* 30:4105-4100 (1989).
144. DeFrees, D.J., M.D. Miller, D. Talbi, F. Pauzat and Y. Ellinger. "Theoretical IR spectra of naphthalene neutral and ionized," *Ap. J.* Submitted:(1992).

145. Muir, D.C.G. and N.P. Grift. "Extraction and cleanup procedures for determination of diaryl phosphates in fish, sediment, and water samples," *J. Assoc. Off. Anal. Chem.* 66:684-690 (1983).
146. Maier, J.P. and O. Marthaler. "Emission spectra of the radical cation 1,3-dichlorobenzene, 1,4-dichlorobenzene, and 1,3,5-trichlorobenzene in the gas phase," *Chem. Phys.* 32:419-410 (1978).
147. Pople, J.A., D.L. Beveridge and J. Dobosh. "A self-consistent molecular orbital theory. V. Intermediate neglect of differential overlap," *J. Chem. Phys.* 47:2026-2020 (1967).
148. Bacon, A.D. and M. Zerner. "An intermediate neglect of differential overlap technique for spectroscopy: Pyridine," *Theoret. Chim. Acta* 53:31-30 (1979).
149. Ridley, J. and M. Zerner. "An intermediate neglect of differential overlap technique for spectroscopy: Pyrrole and the azines," *Theoret. Chim. Acta* 32:111-134 (1973).
150. Zerner, M., G.H. Loew, R.F. Kirchner and J. Mueller-westerhoff. "An intermediate neglect of differential overlap technique for spectroscopy: Transition-metal complexes, ferrocene," *J. Am. Chem. Soc.* 102:589-580 (1980).
151. Dupuis, M., D. Spangler and J.J. Mendolski., (Berkeley, Ca: University of California, Program QG01, 1980).
152. Schmidt, M.W., K.K. Baldridge, J.A. Boatz, J.H. Jensen, S. Koseki, M.S. Gordon, K.A. Nguyen, T.L. Windus and S.T. Elbert. "Normal coordinate calculations," *QCPE Bulletin* 10:52-54 (1990).
153. Almlof, J. *Geometrical Derivatives of Energy Surfaces and Molecular Properties*, D.Reidel: Dordrecht, (1986)
154. DeFrees, D.J. and A.D. McLean. "Molecular orbital predictions of the vibrational frequencies of some molecular ions," *J. Chem. Phys.* 82:333-330 (1985).
155. Rohlfing, E.A. and C.M. Rohling. "Resonant two-photon ionization spectroscopy of jet-cooled p-dichlorobenzene," *J. Phys. Chem.* 93:94-90 (1989).
156. Boatz, J.A. and M.S. Gordon. "Decomposition of normal coordinate vibrational frequencies," *J. Phys. Chem.* 93:1819-1810 (1989).

157. Prochaska, F.T. and L. Andrews. "Matrix photodissociation and photoionization of carbon tetrahalides with noble gas resonance radiation," *J. Chem. Phys.* 67:1091-1090 (1977).
158. Andrews, L. "Infrared detection of trichloromethyl radical in solid argon," *J. Phys. Chem.* 71:2761-2760 (1967).
159. Andrews, L. "Infrared spectrum of the trichloromethyl radical in solid argon," *J. Chem. Phys.* 48:972-970 (1968).
160. Jacox, M.E. and D.E. Milligan. "Matrix isolation study of the vacuum-UV photolysis of chloroform. Infrared spectra of the  $\text{CCl}_3^+$ ,  $\text{HCCl}_2^+$ , and  $\text{HCCl}^-$  molecular ions," *J. Chem. Phys.* 54:3935-3930 (1971).
161. Andrews, L., B.J. Kelsall, J.H. Miller and B.W. Keelan. "Absorption spectrum of carbon tetrachloride molecular cation in noble-gas matrices," *J. Chem. Soc. Faraday Trans. 2*, 79:1417 (1983).
162. O'Neill, P., S. Steenken and D. Schulte-Frohlinde. "Formation of radical cation of methoxylated benzenes by reaction with OH radicals,  $\text{Tl}_2^+$ ,  $\text{Ag}_2^+$ , and  $\text{SO}_4^-$  in aqueous solution. An optical and conductometric pulse radiolysis and in situ radiolysis electron spin resonance study," *J. Phys. Chem.* 79:2773-2770 (1975).

**SECTION IX**

**APPENDIX**

# MASS SPECTROMETER PGM: MASSSPEC

```

/* MASSSPEC.C : ACQUISITION PROGRAM FOR THE MASS-SPECTROMETER */

/*=====*/

#include <dos.h>
#include <stdio.h>
#include <math.h>
#include <stdlib.h>
#include <conio.h>

/*=====*/
/* DEFINE 16 bit words for controlling the IBM BOARD */

#define IBM_BOARD      0x02e2 /*CARDNUMBER*/
#define REGISTER_0     0x0000 /*ARCRO*/
#define REGISTER_1     0x1000 /*AWCRO*/
#define REGISTER_2     0x2000 /*ARRO*/
#define REGISTER_3     0x3000 /*AWRO*/
#define INTERRUPT      0xD000 /*ICRO*/
#define DEVICESELECT    0xC000 /*IDNRO*/
#define ANALOGINOUT     0x0009 /*ADC*/
#define SET_TO_0        0x0000 /*DAI*/
#define ENABLE          0x0001 /*EAAD*/
#define DISABLE         0x0000 /*DAAD*/
#define CHANNEL_0       0x0000

#define READY          -14    /* -14 = 0xfff2 which means conversion
complete */

/*=====*/

#define CONSTANT 5.12 /*4096./800*/

/*=====*/

main()
{
FILE *filehandle;
char filename[20];
unsigned long int in[5000], cum[5000];
float masslow = 0., masshigh = 0., inttofloat = 0;
unsigned int scannumber = 0, i = 0, voltlow = 0, volthigh = 0, j = 0;
unsigned int status;
char choice;

/*=====*/

for( i = 0 ; i<= 5000 ; i++)
{
    cum[i] = 0; /* set cum[] to 0 */
    in[i] = 0; /* set in[] to 0 */
}; /* end for */

/*=====*/
/* ASK the name of the data file, the mass range and the number of scans
*/

```

# MASS SPECTROMETER PGM: MASSSPEC

```

/* A do {} while loop controls that the mass range is acceptable */
printf("\n\t\t - MASS SPECTROMETER -\n\n");

printf("\nName data file : ");
scanf("%s", filename);
if ((filehandle = fopen(filename, "w")) == NULL)
{
    fprintf(stderr, "\nCannot open data file. Press RETURN\n");
    getch();
    exit(1);
}

do {
    printf("Enter mass range (Min,Max - between 1 and 800): ");
    scanf("%f,%f", &masslow, &masshigh);
} while (masslow < 1 || masshigh > 800 || masslow >= masshigh);

voltlow = floor(masslow * CONSTANT);
volthigh = floor(masshigh * CONSTANT);
/*printf("\n voltlow = %d\t volthigh = %d\n", voltlow, volthigh);*/

printf("Enter number of scans : ");
scanf("%d", &scanumber);

printf("\n PRESS ANY KEY WHEN READY");
getch();

/*=====*/
/* PREPARE THE BOARD */

outport(IBM_BOARD + INTERRUPT, SET_TO_0);
outport(IBM_BOARD + DEVICESELECT, ANALOGINOUT);
outport(IBM_BOARD + REGISTER_1, CHANNEL_0);
outport(IBM_BOARD + REGISTER_0, CHANNEL_0 + DISABLE);

delay(1);

/*=====*/
/* ACQUISITION LOOP */

printf("\n Acquisition running");
for( j = 1 ; j <= scanumber ; j++)
{
    for( i = voltlow ; i <= volthigh ; i++)
    {
        outport(IBM_BOARD + REGISTER_3, i);
        delay(10);*/
        outport(IBM_BOARD + REGISTER_0, ENABLE);
        do {} while (inport(IBM_BOARD + REGISTER_0) != READY);
        outport(IBM_BOARD + REGISTER_0, DISABLE);

        in[i] = inport(IBM_BOARD + REGISTER_2);
        cum[i] += in[i];
    }; /* end for 2 */
}

```

# MASS SPECTROMETER PGM: MASSSPEC

```

    }; /* end for 1 */

/*=====*/

printf("\n Acquisition complete\n");
printf("\n\t %d %d\n", voltlow, cum[voltlow]);
printf("\t %d %d\n", volthigh, cum[volthigh]);
printf("\n\t WAIT");

do
    {
        printf("\n Saving data for: (1) QUATTRO PRO / (2) SPECTRA-CALC\n");
        } while ((choice=getch()) != '1' && choice != '2');

printf("\n Data storage");
if (choice == '1')
    {
        for(i = voltlow ; i <= volthigh ; i++)
            {
                fprintf(filehandle, "%f %f\n", (inttofloat=i)/CONSTANT,
(inttofloat=cum[i])/scanumber);
            }; /* end for */
    }
else
    {
        fprintf(filehandle, "%d\n%f\n%f\n0\n0\n1", 1 + volthigh - voltlow,
(inttofloat=voltlow)/CONSTANT, (inttofloat=volthigh)/CONSTANT);
        for(i = voltlow ; i <= volthigh ; i++)
            {
                fprintf(filehandle, "\n%f", (inttofloat=cum[i])/scanumber);
            }; /* end for */
        }; /* end if */

fclose(filehandle);
} /* end main */

/*=====*/

```

# MASS SPECTROMETER PGM: MASSTRAC

```

printf("\nName data file : ");
scanf("%s", filename);
if ((filehandle = fopen(filename, "w")) == NULL)
{
    fprintf(stderr, "\nCannot open data file. Press RETURN\n");
    getch();
    exit(1);
}

do {
    printf("\n Enter mass (between 1 and 800): ");
    scanf("%f", &mass);
} while (mass < 1 || mass > 800);

volt= floor(mass * CONSTANT);

printf("\n Enter number of accumulations : ");
scanf("%d", &cumnumber);

do {
    printf("\n Enter number of points recorded : ");
    scanf("%d", &pointnumber);
} while (pointnumber < 1 || pointnumber >= 5000);

for( time=0 ; time<pointnumber ; time++)
{
    cum[time] = 0;
    in[time] = 0;
} /* end for */

/*=====*/
/* PREPARE THE BOARD */

output(IBM_BOARD + INTERRUPT, SET_TO_0);
output(IBM_BOARD + DEVICSELECT, ANALOGINOUT);
output(IBM_BOARD + REGISTER_1, CHANNEL_0);
output(IBM_BOARD + REGISTER_0, CHANNEL_0 + DISABLE);

delay(1);

/*=====*/
/* ACQUISITION LOOP */
printf("\n PRESS ANY KEY FOR STARTING");
getch();
printf("\n Acquisition running");

for(time=0 ; time<pointnumber ; time++)
{
    for( scannumber=1 ; scannumber<=cumnumber ; scannumber++ )
    {
        output(IBM_BOARD + REGISTER_3, volt);
        output(IBM_BOARD + REGISTER_0, ENABLE);
        do {} while (inport(IBM_BOARD + REGISTER_0) !=
READY);
    }
}

```

# MASS SPECTROMETER PGM: MASSTRAC

```

/* MASTRACK.C : ACQUISITION PROGRAM FOR THE MASS-SPECTROMETER */
/*          PULSE VALVE ARGON ION SOURCE */
/* On this program, we will set the output voltage to a value
/* corresponding a specified mass . Then we will scan and accumulate */
/* cumnumber times. */

/*=====*/

#include <dos.h>
#include <stdio.h>
#include <math.h>
#include <stdlib.h>

/*=====*/
/* DEFINE 16 bit words for controlling the IBM BOARD */

#define IBM_BOARD      0x02e2 /*CARDNUMBER*/
#define REGISTER_0     0x0000 /*ARCRO*/
#define REGISTER_1     0x1000 /*AWCRO*/
#define REGISTER_2     0x2000 /*ARRO*/
#define REGISTER_3     0x3000 /*AWRO*/
#define INTERRUPT      0xD000 /*ICRO*/
#define DEVICESSELECT  0xC000 /*IDNRO*/
#define ANALOGINOUT    0x0009 /*ADC*/
#define SET_TO_0       0x0000 /*DAI*/
#define ENABLE         0x0001 /*EAAD*/
#define DISABLE        0x0000 /*DAAD*/
#define CHANNEL_0      0x0000

#define READY          -14    /* -14 = 0xffff2 which means conversion
complete */

/*=====*/

#define CONSTANT  5.12 /*4096./800*/

/*=====*/

main()
{
FILE *filehandle;
char filename[20], choice;
unsigned long int in[5000], cum[5000];
float inttofloat = 0., mass = 0.;
int time = 0, volt = 0;
int cumnumber = 0, pointnumber = 0, scannumber = 0;

/*=====*/
/* print title */

printf("\n\t\t- MASS TRACKING PROGRAM -\n\n");

/*=====*/
/* ASK the name of the data file, the mass and the number of scans */
/* A do {} while loop controls that the mass is acceptable */

```

# MASS SPECTROMETER PGM: MASSTRAC

```

        output(IBM_BOARD + REGISTER_0, DISABLE);

```

```

/*          in[time] = inport(IBM_BOARD + REGISTER_2);
           in[time] = 1.;*/
           cum[time] += in[time];
           }; /* end for 2 */
/*      delay(25);*/
           }; /* end for 1 */

```

```

. /*=====*/
/* DATA STORAGE */

```

```

do
{
    printf("\n Saving data for: (1) QUATTRO PRO / (2) SPECTRA-CALC\n");
    } while ((choice=getch()) != '1' && choice != '2');

```

```

printf("\n Data storage\t-\tWAIT");

```

```

if (choice == '1')
{
    fprintf(filehandle, "%f\n\n", (inttofloat=volt)/CONSTANT);
    for( time=0 ; time<pointnumber ; time++)
    {
        fprintf(filehandle, "%d,%f\n", time,
(inttofloat=cum[time])/cumnumber);
    }; /* end for */
}
else
{
    fprintf(filehandle, "%d\n0\n%d\n0\n0\n1", pointnumber, pointnumber);
    for(time = 0 ; time <= pointnumber ; time++)
    {
        fprintf(filehandle, "\n%f",
(inttofloat=cum[time])/cumnumber);
    }; /* end for */
}; /* end if */

```

```

fclose(filehandle);
} /* end main */

```

```

/*=====*/

```

# MASS SPECTROMETER PGM: PULSE\_AC

```

/* PULSE_AC.C : ACQUISITION PROGRAM FOR THE MASS-SPECTROMETER */
/* This program synchronizes a laser pulse or a pulsed valve and the */
/* acquisition of data from the mass spec. */
/* */
/* The timing is the following : */
/*   - Set the mass-spec voltage to one particular mass */
/*   - Initialise the counter/timer of the IBM board, */
/*   - Initialise the Analog-input system of the board, */
/*   - Start the countdown of the clock, */
/*   - Start the acquisition loop while the countdown finishes and */
/*     trig the laser. */
/* We will scan SCANUMBER time 2000 25-ms-long periods during which we */
/* will perform 100 accumulations. */
/* */
/*           { *---/---/---/---/---/... (2000 x) .../---/--- */
/*           { *---/---/---/---/---/... (2000 x) .../---/--- */
/*           { *---/---/---/---/---/... (2000 x) .../---/--- */
/* (scanumber x) . */
/* . */
/* . */
/*           { *---/---/---/---/---/... (2000 x) .../---/--- */
/* */

/*           - DESCRIPTION OF THE ACQUISITION LOOP - */

/* { *           ---           ---           ...           --- */
/* (launch the) (1st period) (2nd period)           (2000th period) */
/* (counter)    (accumulate) (accumulate)           (accumulate) */
/*           (100 records) (100 records)           (100 records) */

/*=====*,
#include <dos.h>
#include <stdio.h>
#include <math.h>
#include <stdlib.h>

/*=====*,
/* DEFINE 16 bit words for controlling the IBM BOARD and the Analog-In-out
*/
/* system. */

#define IBM_BOARD      0x02e2

#define DEVICESSELECT  0xc000
#define ANALOGINOUT    0x0009
#define INTERRUPT      0xD000
#define CHANNEL_0      0x0000

#define REGISTER_0     0x0000
#define REGISTER_1     0x1000
#define REGISTER_2     0x2000
#define REGISTER_3     0x3000
#define REGISTER_8     0x8000
#define REGISTER_9     0x9000
#define REGISTER_10    0xa000

```

# MASS SPECTROMETER PGM: PULSE\_AC

```

#define REGISTER_11    0xb000

#define SET_TO_0       0x0000
#define ENABLE         0x0001
#define DISABLE        0x0000
#define CHANNEL_0      0x0000

#define READY          -14/* -14 = 0xfff2 which means conversion complete */
/*=====*/
/* DEFINE words for controlling the counter/timer of the IBM board.
*/

#define COUNT_2        0x80
#define LSB_MSB        0x30

#define MODE_0         0x00
#define MODE_2         0x04
#define MODE_3         0x06
#define MODE_4         0x08

#define BINARY_COUNT   0x00

/*=====*/

#define CONSTANT        5.12 /*4096./800*/
#define SIZE            5000
#define KILO_HERTZ      10 /* The clock of the counter must be set at 10 kHz.*/
/*=====*/

main()
{
FILE *filehandle;
char filename[20];
unsigned long int record =0, accumulated[SIZE];
float inttofloat = 0., mass = 0.;
int trigdelay =0, countdelay =0, pulse =0, point =0, increment =0;
int volt =0, pulsenummer =0, pointnumber =0, cumnumber =0;

/*=====*/
/* ASK the name of the data file, the mass range and the number of scans
*/
/* A do {} while loop controls that the mass range is acceptable */

printf("\n\t\t - MASS SPECTROMETER -\n\n\t\t - PULSE ACCUMULATION PROGRAM
-");

printf("\n\nName data file : ");
scanf("%s", filename);
if ((filehandle = fopen(filename, "w")) == NULL)
{
fprintf(stderr, "\nCannot open data file. Press RETURN\n");
getch();
exit(1);
}

```

# MASS SPECTROMETER PGM: PULSE\_AC

```

/*=====*/
/* Ask mass tracked, number of accumulation and number of points recorded.
*/

do {
    printf("\n Enter mass tracked (between 1 and 800): ");
    scanf("%f", &mass);
} while (mass < 1 || mass > 800);

volt= floor(mass * CONSTANT);

printf("\n Enter number of pulses added : ");
scanf("%d", &pulsenumber);

do {
    printf("\n Enter number of points recorded (<= 4999): ");
    scanf("%d", &pointnumber);
} while (pointnumber < 1 || pointnumber >= 5000);

printf("\n Enter number of accumulation : ");
scanf("%d", &cumnumber);

for( point = 0 ; point < pointnumber ; point++)
    {
        accumulated[point] = 0;
    } /* end for */

/*=====*/
/* Ask the time delay before triggering the lamp of the laser. */
/* The time delay will be entered in milliseconds and converted into a
*/
/* number of count (countnumber). */
/* NOTICE : IT IS ASSUMED THAT THE CLOCK USED TO TRIGGER THE COUNTER 2 OF
*/
/* THE IBM BOARD IS SET TO 10 kHz. */
/* IF THE FREQUENCY IS CHANGED, DO NOT FORGET TO MODIFY "KILO_HERTZ"
*/

printf("\n Verify clock frequency , must be 10 kHz.");
printf("\n Enter laser trigger delay (ms) : ");
scanf("%d", &trigdelay);
countdelay = trigdelay * KILO_HERTZ;

/*=====*/
/*=====*/
/* PREPARE THE BOARD */

outport(IBM_BOARD + INTERRUPT, SET_TO_0);
outport(IBM_BOARD + DEVICESSELECT, ANALOGINOUT);
outport(IBM_BOARD + REGISTER_1, CHANNEL_0);
outport(IBM_BOARD + REGISTER_0, CHANNEL_0 + DISABLE);

delay(1);

```

MASS SPECTROMETER PGM: PULSE\_AC

```

/*=====*/
/* ACQUISITION LOOP */
/*=====*/

printf("\n\n\t\t PRESS ANY KEY FOR STARTING\n\n\n\n\n\n\n\n");
getch();
printf("\n\n\t\t - Acquisition running -");

for( pulse = 1 ; pulse <= pulsenummer ; pulse++ )
{
    /*=====*/
    /* Prepare the counter/timer and launch it to trigger the laser */
    /* LAMP. */
    /* NOTICE : the laser pulse will be delayed by the counter/timer */
    /* and the Q-SWITCH delay of the Nd-Yag laser. */
    /*=====*/

    output(IBM_BOARD + REGISTER_11, COUNT_2 + LSB_MSB + MODE_0 +
BINARY_COUNT);
    delay(1);
    output(IBM_BOARD + REGISTER_10, countdelay);

    /*=====*/
    for(point = 0 ; point < pointnumber ; point++)
        {
            for( increment=1 ; increment<=cumnumber ; increment++ )
                {
                    output(IBM_BOARD + REGISTER_3, volt);
                    output(IBM_BOARD + REGISTER_0, ENABLE);
                    do {} while (inport(IBM_BOARD + REGISTER_0) !=
READY);

                    output(IBM_BOARD + REGISTER_0, DISABLE);

                    record = inport(IBM_BOARD + REGISTER_2);
                    record = 1.;*/
                    accumulated[time] += record;
                }; /* end for 3 */
            }; /* end for 2 */
            delay(1);
        }; /* end for 1 */

    /*=====*/
}
/* DATA STORAGE LOOP. */
/*=====*/

printf("\n acquisition complete.");
do
{
    printf("\n Saving data for: (1) QUATTRO PRO / (2) SPECTRA-CALC\n");
    } while ((choice=getch()) != '1' && choice != '2');

printf("\n Data storage\t-\tWAIT");

if (choice == '1')
{
    fprintf(filehandle, "%f\n\n", (inttofloat=volt)/CONSTANT);
    for( point = 0 ; point < pointnumber ; point++)
    {

```

# MASS SPECTROMETER PGM: PULSE\_AC

```

        fprintf(filehandle, "%d,%f\n", point,
(inttofloat=accumulated[point])/cumnumber);
    }; /* end for */
}
else
{
    fprintf(filehandle, "%d\n0\n%d\n0\n0\n1", pointnumber, pointnumber);
    for(point = 0 ; point <= pointnumber ; point++)
    {
        fprintf(filehandle, "\n%f",
(inttofloat=accumulated[time])/cumnumber);
    }; /* end for */
}; /* end if */

fclose(filehandle);
} /* end main */

/*=====*/

```